Interferometric observations to analyze circumstellar environments and planetary formation

Guillaume Schworer

Ph.D. Manuscript

of Paris Sciences and Lettres PSL Research University
and The University of Sydney

Prepared at L'Observatoire de Paris
& at The University of Sydney

Interferometric observations to analyze circumstellar environments and planetary formation

Ecole doctorale n°127
Astronomie & Astrophysique d'Île-de-France

ASTRONOMY & ASTROPHYSICS

JURY MEMBERS:

Astronome PELAT Didier
Observatoire de Paris, President

Prof. WYATT Mark
University of Cambridge, Reviewer

Dr. FEDELE Davide
Osservatorio Astrofisico di Arcetri, Reviewer

Dr. KELLERER Aglaé
University of Cambridge, Examiner

Astronomer RIDGWAY Stephen
National Optical Astronomy Observatories, Examiner

Prof. TINNEY Christopher
University of New South Wales, Examiner

Astronome COUDE du FORESTO Vincent
Observatoire de Paris, Director

Prof. TUTHILL Peter
The University of Sydney, Director

Defended by Guillaume **SCHWORER**
On the 11th of October 2016

Directed by **Vincent Coudé du FORESTO**
& **Peter TUTHILL**
& **Sylvestre LACOUR**

l'Observatoire de Paris

THE UNIVERSITY OF SYDNEY

PSL RESEARCH UNIVERSITY PARIS

The University of Sydney
Observatoire de Paris

Ecole doctorale 127
Astronomie & Astrophysique d'Île-de-France

Laboratoire d'Etudes Spatiales et d'Instrumentation en Astrophysique
Sydney Institute for Astronomy

Ph.D

To obtain the title of Ph.D of Science
Astronomy & Astrophysics

Guillaume Schworer

Interferometric observations to analyze circumstellar environments and planetary formation

Thesis Advisors : Peter Tuthill
Vincent Coudé du Foresto
Sylvestre Lacour

Oral Defense on the 11th of October 2016
Jury :

Mr Didier Pelat	*President*
Mr Mark Wyatt	*Reviewer*
Mr Davide Fedele	*Reviewer*
Ms Aglaé Kellerer	*Committee Member*
Mr Stephen Ridgway	*Committee Member*
Mr Christopher Tinney	*Committee Member*
Mr Vincent Coudé du Foresto	*Director*
Mr Peter Tuthill	*Director*

United Nations Universal Declaration of Human Rights

1948

Article 27

1. Everyone has the right freely to participate in the cultural life of the community, to enjoy the arts and to share in scientific advancement and its benefits.

2. Everyone has the right to the protection of the moral and material interests resulting from any scientific, literary or artistic production of which he is the author.

Abstract

Interferometric observations to analyze circumstellar environments and planetary formation

Abstract: The dust- and gas-rich disks surrounding numerous pre-main-sequence stars are of key interest for unveiling how planetary system are formed, and are the initial conditions for planetary formation. Protoplanetary disks have a rich structure, with different physics, e.g., radiation, gravitation, electrostatic, magnetohydrodynamics, playing a role in different regions of the disk. They are under constant evolution, due to a combination of various physical and chemical processes, e.g., accretion, photo-evaporation, gas-dust interactions, grain growth, and the potential interaction with massive bodies forming within the disk. The overall disk structure, and hence its observational appearance, is a good proxy for the ongoing processes.

The dynamic ranges involved span two to five orders of magnitudes on spatial scales, orbital times, temperatures, and much more in dust- or gas-densities. The extreme dynamic ranges involved in the structure and composition of these objects mean that very different observational techniques have to be combined together to probe their various regions. This work makes use of new interferometric and spectroscopic measurements in the infrared, together with published mid-infrared images and spectral energy distribution (SED) fluxes from UV to mm-wavelength, to instruct a new comprehension of the well-known IRS-48 object, and uncover part of the delicate balance of physical processes at stake.

This PhD reports the first direct imaging of the full extents of a polycyclic aromatic hydrocarbon and very small grains ring in a young circumstellar disk, presents a revised model for the IRS-48 object to explain the rich and complex dust- and gas-environment observed from near-infrared to centimeter wavelengths, and sets limits on how much silicates grains, hence replenishment, is to be expected in the PAH and VSG ring. Finally, the spectral type of the spectroscopic binary MWC-361 is tentatively determined. This should lead to a precise characterization of the stellar parameters of this binary, open a new window on the studying of the disappearance of the circumsecondary disk of the binary, while the circumprimary disk is present.

The leitmotif throughout this thesis is the understanding of the last moments of circumstellar disks, and the search for the processes which dissipate them. This particular step of the disk-evolution is one the most mysterious to date, yet it sets critical constraints on the by-product of circumstellar disks, exoplanets. Indeed, disk-dissipation corresponds to the removal of the material available in the disk, de facto setting an end to planetary formation.

Keywords: Disk dissipation – circumstellar disk – young stellar object

Réesumé

Observations interférométriques pour l'analyse des environnements circumstellaires et de la formation planétaire

Abstract:

La poussière et le gaz qui entourent beaucoup d'étoiles jeunes est d'un intérêt critique pour comprendre la formation planétaire; ils représentent les conditions initiale de la formation planétaire. Les disques proto-planétaire ont une structure riche, avec différents processus physiques à l'œuvre dans différentes régions du disque. Les grandeurs en jeu s'étalent sur 2 à 5 ordres de grandeur en échelles spatiales, période orbitale, températures, et bien plus en ce qui concerne la densité de gaz et poussière. Les variations extrêmes de ces paramètres clés impliqués dans la structure et la composition de ces objets implique nécessairement l'utilisation combinée de différentes techniques d'observation.

Cette recherche se base sur l'utilisation de nouvelles données d'imagerie et de masquage de pupille (SAM) en bandes K, L et M, de spectres entre 3 et 4 microns, en plus d'images à 8.6 et 18.7 microns et de données de densité spectrale de flux (SED) issus de la littérature. Ces données des UV aux longueurs d'ondes millimétriques ont permis de construire une nouvelle compréhension de l'objet IRS-48, et de mettre en avant l'équilibre subtil des processus physiques en jeu.

Ce travail a permis d'imager pour la première fois l'intégralité spatiale d'un disque composé d'hydrocarbures polycyclique aromatique (PAH) et de très petits grains (VSG) autour d'un objet stellaire jeune. Il propose un modèle révisé pour cet objet de faÃ§on à expliquer l'environnement riche et complexe de gaz et poussières observé en proche infrarouge et en ondes millimétriques, et pose des limites sur la quantité attendue de grains silicatés - synonymes de renouvellement du disque - qui peut se trouver dans ce disque de PAH/VSG.

Une modélisation en transfert radiatif de la structure du disque et de la composition des grains converge vers un disque externe à 55 AU composé de grains classiques, en plus d'un disque non-sédimenté de PAH et VSG dont les bords internes et externes sont résolus: 11 et 26 AU. Une étoile plus brillante - donc plus large - associée à une adaptation des courbes de rougissement permet d'expliquer les flux observés dans le proche-infrarouge: le disque très interne à l'étoile, à 1 AU environ, n'est plus nécessaire. Les nouveaux paramètres stellaires permettent d'estimer un âge de 4.2 millions d'années pour cet objet, beaucoup plus jeune que les estimations précédentes, et en meilleur accord avec l'enviornnement direct de l'étoile et les statistiques de dispersion de tels disques. L'utilisation de clôtures de phase a permis de détecter deux sur-brillances au sein du disque de PAH, dont la température de couleur correspond à la température des grains de ce disque trouvée grâce au transfert radiatif. Une surbrillance suit une orbite circulaire sous-Keplerienne. Ce travail a permis de montrer qu'une quantité limitée de grains classiques silicatés est localisée dans le disque de PAH, avec un facteur de déplétion de 5-6 par rapport aux abondances classiques de

poussière-à-PAH. Un compagnon d'environ 3 masses de Jupiter sur une orbite à 40 AU est compatible avec la nouvelle structure du disque et la précédente observation d'une asymétrie de grain millimétriques.

Le disque d'IRS-48 est dépourvu de poussière dans ses premiers 55 AU, à l'exception de 3.7×10^{-10} masses solaire d'une mixture de PAH neutres, ionisés, et de VSG. Ceci place IRS-48 au stade final des disques de transition, lorsque la photo-évaporation commence á dominer l'évolution du disque jusqu'á dispersion.

Mots-clés: Dissipation des disques – disques circumstellaires – objets stellaires jeunes

Acknowledgments & Foreword

This report presents research work carried out during a 37.5 month PhD Thesis performed jointly (in the frame of a "cotutelle") at the University of Sydney, in the Sydney Institute for Astronomy (SifA), under the supervision of Professor Peter Tuthill and at Observatoire de Paris, in the Laboratoire d'Etudes Spatiales et d'Instrumentation en Astrophysique (LESIA), under the supervision of Astronome Vincent Coudé du Foresto. The first half of this research period was spent in Sydney (until March 2015); I spent the second half in Paris up until the oral defense which took place on the 11th of October 2016 at L'Observatoire de Paris. This led to the granting of the "joint PhD in Astrophysics" degree from both universities.

The "science" part on IRS-48 an MWC-361 was carried out mainly in Paris, while the Sydney part mainly focused on instrumental and observational work. For the sake of presenting a manuscript having a consistent story-line (this was a requirement), the main body – chapter 3 – only focuses on the science of IRS-48. Other projects and works are left in appendices, although they represent more work than that done on IRS-48.

Unless specifically noted, every single line of code used in that work was designed, written and tested by myself, in python: the interferometric data model-fitting, the orbital-fitting, the vampires quickview, and many other utilities and plotting procedures that I could not possibly fit in this section.

I thank Mike, Olli, Gael, Chris, Nic who all played a direct role in the CHARA data I acquired on MWC-361. Vicente for teaching me LBI at CHARA and how to prepare an observation on Mount Wilson, both logistically and technically.

Theo, Lazlo, Judith, Larry for showing me the labs and old telescopes at the Mount Wilson Observatory and giving me much appreciated lifts to and from the summit; more generally for all the work they put on Mount Wilson (among many others).

Nem, Olivier, Garima from the Subaru Telescope for the work, hikes and fun at

the summit. Although the work load up-there was quite insane (who would have guessed that people actually go to Hawaii to work), they were always up for a beer, a hike, a talk or weird cross-fit videos.

Stephen, Daniel, Guy for the wealth of information I learnt from our talks on stellar parameters, PAH, interferometry.

Tricia, Geraldine, Alexis and all administrative ladies and gents who made this incredible experience (officially) possible.

Sylvestre, Nuria, Christophe for observing IRS-48 and providing insightful comments on the draft of the article.

Peter and Vincent who gave me the right amount of freedom (and guidance) in their PhD directors role to help me access the private club of "Dr".

I thank my parents and brother for their perpetual support in my crazy projects, as well as all mates and colleagues from France and Australia who enormously contributed to putting some fun into my PhD. Random keywords which will for sure ring bells for the years to come: pork roll, Raglan, Astro-Grad-Beer talks, Manly beach, Le Central, reduced χ^2, PicSat, ... among many others.

Many people had various levels of implication and support in my Ph.D. If I were to thank only two people, it would be Nick, a Kiwi post-doc who took time to read/hear and profusely comment my manuscript and oral presentation when I critically needed proofing (along with coffees in Sydney & Paris and Mai-tais in Hawaii), and Aygul, my wife, for her constant support and understanding.

And to finally put some philosophy into this Ph.D (Doctor of Philosophy), here is one of my favorite quotes (which becomes interesting once you look at it through contraposition):

If you are out to describe the truth, leave elegance to the tailor.
Albert Einstein

Ne me trompé-je point, s'écria la Marquise, ou si je vois où vous me voulez mener ? M'allez-vous dire "Les étoiles fixes sont autant de soleils ; notre soleil est le centre d'un tourbillon qui tourne autour de lui ; pourquoi chaque étoile fixe ne sera-t-elle pas aussi le centre d'un tourbillon qui aura un mouvement autour d'elle ? Notre soleil a des planètes qu'il éclaire ; pourquoi chaque étoile fixe n'en aura-t-elle pas aussi qu'elle éclairera ?" Je n'ai à vous répondre, lui dis-je, que ce que répondit Phèdre à Oenone : "C'est toi qui l'as nommé".

Mais, reprit-elle, voilà l'univers si grand que je m'y perds ; je ne sais plus où je suis, je ne suis plus rien. Quoi! tout sera divisé en tourbillons jetés confusément les uns parmi les autres ! Chaque étoile sera le centre d'un tourbillon, peut-être aussi grand que celui où nous sommes ! Tout ce espace immense qui comprend notre soleil et nos planètes, ne sera qu'une petite parcelle de l'univers ! autant d'espaces pareils, que d'étoiles fixes ! Cela me confond, me trouble, m'épouvante. Et moi, répondis-je, cela met à mon aise. Quand le ciel n'était que cette voûte bleue où les étoiles étaient clouées, l'univers me paraissait petit et étroit, je m'y sentais comme oppressé. Présentement qu'on a donné infiniment plus d'étendu et de profondeur à cette voûte en la partageant en mille et mille tourbillons, il me semble que je respire avec plus de liberté, et que je suis dans un plus grand air, et assurément l'univers a toute une autre magnificence. La nature n'a rien épargné en le produisant ; elle a fait une profusion de richesses tout-à-fait digne d'elle. Rien n'est si beau à se représenter que ce nombre prodigieux de tourbillons, dont le milieu est occupé par un soleil qui fait tourner des planètes autour de lui. Les habitants d'une planète d'un de ces tourbillons infinis voient de tous côtés les soleils des tourbillons dont ils sont environnés...

Entretiens sur la pluralité des mondes (1686), Bernard Le Bouyer de Fontenelle

Contents

List of Figures

List of Tables

List of acronyms

ALMA	Atacama Large Millimeter/submillimeter Array
AO	Adaptive Optics
AU	Astronomical Unit
BIC	Bayesian Information Criteria
CONICA	COude Near-Infrared Camera
CR	Contrast Ratio
CTG	Classical Thermal Grains
CTTS	Classical T-Tauri Star
DEC	Declination
ELT	Extremely Large Telescope
ESO	European Southern Observatory
FFT	Fast Fourier Transform
FIR	Far InfraRed
FOV	Field Of View
FS	Flat Spectrum
FT	Fourier Transform
IR	InfraRed
ISM	InterStellar Medium
JD	Julian Date
LBI	Long Baseline Interferometry
LBT	Large Binocular Telescope
LRT	Likelihood Ratio Test
LTE	Local Thermodynamic Equilibrium
MC	Monte-Carlo
MCMC	Markov-Chain Monte-Carlo
MIR	Mid InfraRed
MS	Main Sequence (star)
NaCo	NAOS + CONICA

NAOS	Nasmyth Adaptive Optics System
NIR	Near InfraRed
NRM	Non-Redundant Masking
PA	Position Angle
PAH	Polycyclic Aromatic Hydrocarbon
PMS	Pre Main Sequence (star)
PSF	Point Spread Function
RA	Right Ascension
RMS	Root Mean Square
SAM	Sparse Aperture Masking
SED	Spectral Energy Distribution
SNR	Signal to Noise Ratio
SUSI	Sydney University Stellar Interferometer
T3	Closure phases
TTS	T-Tauri Star
UV	Ultra Violet
VIS2	Squared visibility
VLT	Very Large Telescope
VSG	Very Small Grains
VSP	Very Small Particles
WTTS	Weak T-Tauri Star
YSO	Young Stellar Object

Chapter 1

Introduction to Young Stellar Environments

Contents

Never memorize something that you can look up.
Albert Einstein

This chapter will detail theories and facts on circumstellar disks; their structure, their evolution and the key physical processes that drive their dispersal and planetary formation. The aim is to bring all necessary disk-related information to be defined for the chapters to come. It should be read as a condensed view of the state-of-the-art, providing a wealth of references on the main disk topics. After bringing some general context to the reader, this chapter will focus first on the initial conditions and constraints that lead to disk formation, and later on the evolution and properties of disks once the stars have formed. Finally, it will give the outline of this thesis.

1.1 Context

The dust- and gas-rich disks surrounding numerous Pre-Main-Sequence (PMS) stars are of key interest for studying how planetary system are formed. Indeed, they are the initial conditions for planetary formation and can be defined as gravitationally rotating structures of gas and dust that surround young stars. The first Hubble Space Telescope images of such objects in silhouette against the background light in the Orion

Nebula (McCaughrean & O'dell 1996; O'dell & Wen 1994) and the subsequent observational and theoretical studies have spawned and fostered an enormous momentum around such objects, leading to a better understanding of how they are formed, how they evolve, what they look like, and how they are finally dissipated. Even though current models fail to explain the complexity of circumstellar disks and bind their birth and evolution to the tremendous variety of observed planetary systems, a general understanding is achieved.

Protoplanetary disks are the remnants of the star-formation process which extracts the most naturally the excess angular momentum of an original parent cloud as compared to that of a single central-star. Similarly, debris disks are the remnants of the planetary-formation process: gas-poor structures around older stars whose properties reflect the collisional evolution of a population of small bodies such as comets or asteroids (Wyatt 2008).

Like most extensive phenomena in astronomy, the evolution of such young circumstellar disks can hardly be observed in individual objects and hence must instead be inferred from statistical studies of populations. Indeed, protoplanetary disks are persistent: the typical disk-lifetime of a few million years relates to thousands of dynamical times at 100 astronomical unit (AU) to millions of dynamical times at 0.5 AU (Haisch et al. 2001). Furthermore, the problem is compounded by the fact that disks dissipate quickly enough compared to the life-time of stars, such that only a small sample is at reach in our neighborhood. Astronomers are left with a few hundreds of objects, making difficult the statistical study of their numerous properties.

Protoplanetary disks have a rich structure, with different physics playing a role in different regions of the disk. A schematic representation of a typical object is shown in Figure 1.1. The dynamic ranges involved span four to five orders of magnitudes on the spatial scales ($\sim$ 0.02 to 1000 AU), four to five in orbital times ($\sim$ a month to thousands of years), two to three in temperatures ($\sim$ 20 K to $\gg$1000 K), and much more in dust or gas densities. The extreme dynamic ranges involved in the structure and composition of these objects means that different observational techniques have to be combined together to probe their various regions.

Long wavelength telescopes, far-infrared (FIR) and (sub-)millimeter, usually spatially resolve regions outside of $\sim$ 20 AU while mid-infrared (MIR), near-infrared (NIR) and visible light predominantly probe down to the first AU of such objects. In practice, however, because of current technical limitations (i.e. the extreme contrast-ratios between the disk and the star), NIR and visible instruments can only probe outside of several resolution elements, $\sim$ 8 AU, at low signal-to-noise ratio (SNR). High-energy radiation such as ultraviolet (UV) or Xray are often associated highly-energetic accretion mechanisms or corona physics, happening in the regions very close to the stellar surface.

While spatially resolved observations give a direct localization of emitting regions, allowing precise disambiguation of structures in the spatial domain, a somewhat similar approach exists in the spectral domain through the analysis of the relative brightness distribution of parts (or all of) the disk. The discovery of a medium-age sub-class of

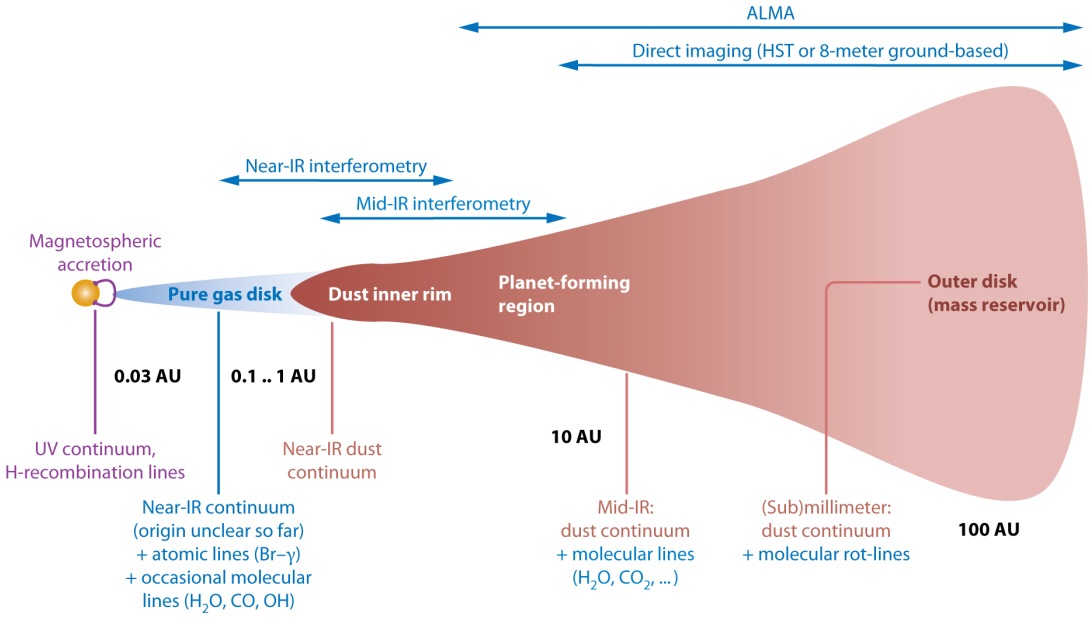

Figure 1.1: Schematic structure and spatial scales of a protoplanetary disk. Note that the radial scale on the x-axis is not linear. Above the pictogram shows which techniques can spatially resolve which scales. Below shows which kind of emission arises from which parts of the disk. Originally in Dullemond & Monnier (2010).

young circumstellar disks, known as transition disks, characterized by a distinctive dip in their infra-red spectral energy distribution (SED) suggests that a partially evacuated gap exists in the inner region of the protoplanetary disk (e.g. Calvet et al. 2002). The profound implications for studies of planetary formation have become increasingly apparent with the confirmation of the disk-gap architecture by (sub-)millimeter measurements and optical interferometry (e.g. Andrews et al. 2011).

A number of mechanisms have been proposed to cause these gaps, including extensive grain growth (Dullemond & Dominik 2005), photo evaporation (Clarke et al. 2001), binarity (Ireland & Kraus 2008), and tidal barrier created by dynamical interaction with low-mass disk objects (e.g. Bryden et al. 1999). These different mechanisms can be distinguished by studying the distribution of the gas and dust within the gaps: a large (stellar) companion or photo-evaporation would almost completely evacuate the inner regions while a less massive planetary companion would allow gas and small dust grains to exist within its orbit (Lubow et al. 1999). Furthermore, in the latter case, the measurement of the size and distribution of this material would allow the orbit and mass of the planetary companion to be constrained.

While the physical processes are reasonably well understood for the regions of the disk beyond about a few AU, the structure of the inner-disks remains a complete puzzle. This is both because the complexity to observing such regions so close from their

brighter host-stars is extremely challenging, and because the physics of this region, where the disk becomes so hot that the dust starts to evaporate, is poorly understood.

With the advent of Infra-Red (IR) interferometry, it has become possible to spatially resolve the innermost regions of disks, allowing a closer look at the first few AU, down to the inner rim of dust. Analyzing unresolved spectroscopic observations jointly with high-resolution IR interferometric data brings into life a new method to comprehend these complex objects. This work aims at observing such young circumstellar disks using interferometric techniques in order to analyze their inner-disk shape and composition.

1.2 Birth of Stellar Systems

The vast between stars is not filled with emptiness. In this section, the reader will be reminded the principles and constraints that govern the circumstellar disk around young stars. It will describe why circumstellar disks are an inevitable step of star-formation scenarios, and comment on major concepts such as the initial abundances of gas and dust, the grain size-distribution law, or the various means of extracting angular momentum accumulated from the initial cloud-collapse.

1.2.1 Origin of stellar systems

Large Inter-Stellar Medium (ISM) clouds are reported throughout our galaxy; invisible to the naked eye on a dark-night sky, they are revealed best in radio wavelengths or ultra-violet (although, technically, Aborigines and Columbian civilizations made constellations out of the dark patches of the ISM in the milky way, e.g. the "Emu"). A schematic view of our local galactic environment is shown in Figure 1.2.

What strikes at first is that most of the stars – and especially the star associations – are located outside the diffuse HI regions, which take the shape of filaments around "bubbles". This current situation is the result of a previous large-scale star-formation phenomena, of which the current molecular clouds, depicted in red, are the still-active belated remainings. The most famous star-forming regions are named "Rho Ophiuchus" ($\sim$ 130 pc), "Taurus-Auriga" ($\sim$ 140 pc), "Orion-Trapezium" ($\sim$ 450 pc), "Chamaeleontis" I and II ($\sim$ 140, 200 pc), "Scorpius-Lupus" ($\sim$ 150 pc) and "CrA" (for Coronae Australis, $\sim$ 130 pc). A study by Kroupa (2002) showed that stars and star clusters follow a universal mass function at birth; star-forming regions share the same density patterns and scales.

HI regions consist of the simplest components to be found in the universe: neutral atomic hydrogen ($\sim 90\%$) in addition to local helium abundance and $\sim 1\%$ of small dust grains made of a combination of hydrogen and other heavier elements. These clouds are fundamentally inhomogeneous: gravitational or thermal instabilities and turbulent compression (e.g. from shocks due to supernovae explosions) create complex structures of filaments and blobs of over-densities. When involving a critical amount of gas called Jean's mass M_J, these inhomogeneities can impart an initial angular momentum to

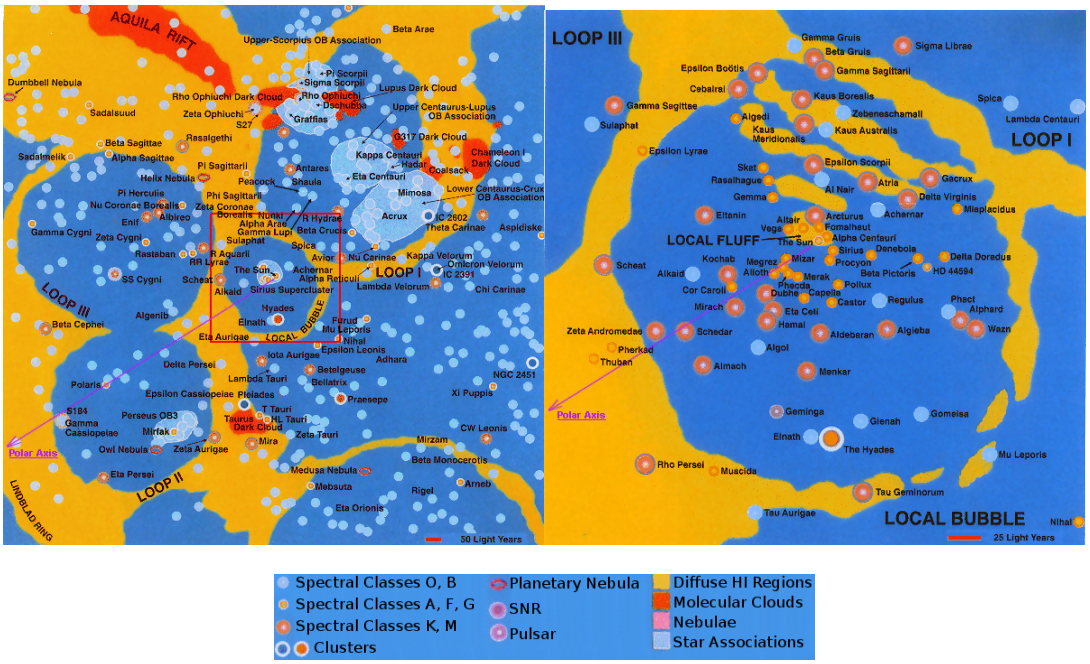

Figure 1.2: Maps and legend showing the (flattened) neighborhood of the Sun. The left map shows a 1600 light-years-side (490 parsec) square part, while the right one corresponds to the red-frame zoom and shows the inner 380 light-years-side (115 parsec) square-portion. These maps corresponds to our current best guess of the interstellar hydrogen and molecular gas structure, constructed from various observations and deductions. High-density molecular clouds including the Aquila Rift surround star forming regions, each shown in red. Most if not all stars named here can be seen with the naked eye; many well known objects, such as the Dumbell Nebula or the Pleiades, are also depicted. The electronic version of the Thesis provides a higher-resolution version of these maps. Originally in Henbest & Couper (1994)

the surrounding region. Jeans (1902) showed that in such context, when gravitational forces are larger than the internal pressure of a medium, a rotating cloud of gas starts collapsing under its own weight, along its rotation axis. The characteristic length of this region of gas is given by:

$$\lambda_J = \left(\frac{\pi}{G\ \rho_0}\right)^{\frac{1}{2}} c_S, \tag{1.1}$$

where G is the gravitational constant, ρ_0 is the initial density and c_S is the speed of sound in this medium. This length can be directly related to Jean's mass through density: $M_J \propto c_S^3 \rho^{-\frac{1}{2}}$, which is defined as the largest gravitationally stable gas-mass under a given density and temperature (through c_S). For a typical cold HI ISM region with a temperature of 40 K and a density of 30 atoms per cm^3, one finds $\lambda_J \sim$ 10 pc and $M_J \sim 10^4\ M_\odot$.

The density increases as the collapse happens, which in turn decreases Jean's critical-mass value: new sub-regions start to collapse within the initial gas-cloud. After several steps of this gravo-turbulent fragmentation phenomena, density increases to a point where all atomic elements bound to form molecules: from the initially large atomic gas-cloud, many smaller higher-density cold molecular-gas clouds have formed. Until there, the collapse remained isothermal and the gravitational energy was evacuated through radiation. Such cores typically possess a density of 10^3-10^4 atoms per cm^3, and display a temperature of $\sim$ 40 K, unchanged since the start of the collapse. They show a characteristic Jeans length of $\lambda_J \sim$ 1 pc and a maximum mass of $M_J \sim$ 100 $M_\odot$. This value corresponds to the estimation of highest possible stellar mass.

At this stage, density reached a point where photons are no longer free to escape the medium. The temperature hence increases with opacity; the collapse becomes adiabatic. The further fragmentation of each core now mostly relies on turbulence, and whether it can counter-act gravitation or not. When fragmentation does dominates the energy budget, it continues and all sub-cores (or proplyds) tend to collapse individually, forming a large cluster of low-mass stars. If turbulences decays before gravitation, the core undergo a global collapse where competitive mass growth becomes pre-dominant. In this scenario, low-mass objects may become ejected and as accretion stops, only a few massive proplyd remain: this tends to create small clusters with high-mass stars.

One can easily show that the characteristic time for the gas-cloud to collapse, based on the free-fall time for a particle on the periphery to reach the cloud center, only depends on the cloud initial density; it is given by:

$$\tau_J = \sqrt{\frac{3}{32\pi G\rho_0}} = \frac{R^{3/2}}{\sqrt{8GM}}, \tag{1.2}$$

assuming a spherical distribution of total mass M and radius R. This qualitative result ignores angular momentum and magnetic fields, both of which will resist collapse and hence lengthen the true collapse time. The free-fall collapse time given above should be understood as a lower limit rather than a realistic collapse time calculation. For a typical cold HI ISM region, this minimum characteristic time is of order a few million years. See Section 3.7.2.4 for the discussion of the accretion of IRS-48.

The initial collapse phenomena highlights a few key ideas and principles that set basis to the further study:

- Dust-to-gas mass ratio in the ISM averages 1%.
- Stars form in clusters because of the gravo-turbulent cascade fragmentation of an initial large ISM gas-cloud.
- All stars in a cluster share approximately the same age and initial composition (see Section 3.7.1 for a discussion on IRS-48 age).
- Complex molecules naturally form as temperature and density increase with gravitational collapse.

1.2.2 Birth of disks

As detailed in the previous section, the process of star and planet formation happens with the fragmentation and collapse of a molecular gas-cloud. Note that for the sake of conciseness, only a small amount of core principles will be detailed below; indeed, in the bigger picture, there is enough complexity and terminology associated with planetary formation to form its own "diskionary" (Evans et al. 2009a).

Initially, the mass is (relatively) homogeneously spread in each sub-region of the gas-cloud, also called proplyds (for ionized protoplanetary disk/nebula). It is however rapidly ($\sim$ 10 to 30 thousands years) processed through a flattened accretion disk inward onto the protostar in accretion bursts and outward through outflows and jets. At this stage arises the issue of angular momentum conservation as the proplyd shrinks and flattens into a proto-stellar disk. The angular momentum contained in the rotation of a central-star represents an extremely small fraction of that of a large-scale gas-cloud. Would the mass be entirely concentrated in a central proto-star, no star could emerge from it and light up because of the enormous centrifugal force tearing it apart.

There is hence a critical need for the dissipation of this excess angular momentum from the very first beginning of the proplyd-collapse. As a matter of fact, it can be calculated that the Sun contains more than 99.8% of the total solar system mass; it however holds only 0.6% of the total angular momentum in the solar system. Circumstellar disks are an inevitable, efficient and natural consequence of angular momentum conservation during the formation of a star through gravitational collapse. Other mechanisms also play an important part in the early collapse of a proplyd, like jets or strong magnetic fields; they are not covered in this work.

Eventually, as the star lights up, its radiation creates a strong negative-feedback which disperses the remainings of the proplyd and terminates the stellar formation. The accretion rate decreases and only a small amount of material persists in a thin and self-shadowing disk perpendicular to the rotation axis of the stellar system. For the stellar system to remain gravitationally stable, the disk mass is much lower, about 1% of the stellar mass (Williams & Cieza 2011). This mass-estimate observation is valid from brown dwarfs to B stars, although there is a somewhat large dispersion of $\pm$ an order of magnitude (Natta et al. 2000).

Several high-density molecular clouds exist in the direct neighborhood of the Sun; they host the most active star-forming regions currently studied. They coincidently happen to be the same age, about one to two million years old with moderate dispersion, and at the same distance from Earth ($\sim$ 120-150 parsec). Each of them contains a few dozens to a few hundreds of Young Stellar Objects (YSO), providing a wealth of statistical populations at the earliest stages of their evolution.

The transformation from a proplyd into a YSO with a gas- and dust-disk only takes slightly more time from the initial impulse once taken out of the large-scale gas-cloud. Key facts for this work are:

- Circumstellar disks are the most natural means to dissipate the excess angular momentum from the star-forming gas-cloud,

- The final collapse from a proplyd to a YSO only takes 30 to 40 thousand years,
- The gas- and dust-remnants surrounding the newly formed star take the shape of a thin flattened and self-shadowed disk rotating with Keplerian velocity for the dust, and slightly sub-Keplerian for the pressure-supported gas,
- Independently from the stellar type, a young disk averages 1% of the stellar mass, with a factor of ten dispersion.

1.2.3 Stellar binarity

From the time the circumstellar disks are formed, many evolutionary path exist; the sole purpose of which is extract excess angular momentum. Last section showed that one of the most natural means to extract angular momentum from the initial collapse. Stellar binarity (i.e. forming two low-mass stars orbiting each other rather than a single central star) appears to be another excellent means of extracting it. An consequence of this was shown by studies on Main-Sequence (MS) stars binarity, which highlighted that binaries are extremely common, e.g. 53% among G dwarfs (Duquennoy & Mayor 1991).

Artymowicz & Lubow (1994) showed that binarity does not imply a complete clearing of the circumstellar matter: for typical viscous disk parameters and a binary system with semi-major axis a, the inner edge of the circumbinary coplanar-disk is truncated at $1.8\times a$. Similarly, coplanar disks around each star (circumprimary disks) are truncated at the outer edge at about $a/2$. They also show that higher eccentricities lead to greater disk erosion (either inward or outward).

The detection of an over-abundance by a factor of two of binaries among the young stars in Taurus when compared to the results for the MS-stars (Ghez et al. 1993; Leinert et al. 1993; Reipurth & Zinnecker 1993) made it clear that binarity indeed is the dominant mode of star formation. Further large-population studies by Duchêne (1999) confirmed that the Taurus members have a significant binary excess of 2.8σ compared to MS stars. This means that for this region and given the completeness of the observations, no less than $\sim 95\%$ of stars are multiple systems, assuming that the orbital period distribution has the same shape as the MS binaries. Duchêne (1999) also finds a 1.6, 1.9 and 2.7σ binary excess for CrA and two different star-forming regions in Ophiuchus.

This shows that YSOs do indeed tend to have a binarity over-abundance compared to MS stars, to a degree that is however still under discussion as underlined by Ratzka et al. (2005). The reason is that the population samples studied are usually small and biased towards the brightest stars ($\lesssim$10 magnitudes in K-band). Also, binary star detection is mostly done through speckle imaging, that have lower detection limits of, in best cases, $\sim$ 15 AU (for the considered 120-150 parsec dark clouds distances) and $\sim$ 0.1 flux ratio (2.5 mag) between the primary star and its companions. The flux ratio detection limit leads to an intrinsic bias in binarity characterization, that cannot be statistically corrected.

The extraction of angular momentum is best achieved when forming heavy companion(s) to the star. Key facts about binarity for this work are:

- YSOs tend to have a binarity over-abundance compared to MS stars, to a degree still under discussion.
- Both circumprimary and circumbinary disk exist and have been observed; a binary star does not imply immediate and systematic clearing of its circumstellar material.
- A large-scale high-resolution and high-contrast measurements of YSO binarity has yet to be done; it would allow a precise characterization of the orbital period distribution.

1.3 Of Stars and Disks Evolution

Now that the scene is set on how and why circumstellar disks are an usual step in stellar-formation, their evolution from primordial, hot and gas-rich disks to cold, collisional and gas-poor debris remains to be addressed. In this section, the reader will be reminded the main physical phenomena and critical properties of disks that drive their evolution and eventually dispersal in a few million years. After focusing on means to assess and classify the evolutionary stage of disks, the main disks properties and parameters will be described. Finally, the physical processes at stake in disk evolution will be detailed, to eventually conclude on the mechanisms of dispersal.

1.3.1 YSO classification

There are many observational ways to characterize the disk evolution process once the central star(s) became optically revealed. The most direct, measuring the disk, stellar masses and disk age, would probably be ideal if only they were not extremely hard to achieve and moreover, model-dependent. In practice, more practical means are generally used, principally based on disk accretion signatures in the optical, or through the distribution of warm circumstellar material in the IR. A IR-based classification was introduced by Lada & Wilking (1984), who showed that YSOs in Ophiuchus region formed three distinct groups based on whether the emitted energy was rising in the mid-IR, declining but with a notable excess over the blackbody stellar photosphere, or with negligible IR excess. This was formalized later on by Lada (1987); Andre et al. (1993); Greene et al. (1994) into five main classes (0-I-FS-II-III; FS stands for flat spectrum) based on the slope of the SED between ~ 2 and 25 μm,

$$\alpha_{IR} = \frac{\Delta\ log(\nu F_\nu)}{\Delta\ log(\nu)} = \frac{\Delta\ log(\lambda F_\lambda)}{\Delta\ log(\lambda)}, \tag{1.3}$$

or the absence of 2 μm flux in the case of class-0 YSOs.

Table 1.1 describes the main characteristics and approximate durations of disk classes. This classification underlines that the disk and the envelope both gradually

Class	α_{IR} slope	Mass properties	Observational characteristics	Duration
0	–	$M_{env} > M_* > M_{disk}$	No optical or NIR emission	10-30 Kyr
I	> 0.3	$M_* > M_{disk} \sim M_{env}$	Optically obscured	0.5 Myr
FS	0.3 – -0.3	$M_*/M_{disk} \sim 100$ [1]	Intermediate class-I and II	2-3 Myr
II	-0.3 – -1.6		Accreting disk, strong Hα and UV	
III	$<$ -1.6	$M_*/M_{disk} \gg 100$ [1]	Debris disk, passive, no accretion	

[1] $M_{env} \sim 0$

Table 1.1: Classification of young stellar objects. Durations represent the typical phase duration, which can however greatly vary in individual disk cases. Adapted from Greene et al. (1994); Williams & Cieza (2011).

dissipate with time. Consequently, the SED-IR signature of the object, dominated by the dust of the disk, strongly decreases until only the star influence is left, as illustrated in Figure 1.3.

On average, the embedded phases through class I last for about 0.5 Myr (Evans et al. 2009b), however the surrounding envelope and strong proto-stellar outflows can hinder measurements of disk properties at these early times. After the embedded phase, the median disk lifetime is 2 to 3 Myr, with very high dispersion (approximately from 1 to 15 Myr). Since the manner and the rate at which any individual star-disk system evolves vary greatly, only large-population statistics can underline trends. A recent large-scale study of 13 star-formation regions questions these durations and globally increases them by a factor of two, showing once more that age determination of such early-type star is a complex issue (Bell et al. 2013).

It is also important to note that the SED classification does not give a unique description of the amount and distribution of circumstellar material. In particular, YSOs with edge-on disks are more embedded hence highly extincted and can be misinterpreted as less evolved objects: an edge-on class I can have characteristics of a class 0 (Robitaille et al. 2006).

It was seen in Section 1.2.2 that, independently from the stellar type, a disk in the longest phase of the circumstellar evolution, classes FS/II, averages 1% of the stellar mass (with some dispersion). Disk structure does however appear to be dependent on stellar mass, at least for the lower-mass stars regime. From SED analysis and fitting, Szűcs et al. (2010) find that, given a star-forming region, very low-mass stars have flatter disks than low-mass stars, consistent with a higher dust settling mechanism. It is risky to make a direct comparison to higher mass A-B types PMS stars in other regions, because of the difficulty in distinguishing initial conditions, from evolution due to grain growth and settling. On the other side of the stellar spectra, O-type ($>$8 $M_\odot$) stars seem to be exceptions since no disks are detected at (sub-)millimeter wavelengths. This may be due to very high photo-evaporation rates leading to an extremely short disk lifetime, such that disks are nearly dissipated by the time an O-star is optically visible, or due to an altogether different star-formation mechanism (Zinnecker & Yorke

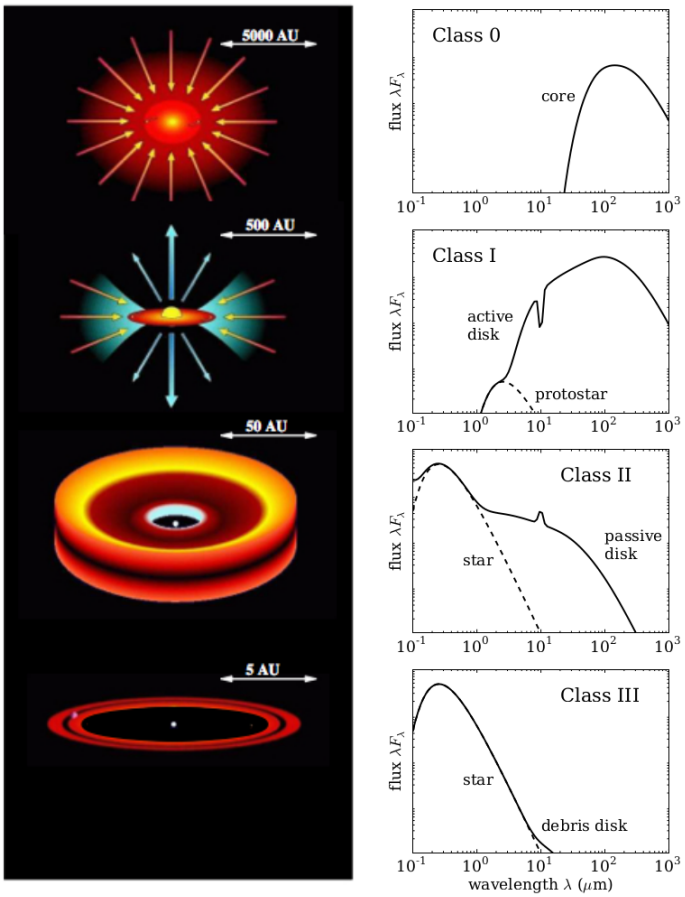

Figure 1.3: Schematic overview of the different evolutionary stages of low/intermediate-mass star formation. The left column of the figure is a pictorial representation of the objects, the right column represents the SED of the corresponding objects. Originally in Menu (2015).

2007).

A distinction in nomenclature exists between disks surrounding massive stars and lower-mass stars. A-B types YSOs with circumstellar matter are called Herbig Ae or Be stars, respectively. Analogs of these in the smaller mass range (<2 $M_\odot$) – F, G, K, M spectral type PMS stars – are called T Tauri stars (TTS). Several flavors of TTS exist: classical (CTTS) and weak-lined T Tauri stars (WTTS), which correspond closely (though not exactly) to class II and III YSOs, respectively.

Disk and star classification allow to group objects to perform statistical analysis and unveil trends in star- and disk-evolution mechanisms; key ideas are summed up here:

- YSO classes, 0-I-FS-II-III, are based on the IR-excess slope between 2 and 25 μm.

- This classification does not account well for corner cases induced by observational bias; a theoretical/modeling approach is often necessary.
- O-stars do not show disks.
- Among stars showing disks, A-B types PMS stars are called Herbig Ae or Be, while F, G, K and M types stars are called T Tauri.

1.3.2 Protoplanetary disks and their properties

The classification presented previously is an empirical law based on standard disk morphology. In order to achieve a precise comprehension of individual objects, one must dive into the characterization of the main disk properties, namely mass, dust composition, radial and vertical density profiles, among the most important ones. They will be described in here-after. Although gas composition and structure play a crucial role in disk evolution, it will not be addressed here given that the observations in made in the frame of this work are not sensitive to such species.

1.3.2.1 Dust and PAH composition

Mathis et al. (1977) showed that, in order to reproduce the ISM extinction, graphite is a necessary component, with a particle size distribution roughly power law in nature $n(a) \propto a^{-p}$ with an exponent p between 3.3 and 3.6, and sizes between $5nm$ and 1 μm. Other components, such as silicates, provide an improvement to the fit when introduced with the same power-law and sizes in a somewhat narrower range, about $25nm$-0.25 μm.

(Draine 2003) shows that an additional species, Polycyclic Aromatic Hydrocarbons (PAH), exists in the ISM as the by-product of catastrophic destruction of carbonaceous grains; Geers et al. (2006) estimate a PAH-to-dust mass fraction of $\sim 6\%$ using carbon atoms to hydrogen nuclei abundances. The ISM composition is thought to be the initial composition of disks, although there is a substantial processing of both gas and dust as disk forms and evolves. For example, during the passage through dark clouds to protoplanetary disks, molecules precipitate onto dust grain surfaces, producing coating icy mantles (Bergin & Tafalla 2007). Therefore, the particle size distribution exponent is expected to evolve with the disk. Evidence for further growth to millimeter sizes follows essentially from the determination of the (sub-)millimeter slope (refer to Section 1.3.3 for grain growth).

Dust dominates the opacity of protoplanetary disks and is the raw material for planetesimals. The opacity of a disk scales as $\sim a_{min}^{\frac{-1}{2}}$ in the optically-thin regime (i.e. low opacity). This means that nanometer- to a tens of μm-grains, extremely abundant given the grain-size distribution of $\sim$ -3.5, will very rapidly generate a high opacity and create optically-thick disk-structures. Dullemond et al. (2007) suggested that extremely small grains, e.g. PAH, can "hide" a substantial amount of settled

thermal silicate grains under conditions of low turbulence. Such phenomena could be taking place in IRS-48, it is discussed in Section 3.5.5.

Silicates are often the main contributors to the IR-SED of protoplanetary disks. They are identified through broad spectral bands at 10 and 18 μm (Henning 2010) and when compared to the ISM silicate grains, their spectral signature clearly show a growth to sizes larger than μm. Interestingly, this is not the case for IRS-48, see Section 3.4.7.

PAH have many specific NIR and MIR features (Tielens 2008), specifically at 3.3, 6.2, 7.7, 8.6, 11.2, 12.7, and 16.4 μm and show very clear imprints to the MIR spectra. Since PAHs are easily excited by UV radiations even far away from the star, Maaskant et al. (2014) show that the ionization state of the PAH emission can be related to the disk structure up to tens of AU.

The combination of PAHs and amorphous/crystalline silicates of (sub-)micron sizes was shown by Juhász et al. (2010) to be is sufficient to model the mid-infrared spectra of protoplanetary disks. This however might not prove to be correct for special cases for that IRS-48 precise SED and interferometric data modelling required the presence of Very Small Grains (VSG) of carbon.

1.3.2.2 Mass

The estimation of disk masses is essentially based on the millimeter flux of the dust that maps the large-scale gas reservoir. The conversion to the total disk mass is however based on several critical parameters: the dust-opacity, the dust-to-gas ratio and the fraction of the mass contained in large dust-grains (a$\gtrsim cm$). These characteristics of disk are for now highly model-dependent, and the inferred masses suffers considerable uncertainties.

Indeed, as a rule of thumb, observations at a wavelength λ only constrain the properties of dust grains out to a maximum size $a_{max} \sim 3\lambda$ (Draine 2006). Only a few disks have been detected beyond millimeter wavelengths, and thus we know little about the general occurrence and distribution of centimeter- and larger-sized particles. For a grain-size distribution $n(a) \propto a^{-3.5}$ (refer to 1.3.2.1), the total mass scales as $\sim a_{max}^{\frac{1}{2}}$, and substantial mass may be undetected.

Disks of class II and beyond possess a small fraction of the central stellar mass, see Section 1.2.2, their motion are therefore expected to be Keplerian for dust and slightly sub-Keplerian for pressure-supported gas.

1.3.2.3 Radius and surface density

The disk outer radii are hard to measure because they are populated with cold, low-density gaseous matter, which only weekly emits. They are still efficient absorbers however, and several imaging of such objects in front of bright HII region backgrounds provided radii ranging from 50 to 200 AU for 22 Orion proplyds (Vicente & Alves 2005). Imaging disks at millimeter wavelengths allowed a precise estimate of the disk's

material radial distribution: Piétu et al. (2005); Isella et al. (2007) found that pure power laws could not reconcile rotational lines of CO and continuum images in the outer regions. McCaughrean & O'dell (1996) found that an exponential decay at the outer boundary as required to reproduce Orion proplyd silhouettes. To describe a viscous accretion disk, a general consensus exists on using an exponentially tapered profile of the form:

$$\Sigma(R) = C_{mass} R^{-\gamma} \exp\left[-\left(\frac{R}{R_c}\right)^{2-\gamma} \right], \tag{1.4}$$

where $C_{mass} = (2-\gamma) \times M_{disk}/(2\pi R_c^{2-\gamma})$ is a mass normalization constant, γ is the surface density exponent that specifies the radial dependence of the disk viscosity and R_c is a characteristic radius, which sets limits to where the surface density begins to steepen significantly from a power law. However, as the disk does not have a sharp outer edge, a physical disk size must be specified in terms of an intensity threshold. Andrews et al. (2009, 2010) show that a rough estimate of R_c may be obtained by noting that about two-thirds of the total disk mass lies within it, which corresponds to $\mathrm{R}_c \sim\ 30 - 200$ AU most generally.

They also find a tight range of possible γ values from 0.4 to 1.0, and $\langle\gamma\rangle = 0.9$. The Eq. (1.4) naturally approximates a power law $\Sigma \propto R^{-\gamma}$ for $R \ll R_c$. Negative values of γ indicate decreasing surface densities as radius increases (for $R < R_c$), which may be an important signature of disk evolution (see Section 1.3.3).

1.3.2.4 Vertical density profile

Protoplanetary disks are flared with a vertical scale height that increases with radius. Direct evidence for this phenomena can be seen in silhouette Hubble images of disks. A passive circumstellar disk is assumed to be in vertical hydrostatic equilibrium, where the the vertical component of the stellar gravity is supported by the vertical gas-pressure gradient. Under geometrically thin disks and vertically isotherm assumptions, this equilibrium leads to a vertical density profile such as:

$$\rho(z|R) = \rho(z=0) \exp\left[-\frac{1}{2}\left(\frac{z}{h}\right)^2 \right], \tag{1.5}$$

where h is the disk scale height; h varies with radius as $h = h_0(r/r_0)^\beta$ with β the flaring exponent ($\beta > 0$, of order ~ 1) and h_0 the scale height at radius r_0. More advanced analytical solutions taking into account the stellar radiation that heats the flared surface of the disk-structure exist. However, the modern approach is to use radiative transfer simulations which allow iterative determination of vertical density and temperature from reprocessing of stellar photons interacting with the disk material. Such tool will be used in Chapter 3 to infer the structure of its disk.

1.3.3 Disk evolution

As depicted before, disks display temperatures, densities, radii, grain sizes, etc, that span several orders magnitudes. For this reason, their evolution and shaping are driven by many different physical processes which are, directly or indirectly, all connected to each-other. The main phenomena will be described below.

1.3.3.1 Viscous transport

The evolution of disks up to class-II is mostly driven by viscous transport, also known as inward drift. It is also one of the most predominant reason for the flattening of disks and accretion onto the star. Indeed, large dust grains are less coupled to the gas, simply because of their high volume/surface ratio that favors inertial on pressure effects. Their higher mass requires them to maintain Keplerian velocities in order to keep a stable orbit. However, since the pressure-supported gas has a slight sub-Keplerian orbital velocity, these larger dust grains experience a systematic drag, leading to a gradual loss of angular momentum. This viscous effect happens both in the radial and the vertical planes, as grains may have inclined orbits. Vertical viscous transport is called dust settling and increases the density of dust in the interior of the disk. The disk surface is left with the smaller and lighter dust particles, effectively leading to a flattening of the disk through photo-evaporation and radiation pressure. Radial viscous transport leads to a slow yet unswerving spiraling in and eventually accretion on the star (Weidenschilling 1977). Obviously, turbulence shall be considered as a strong mixing counter-effect to the smooth and hierarchically layering consequence of viscous transport.

Viscous evolution models are broadly consistent with the observational constraints for disks masses and sizes, and the decrease in accretion rate over time due to disk depletion. This process has also a direct effect of spreading out the disk, as angular momentum is conserved, hence transported outwards. Accretion as observed through emission lines such as $H\alpha$, $Br\gamma$, and CaII can be successfully reproduced by magnetospheric accretion models (Muzerolle et al. 1998). However, a purely viscous disk does not account for the large variety of SEDs and shapes: such phenomena is the main component of a much larger and complex evolution involving several other important physical processes.

1.3.3.2 Radiation effects

Through gravitation and radiations, the central star is by far the main source of energy in the disk, and is the foremost driver of its evolution. With viscous transport and dust settling, gas photo-evaporation is the physical process that affects disk during the largest time of their existence. Photo-evaporation is driven by energetic photons emitted by stars in the UV and X-ray spectra ($\lambda < 6eV/(hc)$), which ionizes and heats the gas at the disk surface. The main and closest source of high-energy radiation is mostly the host-star of the disk. However, it has been shown that (very) near-by

massive stars in case of dense clusters may also have some impact on the outer-most regions of circumstellar disks (Johnstone et al. 1998), effectively dissipating it on both ends.

Combining both viscous transport and photo-evaporation physical processes led to a "UV-switch" theory to explain the inner disk clearing observed in transition disks and the so-called "two-times problem" (i.e. disk appear smooth and dense for a few million years until the time where they are suddenly dissipated, in $\sim$ half a million years):

1. At early stages of the disk evolution, the accretion rate dominates over the evaporation rate, and the disk undergoes standard viscous evolution: material from the inner disk is accreted onto the star, while viscous transport provides replenishment from the outer-disk reservoir.

2. After some time, as the outer disk is spread out and partly emptied from its material – hence no longer able to supply the inner disk – the accretion rate drops to $\sim 10^{-10} - 10^{-9}$. The inner disk remains, unsupplied, and it is swiftly drained onto the star due to viscous transport, creating an inner cavity in the disk.

3. This latter cavity implies that the disk is now split into an inner and outer disk. The inner rim of the outer disk is exposed to the direct radiation of the star, and rapidly photo-evaporates from inside-out, while the inner-rim subsists for a short time until it is fully accreted.

While FUV photo-evaporation is limited to the first few AU of the disk, EUV and X-rays are able to penetrate much deeper in disks, effectively heating them from the inside up to tens of AU from the star.

Radiations of the star does also effect dust, in at least two possible ways. Radiation pressure, often known as stellar wind, blows away the smallest dust particles ($a \lesssim 1\ \mu m$) which are not sheltered by larger dust particles. This mostly happens at the surface of disks, which was coincidently left with the smallest dust particles because of dust settling. Like photo-evaporation, this tends to flatten and spread disks out. The second case where radiation strongly affects dust happens much closer to the star, as dust particles are dragged in by viscous transport, heated, and reach their sublimation temperature. The gas produced may be equally accreted or photo-evaporated.

The stellar spectra and the nature of the grains are direct constraints to the disk inner-radius location, wherein dust systematically sublimates. However, it is expected that shadowing from larger dust grains (longer to sublimate) or carbonaceous grains (effective heat absorbers), may modulate the inner-rim radius and shape of the disk (Isella & Natta 2005). As a consequence, NIR excess is very well correlated to accretion and the presence of an inner disk (Hartigan et al. 1995). In the case of IRS-48 it is proven that the inner-most disk is most probably dissipated, leaving no other NIR excess than that produced by other species at a larger radii, see Section 3.5.

1.3.3.3 Grain growth

Solid dust particles only account for an extremely small fraction of the total initial mass of a disk, $\sim 1\%$. However, they dominate the opacity and are the cause for gravitational disruptions in the disk in that they are the main constituents of massive bodies. Grain growth and dust settling are closely related in that dust settling tends to create layers of equal sized particles in a disk, favoring grain growth.

A range of ~ 13 orders of magnitudes exists from sub-micron size grains to planets, which grain growth, as a combination of many different physical processes, can not explain yet. Excellent reviews give much details about the processes at stake and issues to be overcome in our comprehension (e.g. Chiang & Youdin 2010; Williams & Cieza 2011; Drążkowska et al. 2014).

Key theories are able to explain growth from sub-microns to millimeters, and then hectometer to planets. Several possible solutions have been proposed to account for the formation of bodies up to meter-sizes, such as turbulent vortices (Heng & Kenyon 2010). However the problem known as the meter-size barrier is still unaddressed: such bodies are expected to suffer from both destructive collisions and high drag leading to rapid spiraling migration to inner regions of disks. However, phenomena such as dynamical effects may provide a solution to the meter-size barrier, see Section 1.3.3.4.

1.3.3.4 Dynamical clearing

The previously exposed mechanisms can account for many observations. However, apart from turbulent effects, they do not account for any azimuthally inhomogeneous effects. Similarly, the previous dust density prescriptions exposed in 1.3.2.3 and 1.3.2.4 only account for radial or vertical variations of disk properties as a result of the dominant gravity and radiation of the central star.

The gravitational effect of planets on debris disks was first reported by Chiang et al. (2009) in Fomalhaut. Using the capability of high-resolution imaging of coronography and large-scale gas and dust mapping ability of millimeter interferometry, indirect disruptions of (supposedly) stellar binarity or planetary companions (which are in essence identical, at least on the gravitational point of view) are finally at reach of our instruments. Large-scale asymmetries taking the appearances of dust-traps or spiral features were reported first by Muto et al. (2012), van der Marel et al. (2013a) or Christiaens et al. (2014). These results are an important milestone in that they underline azimuthal asymmetries in the disk structure itself, and not asymmetries consequent to a viewing angle of an axisymmetric structure.

Azimuthal variations are of great interest, given that they would highlight an additional influence like a self-gravitating disk, or protoplanets. Disks are extremely small compared to distances between stars, and beyond their embedded phase where the influence of close-by proto-stars may still play a role for dense clusters, any disruptive encounter are highly unlikely. Also, by the time of class-II phase, where the disk-mass represents $\sim 1\%$ of the stellar mass, self-gravity in smooth disks is negligible. Only protoplanets or over-densities are left to explain the observed azimuthal

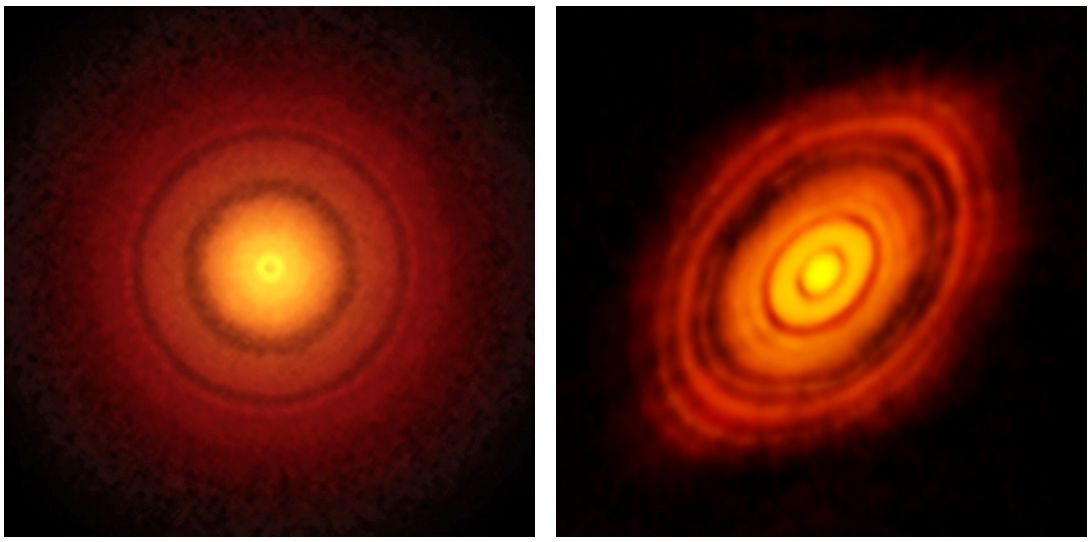

Figure 1.4: ALMA's best images of protoplanetary disks to date. These picture of the nearby young stars TW Hydrae (left, 3 arcsec-size box) and HL Tau (right, 2 arcsec-side box) reveal the classic rings and gaps that signify planets are in formation in these systems. Credit: Andrews et al. (2016) (left) and ALMA Partnership et al. (2015) (right).

inhomogeneities.

Gravitation and turbulence, often coupled in gravo-turbulence, appear to be both the cause and the consequence of azimuthal asymmetries in disks, in that they are the only sufficiently energetic and intrinsically asymmetric phenomena that can create and maintain large scales structures. Significant progress has been made in the direction of self-gravity planetesimal formation by Johansen et al. (2006); Cuzzi et al. (2008). In particular, it was understood that turbulence and formation of planetesimals through gravitation were not necessarily mutually-exclusive. The reason is that turbulence can locally lead to large-scales over-densities as high as 80 compared to the normal dust- and gas-density, and up to 1000 on smaller scales. Johansen et al. (2007) showed that gravo-turbulence can lead to the formation of gravitationally bound clusters with masses comparable to dwarf planets on timescales much shorter that the drift timescale, effectively allowing to overcome the grain-growth meter-size barrier.

Such planetesimals are well known to carve rings and gap in disks, and generate gravity waves like the ones observed on the edges of the rings of Saturn. The best proof to date of such phenomena is depicted in Figure 1.4.

1.3.3.5 Dispersal and Lifetime

Transition disks were first identified by IRAS as objects with a significant dip in their NIR and MIR spectrum leading to (almost) no NIR excess, while they still have clear

and prominent FIR and millimeter excess (Strom et al. 1989). A large variety of transition disks were discovered and many sub-names were invented to describe this phenomena, mostly because of a lack of specific understanding of the particularities that make each and every disk unique in its evolution, and also because of the irrepressible need to sort things into labeled boxes.

A more general approach gives a more generic definition, independent of the mechanisms in action. Disks until class-II are characterized by their large outer-disk reservoir providing an (almost) everlasting amount of material to be accreted onto the star, or photo-evaporated; the opacity of an abundant dust easily hides azimuthal asymmetries. However, once the outer-material reaches a level of depletion that breaks the delicate balance among the different physical processes at stake, one of these mechanism starts dominating the physics of the disk. Indeed, even if the disk dispersal starts from the very first times of a proplyd, it becomes evident only later, when its radial or azimuthal smoothness appears broken. The "UV-switch" theory corresponds to a dominating photo-evaporation leading to an inner-truncation of the disk, while major gravo-turbulence lead to gravitational disruptions and vortices or active carving of gaps by their by-product: planetesimals.

In a nutshell, transition disks are young and active circumstellar disks for which inner-regions, associated to NIR or MIR emission, started showing a clearing mechanism.

Wyatt et al. (2015) detail five observational facts in the evolution of circumstellar-dust from a pre-transition stage to a debris-disk. Given the inherent chaos in disk-evolution mechanisms, these should be taken as five (nearly independent) observable evidences towards the making of a debris-disk, rather than a linear and chronological process. They propose a classification of A-type stars disks according to their 12 and 70 μm IR excess, marginalizing the (often-unknown) disk-age.

The relatively small number of observed transition disks suggests that the evolutionary path through this phase is either uncommon or rapid. Given that no observation shows the presence of strong NIR- and MIR-excesses simultaneously with the disappearance of FIR- and millimeter-excesses, and given that no physical process detailed previously could explain it, one can reasonably state that NIR- and MIR-excesses disappearance would tend to be the first hints of disk dispersal. Also, one could note that no matter the disk structure and composition, the only immutable evolutionary process, photo-evaporation, will always eventually dissipate the disk inside-out (i.e. from NIR to millimeter excess regions), naturally re-producing the transition disk morphology of an inner-cavity.

We can state that transition disks may represent a common but relatively short phase in the evolution of a circumstellar disk. The duration of the clearing will be closely linked to the precise mechanism undergoing in each disk.

Disks lifetime and evolution timescales observed are critical parameters that imposes hard constraints on several mechanism of disks evolution, such as planetary formation and disk dispersal through various processes. Early studies show that the inner disk – hence accretion – is detected through NIR excess in 60 to 80% of stars

younger than 1 Myr; no more than 10% of stars older than 10 Myr seem to possess one (Strom et al. 1989). Studies on Upper Scorpius OB association (Carpenter et al. 2006; Williams & Cieza 2011) showed that $\sim$ 20% of 127 K- and M-stars are surrounded by optically thick disks while none of 30 F- and G-stars showed such disk for wavelength $\sim$ 16 μm, implying that primordial circumstellar disks are consumed faster by a massive star. This result is confirmed by Ribas et al. (2015) who show that only 2% of M$\geqslant$2 $M_\odot$ stars aged $\geqslant$3 Myr show a protoplanetary disk. Median disk lifetimes was estimated to be between 2 and 3 Myr, with an exponential decay of 2.5 Myr characteristic-time citepMamajek09. However, the estimation of stellar ages suffers from large uncertainties for such young and partially embedded objects; only a general trend should be considered.

1.4 Aims of the Thesis' work

This thesis will focus on the observational study of protoplanetary disks using high-angular-resolution techniques, in order to constrain the last steps of their evolution.

Over the last decade, the improvement of instruments sensitivity and resolution has provided circumstellar disk-evolution theories with an unprecedented wealth of data. The discovery of nearly four thousand planets has set valuable constraints on the final product of disk-evolution and planetary-formation. Sub-millimeter interferometric imaging, i.e. ALMA, and the observation of rovibrational bands using high-resolution spectroscopy is providing maps of the gas densities inside transition disks. The advent of adaptive optics providing IR and visible interferometry with unprecedented stabilization, it is possible to spatially resolve the innermost regions of disks down to the inner rim of dust, and the sublimation radius. Softwares involving radiative transfer, magnetohydrodynamics, accretion and dynamical provides unique tools to reproduce observations. Yet, the modelling effort to jointly comprehend these disparate datasets and encompass previous results is extremely challenging.

The aim of this work is twofold. First, by focusing on the in-depth observational study of IRS-48, it is demonstrated how high-angular resolution data in the NIR/MIR jointly analyzed with spectral energy distribution data, and provides Science with critical information on the structure of the inner disk regions around young stars. Such observations would not make sense without state-of-the-art radiative-transfer modelling, allowing for the reproduction and interpretation of the observational data. Such methods takes us to the limits of current observational and modelling capacities. Second, in the attempt to extract the pith and marrow from several datasets, this work proposes a set of new tools and methods for interferometrists to fit models to complex interferometric data and extract robust confidence domains out of parameter estimation.

All of the new data used in this work comes from interferometers. Chapter 2 will describe interferometry in its largest sense, including physics theory, interferometric instrumentation, data acquisition, and model fitting. It is mainly based on personal experience, as an observer, an interferometrist and a numerical analyst. Mostly qual-

itative, the aim is not re-demonstrate the scientific roots of interferometry. Rather, it provides a fresh view on some aspects of interferometry, observation or numerical analysis, and most importantly introduces new techniques, tools and methods specifically developed for the particular needs of this work.

Chapter 3 is the main scientific contribution of this work. It brings some light on a major and complex disk target, IRS-48, and analyzes it through the unique eye of high-resolution interferometry to provide a new interpretation of it: a brighter a younger central star with a later evolution-stage disk showing a dust-cleared inner region up to 11 AU. This chapter makes intensive use of the information contained in the first two chapters.

Appendix A is a preliminary and tentative modelling of the very-high resolution optical interferometry data acquired on MWC-361, a spectroscopic binary. This object is known to possess a large-scale circumbinary disk, in addition to a circumprimary disk consistent with the sublimation-radius of the primary star; however no circumsecondary disk was detected, no explanatory phenomena was found yet. Given the complex intricacy of disks and stars at spatial scales of a few milli-arc-seconds, the stellar parameters for both stars are still uncertain. This work proposes a solution to the spectral types of both stars, which will open a new window on the object, allowing precise modelling of its complex structure.

Chapter 2

Rough Guide to Interferometry

Contents

Nature permits us to calculate only probabilities. Yet science has not collapsed.
Richard P. Feynman

This chapter describes interferometry in its largest sense, including most of the necessary concepts required to acquire and analyze interferometric data: physics theory, interferometric instrumentation, data acquisition specificities, and parametric model fitting to the data. It is mainly based on personal experience, as an observer, an interferometrist and a numerical analyst. Mostly qualitative, the aim is not re-demonstrate the scientific roots of physics. Rather, it provides a fresh view on some aspects of interferometry (Section 2.1 and 2.2), model fitting, and most importantly introduces new techniques, tools and methods (Section 2.3) specifically developed for the particular needs of this work.

2.1 Physics of Interferometry

This section will begin with the philosophy and grounds of interferometry and atmospheric turbulence, in order to present the physical concept and limitations behind interferometry. It will end with the description of how to relate interferometric data to the geometry of the observed object.

2.1.1 Size does not always matter

Over centuries, astronomers have relied on the increase of the diameter of telescopes to improve the resolution of their observations. Telescopes grew from a few centimeters at Galileo's times (1564-1642), to 8-10 m class telescopes since the 1990s. The angular resolution of a telescope can be approximated by:

$$\theta[rad] = \frac{\lambda[m]}{D[m]}, \tag{2.1}$$

where λ is the wavelength used in the observation, D is the diameter of the (single) telescope, and θ is the smallest spatial frequency that can be measured by the telescope.

Although astronomers would love to increase the telescope diameter endlessly to improve the resolution of observations, many issues arise when working with high angular resolution instruments, independently from the good will of the observer: atmospheric movements, aberrations in the optics, engineering of the telescope, etc. While these many factors limit the ultimate resolution of an instrument, by far the most dominant part is wavefront perturbations caused by the Earth's turbulent atmosphere.

2.1.1.1 Atmospheric turbulence

The effect of atmospheric movements, at first order, can be modelled by the swift movement of "atmospheric temperature-cells" through the air-column above the telescope. Such cells are defined by a characteristic (angular) size, and by their "lifetime" (related to the speed of the atmospheric cells in front of the telescope). The atmosphere structure is such that one can simplify its main movement to a single high-altitude layer of several hundreds of meters thick, related to jet-streams. Qualitatively, each atmospheric cell has a specific temperature, slightly different from the surrounding ones. Given that the speed of the light-phase in a transparent media depends on its temperature (through the index of refraction), light passing through an atmospheric temperature-cell acquires a phase-delay, different from the surrounding cells. This creates random delays, which when integrated over the atmospheric height, greatly affects the light for ground-based astronomy.

One often uses r_0 as a measure of the "strength" of turbulence, or more precisely as to be the characteristic size of an atmospheric cell with Root-Mean-Square (RMS) phase-errors of one radian. Since r_0 scales as $\lambda^{6/5}$ (Kolmogorov 1941); visible and NIR instruments will always suffer from a much larger turbulence than MIR or submillimeter observations. In practice, this means that in the visible, a 10 m telescope will display the same angular resolution as a $\sim$ 15 cm telescope.

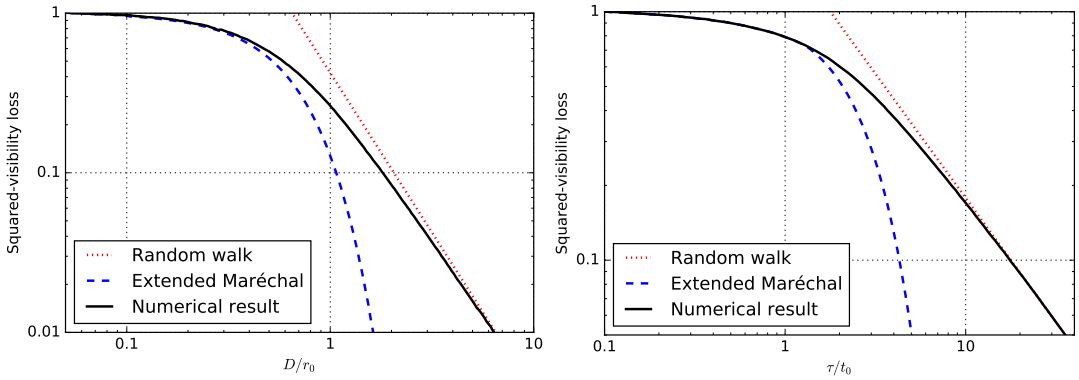

Figure 2.1: Measurement loss as a function of telescope diameter D (left) and integration time τ (right) normalized to r_0 and t_0. The ideal measured signal of unity is reached for $\tau \ll t_0$ and $D \ll r_0$. The numerically simulated curves can be approximated in $\tau/t_0 \ll 1$, $D/r_0 \ll 1$ and $\tau/t_0 \gg 1$, $D/r_0 \gg 1$ regimes with a single-atmospheric cell using Maréchal approximation and a random walk, respectively. Figures initially in Buscher & Longair (2015).

Atmospheric movements affect the light in two ways: in amplitude (scintillation) and phase. With the exception of very specific instrumental cases, the scintillation effect of turbulence is negligible compared to the turbulent phase-errors they induce. Neglecting scintillation is conventionally called the near-field approximation (Roddier 1981).

If an observer wishes to observe through turbulence without being affected by it, he must – ideally – observe through a single atmospheric temperature-cell, during the time t_0 when it remains stable above the telescope. Hence, he must adapt both the diameter of his telescope to achieve a satisfactory spatial-coherence of light (or phase-coherence), and the integration time on his detector (i.e. temporal-coherence) to literally "freeze" the turbulence state. This allows the observer to get a fully coherence beam of light. Typical t_0 in the visible is $\sim$ 3 milli-second (ms), and $\sim$ 36 ms at 4 μm, although, similarly to r_0, it varies greatly with weather condition and wavelength. r_0 and t_0 are related, such that:

$$t_0 \times v = 0.314 \times r_0 \propto \lambda^{6/5} \tag{2.2}$$

where v is the transversal wind speed above the telescope.

Buscher & Longair (2015) show the effect of integration time and the diameter of the telescope on the "quality" of the measurement, see Figure 2.1. A "quality" of $\sim$ 90% is reached for integration times $\tau \sim 0.5\ t_0$ (infinitesimal r_0), or a diameter of $D \sim 0.16\ r_0$ (infinitesimal t_0); an observation is usually a trade-off between these two parameters in order to achieve a good light coherence.

When one talks of the coherence of light, one should consider the light as a wave. The wavefront of a beam of light is an imaginary surface that represents the locus of the photons (or waves) that show a constant travel-time since their emission (or more

frequently, since the top of the atmosphere). Consequently, a wavefront has a constant light-phase. In short, without turbulence, a wavefront is a sphere centered on the emitter, which is seen to be (locally) flat when observed from far-enough. However, as was seen, turbulence induces random phase-delays, hence time-delays, which scrambles the initially flat wavefront. Although turbulence introduces random phase-errors and dents the wavefront, it can still be assumed to be flat at small spatial scales $<r_0$, and stable during a short time $<t_0$. One can observe through turbulence to achieve a fully coherent beam of light, i.e. constant phase, with a telescope of diameter $D \ll r_0$, and with an integration time $\tau \ll t_0$.

2.1.1.2 So why build bigger?

There are several reasons why building bigger telescopes, in spite of turbulence.

First, many astronomical observations are not seeing-limited in that they require a large field of view and a high sensitivity rather than a high angular-resolution (e.g. surveys): building a bigger telescope increases the photon-collecting area of the instrument, directly increasing the limiting magnitude of the observations.

Second, new technologies such as Adaptive Optics (AO) – and the very new developments of Extreme-AO systems – can compensate for (some) of the atmospheric turbulence and the optical aberrations in the optics, which directly increases the spatial and temporal coherency of the observation. This technology makes possible the use of 8-10 m class telescopes to their nearly-full resolving power – at least in the NIR where the AO correction is the most accurate –.

2.1.1.3 Interferometry, how?

We have seen that, with a small-enough telescope (possibly with an AO system) and a short-enough integration time, an observer could obtain a nearly fully-coherent beam of light through the atmosphere and to the telescope. This means that the phase-error induced by turbulence will be nearly constant over the whole mirror of this telescope. Consequently, one could build two telescopes arbitrarily far from each other, and observe nearly constant phase-errors on each of the two telescope mirrors. With a system (e.g. "fringe tracker") able to compensate for the rapidly varying difference of constant phases between the two telescopes, at a frequency higher than t_0^{-1}, one could coherently combine the light of two telescopes pointing at the same target. This is the principle of interferometry.

While a single telescope acts as a two dimensional detector able to sample the spatial domain very efficiently in both RA and DEC axes (whose efficiency depends on the plate-scale of the detector), a single telescope as part of an interferometer acts as a single-pixel photometric receiver, from which the light is re-combined to that of other telescopes in the interferometric array. In this configuration, the two telescopes situated far from each other can be modeled as two segments of a single very large mirror.

The benefit of interferometry is that, while the angular resolution of a single telescope was limited to its diameter, the resolution of an interferometer depends on the "equivalent diameter" of this very large mirror containing the mirror-segments. This distance between both telescopes is called the baseline. Moreover, since interferometry makes use of the phase information of light and not just its amplitude, the resolution criteria benefits from an additional typical 0.5 improvement:

$$\theta_{Interferometry}[rad] \sim \ 0.5 \times \frac{\lambda[m]}{B[m]}, \tag{2.3}$$

where B is the baseline, as seen from the target (i.e. not the ground-distance, but the projected baseline). An interferometer made of two telescopes of D=1 m located 50 m apart have a typical resolution of ~ 0.001 arcsec ($\sim$ 1 milli-arcsec (mas)), rather than ~ 0.05 arcsec (50 mas), in the visible.

The disadvantage of interferometry is that it samples the Fourier domain, instead of the spatial domain, at as many point as the number of baselines in the array: a two-apertures interferometer will only get a single Fourier-measurement on the source. Also, similarly to single-dish telescopes, interferometry requires an exquisite precision such that the travel-time of each beam of light in each arms of the interferometer is identical, at a certain tolerance called the coherence-length. In non-interferometric single-aperture telescopes, this is achieved with high-quality polishing of mirrors. However, for interferometers using several telescopes, one requires an additional layer of complexity to track the target simultaneously on all telescopes in order to null the path-difference through each arm of the interferometer; the precision required is typically of order several λ (i.e. 5 μm in the visible) when telescopes are located tens of meters from each-other.

2.1.2 Physics at stake

Interferometry uses the wave-properties of light, however one must also consider light as grain, i.e. photons, to illustrate the concept of coherence-length. Photons are quantum beasts, touched by non-locality: they cannot be detected in two (or more) places. Interferences are only achieved with coherent light, or between photons coherent between each-other. In nature, coherent sources of photons (like lasers) are excessively rare (this is not true at very short timescale, of order THz or more, because photons arising from thermal emission are emitted in packets; intensity interferometry is the illustration of it); this means that photons must interfere with themselves.

Detectors in the visible or in the infrared do not run fast enough to measure the full electric field of light (wave frequencies of order femto-seconds); they only measure a time-averaged intensity of this field. Hence, for $\lambda \lesssim 400$ μm one must make light interfere first, and measure only then the interference patterns.

One can see each photon as a pulsed wave function, or a pulsed-wavefront, going through all telescopes of an interferometer simultaneously. When the path-difference of this wavefront through all arms of an interferometer is smaller than the coherence-

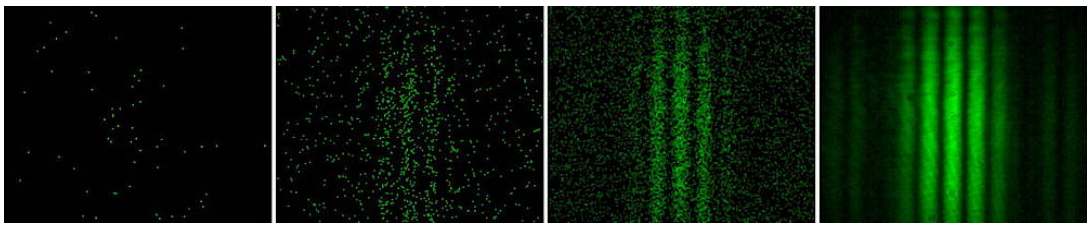

Figure 2.2: Single-photon camera recording of photons from a double slit illuminated by very weak laser light. Left to right: single frame, superposition of 200, 1 000, 50 000 and 500 000 photons. One sees the fringe pattern of a double-slit experiment appear as more and more interfering photons are recorded. Initially in Dimitrova & Weis (2008).

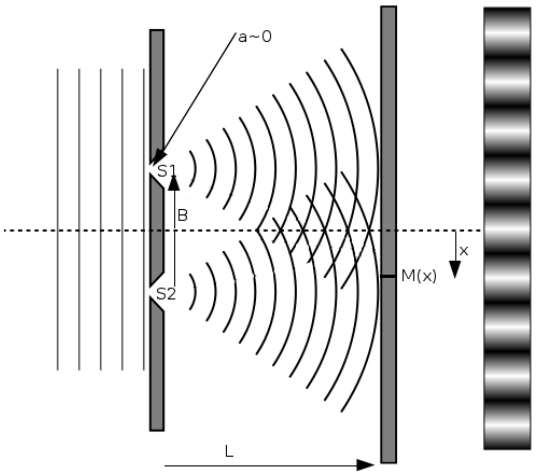

Figure 2.3: Optical scheme of Young's slits experiment.

length, it will reach the detector through each arm at the same timestamp. Under this condition only will the pulsed wave function overlap with itself, and interfere.

In case of interference, the probability distribution function of the location of the photon-count on the detector is the pattern of fringes. Dimitrova & Weis (2008) designed an experiment to easily illustrate (e.g. in a classroom) the wave-particle duality of photons in interferometry. Figure 2.2 shows the interference pattern of a two-slits setup (i.e. Young's slits), for an increasing amount of photons detected.

In order to set out the main physics interferometry equations, let us first consider a two-telescopes (or two-apertures) interferometer, similarly to the Young's holes, which will be simplified to a one-dimensional problem using slits instead. The light-source is located far-enough to consider a flat wavefront at the slits. The light is monochromatic of wavelength λ, the distance between the slits and the detector is L, the distance between the two slits is B, as shown in Figure 2.3, their width is considered infinitely small.

The intensity at a location M depends on its coordinate x, and the timestamp of observation t. We consider a flat wavefront arising from an infinitely small source S,

defined by its electrical field:

$$V(S,t) = A\exp\Big(-\mathbf{j}\frac{2\pi c}{\lambda}t\Big) \tag{2.4}$$

with A the wave amplitude (taken to be 1) and c the speed of light in vacuum. The detector will only be sensitive to the time-averaged intensity of this field, i.e. time-averaged squared-modulus. One can define the intensity observed at location M, timestamp t and during Δt, arising from each or both sources, respectively, to be:

$$\begin{aligned} I_i(M) &= \Big\langle \big|V(S_i, t-\tau_i)\big|^2 \Big\rangle_{\Delta t} \\ I_{12}(M) &= \Big\langle \big|V(S_1, t-\tau_1) + V(S_2, t-\tau_2)\big|^2 \Big\rangle_{\Delta t} \end{aligned} \tag{2.5}$$

with τ_i the travel-time of the wave between the slit i and the location M on the detector. When expending the square of $I_{12}(M)$ in Eq. (2.5), and using τ=τ_2-τ_1, $t_0 = t - \tau_1$, and the mutual coherence factor Γ of the source at S1 et S2 defined to be:

$$\Gamma_{12}(\tau) = \Big\langle V(S_1, t_0-\tau) \times V^*(S_2, t_0) \Big\rangle_{\Delta t}, \tag{2.6}$$

one gets:

$$\begin{aligned} I_{12}(M) &= I_1(M) + I_2(M) + \Gamma_{12}(\tau) + \Gamma_{12}^*(\tau) \\ &= I_1(M) + I_2(M) + 2\mathcal{R}e\big(\Gamma_{12}(\tau)\big). \end{aligned} \tag{2.7}$$

We introduce the normalized mutual coherence factor γ_{12} to be:

$$\gamma_{12}(\tau) = \frac{\Gamma_{12}(\tau)}{\sqrt{\Gamma_{11}(0) * \Gamma_{22}(0)}}. \tag{2.8}$$

S1 and S2 being identical, one has $\Gamma_{ii}(0)$=I_{Si} and $I_i(M)$=$I(M)$. Hence one obtains:

$$\gamma_{12}(\tau) = \frac{\Gamma_{12}(\tau)}{I(M)}, \tag{2.9}$$

and:

$$I_{12}(M) = 2\ I(M)\Big[1 + \mathcal{R}e\big(\gamma_{12}(\tau)\big)\Big]. \tag{2.10}$$

Using Eq. (2.4) into Eqs. (2.6) and (2.5), and into Eq. (2.9), one gets,

$$\gamma_{12}(\tau) = \exp\Big(-\mathbf{j}\frac{2\pi c}{\lambda}\tau\Big) \tag{2.11}$$

and finally:

$$I_{12}(M) = 2I(M)\Big[1 + \cos\Big(\frac{2\pi B}{\lambda}x\Big)\Big] \tag{2.12}$$

with Bx=cτ the path-difference of light between both sources and M, considering L$\gg$B, x, variables as in Figure 2.3.

This intensity pattern as a function of x is depicted on the right-most side of Figure 2.3. It is a pattern that alternates bright and dark regions: fringes. The distance between two successive bright regions is given by:

$$l_i = \frac{\lambda L}{B} \tag{2.13}$$

which, when $l_i \gg$L, can be re-written similarly to Eq. (2.3) defining the typical resolution of an interferometer:

$$\frac{l_i}{L} = \frac{\lambda}{B} \sim \arctan\left(\frac{l_i}{L}\right) \sim \theta. \tag{2.14}$$

The 0.5 factor difference comes from the fact that the resolution criteria is taken to be half the fringe separation. However, this is not a strict definition, and in case of small errors on measurements, the resolution of the interferometer is effectively only a fraction of 0.5λ/B.

Once having measured fringes with the detector, one must undergo heavy numerical analysis to produce a "measurement" that can be related to the science-object observed.

2.1.3 Fourier and spatial domains

The Zernike-Van Cittert theorem (van Cittert 1934) builds the mathematical framework to treating resolved sources as the superposition of unitary point-like sources. This theorem, demonstrated by Born & Wolf (1980) and later by Goodman (1985) on a purely statistical basis, is considered to be the basis of modern interferometry:

If the typical dimension of the quasi-monochromatic source as well as the detector size are small compared to the distance between the source and the detector, the complex coherence factor is the spatial Fourier transform of the source intensity, normalized to the total source intensity.

In other words, the complex visibility $\widetilde{\mathcal{V}}_{12}$ of a source seen through two identical apertures with spatial separation (u,v) is:

$$\widetilde{\mathcal{V}}_{12} = \frac{FT\big[I(\alpha,\delta)\big](u,v)}{\iint_{source} I(\alpha,\delta)d\alpha d\delta} \tag{2.15}$$

where I(α, δ) is the intensity map of the source projected onto the right-ascension (α) and declination (δ) coordinates on the sky, and (u, v) are the conjugated spatial coordinates in the Fourier domain, expressed in spatial length ≡[meter] or in spatial frequencies (or cycles) ≡[m/λ]. $\widetilde{\mathcal{V}}$ is indirectly measured from the fringe pattern acquired by the detector. Indeed, one measures the squared-modulus (VIS2) and the phase of the complex visibility, although the phase is usually altered by turbulence and cannot be used as-is, see Section 2.2.2 for a post-processing get-around.

These results are fundamental since they demonstrate that measuring a visibility from fringe patterns is equivalent to measuring the intensity distribution of the

source in the Fourier domain, independently from the point-spread-function (PSF) of the apertures. This highlights that interferometry naturally provides a "deconvolved" measurement of the geometry of the observed object, and that the theoretical resolution of an interferometric measurement is possibly well beyond the λ/D criteria. However, Eq. (2.15) is not invertible because of sparse (u,v) sampling; this means that the processing of the data is naturally cumbersome and requires to be done in the Fourier domain.

2.2 Targeted Overview of Interferometry Instrumentation

The philosophical and technical grounds for interferometry have been exposed in the previous section, showing how such technique can access spatial frequencies far larger than that of a single-dish telescope. In practice, the observer must adapt the use of interferometers to the reality of an observation and account for polychromatic light, non-infinitesimal apertures, residual phase errors, etc. This following section will detail the caveats of non-ideal interferometry physics, introduce the concept of closure phase which allows self-calibrated observations and finally present two types of modern interferometry at observatories where data was acquired in the frame of this work.

2.2.1 Non-ideal interferometry physics

If one believes Eq. (2.12), fringes are an infinitely repeating pattern. In reality, the wavelength is not monochromatic, and the width of the slits is not infinitely small. Both these factors tend to smear the fringes out, hence diminish their contrast, or visibility.

One must therefore consider a spectral domain $\Delta\lambda$ centered on λ. The physics of interferometry allows us to use the superposition principle on Eq. (2.12). Such double-slits experiment will produce a superposition of fringes arising from each infinitely small wavelength bandwidth $\delta\lambda$ taken in $\Delta\lambda$. Such fringes sum up incoherently on the detector and, apart from the position x=0, they will generate a blurred fringes pattern; their contrast will be progressively diminished as x increases. This phenomena is called bandwidth smearing.

We can define a distance from x=0 from where the fringes reach a certain blur-threshold where they start overlapping. This distance is the coherence length l_c defined by:

$$l_c = \frac{\lambda^2}{\Delta\lambda}. \tag{2.16}$$

The fact that the source is not point-like is accounted by the term $I(M)$ in Eq. (2.12). Instead of unity, this term will be replaced by an expression of x.

Figure 2.4 shows the effect of bandwidth smearing and non-infinitesimal aperture-size on the interference pattern, in case of an interferometer composed of two apertures of 1 m diameter. One can see that the first diffraction null, corresponding to the envelope, is located at $\sim$ 950 mas (out of view for the bottom plot), corresponding to

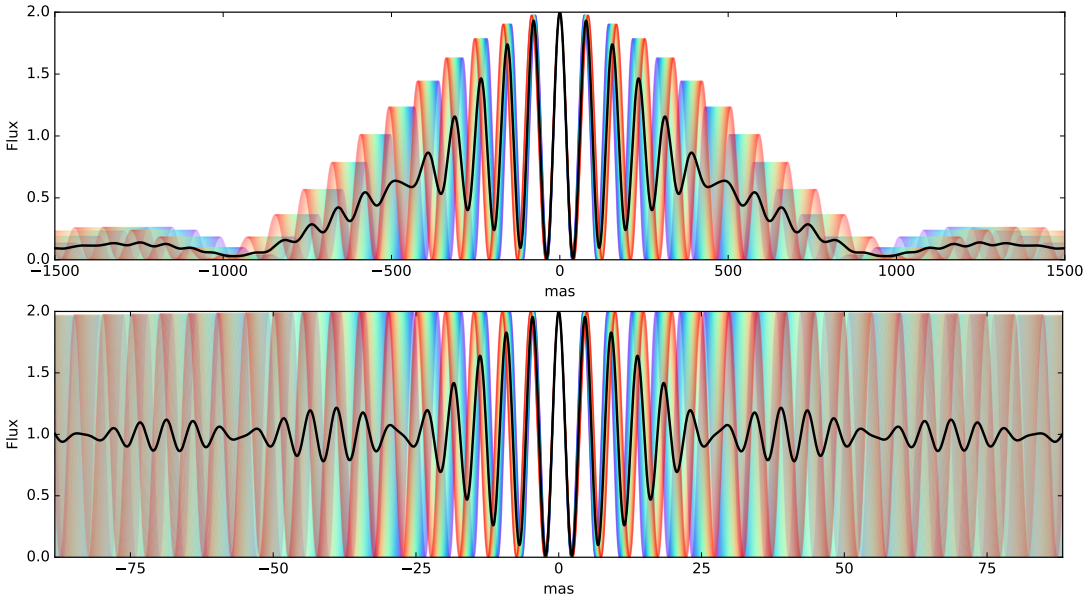

Figure 2.4: Effect of bandwidth smearing and non-infinitesimal aperture-size on the interference pattern. Figure obtained for two apertures of diameter 1 m, located 10 m from each other (top) or 170 m (bottom), for $\lambda = 3.8\ \mu m$ and $\Delta\lambda = 0.62\ \mu m$ (corresponding to Lp filter on the Very Large Telescope (VLT)). The black curve is the average of all color-coded curves; it is the intensity-signal to be expected on the detector.

1.22λ/D having D=1 m the diameter of each aperture. The first null of the interference pattern is located at $\sim$ 40 mas ($\sim$ 2.3 mas for the bottom plot), corresponding to half the peak-to-peak distance, given by Eq. (2.14): 0.5λ/B having B=10 m (170 m for the bottom plot) the distance between the two apertures.

The black curve is the average of all other color-coded curves, and represents the expected signal to be measured on the detector. One sees that beyond the coherence length of $\sim$ 480 mas ($\sim$ 30 mas for the bottom plot), the general shape of the fringes changes to a pseudo-cyclic incoherent mixing of the different color-contributions (the red and blue curves start over-lapping). It is from this black signal that the interferometric squared-visibility (VIS2) is measured.

The direct consequence is that bandwidth smearing and aperture sizes should be taken into account while processing interferometric data. Indeed, the processing of interferometric data must simultaneously combine the knowledge and modelling of both the instrument and the astrophysical object. This will be addressed in Section 2.3.

2.2.2 Closure phases

We have seen in the previous section that both phases and squared-visibilities can be retrieved through the intensity of the fringes on the detector. Phases show non-

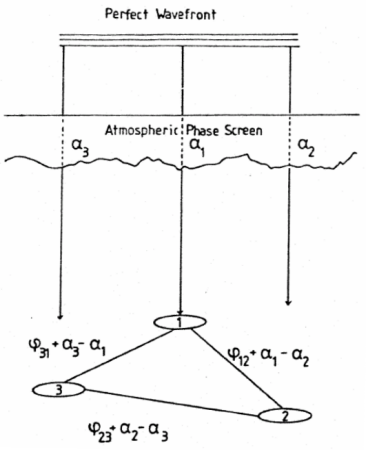

$$
\begin{aligned}
\varphi_{31} &= \varphi_{31,\,real} + \alpha_3 - \alpha_1 \\
\varphi_{23} &= \varphi_{23,\,real} + \alpha_2 - \alpha_3 \\
\varphi_{12} &= \varphi_{12,\,real} + \alpha_1 - \alpha_2 \\
\varphi_{31} + \varphi_{23} + \varphi_{12} &= \varphi_{31,\,real} + \alpha_3 - \alpha_1 \\
&\quad + \varphi_{23,\,real} + \alpha_2 - \alpha_3 \\
&\quad + \varphi_{12,\,real} + \alpha_1 - \alpha_2 \\
\varphi_{31} + \varphi_{23} + \varphi_{12} &= \varphi_{31,\,real} + \varphi_{23,\,real} + \varphi_{12,\,real}
\end{aligned}
\tag{2.17}
$$

Figure 2.5: **Left**: Schematic showing the construction of closure phases as each baseline produces a phase signal φ affected by random phase-errors α arising from both apertures contributing to the baseline.
Right: Proof of the canceling of random error terms arising from the atmospheric phase screen when summing phases along a closing triangle.

constant errors for telescopes having a diameter D>r_0 (i.e. all modern telescopes): phase measurements cannot be directly stacked coherently to increase the SNR. The loss of phase-information has serious consequences, indeed the Fourier phase information from the interferometer fringes encodes non-centrosymmetric details. Hence, without this information, one can only achieve centrosymmetrical characterization of targets.

If one considers interferometric arrays of three or more apertures, one can measure closure phases as described in Jennison (1958); Monnier (2000). As Figure 2.5 depicts, closure phases are based on the fact that each baseline of an array produces a phase signal affected by random phase-errors arising from both apertures contributing to the baseline. When summing such deteriorated phases from three baselines forming a closing triangle (hence *closure* phase), the phase-error terms cancel-out and a pseudo-phase information is retrieved, unaffected by turbulence or even some instrumental systematics.

Although additional information is retrieved out of the observables, the intrinsic nature of this triple-phase-combination makes this data complex to apprehend. Indeed, closure phases (T3) possess certain properties which both are their greatest strength, and their weakness:

1. The closure phases are independent of all telescope-specific phase errors. The

Table 2.1: Phase information contained in the closure phases.

N apertures	# T3	# VIS2	# independent T3	Phase recovery
3	1	3	1	33%
4	4	6	3	50%
7	35	21	15	71%
10	120	45	36	80%
13	286	78	66	85%
18	816	153	136	89%
21	1330	210	190	90%
29	3654	406	378	93%

measurement of non-zero closure phases from a point source result from having non-closing triangles or phase delays after splitting beams.

2. Closure phases are not sensitive to an overall translation of the image.

3. The closure phases of an object with point-symmetry are always 0 or 180°. Detection of other angles implies the object's intensity distribution is skewed.

4. A non-resolved object has no closure phase signal.

Also, the number of independent closure phases measured is lower than that of VIS2, which means that a full characterization of the amplitude+phase parameters at all (u,v) coordinates of the Fourier domain is not achievable. Indeed, for a N-apertures array, there are "N choose 3" T3 ($N(N-1)(N-2)/6$) and "N choose 2" VIS2 ($N(N-1)/2$). The number of *independent* closure phases is however only "N-1 choose 3" ($(N-1)(N-2)/2$), equivalent to holding one aperture fixed and forming all possible triangles with that aperture. Table 2.1 illustrates these quantities for different aperture counts.

Because T3 are robust to turbulence, they allow high-contrast capability without the inevitable "blind-spot" of other techniques such as coronography. Le Bouquin & Absil (2012) showed that one could expect to measure a contrast of ~ 6 magnitudes for T3 errors of $\sim 0.25°$ when stacking five different observation position angles. For simple sources such as binary stars, modelling of the closure phases can be used to reach unprecedented precision in parametrized models. For more complicated objects, the ability to measure even a limited number of closure phases will lead to new astrophysical insight, before true interferometric "imaging" becomes standard practice.

The measurements of squared-visibilities and closure phases can be achieved through two main interferometric techniques: Long-Baseline Interferometry (LBI) which produced the data used in Appendix A, and Sparse-Aperture Masking (SAM), also called Non-Redundant-Masking (NRM), which produced the data used in Chapter 3.

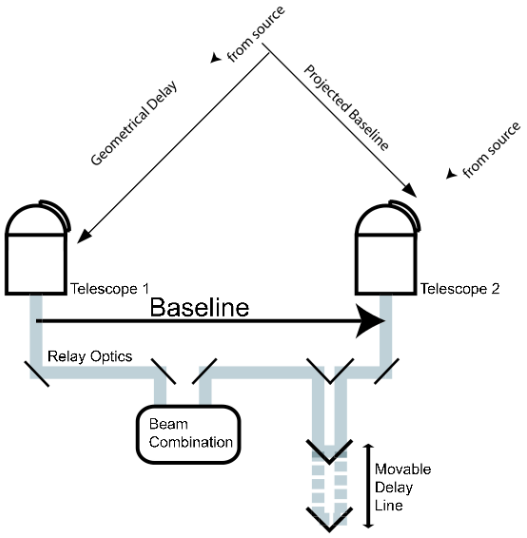

Figure 2.6: Schematic showing the principle of delay-lines in LBI.

2.2.3 Long-baseline interferometry

LBI is what looks most like "classical" interferometry nowadays, although the first interferometer, 6 m baseline, built by Michelson in 1890 was somewhat closer to SAM technique given that only one telescope was used. Long-Baseline interferometers are composed of several telescopes – each telescope being an aperture – which are controlled simultaneously to point at and track the same target; each telescope might benefit from an AO system, in order to increase the performance of interferometers having $D \gg r_0$. LBI has theoretically no limit to the longest baseline: it reaches 640 m for the Sydney University Stellar Interferometer (SUSI) in the visible, and up to $\sim$ 2 km for the Atacama Large Millimeter/submillimeter Array (ALMA).

Because of the rotation of the Earth, the projected baseline-lengths between telescopes vary slightly but predictably as a function of time. A system called delay-lines shown in Figure 2.6 compensates for it, in order to keep the simultaneity of the wavefront through all arms of the interferometer. Delay-lines are able to introduce a delay which can be nearly as long as the longest baseline of a LBI array, leading to the very large sizes of beam recombination facilities. Note that if the modelling of the telescope locations, their pointing and the sky-rotation is accurate, the delay-lines obey to a fully-deterministic displacement.

One of the best example of LBI is probably the CHARA array, see Figure 2.7, located on the Mount Wilson, near Los Angeles, California, whose telescopes surround the 100-inches telescope used by Michelson. Each telescope of the CHARA Array (ten Brummelaar et al. 2005) is a light-collecting mirror of 1 m in diameter, with baselines from 34 to 330 m. Light from the individual telescopes is conveyed through vacuum tubes to a central beam synthesis facility in which several instruments are able to collect and combine the light in different ways: from two to six telescopes,

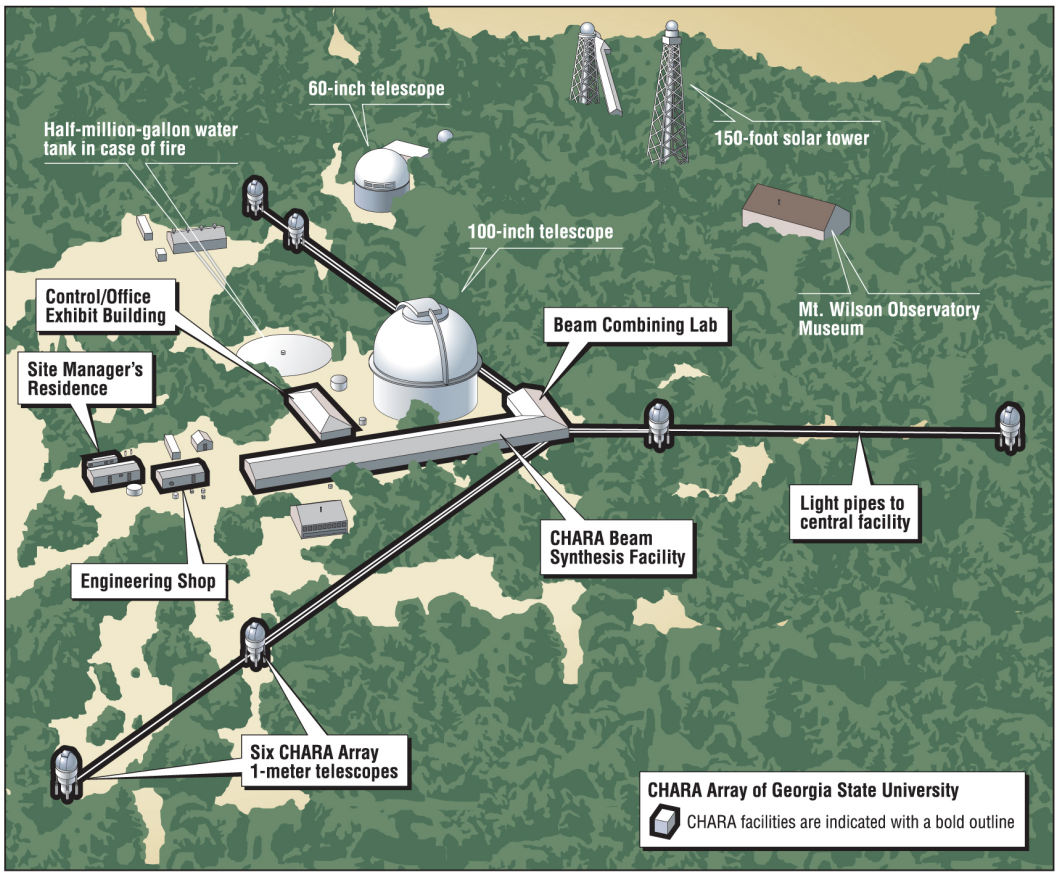

Figure 2.7: Schematic showing the CHARA array six 1 m-telescopes on top the Mount Wilson observatory.

with none to a maximum of 30 000 spectral resolution, in wavelengths from 0.6 μm to K-band (2.18 μm). Data was acquired at the CHARA Array using PAVO instrument, a two-telescopes interferometer with thirty-height wavelength channels between 0.63 and 0.881 μm (Ireland et al. 2008), in order to characterize the spectral types of the spectroscopic binary MWC-361, see Appendix A.

2.2.4 Sparse-aperture masking

Sparse-Aperture-Masking (SAM, or Non-Redundant Masking: NRM) is an observational technique in which a single mirror is transformed into a multi-pupil Fizeau interferometer. A mask placed in the pupil plane of the telescope transforms the usual Airy point-spread function (PSF) of the full-pupil into a pattern made of multiple fringes. Implemented by Baldwin et al. (1986) and developed by Tuthill (1994), this technique provides the benefits of high-angular resolution (0.5λ/D criteria) without the cost and complexity of LBI. Indeed, while delay-lines were required in LBI to

achieve a precise wavefront synchronization from all interferometric arms, the primary mirror of the telescope in SAM technique naturally and very precisely synchronizes the wavefront from all apertures (also called pupils). Typically, the wavefront RMS error arising from mirror-polishing is 20 nm (for the VLT), which represents $\lambda/50$ at 1 μm.

The longest baseline of a SAM observation is inherently limited to the diameter of the primary mirror of the telescope. The Large Binocular Telescope (LBT) currently provides the longest NRM baseline, $\sim$ 22 m, until Extremely Large Telescopes (ELT) are commissioned (up to 39 m for the E-ELT). SAM technique does not show effects of baseline-projection with the rotation of earth, although it does show sky-rotation if the telescope has an alt-azimuthal mount.

While the Fourier-sampling of a LBI depends on the location of its telescopes, that of NRM depends on the location of the holes in the mask. They shall be as dense as possible to provide a good (u,v) coverage. However, in order to avoid overlapping of the sampling-patches in the Fourier domain, the size of the holes must decrease with the number of holes. Figure 2.8 illustrates this effect; on a 8.2 m telescope, a 7-holes mask has 1.1 m diameter apertures maximum ($\sim$ 14% throughput) but only 0.37 m for a 18-holes mask ($\sim$ 4% throughput). A 7-holes mask will be 2.1 mags less sensitive than a full telescope aperture (10% obstructed), and 3.5 mags for a 18-holes mask. In practice, the observer must ideally adapt the mask used to the target observed, in order to get the best compromise between (u,v) coverage and sensitivity.

Although LBI uses longer baselines than SAM, hence benefits from higher resolution, the largest LBI observatory recombines "only" six apertures in the case of CHAMP and MIRC at the CHARA array. Since the interferometric UV coverage (i.e. the number of independent T3 or VIS2 measurements) increases as the square of the number of apertures, SAM masks provide a 1.4 (7-holes) to 10 (18-holes) times denser UV sampling than the largest LBI observatory.

Thanks to the use of closure phases, NRM shows a unique high-resolution capability combined with a high-contrast capacity, able to precisely explore of the inner-most regions of targets. This represents a critical strength over full-pupil imaging. Chapter 3 makes use of SAM data obtained at the VLT .

2.3 Processing Interferometric Data

Interferometric data is only sparsely sampling the Fourier domain, especially in LBI. For this reason, and because the phase information is only partly measured, no inverse Fourier Transform is possible from the interferometric (Fourier) domain to the spatial domain. When the (u,v) coverage of an observation is high, as a rule of thumb $\sim$ 100 measures at different position angles and baselines, one can intend an image reconstruction. Otherwise, one should proceed with building parametric-models from a-priori knowledge of the source and evaluate their likelihood given the interferometric data; i.e. Bayesian inference.

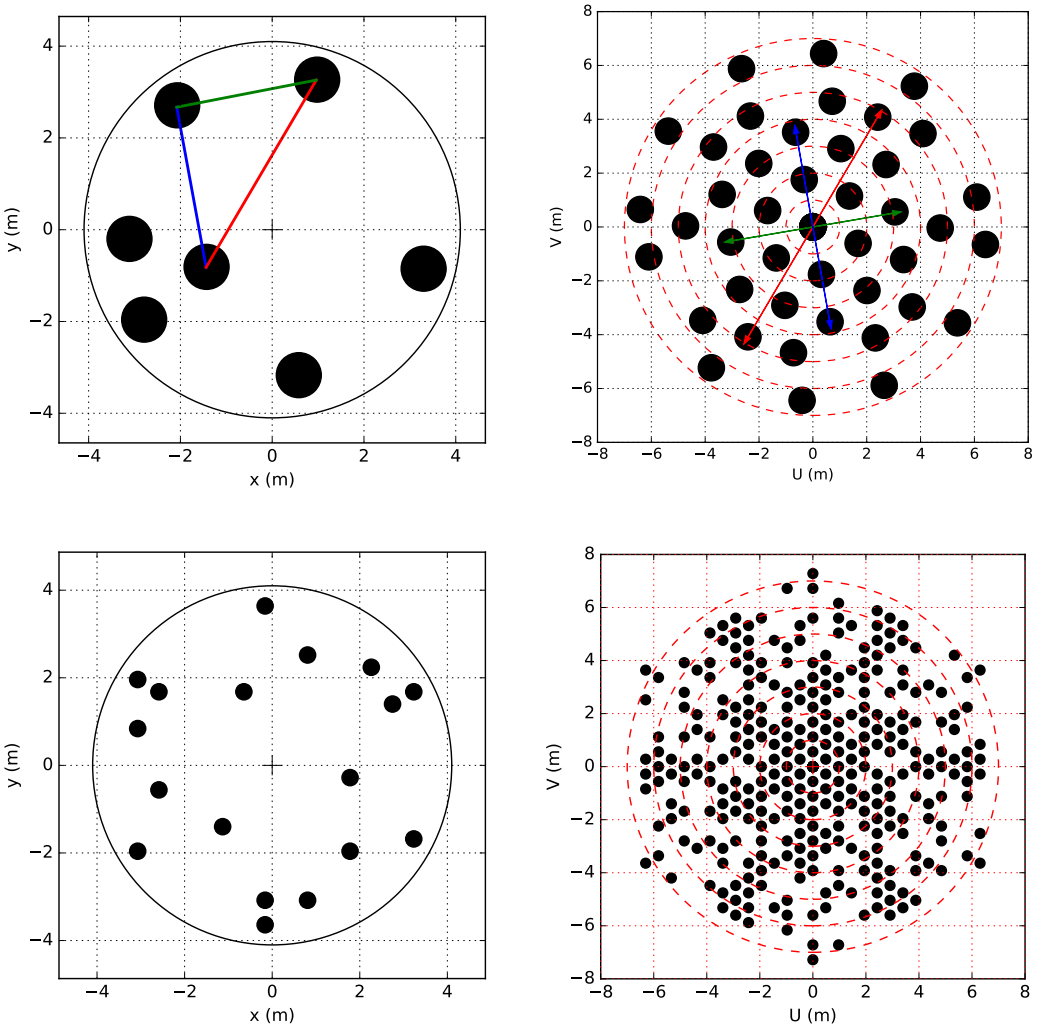

Figure 2.8: Masks in the pupil plane (left column) and their corresponding UV coverage in the Fourier plane (right column) for a 7-holes mask (top row) and a 18-holes mask (bottom row). The throughput of the 7-holes mask is $\sim$ 14% (4% for the 18-holes mask), while typical throughput of a telescope is 70%-97% taking into account the central obstruction and spiders.

Having such highly-structured data forces the scientist to treat the observables as "proper measurements" with error-bars, rather than "turn-key" data. As an illustration of this, one image of 258*258 pixels (66 564 measurements) used in the next chapter contained the same (if not less) information as four position angles of 21 VIS2 points (84 measurements): the information density of interferometric measurements is much larger than that of classical imaging.

This section will details how to build a interferometric parametric-model (Section 2.3.1) in order to perform a mathematical optimization of its parameters using the maximum likelihood estimator (Section 2.3.2). It will later discuss the importance of error-bars in this fitting process (Section 2.3.3) and in order to compare the fitness of different models to explain the data (Section 2.3.4), and finally present a few tools available to do so.

2.3.1 Parametric fitting

In order to fit the interferometric data, most commonly VIS2 and T3 data, one can postulate a model defined by a combination of set- and free-parameters. One then need to search for a particular value of the free parameters that maximizes the likelihood of the model given the data. Such model of complex visibility $\widetilde{\mathcal{V}}_{model}$ is in practice composed of several unitary-models of complex visibility $\widetilde{\mathcal{V}}_i$, which can each comprise none, one or several free parameters each. As an example, a binary model would be composed of two point-source unitary models.

2.3.1.1 Coordinates system

All unitary models are – at least – defined by three parameters: their location along RA and DEC axes, and their flux. Given that the Fourier-Transform (FT) is shift-invariant, one must set the RA-DEC parameters of (at least) one unitary model, as well as the flux of (at least) one of the unitary models to set a reference. I.e. fitting a binary star requires two point-source unitary-models, the RA-DEC and flux of the the primary star are arbitrarily set to (0,0) and 1 respectively, and the three parameters of the companion star are left free for fitting.

The central location $\overrightarrow{L}$ of a unitary model on the sky, along RA (West to East) and DEC (South to North) axes, is expressed in angular units:

$$\overrightarrow{L} = \delta\overrightarrow{North} + \alpha\overrightarrow{East}. \tag{2.18}$$

For m unitary models sorted from the brightest to the faintest, one has:

$$\begin{aligned} \overrightarrow{L_1} &= \overrightarrow{0} \\ \overrightarrow{L_i} &= \delta_i\overrightarrow{North} + \alpha_i\overrightarrow{East},\ with\ i \in [2, m] \end{aligned} \tag{2.19}$$

where the location of the brightest unitary model is set to the center of the field, by convention.

The location $\overrightarrow{H}$ of h interferometric apertures projected on the sky along North and East axes is expressed in meters:

$$\overrightarrow{H_i} = x_i\overrightarrow{North} + y_i\overrightarrow{East},\ with\ i \in [1,h]. \tag{2.20}$$

However, the interferometrist is interested in the b=h(h-1)/2 baselines $\overrightarrow{B}$, which are the separation between each two apertures of the interferometer, in meters:

$$\begin{aligned}\overrightarrow{B_i} &= \overrightarrow{H_j} - \overrightarrow{H_k},\ with\ j \in [1,h],\ k \in [j+1,h] \\ &= u_i\overrightarrow{North} + v_i\overrightarrow{East},\ with\ i \in [1,b].\end{aligned} \tag{2.21}$$

Given the symmetry in the definition of a baseline, the baseline length B_i and angle $\widehat{B_i}$ are defined as:

$$\begin{aligned}B_i &= \|\overrightarrow{B_i}\| = \sqrt{u_i^2 + v_i^2},\ with\ i \in [1,b] \\ \widehat{B_i} &= arctan(\frac{v_i}{u_i}),\ with\ i \in [1,b],\end{aligned} \tag{2.22}$$

such that the modulus of the complex visibility (i.e. interferometric VIS2) is point-symmetrical, and its argument point-anti-symmetrical (i.e. T3):

$$\begin{aligned}\|\widetilde{\mathcal{V}}_{u,v}\| &= \|\widetilde{\mathcal{V}}_{-u,-v}\| \\ \arg\big(\widetilde{\mathcal{V}}_{u,v}\big) &= -\arg\big(\widetilde{\mathcal{V}}_{-u,-v}\big).\end{aligned} \tag{2.23}$$

2.3.1.2 Complex visibilities of a model

We have seen in Section 2.1.3 that the complex visibility of a source is the spatial FT of its intensity map, normalized to its total intensity. Using the linearity of FT, one can generalize this definition: the complex visibility of m unitary models is the sum of the spatial FT of each of their intensity maps, normalized to the integrated intensity of all unitary models. In other terms:

$$\Big(\sum_{i=1}^{m} f_i\Big) \times \widetilde{\mathcal{V}}_{tot} = \sum_{i=1}^{m}\Big[f_i \times \widetilde{\mathcal{V}}_i\Big] = \sum_{i=1}^{m}\Big[f_i \times FT\big(I_i\big)\Big], \tag{2.24}$$

for m unitary models of spatial intensity map I_i, complex visibility $\widetilde{\mathcal{V}}_i$ and integrated flux $\mathrm{f}_i = \iint \mathrm{I}_i$.

The FT of a unitary model with intensity map $\mathrm{I}_{\alpha,\delta}$ whose central-location is $\overrightarrow{L} = (\alpha,\delta)$, can be re-written using the shift property of the FT:

$$FT(I_{\alpha,\delta}) = FT(I_{0,0}) \times \exp\big(-2\pi\mathbf{j}(\xi_x\alpha + \xi_y\delta)\big), \tag{2.25}$$

with ξ_x=u/λ and ξ_y=v/λ being the spatial frequencies in which (u,v) are the baseline lengths along α and δ axes, and λ the wavelength.

In the general case and using the latter result, the complex visibility $\widetilde{\mathcal{V}}$ of a unitary model shifted of $\overrightarrow{L}$ can be written:

$$\widetilde{\mathcal{V}} = FT(I_{\alpha,\delta}) = FT(I_{0,0}) \times \exp\Big(-2\pi\mathbf{j}\frac{\overrightarrow{L}\cdot\overrightarrow{B}}{\lambda}\Big). \tag{2.26}$$

where $\cdot$ is the scalar product of the unitary model location vector $\overrightarrow{L}$ (Eq. (2.19)) with the baseline $\overrightarrow{B}$ (Eq. (2.21)).

Therefore, the total complex visibility $\widetilde{\mathcal{V}}_{tot}$ of a model made of m unitary models is:

$$\Big(\sum_{i=1}^{m} f_i\Big) \times \widetilde{\mathcal{V}}_{tot} = \sum_{i=1}^{m}\left[f_i \times FT(I_{i\ 0,0}) \times \exp\Big(-2\pi\mathbf{j}\frac{\overrightarrow{L_i}\cdot\overrightarrow{B}}{\lambda}\Big)\right], \tag{2.27}$$

Table 2.2: Parametric representation and analytical expression of the FT of several simple unitary models

Unit. model	Parameters	$FT(I_{0,0})$
Point Source	α, δ, flx	1
Circle	α, δ, flx, r	$\mathrm{J}_0(2\pi r\nu)$
Uniform Disk	α, δ, flx, ϕ	$2\times\mathrm{J}_1(\pi\phi\nu)\times(\pi\phi\nu)^{-1}$
Gaussian Disk	α, δ, flx, σ	Gaussian$(\pi\sigma\nu)$

1. $\nu = \frac{\overrightarrow{B}}{\lambda}$
2. Gaussian$(x) = \exp\big(-2*x^2\big)$
3. J_i are Bessel functions of the first kind, of ith order.

Some simple unitary models possess an analytic FT, shown in Table 2.2; they allow a very fast fitting of a model to the data. Some other analytical unitary models exist, such as exponential or power-law radial decrease, for the sake of conciseness they are not detailed here. Note that the Point-Source, Circle, Uniform Disk and Gaussian Disk unitary models can be sheared into two-dimensional ellipsoids using two additional parameters: an aspect ratio ρ, and a position angle θ.

2.3.2 Mathematical optimization

Given that the Eq. (2.27) is not invertible, one must use numerical methods to find the optimal values of the free parameters. In this work, Monte Carlo (MC) randomized algorithms are used to perform the fitting activities. A randomized algorithm is an algorithm that employs a degree of randomness as part of its logic. Such algorithms show a tremendous increase of efficiency to find optimal values over classical deterministic algorithms, e.g. "computational grids". While a Las Vegas algorithm (e.g. genetic) always terminates with a correct result in a bounded amount of time, a MC probabilistic algorithm (e.g. Markov-Chain, "MCMC") will have a chance of producing

an incorrect result, depending on the random input, or fail to produce a result either by signaling a failure or failing to terminate.

However, the critical advantage of a MC technique is that it provides probabilistic uncertainties together with the simulation result; this is not the case of Las Vegas algorithms that only find the "best solution in the time it was given".

The *emcee*[1] (Foreman-Mackey et al. 2013) library is used; it is a pure-Python implementation of Goodman & Weare (2009) Affine Invariant Ensemble sampler to optimize – either minimize or maximize depending on the expression – the quality-function of the fit. This technique is based on a Markov-Chain Monte Carlo (MCMC) algorithm, although more effective in case of badly scaled or highly skewed distributions.

The quality-function of the fit is the log-likelihood of the model given the data, expressed in its most general form as:

$$ln\mathcal{L} = -0.5 \times \sum_i \left[\frac{\left(Data_i - Model_i\right)^2}{\sigma_i^2} - \ln\left(\frac{2\pi}{\sigma_i^2}\right) \right], \tag{2.28}$$

where the index i iterates over each (u,v) coordinates-set of a dataset, and σ is the error-bars on the data. When such error-bars are known, one can simplify this latter expression into

$$ln\mathcal{L} = -\sum_i \frac{\left(Data_i - Model_i\right)^2}{\sigma_i^2}, \tag{2.29}$$

since the term $\ln(2\pi/\sigma_i^2)$ is constant, hence does not affect the convergence of the optimization.

For each iteration, or "step", this quality-function is evaluated, and the step is accepted – or not – depending on whether it brought an improvement compared to the latest step (note that there is also a probability to accept a worse step). The results of such MCMC simulation shall be interpreted using histograms of the step-locations in order to determine the most probable parameters values/domains. The Python package *corner* (Foreman-Mackey 2016)[2] provides a so-called "corner" or "triangle" view for such simulations; used within the *MCres*[3] wrapper, they offer a quick and convenient toolbox to view, filter, zoom in and out on local minima. These corner plots will be abundantly used throughout this work; Figure 2.9 provides guidelines to the reading and comprehension of such plots.

The latter representation of a MCMC simulation is extremely convenient in that it displays the "covariance matrix" of the simulation, from which the confidence domains can be calculated.

2.3.3 Errors and confidence domain

Confidence-domain of the model parameters play a critical role in science-modelling and in model comparison. However, the quality of the confidence domains calculated

[1] https://github.com/dfm/emcee
[2] https://github.com/dfm/corner.py
[3] https://github.com/ceyzeriat/MCres

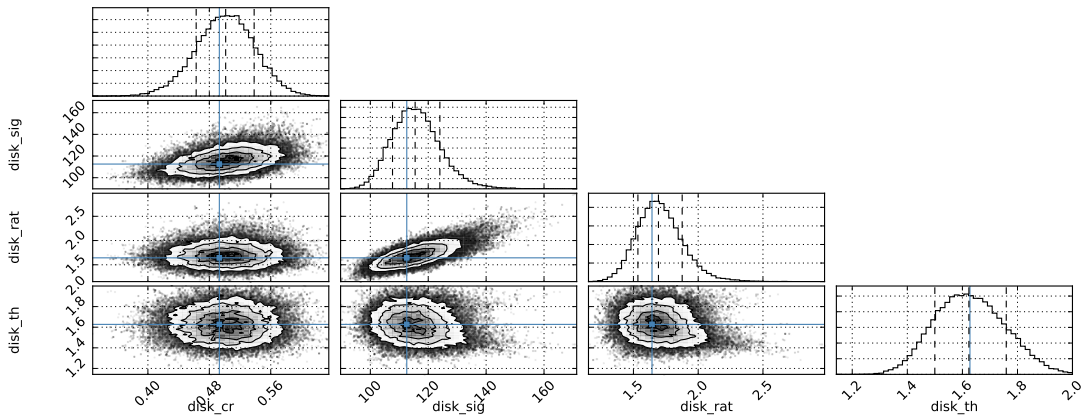

Figure 2.9: Example *Corner* plot obtained with *MCres* and *corner* from fitting a parametric 2D-Gaussian disk to interferometric data using *SOIF* package. The free-parameters are disk_cr, disk_sig, disk_rat and disk_th which correspond to the disk contrast ratio (to the central star), its semi-major axis (in mas), the semi-axes ratio (major/minor) and the semi-major axis position angle (in radian). The one-dimensional histograms show the variances of each parameter, indicated in the x-axis labels. Dashed-lines show the 16^{th}, 50^{th} (i.e. median) and 84^{th} percentiles. The two-dimensional histograms show the covariances of each two parameters; e.g. the bottom left subplot shows how the disk position angle (y-axis) varies with the disk contrast ratio (x-axis). The gray-shaded areas surrounded by thin black lines represent the 0.5, 1, 1.5, and 2-sigma domains. The blue lines represent the most probable values of the parameter estimation.

for the parameter estimation directly linked to the quality of estimation of error-bars on the data. Monte-Carlo simulations provide error-estimations which suffer from heavy biases in case of under- or over-estimation of the error-bars on the data. The next sections will introduce a statistical framework to implement a corrective term on the error-bars, and optimize it simultaneously with the model parameter-estimation.

2.3.3.1 Error-bars estimation

The error estimation of interferometric data is extremely challenging, due to the intrinsic nature of the measurements that go through heavy data-reduction. Systematic errors are calibrated using several PSF-references thanks to the observation pattern "Calibrator–Science Target–Calibrator". Random errors are estimated from the scatter on the data. However, possibly large systematic errors remain even after calibration. The reason for this is a variation of experimental conditions between the measurements on the PSF-reference(s) and the science target: either turbulence (i.e. AO correction), airmass, position on the detector, position angle (i.e. angle-dependent aberrations in the optics), etc. For these reasons, one can assume that, in the general case, the error-bars calculated from random variations are under-estimated.

As an example, let's build a test-signal hereafter called "real", of shape:

$$\Phi(x, a, b) = \exp(-ax) \times \sin(bx) \tag{2.30}$$

and set the "real" values of a=0.5, b=3. The n=51 sampling points x_i are drawn uniformly in $x \in$[0,6] at which data values with error-bars are generated following:

$$\begin{aligned} Data_i &= \Phi(x_i, a_{real}, b_{real}) + \mathcal{N}(\overline{\mu} = 0, \sigma = \sqrt{0.1^2 + \mathcal{N}(\overline{\mu} = 0.3, \sigma = 0.05)^2}) \\ Errorbars_i &= 0.1 \end{aligned} \tag{2.31}$$

where $\mathcal{N}(\overline{\mu} = 0, \sigma = 1)$ is the normal distribution of mean=0 and standard deviation=1. Each data-point at the sampling x_i equals the real value of the example function $\Phi(x_i, a_{real}, b_{real})$, with an additional noise. This noise is the realization of a normal distribution of mean=0, and of standard deviation being the quadratic composition of a random error=0.1 (i.e. the error-bars on the data), and a random systematic error with the probability-law $\mathcal{N}(\overline{\mu} = 0.3, \sigma = 0.05)$. That is, the error-bars are widely underestimated of a factor 3±0.5. Figure 2.10 shows the "real" test-model and the data, as well as the MCMC parameter-estimation of a and b.

The result of the simulation give a parameters estimation for a=0.434±0.025 and b=2.956±0.035, while the "real" values were 0.5 and 3, respectively. One sees that, although the parameter estimation is reasonably close from the real values, the confidence domains are critically under-estimated. Indeed, one sees on Figure 2.10 that the real values of a and b fall well outside the 2-sigma region of the confidence-domain, which correspond to an occurrence of ≤4.5%. This simulation failed to give a robust estimation of the parameters a and b.

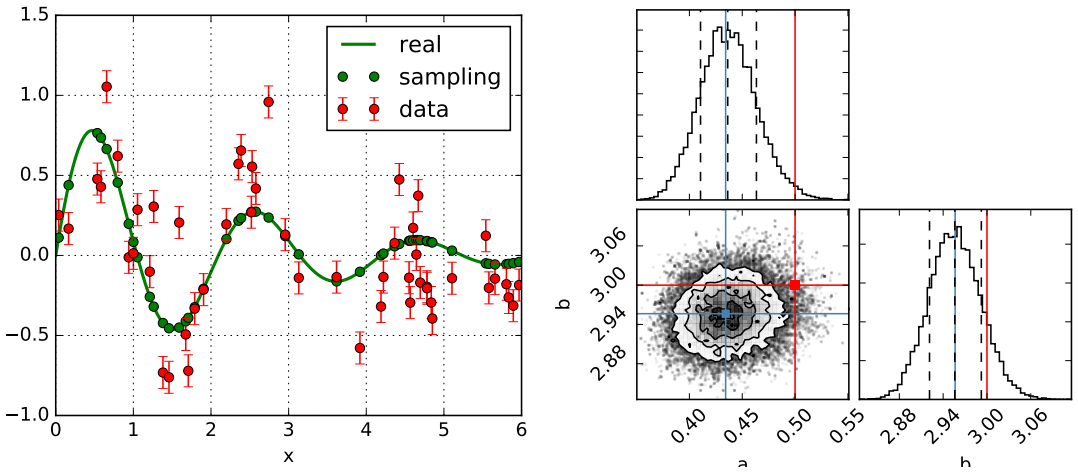

Figure 2.10: **Left**: illustration of the real signal, sampling points and data values with widely underestimated error-bars. **Right**: Corner plot of the MCMC parameter estimation for the data shown in the left sub-plot. The red lines represent the real values of a and b, while the blue lines represent the maximum-likelihood scenario.

NB: although one cannot conclude on the reliability of the parameter estimation with a single trial, this preliminary illustration depicts rightfully the general result that will be detailed in the following sections.

2.3.3.2 Modelling errors-bars

A thorough treatment of the variance-covariance matrix of T3, for example, requires at least as many independent measurements of each target as independent T3 (Ireland 2013), which is in practice not feasible. Instead, the variance-covariance matrix can be modeled (Kraus et al. 2008), or an additional error-term can be tuned in quadrature (i.e. sum of variances) to the error estimation on the data in order to normalize the reduced chi-squared value of the fitting to the expected value, given the sample size and the number of parameters in the model (Hinkley et al. 2011). However, the nonlinear form of the complex visibility expression to evaluate, see Eq. (2.26), makes it mathematically impossible to determine the number of degrees of freedom; the reduced chi-square can not be used to compare models (Andrae et al. 2010), see Section 2.3.4, nor used as a tuning reference.

Rather than tuning the additional error-term using reduced chi-square, the new (to my knowledge, this method has not been used or published yet) statistical method presented below allows to fit it together with the free-parameters of the model according to a maximum likelihood estimation.

The $\sigma^2_{systematic}$ term is added to the errors-bars $\sigma^2_{i,random}$ of the data in the full

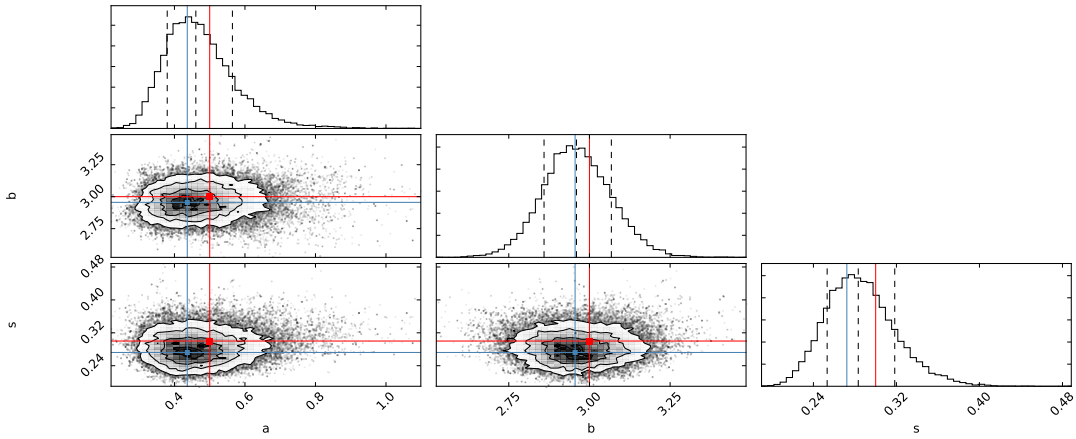

Figure 2.11: Corner plot of the MCMC parameter estimation for the data shown in Figure 2.10 left sub-plot. The red lines represent the real values of a and b, while the blue lines represent the max-likelihood scenario.

log-likelihood expression, in Eq. (2.28):

$$ln\mathcal{L} = -0.5 \times \sum_i \left[\frac{\left(Data_i - Model_i\right)^2}{\sigma^2_{i,random} + \sigma^2_{systematic}} - \ln\left(\frac{2\pi}{\sigma^2_{i,random} + \sigma^2_{systematic}} \right) \right], \quad (2.32)$$

in order to globally account for errors-correlation and uncalibrated systematic errors. One assumes here that these errors terms are independent and identically distributed. For convenience, one defines the total variance $\sigma^2_{i,total}$ (or $\sigma^2_{i,tot}$) to be:

$$\sigma^2_{i,total} = \sigma^2_{i,random} + \sigma^2_{systematic} = \sigma^2_{i,rnd} + \sigma^2_{sys}. \quad (2.33)$$

In essence, this approach consists of increasing the known errors on the data, which would otherwise produce extremely high residuals or chi-square values. The critical difference is that this method uses a maximum likelihood estimator to perform the "tuning" of the additional variance term, given that the errors-bars on the data are underestimated. The convergence of such method is possible due to the fact that the two terms in the sum of Eq. (2.32) have an opposite dependence on $\sigma_{systematic}$; the balance of these two terms ensures the success of the maximum-likelihood estimation of the free-parameters.

Importantly, the amount by which the error-bars are increased is not a-priori set or a-posteriori fine-tuned: it is left free to take the most likely value.

2.3.3.3 Confidence-domain estimation

Figure 2.11 shows a MCMC parameter estimation on the same sampling points and data values as Figure 2.10, using the additional fitted variance term $\sigma^2_{systematic}$.

The simulation yields the estimation of a=0.44±0.09 and b=2.96±0.13, while the "real" values are 0.5 and 3, respectively. One sees that the parameter estimation of

a and b falls between the 0.5 and 1-sigma iso-contours, instead of falling well outside the 2-sigma area in the simulation made without the additional error term. One should also notice that the maximum-likelihood estimation of the parameters is not significantly modified while fitting the additional error term: the MCMC converges to a=0.44±0.09, b=2.96±0.13 (with) and a=0.434±0.025, b=2.956±0.035 (without).

Figure 2.12 compares the data with the result of the parameter-estimation, with and without the adding of the error term. The fitting exercise was reproduced two hundred times: one sees that the Root-Mean-Square (RMS) of the residuals normalized to the error-bars, defined as:

$$Residual_i = \frac{|Data_i - Model_i|}{\sigma_{i,total}}, \tag{2.34}$$

are of order 45±8 for the fitting exercise without the additional variance term. However they equal 1±0.003 when incorporating $\sigma^2_{systematic}$, meaning that the there is no major under- or over-fitting of the dataset given its new error-bar.

This technique allows to scale the error-bars of a dataset according to a maximum-likelihood estimation performed simultaneously with the model-parameters fitting. An interesting consequence of this method is that RMS of the residuals equals unity, as highlighted in Figure 2.12. This effect is not due to any a-posteriori regularization, rather, it is a natural consequence of such error-fitting technique. This study highlights that is one were to fit a model with wrong error-bars, he would find execrable chi-squared values or residuals and might conclude that the model is wrong. This leads us naturally to model comparison, as to be the selection of the most-suited among several to explain the data.

2.3.4 Model comparison

A convenient method to compare parametrized models and select the most fit or most probable is based on the usage of reduced chi-square. However, as seen in Section 2.3.3.2, it is in practice not possible to determine the number of degree of freedom in the case of a non-linear model. As a consequence, it is not possible to calculate the chi-square value of a fit.

Several alternative to chi-square exist, among which the Bayesian Information Criteria (BIC) developed by Schwarz (1978) on the bases of Bayes factor and Bayesian inference. It is defined as:

$$BIC_{Model} = 2\ (k \ln(n) - ln\mathcal{L}_{Model}), \tag{2.35}$$

where k is the number of free parameter in the model and n the sample size. The presence of k weighted with the sample size ensures that the more simple models will be preferred (to a certain extent) over more complex models: Occam's razor. The lower the BIC, the better the model performs. However, the BIC suffers from two main limitations (see Liddle (2007) for further discussions on the use of Information Criteria in Astrophysics):

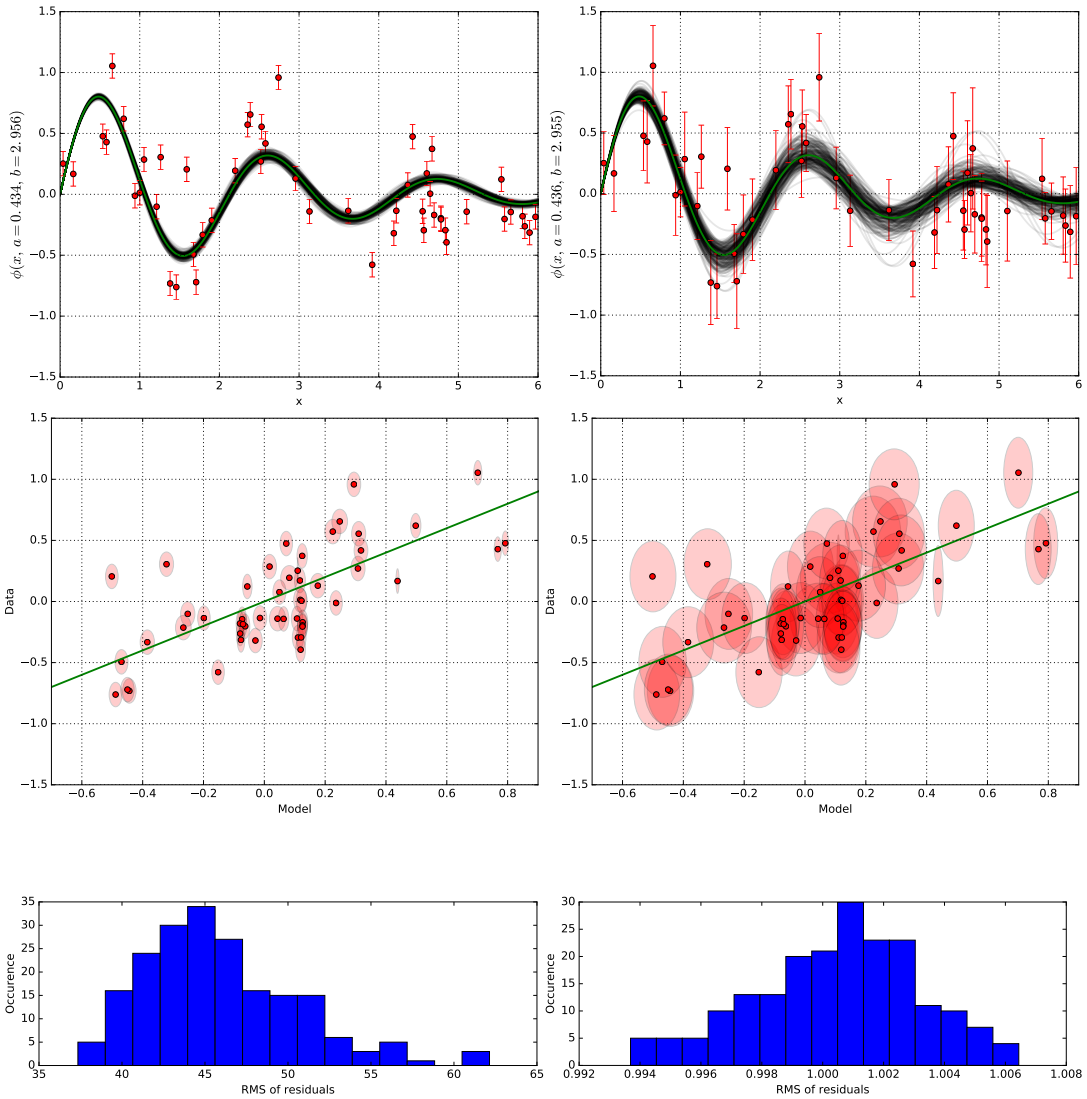

Figure 2.12: **Left column**: Results of the fit without the additional error-term. **Right column**: Results of the fit with $\sigma_{systematic}$. **Top row**: Visualizations of the most likely model (green line), data (red dots) and model-fitting uncertainty arising from the confidence domains on the parameters estimated (black-shaded area). **Middle row**: "Data versus model" views for all sampling points with 1-sigma error-bar ellipses, the 45° green line shows the "perfect" case where model=data. For a satisfactory fit (i.e. not under- or over-fitting), most ellipses should "touch" the green line. **Bottom row**: Histograms of the RMS of residuals computed for 200 model-fitting simulations.

Table 2.3: Interpretation of ΔBIC and Likelihood-Ratio tests made using the BIC.

ΔBIC	Evidence against higher-BIC model	LR against hight-BIC model
0 to 2	Undefined	1:1 to 3:1
2 to 6	Positive	3:1 to 20:1
6 to 10	Strong	20:1 to 150:1
>10	Very Strong	>150:1

- its root-hypothesis is only valid for a sample size n much larger than the number k of parameters in the model,
- it cannot handle high-dimensional model selections as efficiently as variable or feature selection.

One measures the BIC value from the maximum-likelihood value obtain for the parameter-set which performed best: $ln\mathcal{L}_{Model}\,|_{max}$. The relative probability of different models against each-other or against the null hypothesis is obtained from Likelihood Ratio Tests (LR-Test) in its most general formalism:

$$LR_{Model/control} = \exp\left(\frac{BIC_{control} - BIC_{Model}}{2}\right), \tag{2.36}$$

where "control" is the model used as a reference point to evaluate the probability of "Model", see Table 2.3 for example-values of LR-tests. One often uses the "null" model, i.e. no detection, as a reference for measuring the (relative) likelihood of a model. In interferometric data, a "null" hypothesis is equivalent to having VIS2 =1 (unresolved single star) and T3 =0 (no asymmetry).

One should note that a model comparison can only be performed on the same dataset. The use of the BIC and the LR-test in its most general form allows for model-comparison between models which are not hierarchically encapsulated, e.g. one can compare a Gaussian-disk model with a uniform-disk model, even if all Gaussian-disk parameters are not a sub-set of the uniform-disk parameters.

2.3.5 Tools at disposal

Apart from LitPRO[4], part of the JMMC Optical Interferometry suite, very few (if not none) officially released and tested tools are available for model-fitting interferometric data with the specificities of optical-IR wavelengths, such as closure phases. LitPRO fitting-kernel is provided with a graphical unit interface, i.e. a "click-button" interface, highly inconvenient. It cannot be scripted, does not let the user choose the fitting algorithm, or access the results and graphs for further processing. Moreover, in order to work, it requires an active Internet connexion. Indeed, the fits are not performed on the user's machine, but on a distant server (i.e. the data and model is sent to that

[4] http://www.jmmc.fr/litpro_page.htm

server). The fitting-kernel is proprietary code and could not be accessed and edited or improved for the needs of this work.

A pure-Python fitting library was developed, Software for Optical Interferometry Fitting (*SOIF*)[5], which can be installed using `pip install soif` from any terminal. It works with the standard *anaconda* Python distribution (2.7 or 3.5 version); a couple of additional libraries are automatically added with the *SOIF* install.

It provides analytical parametric model-fitting of interferometric data; here are its main features:

- Loading and merging of any number of files under the OIFITS standard (Pauls et al. 2005; Duvert et al. 2015), containing any data types (VIS2, T3, phases, visibilities and triple-product amplitudes (i.e. closure-amplitudes)) taken at any (u,v) coordinates and at any wavelength. E.g. long-baseline interferometry squared-visibilities taken in K-band can be merged with SAM R-band closure phases dispersed over N wavelength-channels.

- * Filtering of this data according to the target ID, the time of acquisition, the wavelength or an arbitrary data-index. This later feature proved particularly useful for GRAVITY data which outputs several tables of the same data type in the same file (calibration and science channels).

- Quick visualization of the data.

- Building of a model that can be composed of any number of unitary-models to be chosen from a default list (point source, uniform disk, Gaussian, etc).

- * New unit-models can be easily added to this list and provided they satisfy some constraints, they will fully benefit from all other features of the library.

- * Loading of custom brightness maps treated as "background image" out of which the complex visibility is computed at the (u,v) point of the data. E.g. incorporating as a set background, a complex disk image obtained from radiative transfer, see Section 3.6.

- Each parameter from any unitary-model can be constrained to a value, or left free for fitting between a lower- and a upper-bound. E.g. fitting a binary-star with two point sources when the flux ratio is known and shall not be fitted requires to constrain the contrast ratio and leave only two free parameters: the angular separation and the position angle of the companion.

- Possibility to set a black-body temperature rather than a contrast ratio in order to determine the relative brightness of unitary-models (still under testing).

- * For each of the free parameter, one can choose a prior distribution among uniform (default), Jeffrey (i.e. logarithmic), normal, triangle, or write any custom one.

[5] https://github.com/ceyzeriat/soif

- * Any free parameter can be spectralized. This means that instead of a single value, it will become a list of N free parameters, N being the number of unique wavelengths contained in the data. E.g. a binary-star modeled with two point sources is usually described with its λ-averaged contrast ratio, its angular separation and its position angle. If the data contains 10 wavelength channels and the contrast ratio parameter is spectralized, this means that the fit will now happen on 2+10 free parameters in order to account for a varying contrast ratio with wavelength. This feature is still under testing.
- * Angular parameters are wrapped at 2π by default, or any other custom value.
- In order to optimize the simulation time, the (anti-)symmetry of the (u,v) field is taken into account such that only unique (U,V,wavelength) sets are processed, providing a tremendous speed-up. E.g. a 10-holes mask produces 45 baselines and 120 T3 triangles (i.e. 360 (u,v) coordinates). However, only 45 (u,v) points are unique and will be calculated, not 360+45 if fitting both T3 and VIS2. A parameter setting the number of significant digits can be used to avoid rounding or machine precision errors on U, V and wavelength values.
- * The fit is done using *emcee* MCMC optimization algorithm. This fitting procedure can be replaced with any other MC algorithm, provided the input and output parameters can be adapted.
- * The default likelihood function can be replaced with a custom one in order to apply a specific weighting to different sets of data or data types.
- Post-processing tools to explore and analyze local minima through the library *MCres*.
- * Full access to the raw MCMC results, and any other simulation or graph values or results.
- * Includes the fitting of the additional variance term presented in Section 2.3.3.2, in order to estimate robust confidence domains.
- * Includes tools for model comparison such as likelihood ratio-test vs. null hypothesis, as presented in Section 2.3.4.
- *? Multi-threaded, based on *emcee*, although multi-threading provides a significant speedup for likelihood functions taking more than $\sim$ 1 sec to process.
- * Display of progress bars to inform the user of the current simulation progress.
- Saving and loading of the simulation results.
- * Open source library under GNU General Public License v3 or later (GPLv3+), and open to constructive contribution, comments and feedback.

In short, it does everything what LitPRO does, with many additional features noted with a "*" in the previous list. Note that *SOIF* is not officially released yet, and does not benefit from a user's manual and tutorials yet.

A broad picture of interferometry was brushed, incorporating most of the necessary concepts required to acquire and analyze interferometric data: physics theory, interferometric instrumentation, data acquisition specificities, and parametric-model fitting to the data. Section 2.1 illustrated that interferometry is the answer to accessing resolutions which are out of reach of single-dish telescopes, although it also suffers from atmospheric turbulence. Section 2.2 focused on some instrumental aspects of interferometry, presenting several techniques and observables together with their specificities. Section 2.3 described part of the numerical and statistical background required to process interferometric data, and introduced a novel fitting tool.

Chapter 3

IRS-48

Contents

Your assumptions are your windows on the world. Scrub them off every once in a while, or the light won't come in.

Isaac Asimov

IRS-48 is known to be a young transition disk in the ρ Oph region located at 120 pc. It shows a major asymmetric dust-trap at 55 AU, believed to arise from a massive planet on an inner orbit. Interestingly, IRS-48 is one of the most well-characterized transition disk: gas densities and temperatures were measured throughout the disk, dust in the outer-disk was imaged from near-infrared to centimeter wavelengths. Yet, the inner 20 AU remain poorly constrained. This chapter brings some light on this major and complex disk target, and analyzes it through the eye of high-resolution interferometry. It reveals the first fully-resolved PAH-ring around a star both younger in age than previously thought, and showing a later-type transition disk than previous measurements, questioning which of the main disk-dissipation processes currently dominates its evolution. This chapter makes intensive use of the information contained in the first two chapters; callbacks links will lead the reader to the information when necessary.

3.1 Introduction

IRS-48 is a spectacular transition disk candidate where the delicate balance of dynamical clearing, photo-evaporation and radial drift of grains is currently questioned. Also referred as $2MASS\ J16273718-2430350$, $GY\ 304$ or $WLY\ 2-48$, it is an highly extinct $A0^{+4}_{-1}$ star, part of the ρ Oph cloud L1688; Table 3.1 sums up its main data.

First listed in Wilking et al. (1989), it shows a substantial far-infrared and millimeter excess without near-infrared counter-part, pointing towards a classification as transition disk (see Section 1.3.1). Since the first resolved images obtained by Geers et al. (2007a) in the near- and mid-infrared, and the first evidence of Polycyclic Aromatic Hydrocarbon (PAH) emission lines in Geers et al. (2007b), IRS-48 has been an object of interest and mysteries. While their 8.6 through 11.3 μm images showed high and unresolved PAH fluxes, the 18.7 μm image uncovered a purely thermal and asymmetric outer-disk from a radius of 55 AU. Using the VLT-CRIRES spectrograph to observe the 4.7 μm CO fundamental rovibrational band, Brown et al. (2012a) imaged a 30 AU thin ring. Additionally, they solve the spectral-type puzzle of the central star and set a luminosity of 14.3 $L_\odot$ combined with an extinction of A_v =11.5, positioning the object on a – suspiciously old – 15 Myr evolutionary track (see Section 1.3.3.5).

Table 3.1: Main literature data of ρ Oph IRS-48

Parameter	Value	Reference
Stellar position	α_{2000} =$16^h27^m37^s18$	B14
	δ_{2000} =-24° 30′35.3″	
Distance	120 pc	L08
Inclination	$i = 50°$	G07, B14
Systemic velocity	$v_{lsr} = 4.55$ km s^{-1}	vdM13
Position angle	PA = 96°	G07, B14
Stellar type	$A0^{+4}_{-1}$	B12
Stellar Temperature	$9000 \pm 550 K$	B12

B14=Bruderer et al. (2014), L08=Loinard et al. (2008), B12=Brown et al. (2012a), vdM13=van der Marel et al. (2013b)

Subsequent ALMA and VLA observation at 0.44, 1.3, and 8.8 mm carried by van der Marel et al. (2013b, 2016) unveiled a millimeter-grains asymmetry at a radius of 63 AU, in the southern extents of the disk. They postulate a planet of 10 M_{Jup} located at $\sim$ 18 AU triggering a vortex-shaped dust-trap. Further work on PAH by Maaskant et al. (2014) using unresolved spectral energy distribution data, revealed that the near- and mid-infrared spectrum of IRS-48 is dominated by a mixture of neutral and ionized PAH, that they postulate to arise from an extended region between the inner-most disk at 1 AU to the outer-disk at 55 AU.

Most recent studies by Bruderer et al. (2014) showed that a single gas-depletion in the inner disk could not explain the complex flux profiles of ^{12}CO and C^{17}O lines measured by ALMA with a resolution of $\sim$ 30 AU. They proposed a slight gas depletion at $\sim$ 20-50 AU in addition to a complete depletion inside 20 AU. Follette et al. (2015) report the first reflected light H- and Ks-band direct images of the disk outside 55 AU, and question the abundance of the innermost-disk at $\sim$ 1 AU using SED modelling, although their fit suffers from over-luminous silicate features in the 9-18 μm window (see Section 1.3.2.1).

A number of mechanisms have been proposed to cause gaps in proto-planetary disks, including extensive grain growth (Dullemond & Dominik 2005), photo-evaporation (Clarke et al. 2001), binarity (Ireland & Kraus 2008), and tidal barrier created by dynamical interaction with low-mass disk objects (e.g. Bryden et al. 1999). These different mechanisms can be distinguished by studying the distribution of the gas and dust within the gaps: a large (stellar) companion or photo-evaporation would almost completely evacuate the inner regions while a less massive planetary companion would allow gas and small dust grains to exist within its orbit (Lubow et al. 1999). Furthermore, in the latter case, the measurement of the size and distribution of this material would allow the orbit and mass of the planetary companion to be constrained.

Key grain-coagulation theories (Williams & Cieza 2011, for a review) are able

to explain growth from sub-microns to millimeters, and then hectometer to planets. Several possible solutions have been proposed to account for the formation of bodies up to meter-sizes, such as turbulent vortices (Heng & Kenyon 2010). Another mystery regarding grain-coagulation exists for the smallest grains, that can arguably be considered as large molecules: PAH, and in a lesser extent, Very Small Grains (VSG). It has been argued that PAH either may take part in the dust coagulation process (Dullemond et al. 2007) or are replenished by mixing processes in the disk (Siebenmorgen & Krügel 2010). However, observational evidence of the role of PAH in these processes is not conclusive and it is presently unclear how important these routes are. The question remains whether these very small particles take part in grain-coating, in the main grain-growth process – and their presence in many disks are to be explained by some replenishment process(es) –, or if their intrinsic properties prevents them to – and their absence in many disks are to be explained by some other assimilation process(es) –. Gorti & Hollenbach (2008) find that the abundance of PAH and small grains in disks is critical to the temperature profile. Indeed, they show that if some PAH are present, their contribution to disk heating via grain photoelectric emission can be larger by a factor of ~ 2 than Xray heating at r$\sim$ 10 AU.

3.2 Observations and Data Reduction

This section will detail the different types of data used in this chapter and present the de-reddening routines used in order to prepare the SED data to fitting.

3.2.1 Observation strategy

In this work, new data sets are used, acquired using the instrument NaCo (abbreviation for Nasmyth Adaptive Optics System (NAOS) & Near-infrared Imager and Spectrograph (CONICA)) commissioned on the Very Large Telescope (VLT) at the Paranal Observatory of the European Southern Observatory (ESO). This data was acquired in different near-infrared bands and at four epochs over a two-years period ; these sets are detailed in Table 3.2. At that time, NaCo was integrated at the Nasmyth platform of the UT4 8.2 m-telescope. This instrument was used in Sparse-Aperture Masking (SAM) and full-pupil imaging modes. For both modes, given the large reddening of the target (>16 mag in the visible), the NaCo built-in infrared wavefront sensor was used to run the Adaptive Optics (AO) correction, increasing the r_0 of the observation well above the diameter D=8.2 m of the telescope (see Section 2.1.1.1). Observing IRS-48 (declination -24°30'35.03") at the VLT (latitude -24°37'31.5") has this particularity that the target will almost hit zenith. This also means that the field rotation is small: the position angle of measurements has a low diversity through time and date, except for a 180° rotation at transit.

Table 3.2: Observations made with NaCo

Date	Band	Calibrators	Cal. Seq.[1]	Observation ID
14 March 2011	Ks[1,2]	Elia 2-35 & 2-37	4	086.C-0497(A)
14 March 2011	Lp[1,2,3]	Elia 2-37[1,2]	4	086.C-0497(A)
		Hip 86311[3]		
14 March 2011	Mp[1,2]	Elia 2-15	2	086.C-0497(A)
1 Sept. 2011	Lp[1]	Elia 2-37	2	087.C-0450(B)
6 March 2012	Lp[1]	Elia 2-37	3	088.C-0527(A)
25 March 2013	Lp[1]	Elia 2-37 & 2-11	4	089.C-0721(A)

[1]: SAM, [2]: Full-pupil image, [3]: Spectra
A calibration sequence (cal. seq. in the headline, also called "bracket") is a unitary interferometric measurement, following the observation pattern "Calibrator–Science Target–Calibrator"
Single-frame exposition time is 0.4 sec for both SAM and imaging modes.

3.2.2 Direct imaging and Spectroscopy

At epoch 1, full-pupil images were acquired in Ks-, Lp- and Mp-bands, as well as spectra between 2.87 and 4.11 μm, with $R_{average} \sim$ 800. The Lp-band image is displayed in Figure 3.1 both with and without PSF-subtraction. One can easily see the East-West elongated nature of the circumstellar emission, at $\sim$ 100 milli-arcsecond (mas), as well as an asymmetry in the disk semi-major axis; the Western extension is $\sim$ 1.15 times brighter than the Eastern one. However, the $\sim$ 100 mas spatial scale is similar to the resolution criteria λ/D=96 mas at these wavelengths, which enormously complexifies the use of these images.

The slit of the spectrograph was orientated along the East-West direction as displayed in the latter Figure. The pixel-scale of the detector is constant over the whole spectra: 1.6 Å $\times$2.7 mas. The slit height is 86 mas; given the short scale extents of the disk and the high inclination ($\sim 50°$), one expects a large contamination of the disk at the stellar position (assumed to be located at the peak intensity in the spectra). Similarly, given the $\sim$ 50 mas full-width-half-maximum of the PSF, one expects a large contamination of the star in the disk. To minimize the stellar contamination on the disk, the spectral-data was only used at the first null of the star, 1.22λ/D$\sim$ 115 mas. The PSF-reference image shows a very low stellar-flux contamination in the null, $\sim$ 3% of the peak-flux; this highlights the high-strehl ratio of the observation.

The spectra in Figure 3.1 shows the flux of the disk – taken at the first stellar null – relative to the peak flux of the spectra. One can see very strong PAH emission features at 3.3 μm, characteristic of neutral PAH: in this emission line the disk-to-peak contrast jumps by nearly a factor of two, compared to the disk-to-peak continuum contrast. Note that this emission line is not recorded in the interferometric data or full-pupil

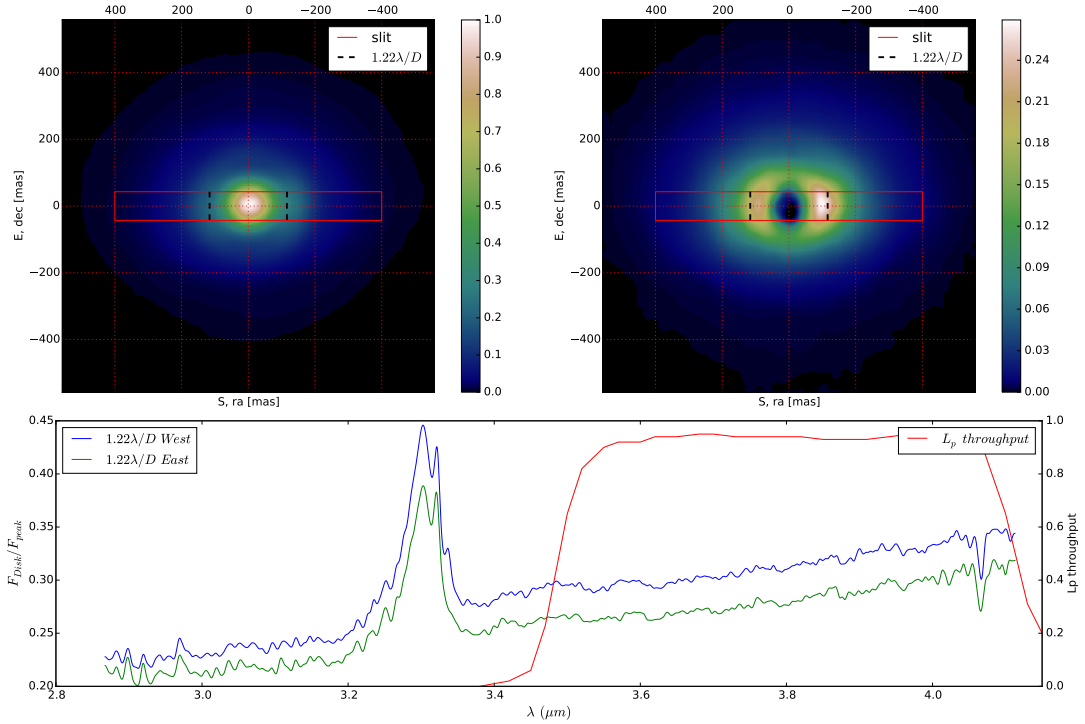

Figure 3.1: Full-pupil image in Lp-band (top left), and PSF-subtracted (top right) in normalized flux (peak of the un-subtracted image). The 86 mas slit height is overlaid in red, while the black dashed-lines lying at $\sim$ 115 mas illustrates the first null of the central star, at 1.22λ/D. The displayed spectra show the disk-spectra taken at the East and West stellar-nulls, divided by the spectra taken at the peak intensity. Prominent PAH emission is seen from the disk at 3.3 μm, and $Br\alpha$ from the star at 4.05 μm. The same East-West asymmetry is seen as the one observed on the image, $\sim$ 15%.

Table 3.3: NaCo filters characteristics, interferometric 0.5 λ/D criteria and field of view with respect to filters at central wavelengths, given a target distance of 120 pc.

	Ks	Lp	Mp
Central wavelength (μm)	2.18	3.8	4.78
Bandwidth (μm)	0.35	0.62	0.59
Smallest Baseline, 1.78 m			
0.5 λ/D (AU)	15.2	26.6	33.5
Field of view radius (AU)	95	163	272
Longest Baseline, 6.43 m			
0.5 λ/D (AU)	4.2	7.4	9.2
Field of view radius (AU)	26.3	45.4	75

images given that it is outside the Lp-band filter bandpass, see Figure 3.1. Although both East and West spectra are very similar in shape, the Western disk-extension is constantly – at all spectrum wavelengths – 1.15 times brighter than its Eastern region. The same West-East asymmetry was measured on the full-pupil image.

3.2.3 Near-infrared Sparse-Aperture Masking

The most interesting data sets are SAM data in that they offer an angular resolution down to a few tens of mas, equivalent to a few AU given the distance of 120 parsec, as shown in Table 3.3, refer to Section 2.2.4 for SAM technique. Except for the longest baselines of ALMA ($\gtrsim$1 km), such resolution cannot be reached with any other instrument nor any other NaCo mode (coronographic, full-pupil, etc). Moreover, new extreme adaptive-optics (AO) systems such as SPHERE usually have their wavefront sensors in the visible and cannot close the AO loop on this extremely extinct target ($>$16 mag in the visible), which means that NaCo-SAM is the only instrument able to observe IRS-48 at such resolution in visible or in the infrared (IR).

The observation strategy for SAM mode was designed to intertwine the science target IRS-48 between two blocks on an interferometric calibrator, here Elia 2-35, 2-37 or 2-15, as detailed in Table 3.2. The mask used was a 7-hole non-redundant mask as portrayed in Figure 3.2, with baselines ranging from 1.78 to 6.43 meters, allowing the simultaneous measurement of 21 visibility-squared (VIS2) and 35 closure phases (T3, among which 15 are independent), refer to Section 2.2.2. In full-pupil imaging mode, the same calibrators were used to have PSF references.

The data was processed using the *SAMP* pipeline (Lacour et al. 2011). It includes sky subtraction, bad pixel subtraction and fringe fitting. T3 and VIS2 measurements are calibrated by the two calibrators for each bracket.

Calibration to PSF-reference help reduce systematic errors in the data, but hardly corrects all of them. A fitting mechanism to account for that is specifically developed, refer to Section 3.6. The error-bars on the data are obtained from statistical measurements on the data, which account for random errors. They average $\sim 0.5°$ in

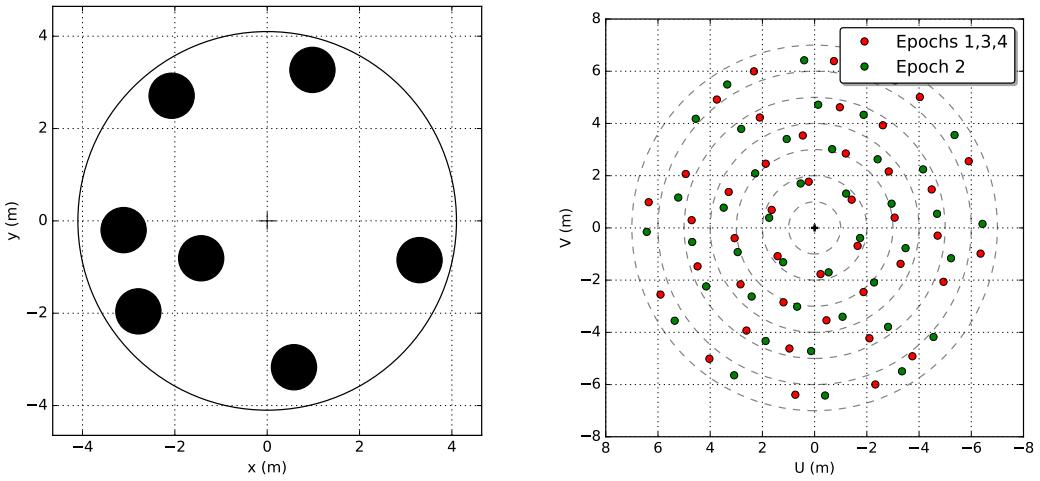

Figure 3.2: **Left**: 7-hole mask used in SAM mode, with baseline from 1.78 to 6.43 m and throughput 14% versus 97% for the unmask-but-obstructed VLT telescope.
Right: UV coverage of the observations of IRS-48. Epochs 1, 3 and 4 were acquired in March, before transit while epoch 2 was acquired in September, after IRS-48 had transited. The low UV rotation between epochs 1, 3 and 4 is due to the fact that 1) the target hits zenith under this latitude which naturally reduces its position angle diversity, and 2) the same observing schedule was followed during all observing run meaning that IRS-48 was observed at a similar elevation.

Table 3.4: Previously published photometry and spectra of ρ Oph IRS-48.

Wavelength(s) (μm)	Instrument	Reference
0.43, 0.64	NOMAD	Z05
0.65, 0.8	Hydra	E11
1.2, 1.6, 2.2	2MASS	C03
3.4, 4.6	WISE	W10
3.6, 4.5	Spitzer IRAC	vK09
5.9-36.9	Spitzer IRS	MC10
60-181	Herschel PACS	F13
450	ALMA	vdM13
850	SCUBA	A07
880, 1300	SMA	B12b

Z05=Zacharias et al. (2005), E11=Erickson et al. (2011), C03=Cutri et al. (2003), W10=Wright et al. (2010), vK09=van Kempen et al. (2009), MC10=McClure et al. (2010), F13=Fedele et al. (2013), A07=Andrews & Williams (2007), B12b=Brown et al. (2012b), vdM13=van der Marel et al. (2013b)

Lp-band and $\sim 1.7^{\circ}$ in Ks- and Mp-band for T3, and 0.03, 0.05 and 0.14 in Lp-, Mp and Ks-bands for VIS2.

3.2.4 Spectral Energy Distribution

In addition to the multi-wavelength interferometric data listed above, IRS-48 SED fluxes were compiled from the literature. All data is listed in Table 3.4 with the corresponding references. As can be seen, the photometry from literature has a broad coverage from visible-blue to mm wavelengths. No detection in the ultraviolet exist because of the very high extinction of the source; measurements in cm-wavelengths are discarded given that they trace cold and large-scale structures outside the region of sensitivity and interest of the observations. For the fitting exercise, the errors on photometry fluxes were assumed to be of 5% if not specified in the literature.

The correction of the interstellar extinction was made according to the method described in Section 3.2.5. An overview of the SED fluxes is portrayed as a black thick line in the Figure 3.3 of the Section 3.2.5.

3.2.5 De-redenning fluxes

Although all fluxes in the literature are available corrected from the interstellar reddening-extinction, it is chosen to apply specific extinction correction on raw fluxes, in order to be able to vary the reddening parameters at will. The extinction curves used are that of Cardelli et al. (1989), improved by O'Donnell (1994) work in the visible; they are parametrized with R_v– the reddening slope – and A_v– absorption in V

band – such that $A_v \equiv R_v \times E(B_{mag} - V_{mag})$.

$$E_V(R_v, \lambda) = \begin{cases} \frac{0.574}{\lambda^{1.61}} - \frac{0.527}{R_v\ \lambda^{1.61}},\ for\ \lambda \geq 0.91\ \mu m \\ \varphi_1(\lambda^{-1} - 1.82) + \frac{\varphi_2(\lambda^{-1} - 1.82)}{R_v},\ for\ \lambda \in [0.3, 0.91]\ \mu m, \\ \varphi_3(\lambda^{-1}) + \frac{\varphi_4(\lambda^{-1})}{R_v},\ for\ \lambda \in [0.17, 0.3]\ \mu m, \end{cases}$$

with

$$\varphi_1(x) = 1 + 0.17699x - 0.50447x^2 - 0.02427x^3 + 0.72085x^4 + 0.01979x^5 - 0.77530x^6 + 0.32999x^7$$

$$\varphi_2(x) = +1.41338x + 2.28305x^2 + 1.07233x^3 - 5.38434x^4 - 0.62251x^5 + 5.30260x^6 - 2.09002x^7$$

$$\varphi_3(x) = 1.752 - 0.316x - \frac{0.104}{(x - 4.67)^2 + 0.341}$$

$$\varphi_4(x) = -3.090 + 1.825x + \frac{1.206}{(x - 4.62)^2 + 0.263}$$

The de-reddened fluxes ϕ are obtained from the red-fluxes ϕ_{red}, A_v, and $E_V(R_v, \lambda)$ following:

$$\phi = \phi_{red} \times 10^{\left(\frac{E_v(R_v,\lambda) \times A_v}{2.512}\right)}. \tag{3.1}$$

Figure 3.3 shows the effect of de-reddening on the IRS-48 data. One sees that the R_v parameter affects the extinction slope between $\lambda \sim 0.4\ \mu m$ and $\sim 1\ \mu m$, while the A_v parameter corrects for the amount of flux depletion, i.e. the SED slope between UV- and MIR-fluxes. One sees that R_v mostly impacts the extinction correction for wavelength below $\sim 5.5\ \mu m$; above that threshold its effect is $\leq$5%. R_v values near 3.1 model the standard diffuse interstellar extinction while $R_v \sim 5.0$ is found in some dense clouds Cardelli et al. (1989). The reddening correction is negligible ($\leq$5% effect) above $\lambda \sim 16.5\ \mu m$.

3.3 VIS2 morphology

Given the complexity of interferometric data and cumbersomeness of radiative transfer, one must first evaluate the characteristic values of quantities encoded into the data. In this section, we use simple analytic morphological models to explore the VIS2.

3.3.1 VIS2 data

The VIS2 measurements are not sensitive to asymmetries, essentially because of their relatively large error-bars, ~ 0.03 or $\Delta VIS2/VIS2 \sim$ 20% in average in Lp-band.

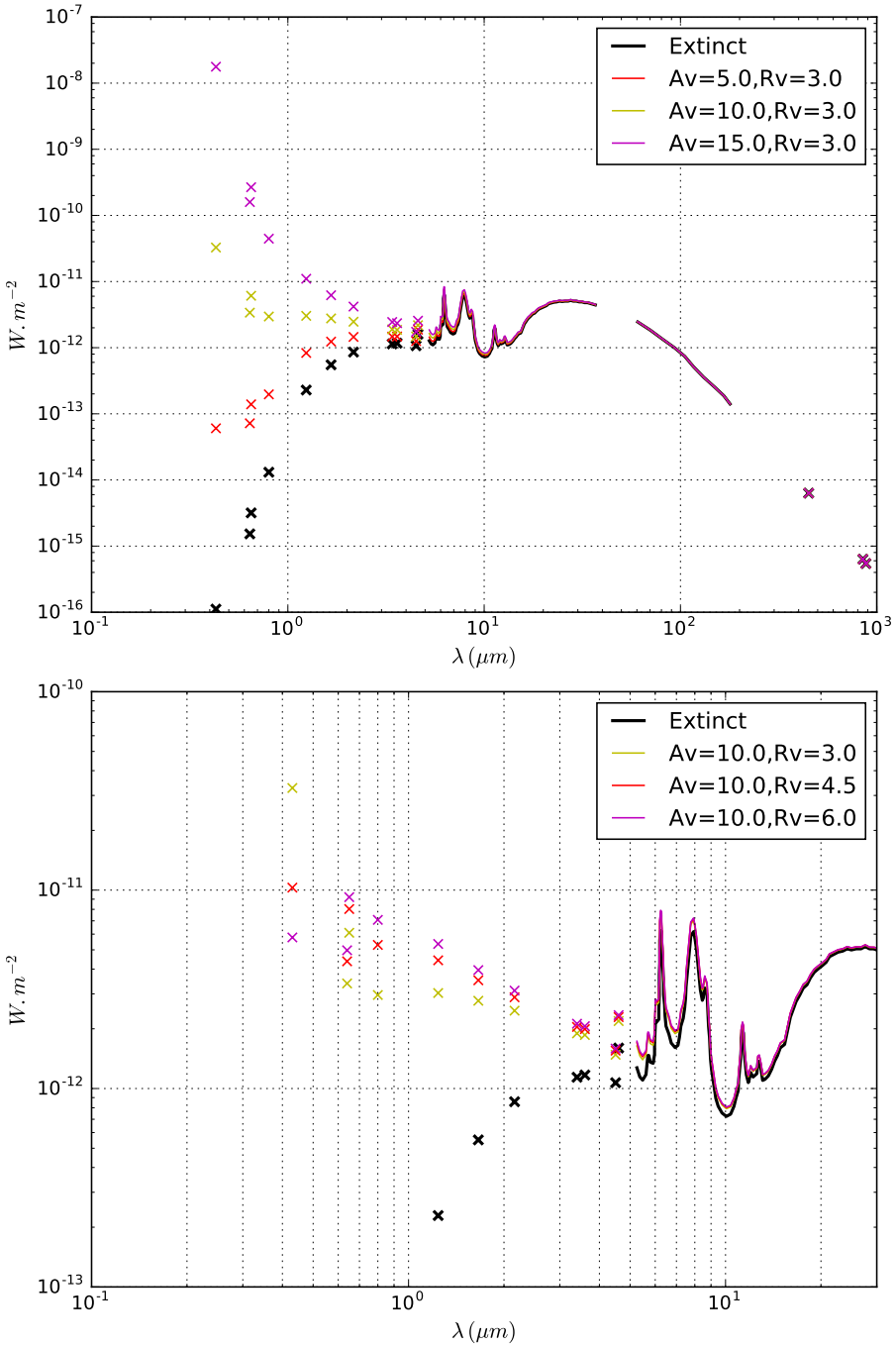

Figure 3.3: **Left**: Effect of a varying A_v value on the IRS-48 SED data, having R_v =3 set.
Right: Effect of a varying R_v value on the IRS-48 SED data, having A_v =10 set.

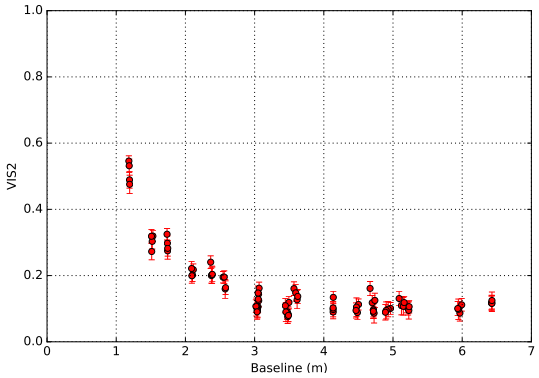

Figure 3.4: Overview of Lp-band VIS2 data at epoch 1, de-projected for a disk-inclination of 50°.

Hence, they encode a point-symmetrical smooth disk-structure and inform on high-level morphology such as position angle, contrast ratio, and inclination of the disk.

In Lp- and Mp-bands, see Figure 3.4, VIS2 lower than unity at the smallest baselines and decreasing steadily to their plateau-value at medium-length baselines ($\gtrsim 3$ meter) clearly show that light-emitting regions are being resolved in the interferometric field of view of the instrument: $\lesssim$26.6 AU and $\lesssim$33.5 AU for Lp- and Mp-bands (see Table 3.3). The *SOIF* library (see Section 2.3.5) is used to get an estimate of the contrast ratio to the star, the characteristic disk size, the position angle (*PA*, measured East from North) and the inclination (i, 0° ≡ face-on and 90° ≡ edge-on). Different models are compared: a two-dimensional Gaussian, Uniform Disk, Gaussian Disk-difference, and a Uniform Disk-difference (hereafter "Uniform Ring"), in addition to the central point-source unitary model. The unitary disk model is centered on the star; the stellar flux is set to unity as a reference.

3.3.2 Morphological models

The 2D-Gaussian and Uniforms Disks unitary models are detailed in Table 2.2. The Uniform Ring unitary model is analytically calculated to be a "large diameter" Uniform Disk minus a "small diameter" Uniform Disk, which both share their other parameters. The aim of that unitary model compared to a Circle or a Uniform Disk, is to provide a ring-like structure with a width and no flux in the center. A Uniform Ring has one parameter more than the Uniform Disk: the "width" of the ring (i.e. the difference in diameters between both Uniform Disks). A Gaussian Disk-difference unitary model follows the same principle as the Uniform Ring, except that it provides a ring-like structure with smooth edges.

To carry out this coarse fit, it is here assumed that in these bands the disk has a point-symmetry and that it is seen with an inclination given by the inverse cosine of its semi-minor & major axes ratio. To estimate the contrast ratio, the *PA* of the

Table 3.5: Ranges for the free-parameters displayed in Table 3.6.

Parameter	Range
CR (flux_*^{-1})	[0.1,10]
PA (°)	[0,180[
Diam_{in} (AU)	[1,30]
Diam_{out} (AU)	[1,60]
Incl. (°)	[0,70]

disk and its semi-axes. The ranges for each free-parameter are shown in Table 3.5. It is checked that while fitting, only one global minimum is found inside the ranges. Ks-band is discarded given that the very large error-bars would not set meaningful morphological constraints.

3.3.3 Morphological results

The detailed results are as listed in Table 3.6. Figure 3.5 shows a corner-plot typically obtained in that exercise. Independent fitting of Lp- and Mp-bands at different epochs and using several unitary models to simulate the disk, give consistent results: the *PA* averages $\sim 93°$, while the inclination is $\sim 54°$.

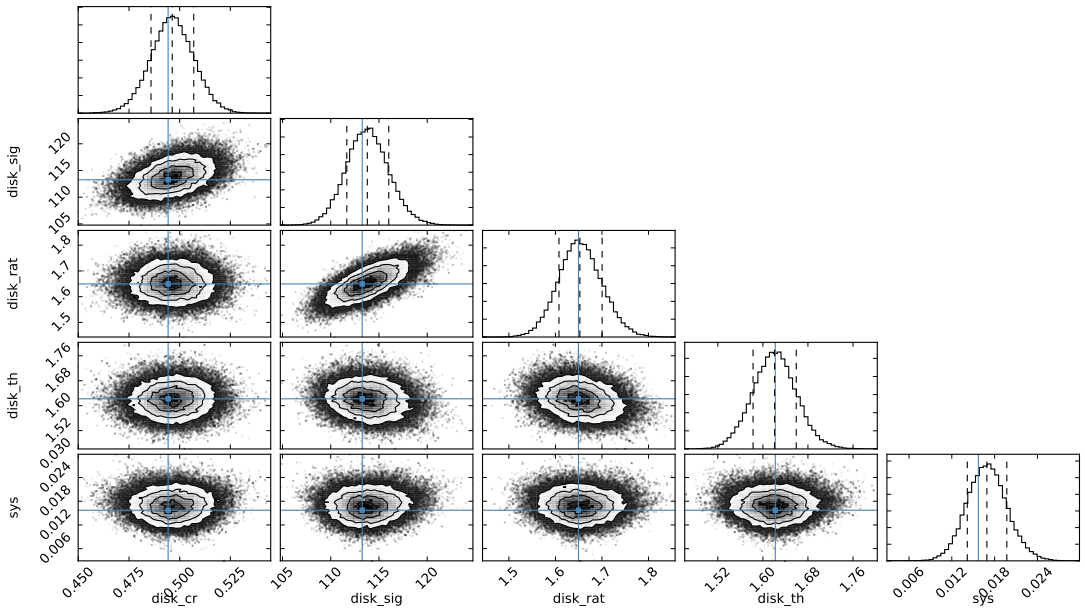

Figure 3.5: Corner plot obtained with *MCres* from fitting a parametric 2D-Gaussian disk to interferometric data using *SOIF* package, corresponding here to the fitting of the Lp-band data at epoch 1. The free-parameters are disk_cr (contrast ratio to the central star), disk_sig (semi-major axis in mas), disk_rat (major/minor axes aspect ratio) and disk_th (position angle in radian). Refer to Section 2.3.2 for how to read this graph.

Table 3.6: Lp- and Mp-bands maximum likelihood parameter estimation to the VIS2 data, for Gaussian Disk, Gaussian Disk-difference, Uniform Disk, and Uniform Ring models. The contrast ratio (CR) is defined such that CR*f_{disk}=f_*. Ranges for this parameter estimation are displayed in Table 3.5.

Gaussian Disk					
Param.	Mp-ep1	Lp-ep1	Lp-ep2	Lp-ep3	Lp-ep4
CR ($flux_*^{-1}$)	0.41 ± 0.03	0.49 ± 0.01	0.48 ± 0.02	0.49 ± 0.01	0.47 ± 0.01
PA (°)	97 ± 4	93 ± 2	88 ± 2	91 ± 2	91^{+3}_{-2}
SMA[1] (AU)	16.0 ± 0.8	13.7 ± 0.3	14.9 ± 0.7	14.0 ± 0.3	14.0 ± 0.3
Incl. (°)	58 ± 3	53^{+1}_{-2}	57 ± 3	55^{+1}_{-2}	55 ± 1
$\sqrt{\langle res.^2 \rangle}$	1.01	1.00	0.99	0.97	1.01
$\langle res. \rangle$	0.01	0.04	0.01	0.02	0.02
Gaussian Disk-difference					
Param.	Mp-ep1	Lp-ep1	Lp-ep2	Lp-ep3	Lp-ep4
CR ($flux_*^{-1}$)	0.42 ± 0.05	0.51 ± 0.02	0.49 ± 0.04	0.51 ± 0.04	0.49 ± 0.02
PA (°)	97 ± 4	93 ± 3	86 ± 3	91 ± 2	93^{+2}_{-3}
SMA^1_{in} (AU)	$1.3^{+4}_{-0.1}$	$1.5^{+1}_{-0.1}$	$1.4^{+2}_{-0.2}$	$1.6^{+1.5}_{-0.1}$	$1.6^{+1.3}_{-0.1}$
SMA^1_{out} (AU)	16.0 ± 4	13.6 ± 1.2	15.0 ± 2	14.1 ± 1.7	14.1 ± 1.6
Incl. (°)	58^{+2}_{-3}	52.5 ± 1.5	57 ± 3	55^{+1}_{-2}	55 ± 1
$\sqrt{\langle res.^2 \rangle}$	1.03	1.00	0.99	0.99	1.00
$\langle res. \rangle$	0.03	0.01	0.04	-0.02	0.03
Uniform Disk					
Param.	Mp-ep1	Lp-ep1	Lp-ep2	Lp-ep3	Lp-ep4
CR ($flux_*^{-1}$)	0.47 ± 0.04	0.54 ± 0.02	0.53 ± 0.04	0.54 ± 0.02	0.51 ± 0.02
PA (°)	98 ± 5	97^{+3}_{-6}	86^{+5}_{-3}	95 ± 5	95 ± 4
Diam (AU)	57 ± 3	48 ± 2	56 ± 5	48 ± 2	49 ± 2
Incl. (°)	56 ± 4	51.5 ± 1.5	56^{+3}_{-5}	52^{+3}_{-1}	52.5 ± 2.5
$\sqrt{\langle res.^2 \rangle}$	1.01	1.00	0.99	0.99	1.00
$\langle res. \rangle$	-0.02	-0.02	-0.01	-0.02	-0.03
Uniform Ring					
Param.	Mp-ep1	Lp-ep1	Lp-ep2	Lp-ep3	Lp-ep4
CR ($flux_*^{-1}$)	0.48 ± 0.05	0.55 ± 0.03	0.52 ± 0.04	0.54 ± 0.02	0.51 ± 0.02
PA (°)	98 ± 5	96 ± 5	86 ± 4	95 ± 5	95 ± 4
$Diam_{in}$ (AU)	2^{+4}_{-1}	$0.8^{+3}_{-0.1}$	$1^{+4}_{-0.1}$	$1.5^{+2.5}_{-0.7}$	$1^{+3}_{-0.2}$
$Diam_{out}$ (AU)	28 ± 5	24 ± 3	27 ± 5	24 ± 3	24 ± 3
Incl. (°)	56 ± 3	52 ± 2	59 ± 4	52^{+3}_{-2}	52.5 ± 2
$\sqrt{\langle res.^2 \rangle}$	1.03	0.99	1.00	1.00	1.00
$\langle res. \rangle$	0.00	-0.02	-0.03	-0.04	-0.02

SMA≡Semi-Major Axis

The plateau-value of the VIS2 gives an estimation of the contrast-ratio between the resolved- and unresolved-flux in the object. The unresolved flux is emitted by regions inside the resolution angle: not only the host-star but also the inner-most regions of the disk, up to $\sim$ 7 AU (Lp-band) and $\sim$ 9 AU (Mp-band), for the longest baseline. The resolved flux is emitted by the disk regions located in the region between the resolution angle and the interferometric field of view. The contrast ratio in Mp-band in $\sim$ 0.42 for the Gaussian Disk unitary models and $\sim$ 0.48 for the Uniform Disk unitary models, meaning that the integrated flux from the resolved-disk is more than two times brighter than the unresolved-flux. The contrast ratio in Lp-band is $\sim$ 0.48 and $\sim$ 0.53 for Gaussian and Uniform Disk unitary models, respectively. The disk is consistently 15% brighter in Mp-band than in Lp-band, which is qualitatively compatible with the fact that the star is fainter at 4.78 μm (Mp) than 3.8 μm (Lp), by a factor of 2.4 when one assumes a 9250 K black-body. The discrepancy between the Gaussian and the Uniform Disk models is due to the difference in flux structure for these models, see Figure 3.6. These contrasts obtained with the visibilities – which are in essence themselves contrasts – put a very hard constraint on the relative SED of the resolved- and unresolved-flux.

The characteristic size of the disk cannot be simply compared between the models, for the same flux-structure reason that made the contrast-ratio estimation vary slightly. Figure 3.6 shows the flux profiles for the four models used in the fitting exercise, as well as their Fourier Transform (FT), over-plotted with all-epoch un-projected data in Lp-band: this shows the general quality of the fit. The two-dimensional Fourier plane model for the Gaussian Disk is displayed for the Lp-band in Figure 3.7. The values of best semi-axes cannot be mapped easily to a ring inner-cavity radius or width. They give however an estimate of the location of the resolved-flux: about 10 to 20 AU from the star. One can notice that the characteristic sizes all four disk models increases by a factor of 1.16 in average between Lp- and Mp-band. This evolution of the radius with wavelength is typical of an extended and resolved structure whose temperature decreases with radius, hence emits further in the infrared and at larger radii.

One sees that the Gaussian Disk unitary models show a flat VIS2 curve for baselines $\gtrsim$3 m while Uniform Disk models have an oscillatory effect – called hereafter "wiggle" –, due to the flat flux profile and the sharp truncature of the disk unitary model. Also, one could notice that the Gaussian Disk-difference unitary model is an elegant analytical solution that approximates best a physical model of a disk since it incorporates a cleared innermost area near the star, a bright maximum corresponding to the inner-rim of the disk, and a steeply decreasing flux profile.

No significant epoch-related variation exist in the parameter estimation results from Table 3.6; this denotes that the high-level disk-structure does not change drastically with time. A mean inclination and position angle are obtained, i =54 $\pm$3°, and PA =93 $\pm$4° from the previous fitting results. This is consistent with the literature values, i =50° (Geers et al. 2007a; van der Marel et al. 2013b; Bruderer et al. 2014), and PA =96° (Geers et al. 2007a; Bruderer et al. 2014).

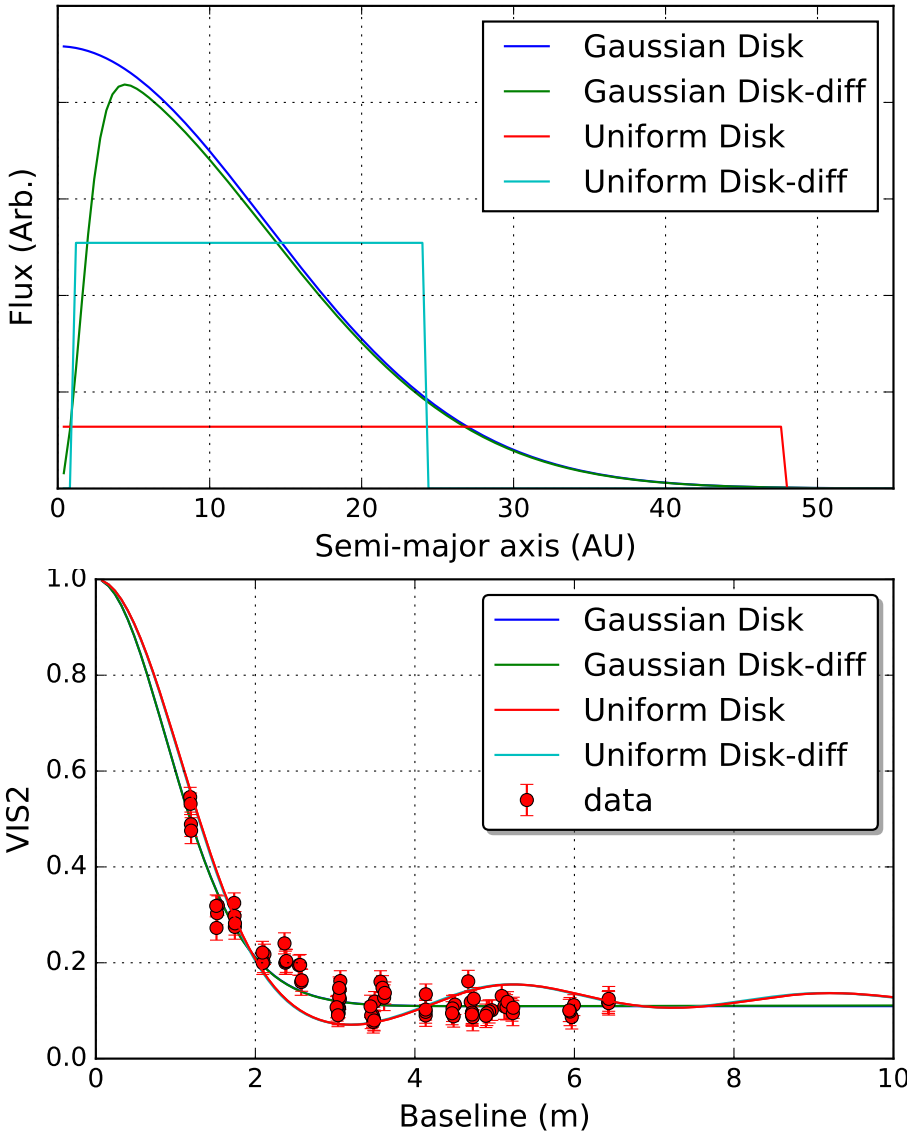

Figure 3.6: **Top**: Flux profile shown as a cut in the semi-major axis, for the four models used in the morphological fit, at epoch 1 and in Lp-band.
Bottom: Fourier transform of the four models, cut in the semi-major axis, at epoch 1 and in Lp-band. All-epoch unprojected-data over-plotted. Gaussian Disk and Gaussian Disk-difference models are perfectly superimposed, which is also the case for the Uniform Disk and Uniform Rings models.

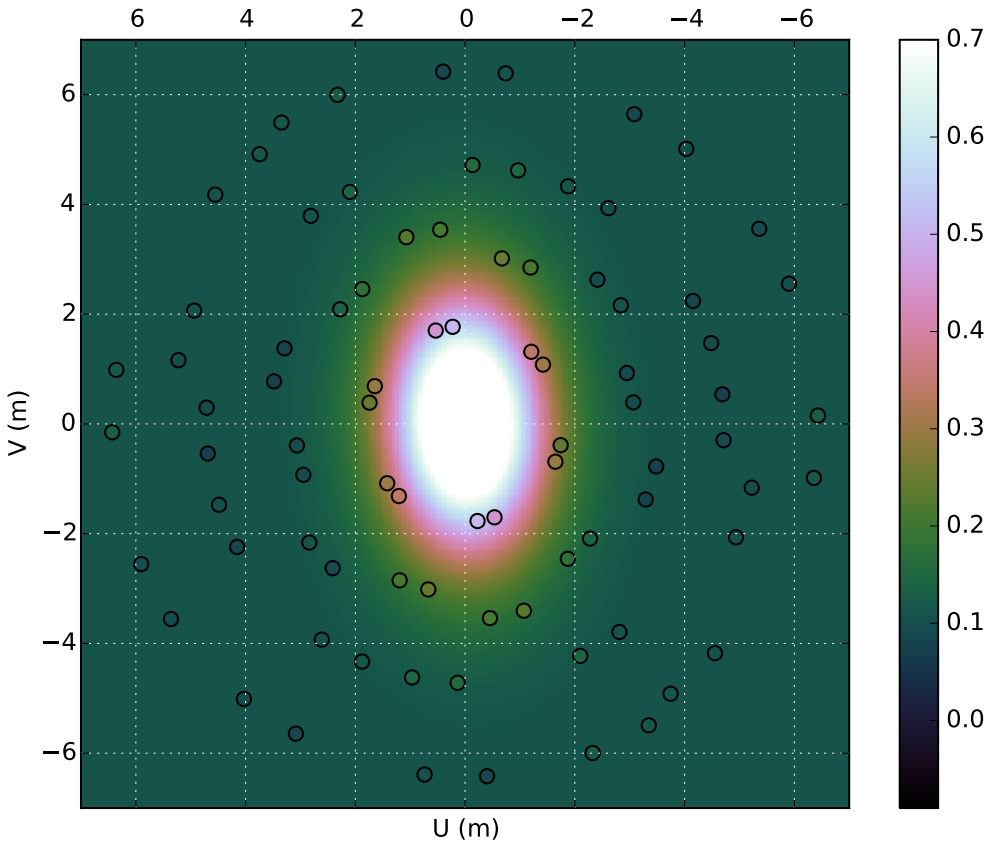

Figure 3.7: Comparison of the VIS2 values (color-axis) between the best-fitting 2D Gaussian model (background image) and the VIS2 data in Lp-band (color-coded circle markers) at the (u,v) interferometric coordinates in meters, at all epochs combined. Note that because this figure shows spatial frequencies, the position angle of the semi-major axis is flipped compared to that of the disk.

3.4 Radiative Transfer Model

In order to jointly analyze the data in Ks-, Lp-, Mp-bands together with the SED fluxes, a radiative transfer model shall be build in order to reproduce such observables from a parametrized disk-model.

3.4.1 MCFOST software

MCFOST, a parallelized 3D radiative transfer code based on a Monte-Carlo method (Pinte et al. 2006), is used to perform radiative transfer calculations. MCFOST outputs SED fluxes and monochromatic images when given an input parameter file, e.g. Appendix C.

The IRS-48 disk contains PAH which are modelled as to be outside the outside Local Thermodynamic Equilibrium (LTE). Indeed, they have very small masses i.e. thermal inertia; their temperature vary greatly (from $\sim$ 150 to $\sim$ 1500) with time, depending on their last photon absorption. Their temperature is defined as a probability distribution function depending on the UV-radiation field of the star. This phenomenon of quantum heating is incorporated into MCFOST and was benchmarked and validated by Camps et al. (2015).

MCFOST includes several built-in disk-models: a disk, an disk with outer tapered-edge, a spherically symmetric envelope and a debris disk. The input parameters for these models are read out of the input parameter file. It also include several atlases of pre-computed stellar spectra (from 3000 to 10000 K, citetHauschildt99, and from 3500 to 50000 K, Kurucz (1979)).

It proceeds in several steps:

1. Calculates iteratively the temperature map of the dust and gas in each cell of the model-grid, taking into account the symmetries of the disk (and independently from the viewing angles),

2. Calculates the SED for the viewing inclination (and azimuth, when the disk is not centro-symmetrical), using the temperature map

3. Calculates the synthetic images for a given wavelength and at the viewing angles, using the temperature map

3.4.2 *alpha* model

The disk structure presented in Bruderer et al. (2014) is taken over. Given the prominence of PAH in the SED of IRS-48, the results of Maaskant et al. (2014) work on ionized PAH in several young disks are merge into this latter model. A disk-structure in three parts is obtained:

1. an inner-most dusty disk between 0.4 and 1 AU

2. an outer dusty disk between 55 and 160 AU

Table 3.7: *alpha* model parameters of the radiative transfer of IRS-48.

Parameter	*alpha* model
Stellar parameters	
Temperature	9250 K
Luminosity	14.3 $L_\odot$
Distance	120pc
R_v	5.5
A_v	11.5
Global disks parameters	
Inclination	50°
PA	96°
Scale height	10 AU
Ref. radius	60 AU

Parameter	*alpha* model		
	Inner-most disk	PAH-disk	Outer-disk
R_{in}	0.4 AU	1 AU	55 AU
R_{out}	1 AU	55 AU	160 AU
Flaring exp. β	1.3	1.3	1.3
Surface density exp p	-1	-1	-1
Grain-size power-law	-3.5	–	-3.5
Dust Mass	8.0×10^{-12} $M_\odot$	8.0×10^{-10} $M_\odot$	1.0×10^{-5} $M_\odot$
Silicate grains Mass	1%	–	70%
Carb. grains Mass	99%	–	30%
Neutral PAH Mass	–	50%	–
Ionized PAH Mass	–	50%	–
Grain sizes a	0.03 - 30 μm	5 Å	0.03 - 4000 μm

3. a PAH disk in-between, from 1 AU to 55 AU.

For the sake of simplicity, this disk model is called the *alpha* model.

After a few minor adjustments, the fit to the SED literature data is remarkable, see Figure 3.8. Its main parameters can be seen in Table 3.7. However, neither this model nor any small variation of it explains the VIS2 data in either Lp- or Mp-band, see Figure 3.9 for Lp-band. This highlights the degeneracy of SED-fitting exercises.

Indeed, the inner dust-disk between 0.4 and 1 AU emits very strongly in NIR, while the PAH grains further out are much dimmer. This creates a very high unresolved-flux (inner-disk and star) compared to the resolved-flux from the PAH in the $\sim$ 9-55 AU region. Hence, the inner regions of the *alpha* model disk pictured on Figure 3.10

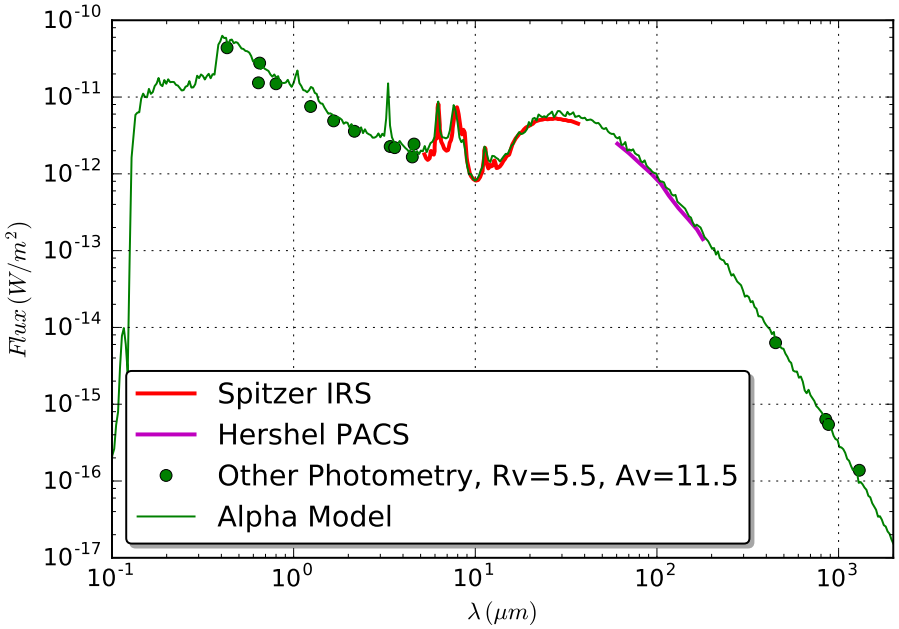

Figure 3.8: SED of IRS-48 obtained from the *alpha* model. The fit is remarkable and explains the photosphere of the star, the NIR-excess, the PAH emission features and the outer-disk SED-bump centered on 20 μm.

appear spatially too small, mostly unresolved. The resulting visibilities are close to unity: much larger than the VIS2 data at all baselines. Given the difference of the VIS2 values, the resolved-flux depletion is estimated to $\sim$ 2.7 for baselines $\gtrsim$3 meter.

The only solution to make such model fit the VIS2 is to incorporate a very high flux in the $\sim$ 9-35 AU region – and in this region only –, to make up for the contrast ratio of $\sim$ 0.48 in Lp-band ($\sim$ 0.42 in Mp-band, see Table 3.6) between the unresolved and resolved fluxes.

This implies changing fundamentally the structure, hence the nature, of the disk around IRS-48.

3.4.3 Fitting strategy

The VIS2 data in Lp-band is merged between all epochs, since they did not show epoch-related variation; the Mp-band is taken at epoch 1, and the SED fluxes are taken from the literature (refer to Table 3.4). Ks-band from epoch 1 are discarded given that their large uncertainties would not set meaningful constraints on the disk structure.

The fitting of the SED is performed "inside-out", or "in increasing wavelengths", so that constraints and parameters obtained from fitting interior structures can remain (mostly) unchanged when fitting structures located further away from the star.

A satisfactory grid resolution is found to be N_z=100 and N_{radial}=150 (log-scale),

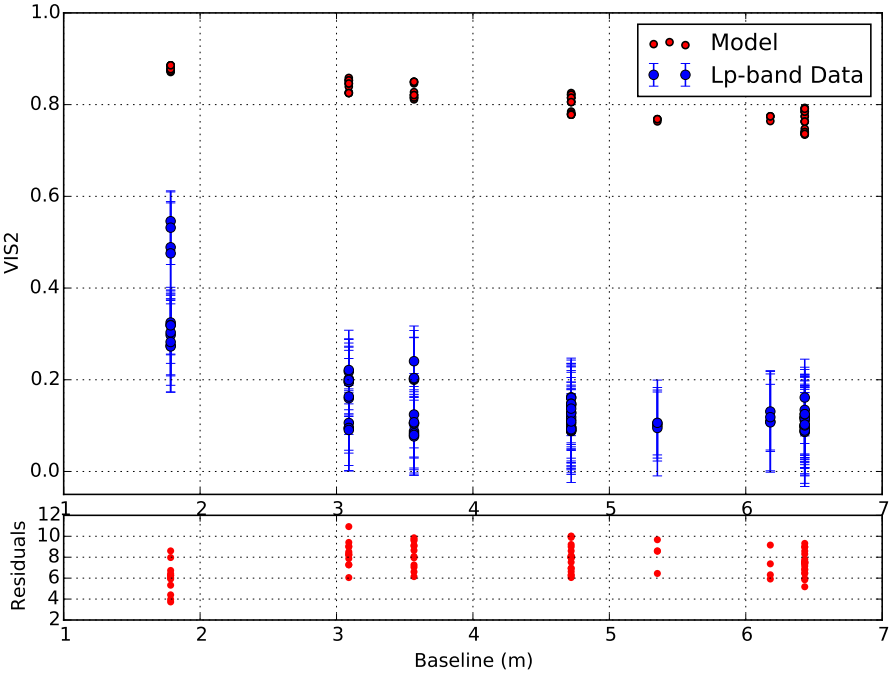

Figure 3.9: Comparison of the VIS2 values as a function of baseline between the VIS2 data in Lp-band (blue 1-sigma error-bar markers) and the corresponding *alpha* model (red markers). VIS2 data values span [0.1, 0.57] at [max, min] baselines while VIS2 calculated from the model-image shown in Figure 3.10 span [0.75,0.9] respectively. Residuals, pictured in the bottom sub-plot, are excessively high (+4 to +11 sigma). This means that the *alpha* model is far too small, and appears spatially unresolved.

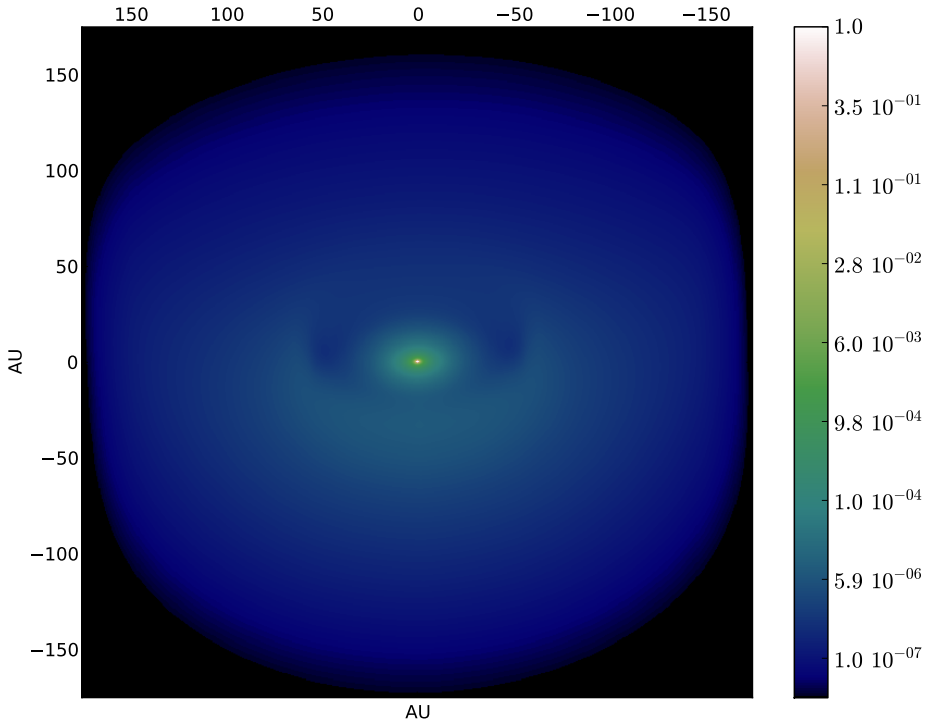

Figure 3.10: Normalized Lp-band synthetic image obtained from the radiative transfer on the *alpha* model. This image was obtained out of fifteen sub-images generated at wavelengths linearly spread in the Lp-bandpass. Due to its proximity to the central star, the inner- and PAH- disks appear much brighter than the outer-disk from 55 AU. Note that the color-scale is highly not linear (fluxes to the power of 0.1).

after analyzing the temperature gradients between consecutive cells in the grid. Given the central-symmetry, N_θ is not defined (or =1). MCFOST allows to over-sample the first cell of a disk in the radial coordinate, in order to properly sample high variations of temperatures in the inner-rim of a disk. This parameter is set to $N_{radial,\ in}$=10.

For the purpose of measuring visibilities on the MCFOST images at the precise (u,v) coordinates corresponding to that of the data, one must calculate the full numerical FT instead of using the Fast-Fourier Transform (FFT) routines and interpolate at the (u,v) coordinates. The FT is calculated at the spatial coordinates (u,v) and the wavelength λ using:

$$FT(I(\alpha,\delta))(u,v) = \sum_x \sum_y \frac{I}{\sum I} \times \exp\big(-2\pi\mathbf{j}\frac{u\ \alpha_{x,y} + v\ \delta_{x,y}}{\lambda}\big), \tag{3.2}$$

where **I** is the over-sampled MCFOST image to calculate complex visibilities on, and (α,δ) represents the angular-coordinates in radian of each pixel in **I** at index (x,y). This double integration is re-evaluated for each (u,v) sampling coordinate.

In order to simulate polychromatic images and replicate the effect of bandwidth smearing, fifteen images linearly spaced within the bandwidth $\Delta\lambda$ of the filter are generated. Given the linearity of the FT, the total FT is the sum of the fifteen FT of each image, or identically the FT of the sum of all images.

However, calculating the FT on each fifteen images is cumbersome: one must sum the images first, and in such a way that the ratios $\alpha(x,y)/\lambda$ and $\delta(x,y)/\lambda$ in the FT expression, see Eq. (3.4.3), are conserved over a variation of λ. To do so, the Field-Of-View (FOV) of each sub-image generated at a wavelength λ_{sub} is set to be

$$FOV_{\lambda,\ sub} = FOV_\lambda \times \frac{\lambda}{\lambda,\ sub}, \tag{3.3}$$

where FOV_λ, the field-of-view at the central wavelength, is chosen to display the full interferometric field-of-view (see Table 3.3) in a constant width of 1001 pixels; i.e. $FOV_\lambda = 1001\gamma_\lambda$. The plate-scale γ is typically 2.7 to 4.5 mas/px for the central wavelength of Lp- and Mp-bands, respectively. This technique however produces a "polychromatic image" that does not represent the real polychromatic view of the object; instead, it is a mathematically-convenient image to perform a faster FT on a sum of synthetic sub-images.

3.4.4 Initial configuration and assumptions

Axial-symmetry perpendicular to the plane of the disk is assumed, as well as plane symmetry above and below the plane of the disk. The standard flared disk prescription (Shakura & Sunyaev 1973) is adopted, described in cylindrical coordinates (r, z) such that the density profile is given by:

$$\Sigma(r,z) = \Sigma_0\ r^p \exp\left(-\frac{1}{2}\left(\frac{z}{h}\right)^2\right), \tag{3.4}$$

where Σ_0 is a density-normalization constant, p is the surface density exponent, and h is the disk scale height, refer to Section 1.3.2.4; h varies with radius as $h = h_0(r/r_0)^\beta$ with β the flaring exponent ($\beta > 0$, of order ~ 1) and h_0 the scale height at radius r_0. This is a built-in disk-model in MCFOST. The outer tapered-edge disk is not used because the VIS2 data can not constrain it over a classical disk, since it is not sensitive to the outer-regions of the disk, further than ~ 90 AU.

The SED shape shows that IRS-48 consists of – at least – two main disk-components: an outer and extended disk beyond ~ 55 AU radius, and a closer one, that emits most of the PAH light, as found by Maaskant et al. (2014). The VIS2 data does not constrain well the outer disk which mostly lies outside its field of view. Hence, the simplest axi-symmetrical fitting solution consistent with the literature is systematically adopted, while the effort is focused on fitting the inner regions.

Similarly to the *alpha* model, a three disk-components model is adopted: two dusty inner- and outer-disks and an additional disk composed of Very Small Particles (VSP) in between. For each of them, the inner radius, outer radius and total dust mass are free parameters. As an initial step, the parameters "scale height" and "flaring exponent" are shared between all three disks.

Other parameters such as the surface density exponent, the grain minimum and maximum sizes, the ratio between carbonaceous (from Li & Greenberg 1997) and silicate (from Draine & Lee 1984) grains, the ratio between ionized and neutral PAH and the grain-size power-law index or the disk inclination are left-aside for the initial fitting exercise and set to standard values from IRS-48 and disk literature.

Several parameters of the outer-disk are not fitted, given that the narrow-FOV VIS2 data in the NIR can not constrain them. They are set to the latest literature values:

- flaring exponent=0.67 (van der Marel et al. 2013b),
- the inclination=50° (Geers et al. 2007a; van der Marel et al. 2013b; Bruderer et al. 2014),
- the surface density exponent=-1 (Andrews et al. 2013),
- the inner-rim radius=55 AU (Geers et al. 2007a),
- the silicate over carbonaceous grains mass-ratio=70/30 (prescriptions span 85/15 in Wood et al. (2002), 45/55 in Kim et al. (1994); 80/20 in Maaskant et al. (2014)),
- the min=0.03 μm, max=4000 μm grain sizes (van der Marel et al. 2013b),
- the effective temperature of the central star=9250 K, mid-way between Follette et al. (2015) work (9500K) and Brown et al. (2012a) work (9000K).

3.4.5 Exploratory fitting

When the radiative transfer of the IRS-48 model is set to a low resolution – N_{radial}=100, N_z=70 – the simulation takes $\sim$ 130 sec to output the modelled SED, and the Lp- and Mp-band synthetic images. This makes impossible the usage of MCMC techniques to fit the full model, which typically require several hundred iterations for each free-parameter in the model.

The exploratory fitting is carried using a coarse grid, where the three-disks model is simplified to its bare minimum. Only five parameters are kept:

- the stellar luminosity at [15, 27, 42, 51] $L_\odot$,
- the inner-most disk mass at [8×10^{-12}, 8×10^{-13}, 0] $M_\odot$,
- the inner-radii of the PAH-disk at [1, 6, 11] AU,
- the outer-radii of the PAH-disk at [55, 40, 26] AU,
- the disk-mass of the PAH-disk at [8×10^{-8}, 6×10^{-8}, 4×10^{-8}] $M_\odot$,

while the extinction parameters A_v and R_v are obtained a-posteriori from a chi-squared fit of the SED fluxes $\lesssim$5 μm. Each first value of the parameter ranges above correspond to the *alpha* model. The inner- and outer-radii of the inner-most disk are set to 0.4 and 1 AU respectively (*alpha* model).

The grid simulation was carried over the 324 models. The difficulty in evaluating the best-fitting model is to combine and balance the chi-squared values of the three different data-types – Lp-band VIS2, Mp-band VIS2 and SED fluxes – into a global quality-function that converges to the truly best disk without bias.

In practice, such a quality-function can not be obtained easily – or even at all –, for different reasons such as (non-exhaustively):

- the fact that error-bars are not consistently set and normalized between the different types of data,
- the inhomogeneous density of information, i.e. the data-density per wavelength or (u,v) coordinates, needs regularization to "evenly" weight data-points between each other,
- incorporating complex scientific constraints on the fitted parameters values, based on an a-priori implementation of the disk-evolution theories,
- the need for changing the model as fitting is undergoing, e.g. adding/removing a type of dust-grains, swapping from a classical disk to a tapered-edge disk.

Rather than fine-tuning such function, a general approach is chosen: for each of the Lp-band VIS2, Mp-band VIS2 and SED fluxes data-types, the chi-squared are

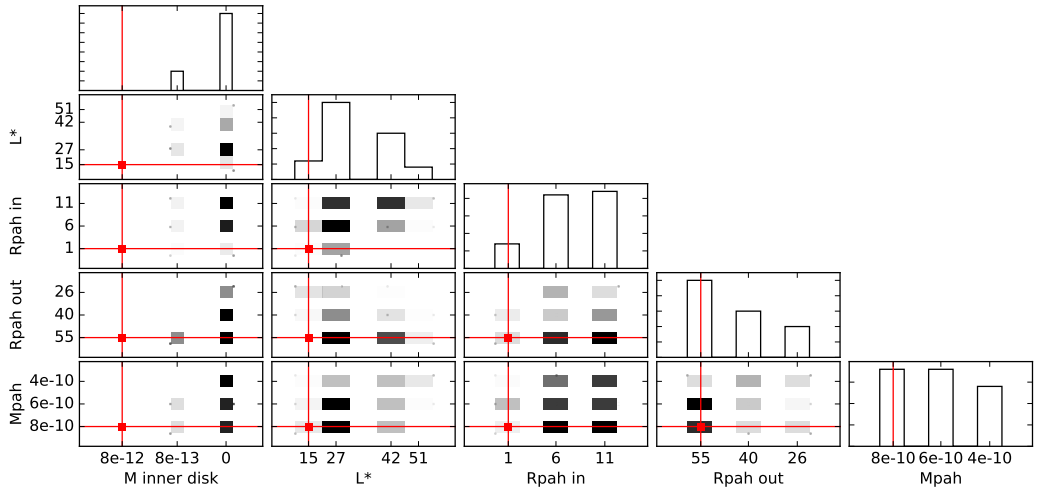

Figure 3.11: Modified corner-plot showing the results of the coarse-grid exploratory fitting, where the five fitted parameters are labeled "M inner disk" (inner-most disk mass in $M_\odot$), "L*" (Stellar luminosity in $L_\odot$), "Rpah in" (inner-radius of the PAH-disk in AU), "Rpah out" (outer-radius of the PAH disk) and "Mpah" (PAH-disk mass in $M_\odot$). The red lines and squares correspond to the values of the *alpha* model.

normalized between 0 (best chi-squared of the grid for that data-type) and 1 (worst), and the global quality-function is defined as:

$$Quality = \chi^2(Lp\ VIS2) + \chi^2(Mp\ VIS2) + 2 \times \chi^2(SED\ fluxes), \qquad (3.5)$$

where the SED fluxes chi-squared is calculated in log scale and per wavelength-decade, for wavelengths $\lesssim 7\ \mu m$ in order to exclude the fluxes of the model which may be affected by the (not fitted) outer-disk.

Rather than focusing on the best-graded model, in order to overcome the bias introduced by the quality-function, the best 15% (in the definition of Eq. (3.5)) of the 324 models are kept for statistical analysis, i.e. the fifty best-fitting models. To make sure that the quality-function does not introduce a bias large enough to compromise the statistical analysis, it is checked by eye that these fifty models provide a satisfactory fit. The results of this statistical analysis is shown in Figure 3.11.

One sees that the occurrence of models taking the values of the *alpha* model, corresponding to the red color, is very low. For instance, there was no disk-model graded in the best 15% that showed a dense inner-most disk (8×10^{-12} $M_\odot$), and 80% of the 50 best models do not show any inner-most disk at all. The two-dimensional histogram picturing the stellar luminosity versus the inner-most disk mass shows that 90% of the 50 best models show a stellar luminosity larger than that of the *alpha* model.

One can however note that the best chi-squared value measured on the SED data only, is obtained for the parameters corresponding to the *alpha* model. While the SED

data pushes towards a three-disks model for IRS-48, the simultaneous fitting of high-resolution VIS2 data converges to a two-disks model, where a brighter stars produces most of the NIR fluxes, de facto diminishing the need for an inner-most disk.

3.4.6 Inner-most Region and Star

Another way to qualitatively demonstrate the latter result, is to consider that VIS2 data gives stringent constraints on both the flux ratio between the unresolved flux (inner-most disk and star) and resolved flux (further than ~ 9 AU). To correct for the resolved-flux depletion of about a factor of 2.7 compared to the unresolved-flux (see Section 3.4.2), one can either

1. decrease the inner-most disk opacity to decrease the unresolved fluxes

2. increase the PAH disk opacity further than 9 AU to increase the resolved flux

Option 2) would immediately lead to a dramatic over-brightness of the main PAH emission features between 4 and 15 μm, with no (or few) degrees of freedom to compensate for it (i.e. structural parameters such as flaring exponent, scale height, etc).

Option 1) would automatically lead to an under-fitting of the NIR flux. This can easily be corrected by increasing the brightness of the star, de facto decreasing the amount of dust-related NIR-excess needed in the fit. Indeed, as discussed by Follette et al. (2015), a hotter and especially larger star questions the existence of a third inner-most disk in the ~ 1 AU area from the star where this disk was usually needed to account for the 1-3 μm IR excess.

The fitting constraints are released by allowing the stellar luminosity to vary between 10 and 100 $L_{\odot}$. This implied adding two additional free parameters to tune the extinction of the target in order to fit the photometric fluxes measured in the visible and NIR (R_v taken in $[4.0 - 10.0]$ and A_v taken in $[10.0 - 15.0]$).

3.4.7 Very Small Particles disk

The morphological fit of a simple two-dimensional Gaussian showed that the characteristic location of the resolved flux should lie in a region between 10 and 20 AU. The PAH disk is a natural candidate to account for this flux, since previous work showed that the cavity up to ~ 55 AU was not depleted of such grains (Geers et al. 2007a; Maaskant et al. 2014). This however means that the bright inner rim of the PAH disk must be fully resolved, i.e. further than ~ 7 to 10 AU, in order to account favorably to the contrast ratio between unresolved and resolved flux. A direct consequence one expects is the decrease of the over-abundant unresolved emission in the *alpha* model.

This effect is seen on Figure 3.11 in the two-dimensional histogram that pictures the co-variance of the PAH-disk inner-radius and the inner-most disk mass, where 70% of the best disk models show both 1) no inner-most disk and 2) a PAH-disk inner-radius at 6 AU or further (34% at 6 AU and 36% at 11 AU).

The MIR SED does not show any bump peeking at 9.5 and 18.3 μm, characteristic of silicate grains smaller than $\sim$ 2 μm. It does instead show a clear deep at 9.8 μm, de facto eliminating any major silicate grains contribution to the MIR flux. Hence, it was decided not to incorporate any small or classical grains in the cavity between the inner- and outer-disks, between 1 and 55 AU.

To model the very small particles, the prescription of Natta et al. (1993) is followed and a mixture of carbonaceous VSG and PAH with a ionized/neutral fraction parameter is used, from Li & Draine (2001); Weingartner & Draine (2001); Draine & Li (2007). For conciseness, Very Small Particles (VSP) will be used instead of PAH&VSG. Following the classification of Tielens (2008) (Table 2), the following grains sizes are set: a_{min}=4 Å and a_{max}=10 Å for PAH (ionized and neutral), a_{min}=10 Å and a_{max}=30 Å for VSG (referred as PAH clusters and VSG in their table). The grain size power-law index for PAH and VSG is set to -4 (Tielens 2008); only the relative abundances of these three species are left as free parameters for fitting. Finally, these VSP are assumed to be quantum heated by UV stellar-flux, i.e. outside Local Thermodynamic Equilibrium (LTE), see Section 3.4.1.

3.5 Resulting Structure

The fit, initialized as detailed in the previous section, was performed. A manual exploration of the parameters was carried in order to identify the most impacting ones. The fit is later refined using low-dimensional grids. Such coarse grids ensure a full exploration of a small subset of the entire parameter space. Verifying smoothness for the outputs of the modelling over these small grid-subsets allowed us to interpolates the results and thus minimize the processing time for these grids. The final convergence was achieved by eye; as will be explained in a later section. Note again that the VIS2 data is mostly blind to the outer-disk; the solution found represents the simplest centro-symmetrical structure that satisfied the SED fluxes.

3.5.1 General results

This best solution is obtained for a scenario where the innermost disk (0.4-1 AU) has such a low mass that it does not contribute to IRS-48 flux in any wavelength. The new IRS-48 model is hence composed of two disk-elements: a VSP-only disk between 11 and 26 AU and an outer-disk from 55 AU, as portrayed in the Lp-band model-image (see Figure 3.12). The star has a higher luminosity L_*=42 $L_\odot$, leading to a larger radius R_*=2.5 $R_\odot$ than previously reported. The main parameters of the solution are listed in Tables 3.8 and 3.9, where they are compared to that of the *alpha* model.

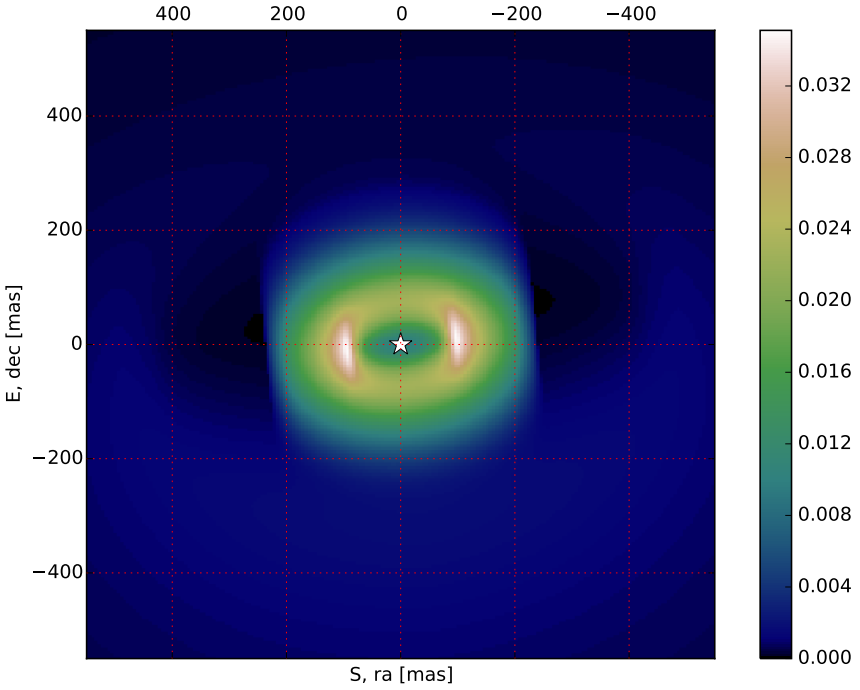

Figure 3.12: Lp-band model-image normalized to the stellar-flux, obtained from the radiative transfer on the new model. This image was produced out of 15 sub-images generated at wavelengths linearly spread in the Lp-bandpass. The inner-disk between 11 and 26 AU appears much brighter in Lp-band than the outer-disk from 55 AU. Two cavities appear, one inside 11 AU and another one between 26 and 55 AU.

Table 3.8: Best-fit and *alpha* model parameters of the radiative transfer of IRS-48. Part I: star- and global disk-parameters

Parameter	*alpha* model	New model
Stellar parameters		
Temperature	9250 K	9250 K*
Luminosity	14.3 $L_\odot$	42 $L_\odot$
Distance	120 pc	120 pc*
R_v	5.5	6.5
A_v	11.5	12.9
Global disks parameters		
Inclination	50°	50° *
PA	96°	96° *
Scale height	10 AU	14 AU
Ref. radius	60 AU	60 AU *

*=set-value parameter

Table 3.9: Best-fit and *alpha* model parameters of the radiative transfer of IRS-48. Part II: inner-most, VSP- and outer-disks parameters

	Inner-most disk	
R_{in} Inner	0.4 AU	–
R_{out} Inner	1 AU	–
Flaring exp. β	1.3	–
Surface density exp p	-1	–
Grain-size power-law	-3.5	–
Total dust mass	8.0×10^{-12} $M_\odot$	–
Silicate grains mass	1%	–
Carb. grains mass	99%	–
Grain sizes a	0.03 - 30 μm	–
	VSP-ring	
R_{in} Inner	1 AU	11 AU
R_{out} Inner	50 AU	26 AU
Flaring exp. β	1.3	0.6
Surface density exp p	-1	-0.1
Grain-size power-law	–	-4*
Total dust mass	8.0×10^{-10} $M_\odot$	3.7×10^{-10} $M_\odot$
VSG mass	0%	25%±15
VSG sizes	–	10 - 30 Å *
Neutral PAH mass	50%	65%±15
Ionized PAH mass	50%	10%±10
PAH sizes	5 Å	4 - 10 Å *
	Outer disk	
R_{in}	55 AU	55 AU *
R_{out}	160 AU	250 AU
Flaring exp. β	1.3	0.67*
Surface density exp p	-1	-1*
Grain-size power-law	-3.5	-3.5*
Total dust mass	1.0×10^{-5} $M_\odot$	9.0×10^{-6} $M_\odot$
Silicate grains mass	70%	70%*
Carb. grains mass	30%	30%*
Grain sizes a	0.03 - 4000 μm	0.03 - 4000 μm *

*=set-value parameter

Figure 3.16 shows the SED for both models with their respective interstellar extinction. The new model provides the same fit quality as the *alpha* model, it matches very closely all the main features of the SED: the photosphere of the star, the NIR-excess, the PAH emission-features and the outer-disk. Most importantly, it improves

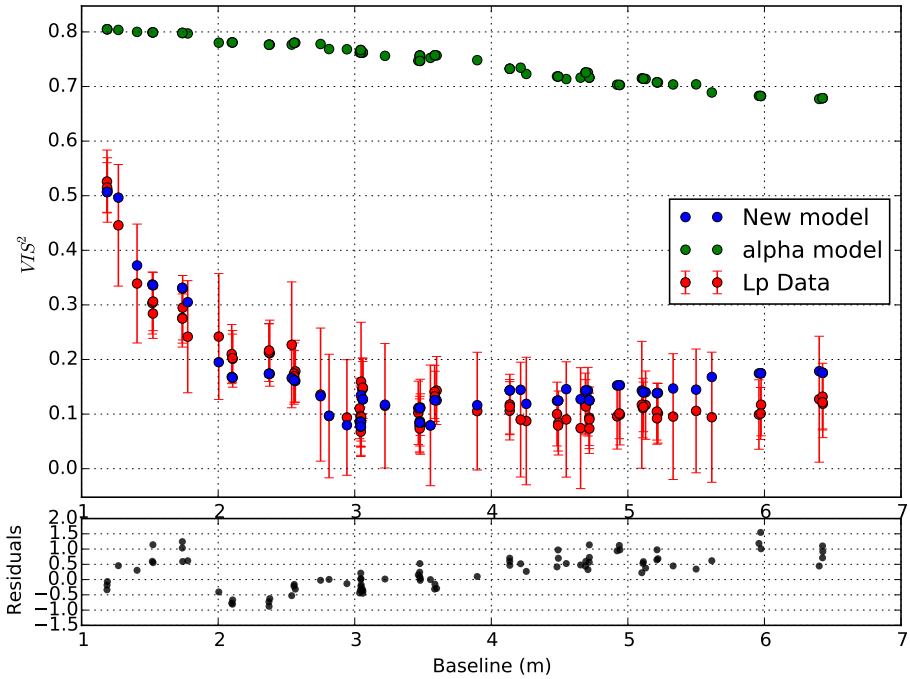

Figure 3.13: Diagram showing the Lp-band VIS2 data at all epochs, the calculated squared-visibility from the *alpha* model-image (green) and those of the new model (blue) as a function of the un-projected baselines in meter (disk inclination of 50°). Most residuals for the new model span ±1 while they exceed +4 for the *alpha* model.

dramatically the fit on the VIS2 data, which it explains entirely: Figures 3.13, 3.14 and 3.15 show the comparison between the VIS2 data in Ks-, Lp- and Mp-band and both models.

3.5.2 Central star

The solution of a L_*=42 $L_\odot$ star with a 3.7×10^{-10} $M_\odot$ mass VSP-ring and no inner-most disk (0.4-1 AU) is a complex and precise balance between the fit to the SED and to the VIS2 data. Indeed, the NIR SED requires either 1) a brighter star than the *alpha* model, or 2) a similar star with an inner-most disk to account for a large NIR-excess. The VIS2 data however pinpoints a precise contrast ratio between the resolved VSP-ring and the unresolved star and inner-most disk together. Adding even the smallest inner-most disk-mass creates an excessive NIR emission which must be compensated with a large increase of the VSP disk-mass to fit the contrast ratio encoded into the VIS2 data. Such an increase however dramatically over-estimates the PAH emission features between 5.5 μm and 18 μm. This strongly pushes to a solution with no inner-most disk inside the VSP-ring, as seen in Section 3.4.5.

A brighter star accounts for most of the NIR flux, it can not however be too bright and account for all of it up to the first PAH features at 5.5 μm, since the VIS2 data at

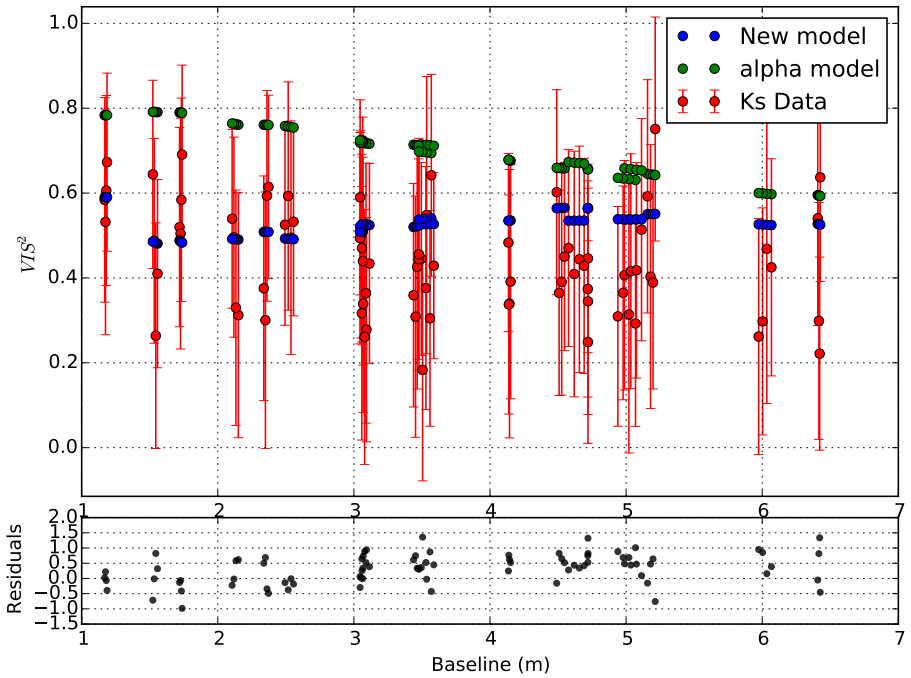

Figure 3.14: Same as Figure 3.13 but for Ks-band VIS2 data. Although the Ks-band data is much noisier, the new model still does provide an improvement over the *alpha* model.

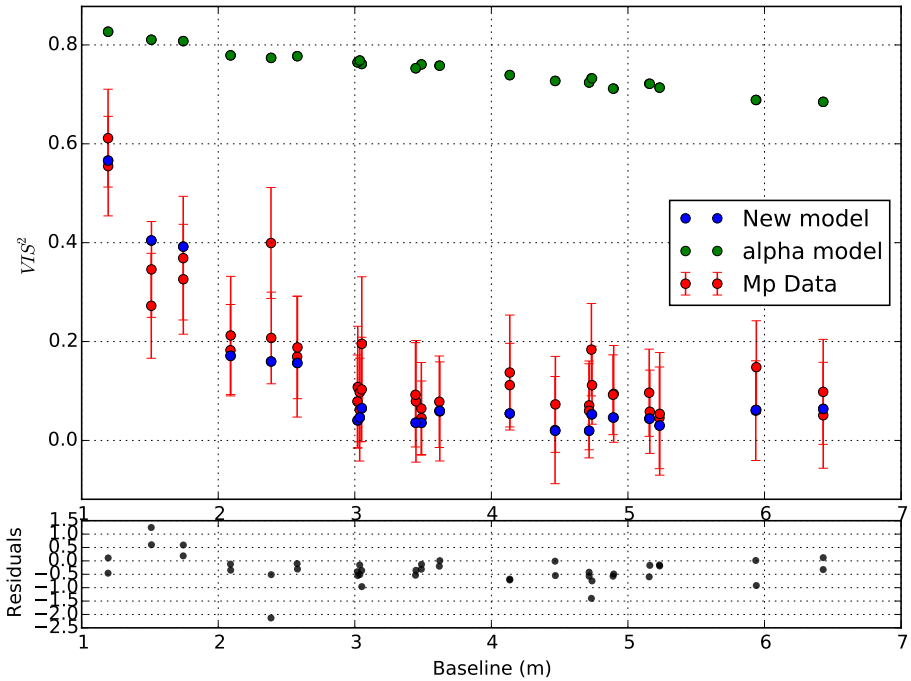

Figure 3.15: Same as Figure 3.13 but for Mp-band VIS2 data.

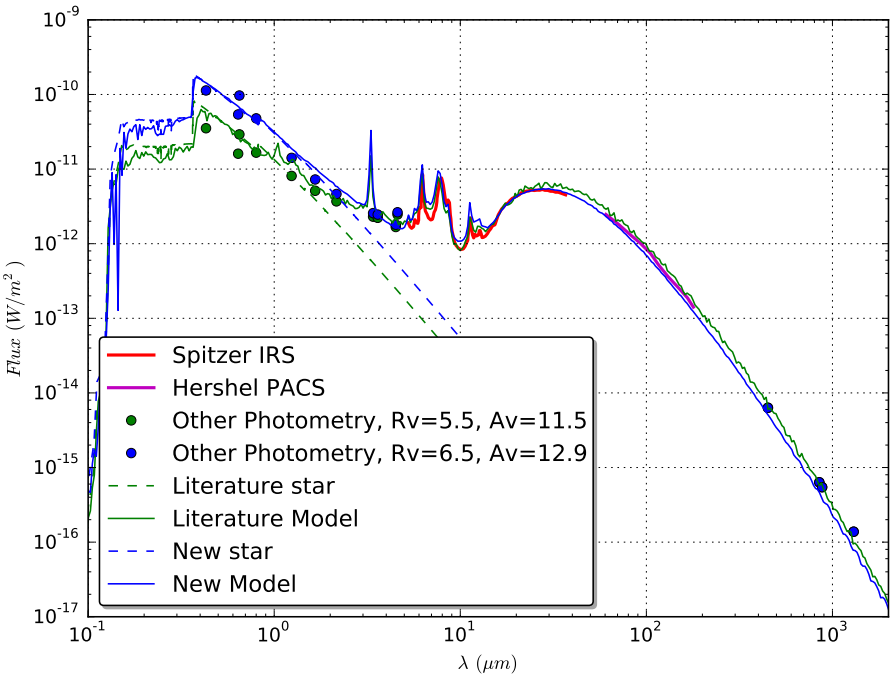

Figure 3.16: SED and photosphere of IRS-48 obtained from the *alpha* model (green line) and the new model (blue line). Both explain the photosphere of the star (although with different extinction parameters), the NIR-excess and the outer-disk SED-bump centered on 20 μm.

2.18 (Ks), 3.8 (Lp) and 4.78 μm (Mp) constrains very precisely the shape and contrast of the extended emission in the NIR. Solutions with a brighter (dimmer) star than L_*=42 $L_\odot$ in combination with a smaller (larger) VSP-ring mass than 3.7×10^{-10} $M_\odot$ would be compatible with the VIS2 data and the NIR SED. However, they would underestimate (overestimate) the PAH features in the MIR SED.

One sees this trend on Figure 3.11, in the subplot depicting the two-dimensional histogram between the inner-radius of the PAH ring and the stellar luminosity: as the stellar luminosity increases, the inner-truncation of the PAH-disk goes away from the star.

Given an effective temperature and a luminosity, one can – with minor degeneracy – estimate the radius, age and mass of a Young Stellar Object (YSO) using, e.g., the Siess et al. (2000) evolutionary models. With grids such as shown in Figure 3.17, the best-fitting stellar parameters for IRS-48 are found to be $\sim$ 2.5 $M_\odot$, $\sim$ 2.5 $R_\odot$ and $\sim$ 4.2 Myr; all parameters are listed in Table 3.10 with a comparison to previous literature. Figure 3.17 shows that the age estimate is robust to a change of luminosity and effective temperature. Indeed, a YSO of T=9250^{+100}_{-400} and L=42^{+5}_{-3} yields a similar age-estimation, between 4.1 and 4.5 Myr. The age estimate is much younger than the 8 or 15 Myr previously inferred. This partly solves the evolutionary puzzle on the presence of a disk. Refer to Section 3.7.1 for a discussion on the age of IRS-48. The time-evolution of the effective temperature and luminosity for YSOs of 2.0 $M_\odot$ (Follette et al. 2015), 2.2 $M_\odot$ (Brown et al. 2012a) and 2.5 $M_\odot$ (new model) is shown on Figure 3.18.

Table 3.10: New stellar model for ρ Oph IRS-48 central star.

	This work	Follette+ 2015	Brown+ 2012
T (K)	9250	9500	9000
R ($R_\odot$)	2.5[(1)]	1.8	1.4
L ($L_\odot$)	42	23.6	14.3
Age (Myr)	4.2[(1)]	8	15
M ($M_\odot$)	2.5[(1)]	2.2	2.0
A_v	12.9	12.0	11.5
R_v	6.5	(4.0)	5.5
A_k	(1.8)	1.5	(1.6)

[(1)] according to Siess et al. (2000) YSO evolutionary models.

To compensate for the higher stellar luminosity, the interstellar extinction was increased to A_v =12.9 and R_v =6.5. This means that IRS-48 is 1.4 V-magnitude more extinct, and with a more gray R_v than the extinction inferred in Brown et al. (2012a) (A_v =11.5 and R_v =5.5). This confirms and reinforces the substantial presence of dust grains of large sizes (>1 μm) in the line of sight (Kim et al. 1994; Indebetouw et al. 2005), typical of star-forming regions such as Ophiuchus. An equivalent value of A_k

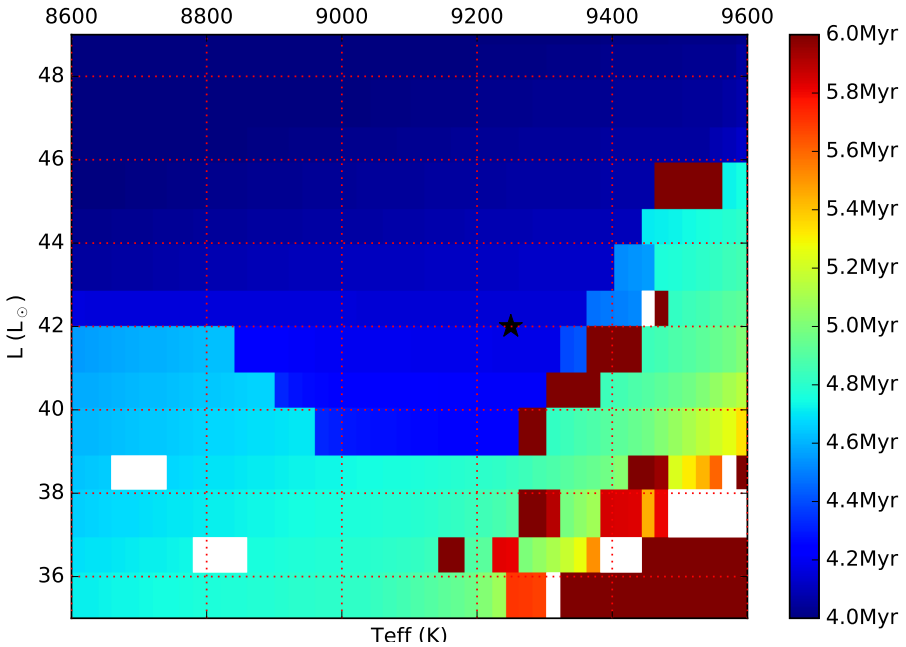

Figure 3.17: IRS-48 age (color-coded) as a function of a luminosity L (y-axis) and effective temperature Teff (x-axis), using the Siess et al. (2000) YSO evolutionary models. The black star symbol represents the new IRS-48 stellar parameters. White regions correspond to a combination of effective temperature and luminosity that do not match any YSO model; dark red areas correspond to regions that led to an excessively old YSO model (>20 Myr). This latter effect is due to the degeneracy of determining the YSO radius, mass and age from the effective temperature and luminosity only. Using this grid-solution, the age of IRS-48 is estimated to 4.2 Myr.

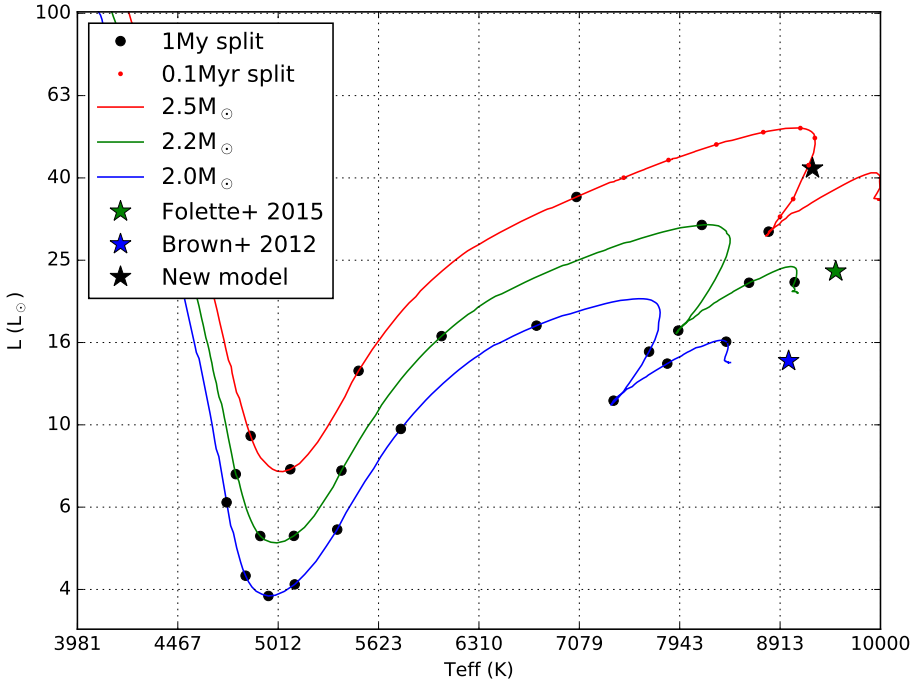

Figure 3.18: Luminosity versus effective temperature loci from Siess et al. (2000) YSO evolutionary models, for a 2.0, 2.2 and 2.5 $M_\odot$ young star. The stars light up as a cold and luminous body (top-left area of the graph), and follow a locus to the right-hand side. The black circles split the loci in equal durations of 1 My (from 1 Myr to 5, 9 and 11 Myr for the 2.5, 2.2 and 2.0 $M_\odot$ stars, respectively). The stellar parameters inferred in the new model fall on the 2.5 $M_\odot$ locus, at an age of $\sim$ 4.7 Myr. The discrepancy in age estimate with the previous grid-estimation is due to the fact that the locus presented here was pre-computed for a 2.5 $M_\odot$ YSO as an input parameter, while the estimation from the luminosity and effective temperature led to an estimate of 2.53 $M_\odot$. Note that this high correlation between YSO mass and age does not affect the best-fitting mass and ages estimates from Table 3.10 given that they are both independently obtained from Teff and L.

=1.8 is consistent with that of $\sim$ 1.6 read on the low spatial-resolution extinction map computed by Lombardi et al. (2008). One should note that their A_k estimate for this particular Ophiuchus core-region suffers from high discrepancy; this is thought to be due to the varying depth into the molecular cloud of their sample targets.

The radiative modelling shows that its $\sim 50°$ inclination is not large enough to extenuate the stellar flux like observed in the case of edge-on disks. There is no extinction due to the circumstellar disk itself, all extinction is due to interstellar extinction most of which arises from the local molecular cloud of ρ Oph, see Figure 1.2.

3.5.3 Very Small Particles ring

This new model consists of a smooth centro-symmetrical and optically thin VSP-only ring between 11 and 26 AU. It is responsible for all of the IR-excess until $\sim$ 13 μm, where the outer disks starts dominating the dust-emission. In the fitting exercise, the VIS2 data constrained mostly the structure of the VSP-ring, while the MIR-SED PAH emission features constrained the relative abundance of the PAH grains and VSG. The VSP density tops at $\sim 1{\times}10^{-17}$ kg.m^{-3} (see Figure 3.19). It is ~ 2 orders of magnitude higher than typical interstellar medium, consistent with the fact that planetary disks show higher material densities.

3.5.3.1 Ring composition and mass

The total VSP-ring mass found is $3.7{\times}10^{-10}$ M$_\odot$ ($1.2{\times}10^{-4}$ M$_{Earth}$). PAH species dominate the VSP-ring with a total mass of $2.8{\times}10^{-10}$ M$_\odot$ (75%) and a neutral fraction of 85%$\pm$15, compared to the VSG mass of $0.9{\times}10^{-10}$ M$_\odot$ (25%). Although Maaskant et al. (2014) did not include VSG, the new model mass and neutral fraction values are both roughly consistent with their work ($7.7{\times}10^{-10}$ M$_\odot$ and 54% respectively). Their higher mass compensates for their fainter star. As found in Natta et al. (1993), carbonaceous VSG have a nearly flat spectrum in the NIR and MIR wavelengths; they provide a significant amount of the NIR flux needed by the VIS2 and the SED data, while the relative amount of ionized and neutral PAH are responsible for the shape of the PAH emission-features.

In order to study the relative abundance of the three species of the PAH disk – namely VSG, neutral and ionized PAH –, one can simulate various VSP-ring compositions using a simulation grid. The total VSP-disk mass is left to $3.7{\times}10^{-10}$ M$_\odot$. The composition of the three species is scanned from 0 to 100%, with the constraint that the three composition sum up to 100%; this leads to sixty-six models.

Similarly to the exploratory fitting in Section 3.4.5, a (biased) quality-function is defined identical to Eq. (3.5). The statistics of the most-probable models is obtained from the best third (seventeen models); a check by eye ensured that all models fit closely the data. The results are shown on Figure 3.20, which displays the histogram of the mass fraction of the three species.

One sees from Figure 3.20 that the composition of VSG converges to 25%$\pm$15, and that of neutral and ionized PAH to 65%$\pm$15 and 10%$\pm$10 respectively, corresponding

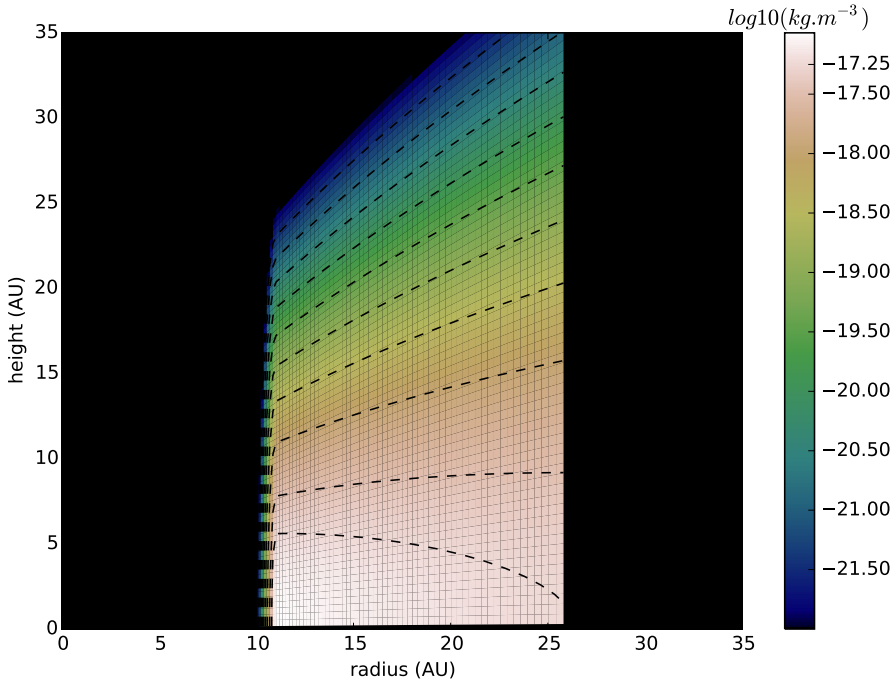

Figure 3.19: Map showing the PAH dust density [kg.m^{-3}] in log10 scale, in a cut perpendicular to the plane of the disk. Iso-contours on the map are shown at the levels of the color-bar ticks. The densest region of the VSP-ring spans from 11 to 20 AU with an average height of $\sim$ 5 AU above the mid-plane. The ring shows a smooth and nearly flat density structure with increasing radius due to the high surface density exponent of -0.1.

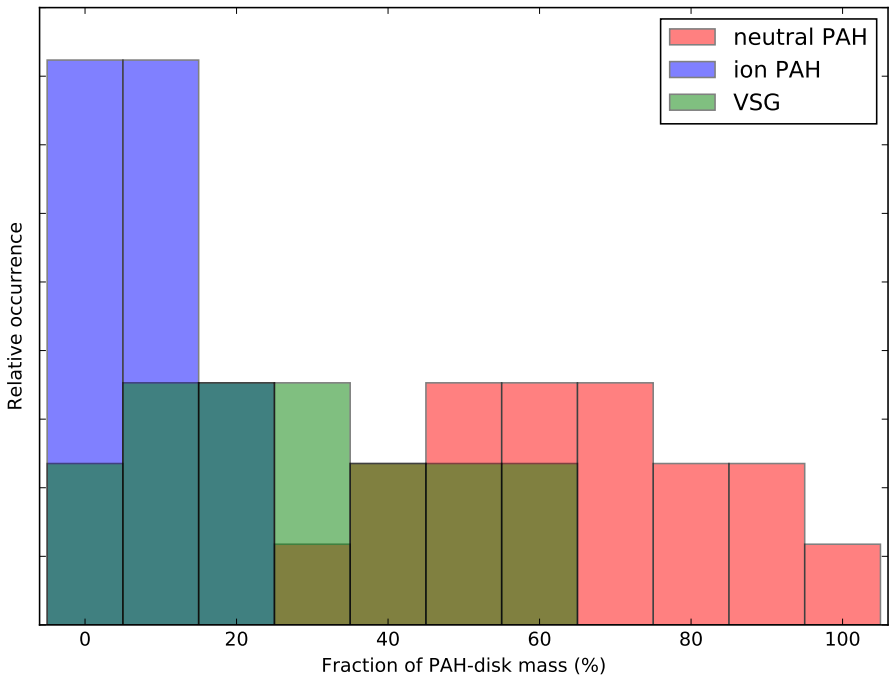

Figure 3.20: Histogram of the mass of VSG, neutral and ionized PAH in the VSP-ring, as a fraction of the total VSP-ring mass (3.7×10^{-10} $M_\odot$). The statistics is obtained from the best seventeen of a simulation grid of sixty-six models spanning all possible three-components compositions of the VSP-disk, with 10% granularity.

to a PAH-neutral fraction of 85%±15.

3.5.3.2 Surface density exponent p

The fit to VIS2 data favors high values of the surface density exponent p (see Section 1.3.2.3), best at -0.1, similarly to what Carmona et al. (2014) find inside the cavity of another transition disk. This is due to the fact that VIS2 data required an homogeneous VSP-ring density to reduce the slope of the radial brightness profile. Indeed, a surface density exponent near -1 would create a very bright inner-rim and a steeply decreasing brightness profile. Such a configuration creates a relatively small VSP-ring which could not explain the extended structure encoded into the VIS2 data. Classical dusty-disk prescriptions of $p \sim$ [-0.8,-1.3] mostly model viscous transport of the dust inwards because of gas friction, spiraling in and eventually accreting on the star (Weidenschilling 1977). This prescription for classical grains does not apply to PAH, and VSG: they remain coupled to the gas, both radially and in height, because of their very small mass (Tielens 2008).

3.5.3.3 Scale-height h_{60AU} & Flaring exponent β

The relatively high scale-height h_{60AU}=14 AU compared to 8 AU from Bruderer et al. (2014) or 10 AU from Follette et al. (2015) and the low flaring exponent β=0.6 were needed to account for the aspect ratio (along RA and DEC axes) of the disk (see Section 1.3.2.4). A high value of h_{60AU} was naturally favored in order to increase the VSP-ring surface facing the star, to increase the PAH emission for a given PAH-mass. Indeed, PAH grains are quantum heated through strong UV radiation from the star. Even though this ring is optically thin in most wavelengths, τ_{UV} is of order 0.5 in the mid-plane (Figure 3.21). This means that a significant fraction of the PAH emission comes from the disk surfaces, either the inner-rim or the top layers.

3.5.3.4 Inner-rim and outer-radius

The extent of the VSP-ring are well-constrained, particularly the inner-rim radius. The VIS2 data imposes a contrast ratio and a precise brightness profile on the fit. Given the low optical thickness in the wavelengths of VIS2 data, see Figure 3.21, the brightness profile is closely related to the grain density profile. Moving the inner-rim closer to the star breaks very rapidly the adequate brightness profile, creating a too small and too bright ring to match the VIS2 data. Moving the inner-rim further away from the star strengthens the first bounce (previously called "wiggle") of the Fourier pattern of the VSP-ring (similarly to the "visibility bounce" of a uniform disk (see Figure 3.6), such that visibilities at spacial frequencies $\gtrsim 5m$ increase back to values $\gtrsim$0.2, incompatible with the data. Under the current assumptions, the inner-rim radius is known at $\sim$ 1 AU.

An extended VSP-ring helps smoothing out the visibility-bounce at large spatial frequencies, inherent to a disk-like structure. For this reason, the outer-rim radius can

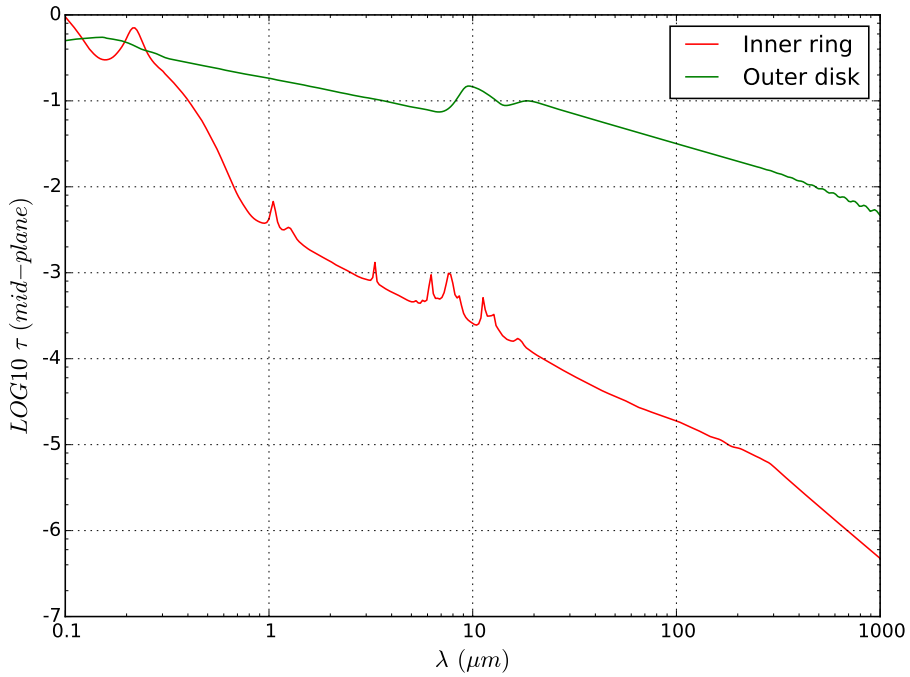

Figure 3.21: Optical thickness τ taken in the mid-plane as a function of wavelength for the VSP-ring and the outer-disk. One recognizes the PAH lines from the VSP-ring and the two silicates bumps of the outer-disk at 9.2 and 18 μm. The VSP-ring becomes extremely thin for wavelengths above a micron.

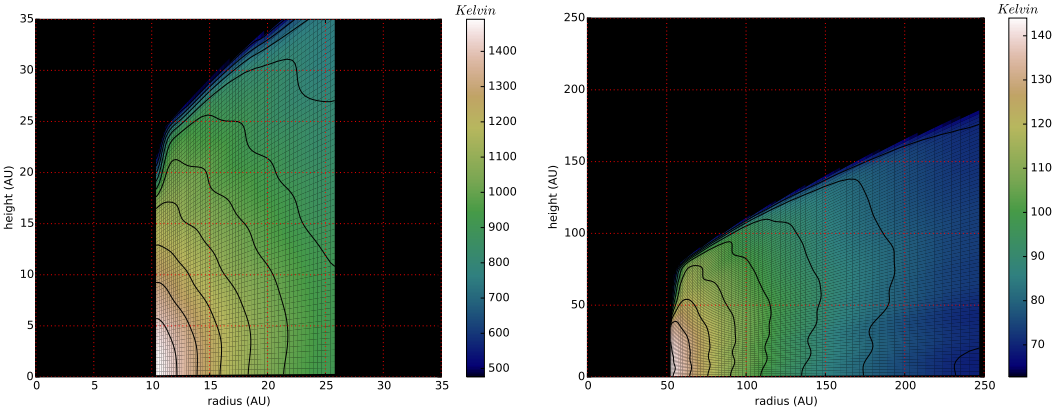

Figure 3.22: Map showing the temperatures (Kelvin) of the neutral PAH dust (left) and of the outer-disk grains (right), in a cut perpendicular to the plane of the disk. Iso-contours on the map are shown at the levels of the color-bar ticks. Compared to neutral PAH, ionized PAH grains and carbonaceous VSG follow a very similar temperature distribution, but with lower temperatures bounds: $T_{max}\sim$ 1100K and $T_{min}\sim$ 400K for ionized PAH and $T_{max}\sim$ 550K and $T_{min}\sim$ 250K for VSG

hardly decrease below its best value of 26 AU. The higher-limit is somewhat looser: it mainly depends on the VSP mass, which is strongly constrained by the MIR-SED. Given the high surface density exponent p, the outer-rim cannot increase substantially without incorporating an excessive amount of VSP grains, hence MIR flux. Its location is known at $\sim$ 4 AU under current assumptions.

The resulting disk temperature is shown in Figure 3.22 for neutral PAH grains. Because of the close proximity to the star, the time between two successive absorptions is lower than the relaxation time of the PAH grains. In this case, MCFOST treats quantum heating as "quasi-equilibrium" and an average temperature can be defined consistently, i.e. low dispersion on the temperature probability distribution. The temperature reaches particularly high values for neutral PAH grains, $T_{max}\sim$ 1500K and $T_{min}\sim$ 600K. Ionized PAH grains and carbonaceous VSG follow a very similar temperature distribution, with lower temperatures due to their difference in electrical charge, mass and structure: $T_{max}\sim$ 1100K and $T_{min}\sim$ 400K for ionized PAH and $T_{max}\sim$ 550K and $T_{min}\sim$ 250K for VSG.

3.5.4 Outer disk

As previously highlighted, the interferometric data is mostly blind to the outer-disk, and is not sensitive in any case to the southern asymmetry observed with ALMA in mm-wavelengths. The simplest centro-symmetric disk model to satisfy the FIR and mm-wavelength SED was systematically adopted.

This centro-symmetric approach is however not void of meaning. Indeed, the outer disk is optically thin in its emission window (for wavelengths $\gtrsim 13\mu m$, τ in the mid-

plane $<10^{-1}$, see Figure 3.21). Hence the precise azimuthal location of grains (azimuthally asymmetric or not) only plays a secondary role in fitting the SED.

In order to satisfy the mm-wavelength SED, the outer-radius of the disk is found at $\sim$ 250 AU, similarly to Maaskant et al. (2014) (225 AU), although SED fitting is not very sensitive to this parameter. For that disk extend, the total mass of the outer-disk in the MCFOST model is 9×10^{-6} $M_\odot$ (3 M_{Earth}) for grains between 30 nm and 4 mm, with a grain-size power law of -3.5. This mass is similar although lower than Bruderer et al. (2014) (1.6×10^{-6} $M_\odot$, 5.3 M_{Earth}) and 9 M_{Earth} found by van der Marel et al. (2013b) for the same grain-size distribution and bounds.

The discrepancy with the latter 9 M_{Earth} estimate can be explained with that fact that it was obtained from the integrated 685Ghz ALMA flux, biased by the fact the authors used a lower temperature, T=60K at 60 AU, than what is currently observed in the new model. Indeed, the new star is brighter, hence heats the outer-disk more efficiently: as seen in Figure 3.22, the inner-rim temperature peaks at T_{dust}=148 K at 55 AU.

One can update their dust mass calculations with the values of the new model to find τ_{685GHz}=0.14 for T=140K at 60 AU, using their expression

$$F_\nu = \Omega \times B_\nu(T_{dust}) \times (1 - \exp^{-\tau_\nu}). \tag{3.6}$$

When one integrates over the whole disk-model the optical thickness at ν=685Ghz (λ=440 μm), one finds τ_{685Ghz}=0.19, closely consistent with the previous 0.14 found independently using ALMA flux. Using $M_{dust} = 21 \times \tau_{685Ghz}\sqrt{a_{max}}$ from Draine (2006); van der Marel et al. (2013b) and under the same hypothesis, one finds M_{dust}=3 M_{Earth} for τ=0.14 and 4 M_{Earth} for τ=0.19. Both are consistent with the outer-disk dust mass in the radiative transfer model (3 M_{Earth}).

Figure 3.23 shows the comparison between imaging data taken at 4.78 μm (Mp-band), 8.6 and 18.7 μm, and model-images generated at the corresponding wavelengths. Geers et al. (2007a) noted that the 8.6 μm image is mostly unresolved, with most flux arising from PAH in the inner 30 AU, while the 18.7 μm image is highly resolved, with most flux arising from the inner rim of the outer-disk located at $\sim$ 55 AU. Although 8.6 and 18.7 μm images were not included into the model fitting – only SED fluxes were fitted at these wavelengths – the new model can reproduce the observed disk-structure accurately at these wavelength.

3.5.5 Classical Thermal Grains in the VSP-ring

Figure 3.24 compares intensity profiles along the semi-major axis of the observed and modelled disks at 18.7 μm. Several models were computed, where the amount of thermal grains (silicates (70%) & carbonaceous (30%)) with sizes between 0.3 and 300 μm (mass power index of -3.5), are introduced in the VSP-ring as settled material (one fifth of the VSP-ring scale-height: h_{60AU}=14/5 AU). Although the axi-symmetrical new model cannot obviously reproduce the eastern asymmetry, it shows a distinctive dip at the star location, corresponding closely to the 18.7 μm observed image.

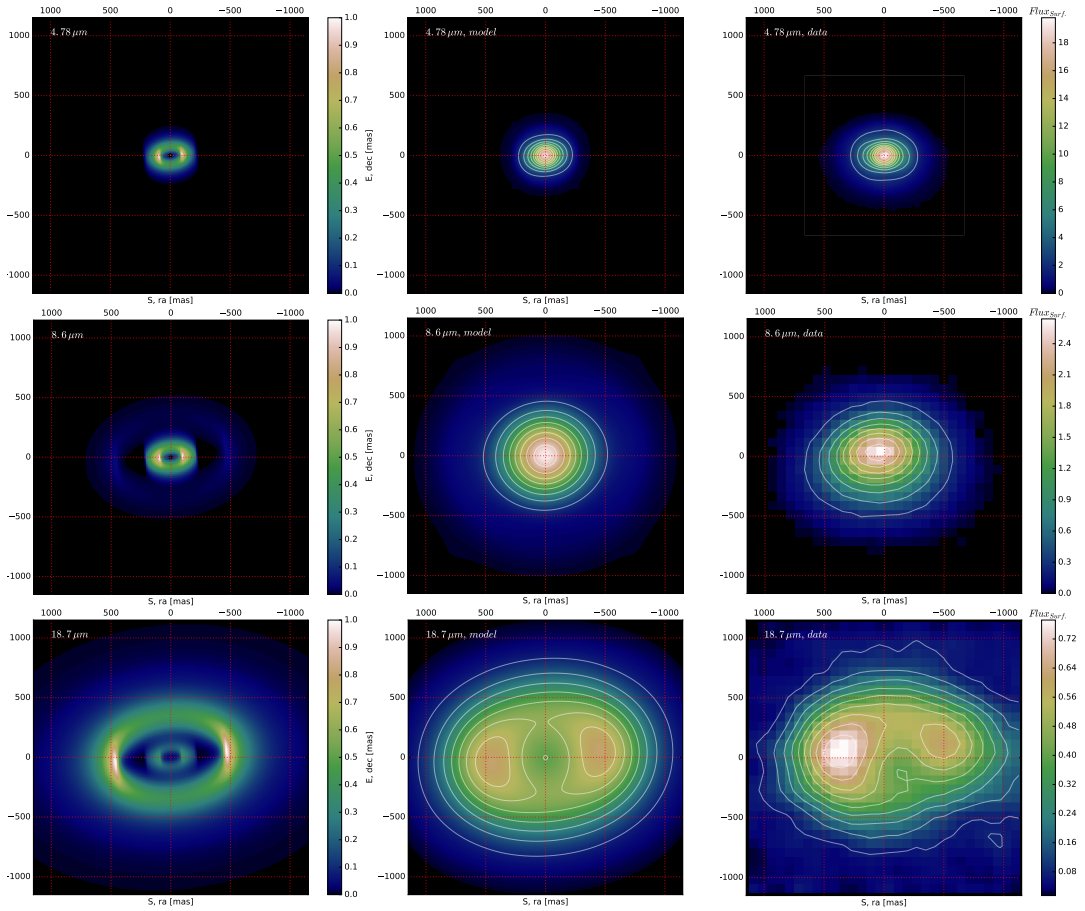

Figure 3.23: Synthetic-images (left and middle columns) and data-images (right column) at wavelengths 4.78 μm (Mp-band, top row), 8.6 μm (middle row) and 18.7 μm (bottom row). Left-column images are shown in arbitrary flux (the central-star being removed). Synthetic-images in the middle column are convolved with a 8.2 m telescope PSF and shown in the same color-scale of the observed data-images seen on the right column. Middle and right columns color-scale are fluxes per square-arcsec, normalized to the total flux of the disk, i.e. fraction of the total disk surface brightness. Data-images are taken from this work (Mp-band) and Geers et al. (2007a) (8.6, 18.7 μm). Iso-contours are overlaid at the color-bar tick-values.

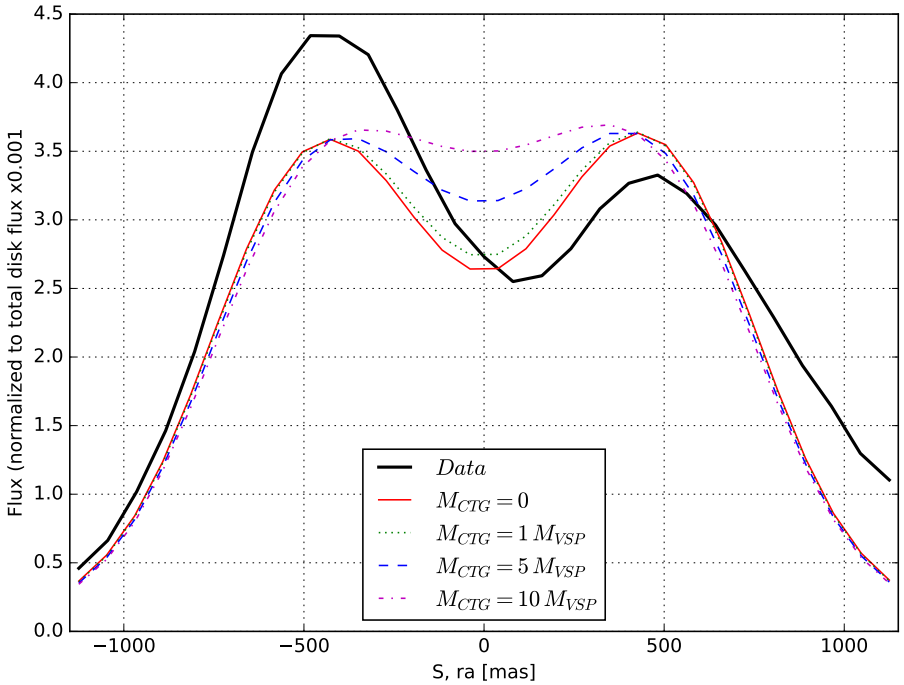

Figure 3.24: Cuts along the semi-major axis of the data-image (thick black line) at 18.7 μm and of the synthetic-images at the same wavelength and computed for an increasing amount of Classical Thermal Grains (CTG) in the VSP ring (0, 1, 5 and 10 M_{VSP} worth of CTG). Each flux-profile is normalized to the integrated flux of the disk in each image.

When the amount of classical thermal-grains increases, the inner-ring becomes brighter due to the efficiency of silicates grains to radiate at 18-19 μm. The central dip progressively disappears until the flux-profile is nearly flat, for a thermal-grains mass of $\sim$ 10 M_{VSP}.

Note that the VIS2 data fitting was not affected by the adding of Classical Thermal Grains (CTG), which emit a negligible amount of flux in Ks-, Lp- and Mp-band. Indeed, the emission of such CTG is mostly visible through the emission "bumps" of the silicate grains, at $\sim$ 9.5 and 18 μm. Until 5 M_{VSP} worth of CTG in the VSP-ring, the fit to the SED do not show any variation. From 10 M_{VSP} however, the model starts to clearly over-estimate the SED fluxes between $\sim$ 8 and 15 μm. Refer to Section 3.7.3 for a discussion.

3.6 Closure phases morphology

T3 are especially robust to atmospheric turbulence and optical aberrations, see Section 2.2.2. They are however in essence only sensitive to asymmetries: a point-symmetrical structure would lead to null T3 signal. As a consequence, an equal-

brightness binary star would not produce any T3 signal either.

In the data, T3 at all epochs vary between -12 and +9° in Lp-band, -18 and +15° in Mp-band, and slightly less in Ks-band. This highlights that strong asymmetries exist in the IRS-48 disk, at all wavelengths and epochs. T3 calculated on the radiative transfer model-image in all bands merely reach 0.5°; a disk alone does not explain the T3 data.

3.6.1 Modelling

N point-sources are fitted to the T3 data in order to highlight the main locations of the asymmetries in the disk. Such simplistic models allow analytical, hence fast, fitting to the data.

Six analytical models are used: from one to three point-sources in addition to the central star, either with or without the disk modeled with MCFOST. The central star is set as a reference to a flux of 1 and in the middle of the field. Each point source is described with three parameters: 1) angular separation to the central-star within [20, 300] mas, 2) position angle (East of North) within [0, 360]°, 3) relative flux within $[\frac{1}{200}, 1]$ stellar flux.

The disk is scaled and has its flux normalized with respect to that of the central star. It is treated as a "background image" on which T3 are measured at the (u,v) coordinates of the data. Complex visibilities from each unitary model-object are added together and T3 values for the global model are obtained from the phases of the complex visibilities at the (u,v) coordinates of each T3 triangle.

The complex visibility $\widetilde{\mathcal{V}}$ at the (u,v) coordinates and for wavelength λ for N point-sources is obtained from Eq. (2.27):

$$\Big(1+\sum_{i=1}^{N} f_i\Big)\ \widetilde{\mathcal{V}} = 1+\sum_{i=1}^{N} f_i\ \exp\Big(-\mathbf{j}\frac{2\pi}{\lambda}\ (U\ \delta_i\ +\ V\ \alpha_i)\Big), \tag{3.7}$$

where λ is the central wavelength of the band. δ_i, α_i are the angular separation and position angle (projected along declination and right ascension axes) of the i^{th} point-source with respect to the central star, and f_i is its the flux ratio.

The error-bars on the data are scaled using an additional variance, fitted together with the model, as presented in Section 2.3.3.1.

In order to compare models, the BIC as described in Section 2.3.4 is calculated at the maximum likelihood of each model-fitting. The relative probability of all models is computed with respect to the null hypothesis: a unique central star without any disk using. The LR-test is carried from Eq. (2.36):

$$LR_{Model/null} = \exp\left(\frac{BIC_{null}-BIC_{Model}}{2}\right) = \frac{1}{n^{3N}}\frac{\mathcal{L}_{Model}\ |_{max}}{\mathcal{L}_{null}}, \tag{3.8}$$

where N is the number of point-sources in the model.

3.6.2 Results

The relative probability is computed for all models on each of the six datasets; it is tabulated in Table 3.11. All six datasets except Lp-band epoch 3 favor the 2 point-source model rather than the 0, 1 or 3 point-source models, and all models favor the presence of a disk over a disk-less star (with the exception of Ks-band epoch 1 where the relative probabilities of a star with and without a disk are nearly identical). Since the fits on all T3 datasets were performed independently, there is a very clear statistical significance for a model that comprises the disk and two additional point-sources. Note that given the relatively low flux from the point-sources compared to that of the central star and the disk altogether, the additional two point-sources do not impact significantly the fit of the radiative transfer disk model on the VIS2 data.

Finding the most probable model among several does not however ensure that the fit, hence the model, is satisfactory. Table 3.12 shows that the additional systematic error $\sigma_{systematic}$ in Ks- and Lp-band is $\sim 0.8°$, and reaches 4° in Mp-band. These uncalibrated systematic errors are consistent with previous performance and slightly worse than SPHERE-SAM mode ($\sim 0.5°$, SPHERE SAM commissioning team, private conversation). This table also shows that on all datasets, the RMS of residuals calculated using $\sigma_{i,total}$ is very close to unity, meaning this model does not under- or over-fit the T3 data. The average of residuals is only a fraction of unity, which denotes only a slight deviation from normally distributed residuals.

The results for the maximum likelihood parameter estimation for the favored model with a disk and two point-source are tabulated in Table 3.12. Although point sources were free to take any positions and fluxes, the parameter estimation locates both point sources at a consistent spot through all epochs and wavelength. The first point-source is $\sim$ 105 mas on the west of the star with a contrast ratio of $\sim$ 3.3 mag in L-band; the second point-source location is somewhat noisier due to its proximity to the star although still consistently found at $\sim$ 45 mas on the north-east with a contrast ratio of $\sim$ 2.5 mag in L-band. These locations correspond closely to the inner-rim of the 50° inclined VSP-disk.

3.6.3 Point-sources characterization

Fitting point-sources to T3 data is equivalent to finding the photo-center of asymmetrically emitting regions; it does not constrain their size nor shape. Instead of point-sources, additional fits were carried using uniform-disks, Gaussian blobs and two-dimensional Gaussian blobs, see their definitions in Table 2.2. However, the data was not able to constrain well the additional parameters: the point-sources are mostly unresolved (i.e. spatial extension $\lesssim$3 AU).

3.6.3.1 Color-temperatures

The color-temperature of both point-sources at epoch 1 was determined using their contrast ratios in Ks-, Lp- and Mp-bands. A black-body behavior was assumed, con-

Table 3.11: Logarithm of the relative probability for each model and all datasets with respect to the null hypothesis of a single unresolved star without disk. The highest value the better. A negative value tells that the model performs worse than the null hypothesis. Bold values highlight the most probable model for each of the dataset. The relative probability values for different datasets cannot be compared between each-other.

Model	NULL	1PS	2PS	3PS
Ks epoch 1, n=60				
S	–	-1.16	**4.68**	-0.70
S+D	0.01	-1.36	**4.64**	-0.02
Lp epoch 1, n=60				
S	–	84	178	166
S+D	-0.46	96	**223**	223
Mp epoch 1, n=30				
S	–	12.4	12.2	4.6
S+D	-2.8	15.1	**15.3**	10.2
Lp epoch 2, n=30				
S	–	32	72	65
S+D	-0.25	38	**108**	87
Lp epoch 3, n=45				
S	–	52	113	131
S+D	-0.21	60	146	**185**
Lp epoch 4, n=60				
S	–	51	176	227
S+D	0.06	59	**215**	210

NULL≡ Null hypothesis i.e. single star without disk
D≡Disk model-image in the corresponding band
PS≡Point source model-object.
All models including the null hypothesis incorporate the additional error-variance parameter.

Table 3.12: **Top Table**: Overview of the quality of the T3 data fit, for all datasets. The maximum likelihood estimation of the additional error term (col. 2) is close to the average data random errors of the data (col. 1), leading to a total resulting error (col. 3, see Eq. (2.33)). The RMS of residuals remains close to unity while its average close to zero.
Two Bottom Tables: Maximum likelihood estimation of the point-sources parameters for the most probable model, consisting of two point-sources in addition to a central star with the disk found in the radiative transfer of VIS2 data fitting, for all datasets.

Data set	$\langle\sigma_{i,rnd}\rangle$ (°)	$\sigma_{sys.}$ (°)	$\langle\sigma_{i,tot.}\rangle$ (°)	$RMS(res._i)$	$\langle res._i\rangle$
Ks epoch 1	1.6	0.86 ± 0.17	1.82	0.97	0.35
Lp epoch 1	0.27	0.68 ± 0.17	0.73	1.01	0.20
Mp epoch 1	1.9	4.0 ± 0.6	4.5	1.00	0.10
Lp epoch 2	0.44	0.63 ± 0.23	0.77	0.97	-0.21
Lp epoch 3	0.25	0.86 ± 0.11	0.89	1.00	0.18
Lp epoch 4	0.26	0.97 ± 0.11	1.0	1.00	0.26

	First Point-Source		
Data set	Sep. (mas)	PA (°)	Δmag
Ks epoch 1	69 ± 5	16 ± 8	4.8 ± 0.3
Lp epoch 1	41^{+9}_{-3}	41 ± 4	2.7 ± 0.5
Mp epoch 1	39 ± 9	52 ± 12	$1.8^{+1.0}_{-0.6}$
Lp epoch 2	34^{+15}_{-2}	47 ± 4	$1.8^{+1.7}_{-1.0}$
Lp epoch 3	39^{+10}_{-2}	44 ± 4	$2.3^{+0.7}_{-0.5}$
Lp epoch 4	50 ± 4	43.3 ± 1.1	2.72 ± 0.22

	Second Point-Source		
Data set	Sep. (mas)	PA (°)	Δmag
Ks epoch 1	101 ± 4	281 ± 4	4.9 ± 0.3
Lp epoch 1	105 ± 2.5	270.3 ± 1.1	3.35 ± 0.12
Mp epoch 1	89 ± 11	269 ± 4	2.9 ± 0.3
Lp epoch 2	111 ± 2.5	275.1 ± 1.3	3.20 ± 0.20
Lp epoch 3	109 ± 3	276.5 ± 1.3	3.40 ± 0.05
Lp epoch 4	119 ± 4	284.6 ± 1.1	3.25 ± 0.06

strained by the effective temperature and the radiating surface, assumed circular and defined by its radius. *emcee* was used to maximize the likelihood of the temperature parameter T taken in [100, 10000] K and the logarithm of the radius parameter R taken in [0.1, 40] $R_\odot$.

The maximum-likelihood color-temperature found for the first point-source is $\sim$ 1350 K, see Figure 3.25. However, one-sigma error-bars yield several hundreds of Kelvin because of large error-bars on the point-source contrast ratios obtained with T3 data. Still, this temperature corresponds closely to PAH-temperatures found with radiative transfer modelling at the unprojected point source location, $\sim$ 12.5 AU; refer to Figure 3.22 for temperature maps.

The second point-source shows a somewhat lower temperature, most likely of $\sim$ 1000 K. Here again, one-sigma errors-bars yield several hundreds Kelvin: from 600 to 1300 K, refer to Figure 3.25.

3.6.3.2 Orbital movements

Due to its close proximity to the star, $\sim 0.5\lambda/B_{max}$, the angular separation of the second point-source is particularly degenerate with its contrast ratio. However, the position angle remains mostly unaffected and shows no significant angular movement with epochs. Discrepancy on the epoch 1 locations of the second point-source between the different bands may be due to several factors, given that fitting T3 data only gives the location of the photo-center of an asymmetrically bright region. First, this location may change with wavelength due to the intrinsic nature of the asymmetry: a clump of segregated grains, an arm of material showing decreasing temperatures as it spirals out from the star, or visual effects of optical depth, opacity and shadows. Second, the data – i.e. the sample size and the error-bars – allowed to fit only two point-sources. This second point source may however well be the (poorly defined) photo-center of a more complex system of asymmetries, unresolved by the data.

The first point-source in Lp-band shows a clear rotational movement through different epochs. This movement is unlikely related to the (u,v) field rotation which shows a much smaller variation over the four epochs (min-max $\sim 2°$); also, this movement is not monotonic with epochs. The point-source movement is compatible with a circular orbit in the VSP-disk and in the same direction as the gas kinematic found by Brown et al. (2012a); Bruderer et al. (2014). If one assumes a circular orbit, the origin of the over-brightness is located at a radius of $\sim$ 14.2 AU, and a height of $\sim$ 3.5 AU (see paragraph below). This over-brightness location corresponds to the densest region of the VSP-ring in the radiative transfer modelling, as Figure 3.19 tells. However, the nature of the over-brightness is not clearly constrained. It may either be 1) an orbiting over-density of VSP material, or 2) a luminosity and opacity effect: the central star may be shifted from the center of the disk due to the presence of a massive companion, hence irradiate asymmetrically the inner-rim of the VSP-ring.

Figure 3.26 shows the Lp-band point-source location in the disk as well as two circular-orbit solutions. The first solution is an orbit with a semi-major axis of a=14.2

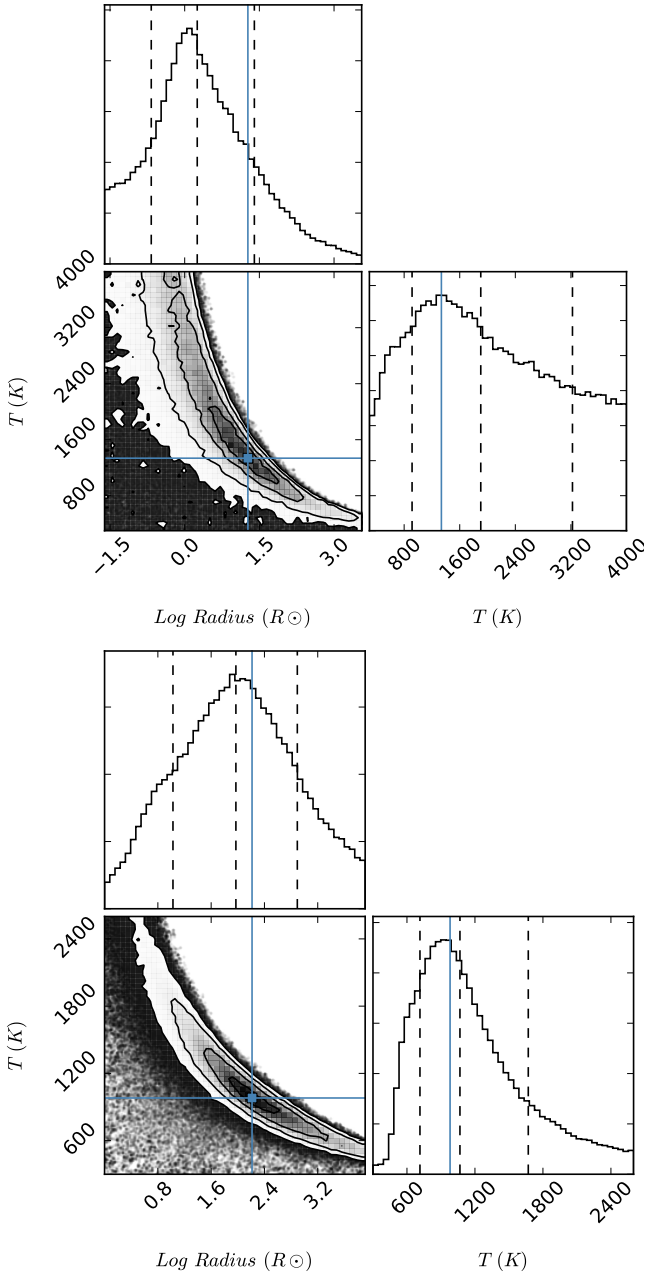

Figure 3.25: Corner-plots of the color-temperature fits for each point-source. First point-source is on top, second one is on bottom. The correlation between both parameters is very large as seen in the two-dimensional histogram. Radii and effective temperature are not well-constrained because of the large errors on contrast ratios of the point-sources.

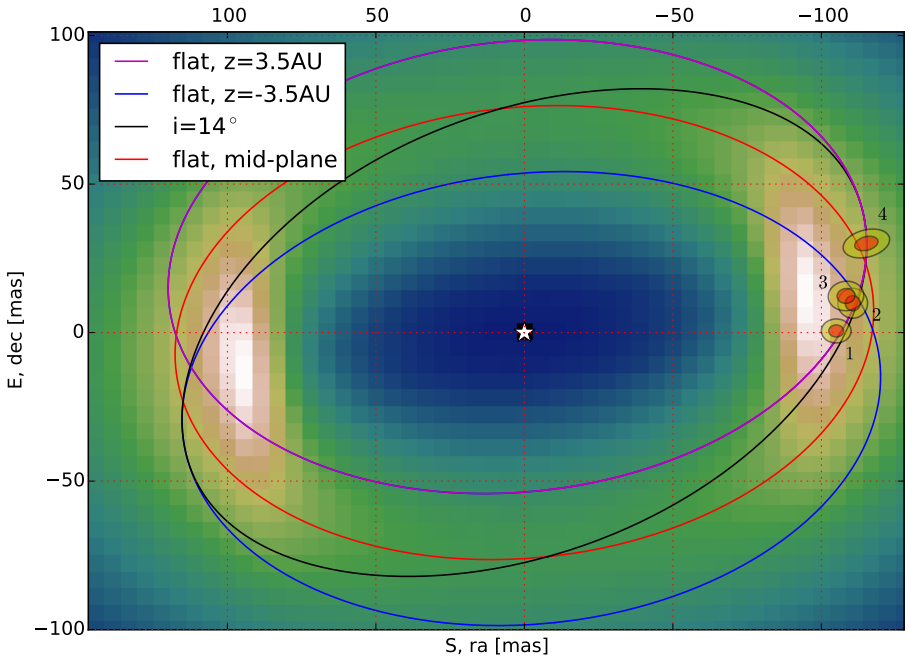

Figure 3.26: Locations of the first point-source in Lp-band through the four epochs (noted 1 to 4). Red and yellow ellipsoids are 1- and 2-sigma uncertainties for these locations, respectively. The background image represents the Lp-band model-image of the radiative transfer disk, and is shown in linear scale; the star was subtracted. Purple, red and blue lines represent a circular orbit of semi-major axis a=14.2 AU for a body located 3.5 AU above the mid-plane, in the mid-plane and 3.5 AU below the mid-plane, respectively. The black line represents a 14° inclined circular orbit with same a.

AU. It lies flat 3.5 AU above the mid-plane (hence inclination $\sim 0°$). This suggests that either the clump of material producing the over-brightness is mostly pressure-supported, or that only the top layer of it is detected. This latter option implies that the center of mass and the photo-center of the clump are not co-located; this is not consistent with the low optical thickness of this disk (Figure 3.21). The second solution is an inclined orbit, i=14°, with a similar semi-major axis, a=14.6 AU. This latter solution would suggest that the over-brightness arises from a clump of material and that it is mostly gravity-dominated in its orbital movement around the star.

In both orbital solutions, the over-brightness moves at a sub-Keplerian velocity: 8.1 km.s^{-1} in average over the four epochs (similar values are obtained for other intervals, between epochs 1-3 and 3-4); the total orbital period at this pace is $\sim$ 52 years. The theoretical Keplerian velocity at such distance given the stellar mass is $\nu = \sqrt{G \times m_*/r}$=12.5 km.s^{-1}.

Dullemond et al. (2007) suggested that PAH and VSG do not settle compared to classical thermal grains as soon as the disk shows some turbulence. The VSP species in the inner-ring do not have a sufficient density to have a pressure-supported behavior; they are expected to be highly coupled to the gas given their very low mass and sizes. Although previous works modelled a gas-depletion in the first $\sim$ 20 AU, it is likely that some gas is still present in this ring, in order to provide the "structure" that holds and supports the PAH and VSG movement.

3.7 A new interpretation of IRS-48

The previous chapters highlighted major changes in the central star of IRS-48, estimated to be brighter and younger, and in the disk morphology: the inner-most disk at $\sim$ 1 AU no longer exists, a tenuous ring of PAH and VSP is stable between 11-26 AU and shows movement over a two-year period, and the outer-disk mass is decreased to 3 M_{Earth}. This section will discuss some of the consequences of these findings.

3.7.1 Age and nature of the disk

Finding a brighter star, hence younger (4.2 Myr), partly solves the evolutionary puzzle on this target.

First, the discrepancy between the molecular Ophiuchus cloud age of $\sim$ 1 Myr (Luhman & Rieke 1999) and the stellar age is widely decreased, even though a fair difference remains that cannot be explained to date. IRS-48 might have been part of an earlier star-formation episode in Ophiuchus, as postulated by Brown et al. (2012a). This however does not seem consistent that star-forming regions tend to show similar age and initial compositions, see Section 1.2.1.

Second, although all disks are unique in their evolution, the median disk lifetimes of 2-3 Myr (see Section 1.3.3.5) strongly pushes IRS-48 towards a 4.2 Myr than a 8 or 15 Myr transition disk. Indeed, IRS-48 clearly displays several of the five "transition observational facts" presented by Wyatt et al. (2015) (see Section 1.3.3.5):

- a total depletion of dust in the innermost-region, (their stage 1)
- a partial depletion of mm-size grains; the modelled $M_{dust}\sim$ 3-4 M_{Earth} is only a factor of a few over the proposed 1 M_{Earth} limit, (their stage 2)
- a total processing of hot dust up to 11 AU, while only a minimal amount (1.2 to 7×10^{-4} M_{Earth}, depending on CTG, see Section 3.5.5) of hot dust exists between 11 to 26 AU, (their stage 3)
- a partial gas depletion inside 55 AU, and possibly total depletion inside $\sim$ 20 AU, (their stage 4)

This implies that the evolutionary stage of IRS-48 is more advanced than what was previously thought, in the middle of its transition. When one places IRS-48 into a larger disk sample, see Figure 3.27, one sees that its 12 μm excesses pins it down to the edge of the luminous-NIR-excess group of disk-objects (top-left sub-plot of the latter figure).

IRS-48 shares many similarities with HD 141569, a disk believed to be on the verge of becoming a debris-disk (Wyatt et al. 2015): 5 Myr B9.5 star, detection of extended CO gas, bright PAH emission, 0.7 $M_\odot$ of sub-mm dust, warm disk-component at $\sim$ 17-50. HD 141569 however show a lower IR-excess at 12, 22 and 70 μm than IRS-48: HD 141569 is most probably slightly ahead of IRS-48 in the process of transiting to a debris-disk.

Third, a younger age for IRS-48 together with a later disk-evolution stage is consistent with the fact that massive stars erode their disk at a larger pace than solar-type stars, as highlighted in Section 1.3.3.5.

3.7.2 Disk morphology, stellar binarity and planetary formation

3.7.2.1 30 AU CO gas-ring

Brown et al. (2012a); Bruderer et al. (2014); van der Marel et al. (2016) find a $\sim$ 30 AU CO-ring with small radial extent, compatible with a Keplerian velocity for a 2.0 $M_\odot$ star with an inclination of 50°. In addition, they find a gas-depleted region inside $\sim$ 20-25 AU.

Although the VIS2 data is blind to gas – consequently the new model does not incorporate any gas structure – the new IRS-48 model and the later disk-evolution stage postulated remain qualitatively compatible with these previous findings. Indeed, a photo-evaporation-dominated disk would show a clear depletion of gas and dust in the inner tens of AU. The VSP-ring from 11 to 26 AU acts as a very efficient shield of UV-radiation, effectively protecting gas further out from aggressive photo-evaporation. A thin ring of gas at 30 AU– and potentially as close as 26 AU – appears to be a consistent consequence of such configuration.

Gas around young stars should rotate with a sub-Keplerian velocity rather than Keplerian, as highlighted by Williams & Cieza (2011) to being the root-cause of the

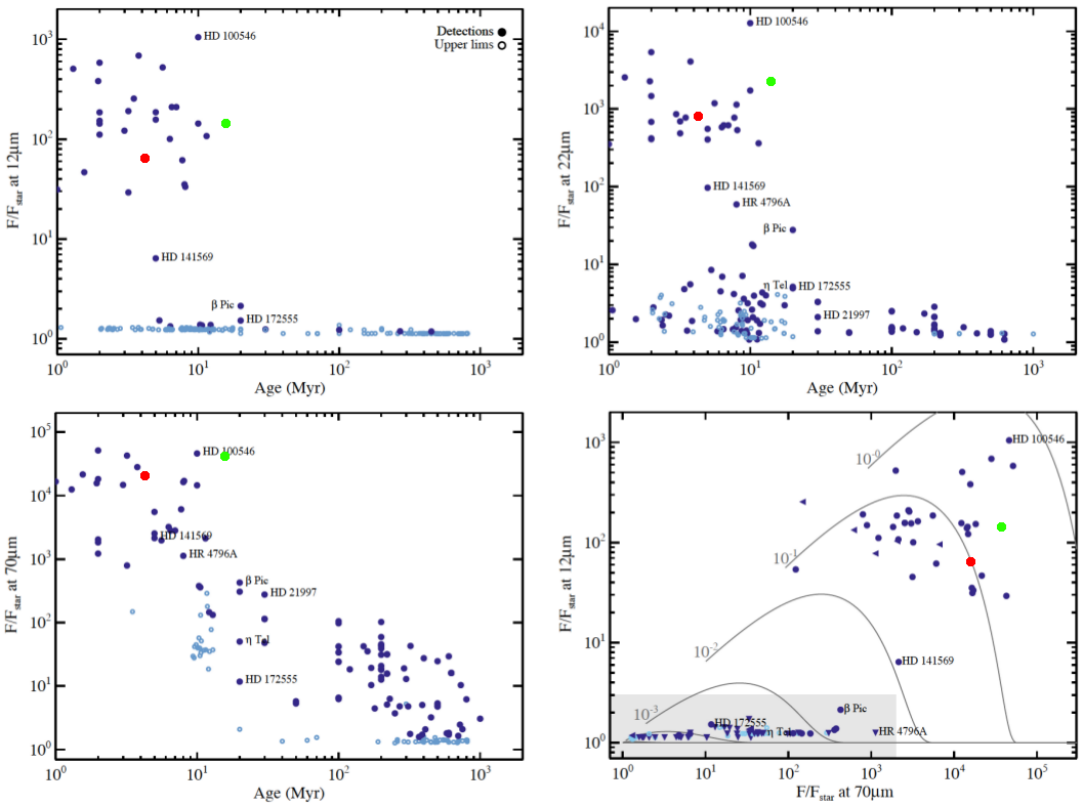

Figure 3.27: Ratio of the total observed flux to stellar fluxes (i.e. IR excess), at 12 (**top-left**, WISE), 22 (**top-right**, WISE) and 70 μm (bottom-right, Spitzer & Herschel), as a function of age. **Bottom-right** shows the IR excess at 12 μm as a function of the IR excess at 70 μm, where the age of the target was marginalized. Filled blue circles are detections; open light circles are upper limits; red dots correspond to IRS-48 (new model) and green dots to the *alpha* model. Initially in Wyatt et al. (2015), their Figure 1; valid for A-type stars.

meter-barrier mystery in planetary formation and grain-growth theories. Brown et al. (2012a) find a 2 $M_\odot$ in the *alpha* model from the hypothesis that the 30 AU CO-ring possesses a Keplerian-rotation; this however is a lower limit. The brighter star (hence heavier $\sim$ 2.5 $M_\odot$) of the new model is consistent with this finding; it virtually increases the theoretical Keplerian velocity expected at 30 AU from 7.7 to 8.6 km.s^{-1}.

3.7.2.2 VSP-ring inner truncation, binarity

Ghez et al. (1993); Leinert et al. (1993); Reipurth & Zinnecker (1993) detect an over-abundance by a factor of two of binaries among the young stars in the Taurus region when compared to the results for the Main Sequence (MS) stars. Although further studies with larger populations slightly lower this over-abundance, it appears clear that YSOs have a binarity over-abundance compared to MS stars, to a degree that is however still under discussion as underlined by Ratzka et al. (2005); see Section 1.2.3.

Our data resolves a somewhat sharp truncation of the inner-rim at 11 AU. Besides photo-evaporation and accretion, a stellar companion with semi-major axis of order a few AU would reproduce such truncation located at 11 AU (Artymowicz & Lubow 1994). No observation already performed in the visible or infrared, had the sensitivity to resolve such binary system. According to the YSO evolutionary models of Siess et al. (2000), a K0-type star (5400 K) of 4.2 Myr has a luminosity of about 7.5 $L_\odot$ and a mass of $\sim$ 2.2 $M_\odot$. This luminosity remains small compared to that of IRS-48 (42 $L_\odot$): any stellar-type cooler than K0 would remain a nearly invisible companion for visible and infrared instruments, especially at $\sim$ 25 mas typical spatial separations.

An indirect way to detect late-type companions is to check if such A-type stars emit in Xray. Stelzer et al. (2006b,a) show that, given that A-type stars are not expected to have a corona and emit Xray, a high-energy emission from these stars is generally associated to late-type binarity. In the case of IRS-48, neither ROSAT and XMM archive data nor Chandra (Imanishi et al. 2001) showed Xray emission at this location. Although soft Xray would be absorbed by interstellar absorption, hard and extreme ones should be detected. Indeed, several very young stars (even Class I) are detected in Xray in the core-region of ρ Oph by Ozawa et al. (2005). Given the completeness of several Xray studies as showed in their Figure 6, and the A_v =12.9 mag for IRS-48, a 4.2 Myr old companion with $T_{eff} \gtrsim$3000 K (M6 star and brighter) should already have been detected around IRS-48 using Xray.

Also, a heavy companion, $\gtrsim$1 $M_\odot$ (corresponding to a star brighter than $\sim$ K6 stellar type on the 4.2 Myr isochrone) would reveal its presence through its mass, and the Keplerian velocities field it imposes on its circumbinary disk. Brown et al. (2012a) find a 2 $M_\odot$ to explain a Keplerian rotation of a gas-ring at 30 AU. Although this mass is lower-limit given that the gas-ring must have a sub-Keplerian velocity, IRS-48 does not likely have a bright and massive secondary star, which would set the total binary mass at above $\sim$ 4 $M_\odot$.

IRS-48 is most probably not a binary star. However, one (or several) low-mass companion with M$\lesssim$0.5 $M_\odot$ and L$\lesssim$0.01 $L_\odot$ would be qualitatively compatible with

Xray non-detection, CO 30 AU rotational velocity, and with the new model; it would provide a plausible explanation to the 11 AU VSP-rim truncation.

3.7.2.3 26-55 AU cavity

Both the presence of the outer-rim of the VSP-ring and the inner-rim of the outer-disk require the existence of an explanatory phenomenon. Based on the mm-asymmetry observed in the southern part of the disk, a 2 $M_\odot$ star and Hill radius estimates, van der Marel et al. (2013b) suggested the presence of a planet at 17-20 AU with $M \gtrsim 10$ M_{Jup}.

Dodson-Robinson & Salyk (2011) find that the outer edge of the gas-cavity created by a planet is expected at ~ 5 Hill radii r_H, defined by:

$$M_p/M_* = 3 \times (r_H/a_p)^3. \tag{3.9}$$

Pinilla et al. (2012) find that for planets $1 < M_{Jup} < 3$, the dust would accumulate at 7 r_H from the location of the planet. When one carries similar first-order Hill radius estimates with the disk-structure of the new model and a higher-mass star, one can speculate a $M_p \sim 3.5$ M_{Jup} planet at a radius of $a_p \sim 40$ AU. With these values, one obtains a dust-bump at 63 AU corresponding to the mm-dust asymmetry (van der Marel et al. 2013b), and at 17AU (at the center of the VSP-ring of the new model). One also finds gas densities peaking at 26 and 56 AU, possibly corresponding to the 30 AU CO ring and the inner rim of the outer disk, at 55 AU (all radii given as distances from the star). A schematic picture of the new IRS-48 disk morphology is showed on Figure 3.28.

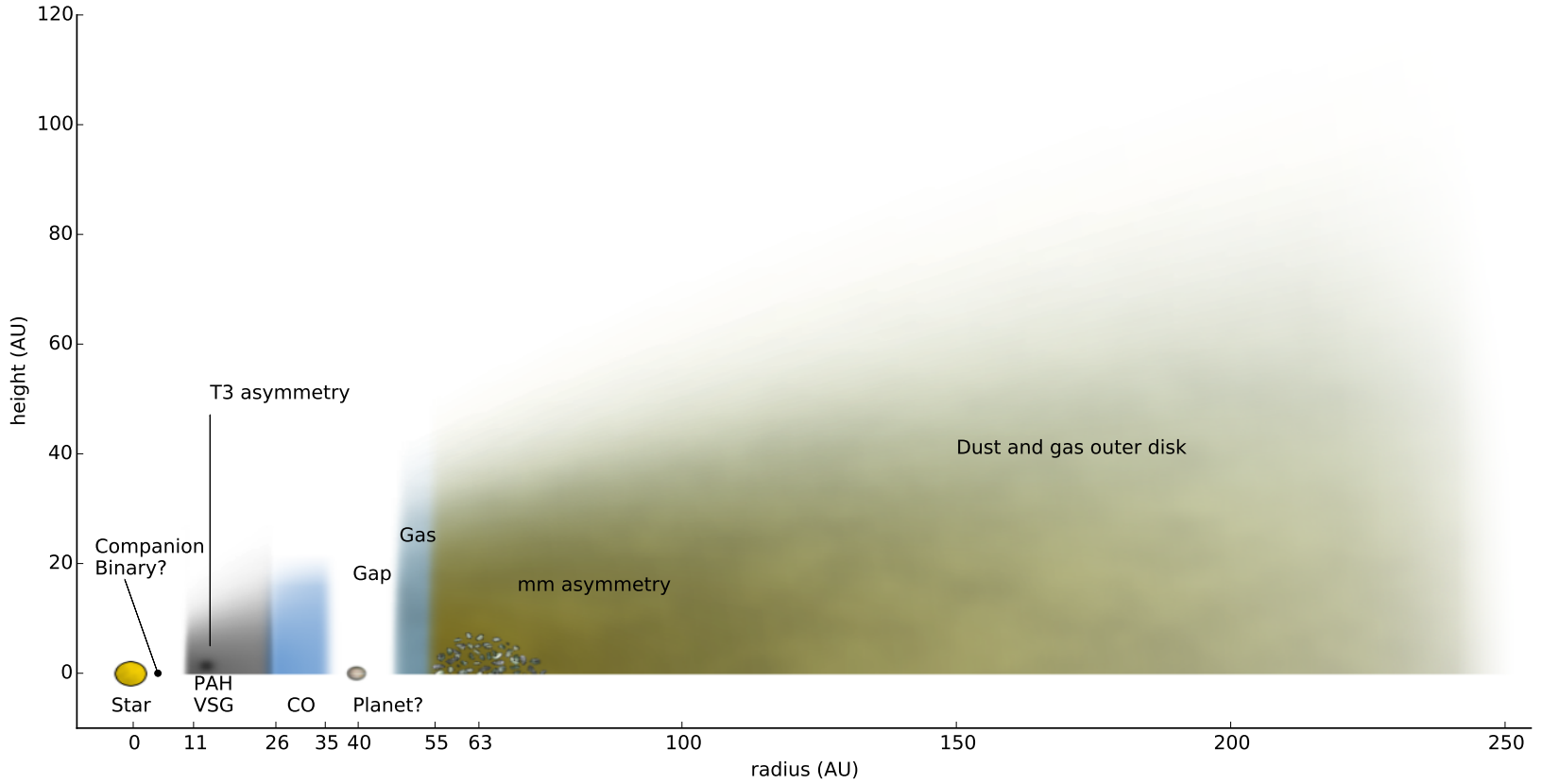

Figure 3.28: Schematic of the IRS-48 disk as presented in the new model. The outer-disk is from Geers et al. (2007a), the CO emission is from Brown et al. (2012a), the mm-asymmetry from van der Marel et al. (2013b), the inner 20 AU gas-depletion from Bruderer et al. (2014). The proposed gas dip from 35 to 50 AU is based upon Bruderer et al. (2014) findings on a first gas-depletion between 20 and 55 AU.

3.7.2.4 Accretion

Accretion was estimated at $\sim 3\times10^{-9}$ $M_\odot$/yr by Salyk et al. (2013); Follette et al. (2015) using $Pa\beta$ and $Br\gamma$ lines. This non-negligible accretion rate raises the question of the origin of such material, and seems well over-estimated compared to the available material in the *alpha* model (where one finds 8.0×10^{-12} $M_\odot$ dust in the inner-most disk, and 8.0×10^{-10} $M_\odot$ PAH until 50 AU), or in the new model (0.37 to 2×10^{-9} $M_\odot$ VSP at 11-26 AU, depending on the amount of "hidden" CTG). Moreover, the disk was found to be partially gas-depleted inside 55 AU and fully depleted inside $\sim$ 20 AU, which puts a very hard constrain on how much material is to be found in the first tens of AU, available for accretion.

Replenishment of dust and gas from the outer disk, or collision of large dust grains, may be possible scenarii to explain the accretion value found. However the replenishment process seems too small to explain the current structure. Indeed, one can estimate the dust- and gas-mass that should be detected inside the outer-disk through the free-fall time of a particle of dust from the inner-rim of the outer-disk, at R=55 AU using (see Section 1.2.1):

$$t_{ff} = \frac{R^{3/2}}{\sqrt{8GM_*}}. \tag{3.10}$$

The numerical value gives t_{ff}=15 years for a 2.5 $M_\odot$ star, and t_{ff}=1.3 year for a particle located at 11 AU.

Given the $\sim 3\times10^{-9}$ $M_\odot$/yr accretion rate, and the fact that a particle may take $\sim$ 14 years between the inner-rim of the outer-disk at 55 AU and that of the VSP-disk at 11 AU, one should detect $\sim$ 14*3×10^{-9}=4×10^{-8} $M_\odot$ worth of available material for accretion in the 11-55 AU region. Such amount is only attained with a VSP-ring containing 5 M_{VSP} worth of CTG, and a gas-to-dust ratio of at least $\sim$ 20.

This estimation is however very conservative in that the free-fall time are only a strict minimum estimate. One indeed expects viscous friction with gas, i.e. the CO ring at 30 AU, angular momentum and magnetic fields to considerably increase the time required for an outer-disk particle to replenish the inner-ring. Also the loss of accretion material in photo-evaporation, grain-growth or radiation pressure is not taken into account.

Unless some extremely efficient channeling of material through the action of a companion is taking place, the accretion rate is over-estimated. In this case, the IRS-48 disk-dissipation is undoubtedly dominated by stellar-effect such as photo-evaporation and radiation pressure.

3.7.3 PAH and VSG evolution

3.7.3.1 Abundance of VSP vs. CTG

Dullemond et al. (2007) suggested that PAH and VSG do not settle well compared to classical thermal grains, and found that, under conditions of low turbulence, strong

PAH emission-features can "hide" a substantial amount of settled thermal silicate grains.

It was indeed possible to add up to five times the mass of the VSP-ring worth of settled classical thermal grains the VSP-ring, without affecting the VIS2 data nor the SED fits. Adding more of these grains in the close vicinity of the star affects the MIR emission in such a way that the 18.7 μm model-image does not display the central dip with two bright spots at $\pm$55 AU from the star like the data-image (Figure 3.23). Instead, a contiguously bright region lies along the whole semi-major axis of the disk. This result shows that the VSP-ring most probably does not contain more thermal grains than $5\times M_{VSP} \sim 2\times10^{-9}$ $M_\odot$ $\sim$ 6e-3 M_{Earth}.

The presence of PAH in many circumstellar disks reveals that in these objects the dust coagulation process was apparently not effective enough to remove these species from the disks, or that some other process continuously replenishes PAH grains (Dullemond et al. 2007). Out of theoretical and laboratory works, Jochims et al. (1994) showed that the largest and most regular PAH species are extremely stable to destructive radiations, i.e. photo-evaporation. Indeed, large PAH of 20-30 carbon atoms will preferably relax through PAH emission in bands rather than photo-fragmentation. As a comparison, one of the most stable PAH species, circumcoronene C54H18, has a typical size of 4.87 Å. PAH used in the new model span 4 to 10 Å (20 to 100 carbon atoms); VSG span 10 to 20 Å (100 to 1000 carbon atoms), see Tielens (2008): the PAH species in the new model are expected to be extremely robust to photo-evaporation.

Geers et al. (2006) find a PAH-to-dust mass fraction of 6% based on the abundance of 5×10^{-5} carbon atoms locked in PAH molecules per H nuclei. Tielens (2008) (Table 2) reports an abundance of 29×10^{-6} Carbon nuclei locked up in grains smalled than 30 Å, per H nuclei. If one updates the VSP-to-dust estimate using a ISM gas-to-dust ratio of 100:1, assuming that gas is predominantly composed of H nuclei, and that PAH and VSG are mostly C atoms, one finds a VSP-to-dust mass fraction of 3.5%. The new model shows a VSP-to-dust mass fraction $>$20% (since $M_{CTG}<5\times M_{VSP}$), in the VSP-ring. This highlights a depletion of a factor at least $\sim$ 5-6 of the classical dust grains to very small particles ratio, compared to the ISM value, in spite of grain growth processes expected in young disks.

3.7.3.2 VSP disappearance vs. creation rates

In order to understand the VSP-ring, one shall study the disappearance rate of VSP through grain-growth, radiation pressure or inward drift/accretion, versus the rate of some replenishment process, e.g. the collisional destruction of larger grains or inward drift from an outer reservoir.

There is presently little experimental data on the size distribution resulting from sub-micrometer grain-grain collisions. Tielens (2008) report that theoretical studies on grain-grain collisions result in a mass distribution with power index of $\sim$-3.3. Although the minimum size is not constrained in this later study, given the layered structure of graphitic materials it is expected that the smallest fragments likely are small, two-

dimensional structures (e.g. PAH-like molecular species). Further processing by atomic reactions, as well as UV processing, may then quickly transform these species into compact PAH (Tielens 2008). In the frame of interstellar medium shocks, (Jones et al. 1996) calculate that the catastrophic destruction (i.e. complete destruction of the grains, rather than cratering) of a 1000 Å grain by a 50 Å grain needs a critical velocity of approximately 75 km.s^{-1}; larger grains need larger collisional energy. They also conclude that interstellar grain-growth processes shall be much more efficient than catastrophic destruction in order to explain the observation that most of the interstellar dust comes in grains larger than $\sim$ 1000 Å.

The orbiting velocity of the first point-source in the VSP-ring around IRS-48 is $\sim$ 8.1 km.s^{-1}, and the Keplerian velocity at that distance is 12.5 km.s^{-1} for the 2.5 $M_\odot$ star (see Section 3.6.3.2). Moreover, A0 stars do not generally show strong winds or emit high-energy radiations like B-type stars. It seems very unlikely that IRS-48 possesses a high catastrophic collision rate within its VSP-ring at 11-26 AU. It is therefore expected that PAH and VSG cannot be replenished easily through grain-grain collisions in the VSP-ring, despite the possible co-located reservoir of classical thermal grains up to five times the mass of VSP.

The radiation pressure estimate of the star can be achieved by calculating the stellar constant W$\sim$ 45,000 W.m^{-2} at 1 AU. The radial acceleration from radiation pressure produced on a particle at radius r is obtained with a_p=W S_{eff} c^{-1}.r^{-2}, with S_{eff} the effective cross-section of the particle and c the speed of light in vacuum. It is found to be 39 (resp. 42, 17) times larger than the gravitational potential (G.M_*.r^{-2}) on the neutral PAH particles (resp. ionized PAH, VSG). This probably shows that the inward drift of such small particles is very low given the high wind from the central star. The previous star with radius 1.8 $R_\odot$ shows a somewhat lower but still overwhelmingly strong radiation pressure compared to gravitational potential: 16, 17 and 7 times larger in average for neutral, ionized PAH and VSG, respectively.

Chapter 4

Conclusion & Perspectives

The "paradox" is only a conflict between reality and your feeling of what reality "ought to be".

Albert Einstein

The improvements of instrument sensitivity and resolution over the last decade have provided circumstellar disk-evolution theories with an unprecedented wealth of data. ALMA, adaptive optics, NIR and visible interferometry have revolutionized the precise study of individual targets. This work makes use of new interferometric and spectroscopic measurements in the infrared, together with published mid-infrared images and spectral energy distribution (SED) fluxes from UV to mm-wavelength, to instruct a new comprehension of IRS-48, a young stellar object in the ρ Oph region known to possess an active circumstellar disk, and uncover part of the delicate balance of physical processes at stake.

The first chapter detailed theories and facts on circumstellar disks; their structure, their evolution and the key physical processes that drive their dispersal and planetary formation. The aim was to bring all necessary disk-related information to be defined for the chapters to come. It described general context on disks, the initial conditions and constraints that lead to disk formation, and the evolution and properties of disks once the stars have formed.

The second chapter brushed a broad picture of interferometry, incorporating most of the necessary concepts required to acquire and analyze interferometric data: physics theory, interferometric instrumentation, data acquisition specificities, and parametric-model fitting to the data. Interferometry was illustrated to be the answer to accessing resolutions which are out of reach of single-dish telescopes, although it also suffers from atmospheric turbulence. Instrumental aspects were presented through the specificities of several techniques and observables. A large fraction of this chapter was dedicated to the understanding and processing of the interferometric data, and introduced a novel fitting tool.

The main science chapter reports the first direct imaging of the full extents of a polycyclic aromatic hydrocarbon and very small grains ring in a young circumstellar disk. It also presented a revised model for the IRS-48 object in order to explain the rich and complex dust- and gas-environment observed from near-infrared to centimeter wavelengths. This models allows the setting of limits on how much silicates grains, hence replenishment, is to be expected in the polycyclic aromatic hydrocarbon and very small grains ring, leading to a paradox on the sustainability of such disk.

Radiative transfer modelling of the disk-structure and grains compositions converges to a classical-grains outer-disk from 55 AU with a revised mass of 3 $M_\odot$, combined with an unsettled VSG & PAH-ring, where the inner- and outer-rim are resolved: 11 and 26 AU. A brighter (42 $L_\odot$) hence larger (2.5 $R_\odot$, 2.5 $M_\odot$) central-star with modified extinction parameters (A_v =12.9 and R_v =6.5) accounts for the near-infrared flux observed in the SED: no inner-most disk at the $\sim$ 1 AU scales is needed. The revised stellar parameters place this system on a 4.2 Myr evolutionary track, much younger than the previous estimations, and in better agreement with the surrounding region and disk-dispersal observations. Using the closure-phases technique, two over-luminosities are found in the VSP-ring, at color-temperatures consistent with the radiative transfer simulations. One follows a sub-Keplerian circular orbit in the VSP-ring at a semi-major axis of $\sim$ 14 AU.

This work combined to previous Xray observations shows that the IRS-48 system is most probably not a binary star although it may however possess a companion that satisfies both constrains on mass ($\lesssim$0.5 $M_\odot$) and luminosity ($\lesssim$0.01 $L_\odot$).

The IRS-48 disk is found to be mostly void of dust-grains in the first 55 AU and shows that only very few settled thermal silicates can be co-located with the VSP-ring at 11-26 AU, with a depletion factor of at least $\sim$ 5-6 compared to classical interstellar dust-to-VSP abundances. The new morphology shows that 3.7×10^{-10} solar-masses (1.2×10^{-4} M_{Earth}) of a mixture of ionized and neutral PAH, and VSG, is located the VSP-ring and possibly up to 2×10^{-9} solar-masses (6.1×10^{-4} M_{Earth}) of additional classical thermal grains. This raises the question of whether accretion is still playing a dominant role in this object, or if IRS-48 is closer to the final evolution-stage of transition disks than previously estimated, when photo-evaporation dominates the disk evolution and eventually causes swift dispersal.

More than anything, the fact that the VSP-ring was observed to be consistently similar at a radius between $\sim$ 11-26 AU through the four epochs of observation spanning two years time, highlights that it is governed by a complex balance of physical processes. In order to remain observationally in-place, it must either be

1. Constantly replenished with high efficiency (see Section 3.7.2.4) from the outer-reservoir outside 55 AU, and possibly channeling triggered by the postulated 40 AU companion.

2. Kept in place as-is through:

   - the gravitational shepherding from additional companion(s) inside 11 AU,
   - the coating of large grains – unaffected by radiation pressure – by PAH molecules,
   - the substantial presence of gas in the VSP-ring despite the – somewhat medium-SNR – non-detection of previous studies.

4.1 Perspectives

In order to better understand this object, several dedicated observations could be attempted. First, high-resolution imaging or interferometry in the 10-20 μm window in order to superseed previous imaging data would allow a precise characterization of the silicate content of the VSP-ring. Such information would set a strict constraint on how much classical thermal grains this ring possesses and give critical information on the inner-disk material available for accretion.

Second, long baseline interferometry measurements of the inner-most regions of the IRS-48 system, to be carried in the NIR where the extinction is only moderate, compared to visible wavelength, could confirm the probable non-binarity of IRS-48 and investigate on the inner-most disk, found to be already dissipated. Such information would allow a direct characterization of the inner-system of IRS-48, and set constraints on the sublimation radius and on-going accretion.

Third, high-resolution ALMA observations with baselines longer than one kilometer can image IRS-48 down to a few AU. Characterizing the gas content in the inner 20 AU of IRS-48 is necessary to pin down the evolutionary stage of this object on its transition to becoming a debris-disk. This will effectively provide valuable information on a statistically poorly-populated process.

Fourth, SAM observations with NaCo, using a mask with higher (u,v) coverage than that of the current seven holes mask will give reach and unprecedented information on the structure of the VSP-ring. It will firstly allow an epoch-tracking of the two over-luminosities found in the VSP-ring to instruct their nature. Secondly, it will make possible the use of image reconstruction algorithms which are an independent and complementary method to the parametric-modelling of interferometric data.

Last, high-contrast coronographic techniques could search for the possible 40 AU companion (between 200 and 350 mas given the inclination). This could open whole new possibility to model the dynamical evolution of the IRS-48 disk.

This work showed that the new model of IRS-48 is believed to be one candidate of a very rare population of transitions disks at a medium evolutionary stage. The better understanding of the evolution of disks and eventually dispersal can at this stage only be achieved through a better and in-depth characterization of individual objects.

Appendix A

MWC-361

Contents

Il faut bien s'arrêter quelque part, et pour que la science soit possible, il faut s'arrêter quand on a trouvé la simplicité.

Henri Poincaré

This part is a preliminary and tentative modelling of the very-high resolution optical interferometry data acquired on MWC-361, a spectroscopic binary. This object is known to possess a large-scale circumbinary disk, in addition to a circumprimary disk consistent with the sublimation-radius of the primary star; however no circumsecondary disk was detected, no explanatory phenomena was found yet. Given the complex intricacy of disks and stars at spatial scales of a few milli-arc-seconds, the stellar parameters for both stars are still uncertain. This work proposes a solution to the spectral types of both stars, which opens a new window on the object, allowing precise modelling of its complex structure, and understanding of why only the primary still shows a circumstellar disk.

The data was acquired by myself, remotely from Meudon observing station on June, 16 2016, after several unfruitful observing runs (one remotely from Sydney, one locally at Mount Wilson), see Appendix F.

A.1 Introduction

MWC-361, also referred as HD 200775, is a massive YSO and a quadruple stellar-system, located at 320±51 pc (Benisty et al. 2013). It consists of a spectroscopic binary (Millan-Gabet et al. 2001, separation $\sim$ 18 mas in average, orbital period $\sim$ 3.6 years), a third companion at 2.5 arcsec (Pirzkal et al. 1997), and a fourth companion at 6 arcsec (Li et al. 1994). The two distant companion will be discarded in this study given their angular distance to the spectroscopic binary.

Using spectral features, Hernández et al. (2004) classified this binary as a Herbig Be star of spectral type B0-3, with a total luminosity of 15 000 $L_{\odot}$; they find the best-fitting extinction at $A_v \sim 3$, $R_v \sim 5.0$. However, because of the large uncertainty on the age of the system, the fundamental parameters of the individual sources remain highly uncertain, although it is likely that at least one of the two is an early Herbig Be star that dominates the spectrum (Benisty et al. 2013).

Monnier et al. (2006) determined the astrometric orbit ($i \sim 65°$, e$\sim$ 0.3, a$\sim$ 15.2, details in Table A.4) and found a H band flux ratio of 6.5±0.5 (currently updated to 1.6±0.3 from unpublished data, John Monnier, private conversation). They supposed that the secondary star is unresolved, and fitted the primary surrounded with a uniform disk of diameter 3.6±0.5 mas.

Based on the radial velocities of the photospheric lines, Alecian et al. (2008) find a mass ratio secondary/primary of 0.81±0.22. Although they derive similar masses and effective temperatures($M_p\sim$ 10 M and 18 600±2 000 K); the discrepancy between the observational properties suggests that the two stellar components must have grown and evolved differently.

Using the VEGA spectrograph at the CHARA Array (see Section 2.2.3), Benisty et al. (2013) resolved H_α emission on the scale of a few mas and showed that the equivalent width of the H_α lines increased at periastron, later confirmed by Bisyarina et al. (2015). The photo-center of the H_α excess was located near the primary star, slightly off-center and opposite to the secondary star location. The resolution criteria 0.5λ/B of their observations is however $\sim$ 2.5 mas, the H_α excess emission was marginally resolved and no precise characterization could be achieved.

Monnier et al. (2009) find in the MIR images obtained with the Keck, a large halo containing 45% of the 10.7 μm flux with a north-south elongation, consistent with the ascending node of the orbital parameters. Using Subaru Telescope MIR images, Okamoto et al. (2009) confirms that this halo is the remnant of a circumbinary disk, with an inner-rim located at 159±25 AU, up to 20 times the semi-major axis of the binary, indicating a large gap in the system.

While the circumbinary disk is mostly evacuated, recent NIR images obtained by the authors of Monnier et al. (2006) confirm the presence of a circumprimary disk. Interestingly, only the primary star shows such disk, which confirms their initial hypothesis (Monnier et al. 2006) that the secondary is unresolved, and that only the primary shows resolved flux.

Given that it was already measured in H band, in order to pin down the spectral type of both components one needs a flux ratio between the two components in a second wavelength.

A.2 Observations and data reduction

Data was acquired at the CHARA Array using PAVO instrument, as part of a YSO proposal (see Appendix F). PAVO is a two-telescopes interferometer with thirty-height

Table A.1: Observations made with PAVO, on June, 16 2015.

ID	Target	Time (mn)	Azimuth (°)	Elevation (°)	Fringes tracked (s)	Baseline (m)
1	HD 204770	0.0	10.5	56.3	120	97.5696
2	MWC-361	6.5	4.5	55.9	120	103.0395
3	HD 204770	20.6	7.0	56.9	120	101.2664
4	MWC-361	26.8	1.1	56.1	120	105.3986
5	HD 204770	33.1	4.8	57.2	120	103.1152
6	MWC-361	41.2	358.7	56.1	36	106.5688
7	HD 197950	52.6	353.1	57.1	120	107.6437
8	MWC-361	59.3	355.7	55.9	120	107.4407
9	HD 204770	65.1	359.0	57.4	120	106.4188

wavelength channels between 0.63 and 0.881 μm (Ireland et al. 2008). The data was acquired on June, 16 2015, after several other unfruitful and/or weathered-out observing nights in 2013 and 2014.

The observation strategy for PAVO was designed to intertwine the science target MWC-361 between two blocks on an interferometric calibrator, here HD 204770 and HD 197950, as detailed in Table A.1. A technical issue while observing calibrator 2 (HD 197950) between acquisition ID 2 and 3, forced to fall-back to calibrator 1 (HD 204770). Difficulty to find and track fringes during the third observation of the science target (ID 6) led to an earlier interruption of the integration (36 s of cumulated fringes integration instead of 120 s), in order to keep the position angle diversity as low as possible.

The MWC-361 binary at this date was expected to have an angular separation of $\sim$ 12 mas, at a position angle of $\sim$ 165°. The measurement of the binary parameters required the usage of a baseline of at least $\sim$ 10 m, ideally 20 m. However, using a longer baseline would result in the measurement of not only the binary, but also of the respective diameters of both companions. Such measurement is at the limit of PAVO capabilities.

Indeed, while the target is bright in the IR, with a H band magnitude of 5.44, the interstellar extinction causes the target to be much dimmer at PAVO wavelengths: a R band magnitude of 6.8. This means in practice that the fringes will be harder to track, leading to the necessity to stay longer on target. Figure A.1 shows the calibrated data as a function of the spatial frequencies. One sees the typical "wave" pattern arising from the binarity of the object. One important note is that this "wave" pattern evolves very quickly with time because of sky rotation: one sees a "crest" wave-pattern (position angles 1 and 3) and "trough" (position angles 2 and 4); the period is $\sim$ 35 mn.

All acquisitions on MWC-361 were time-boxed such that one either observes for 3 mn maximum (for minimal sky-rotation), or acquires 120 sec of "tracked" fringes

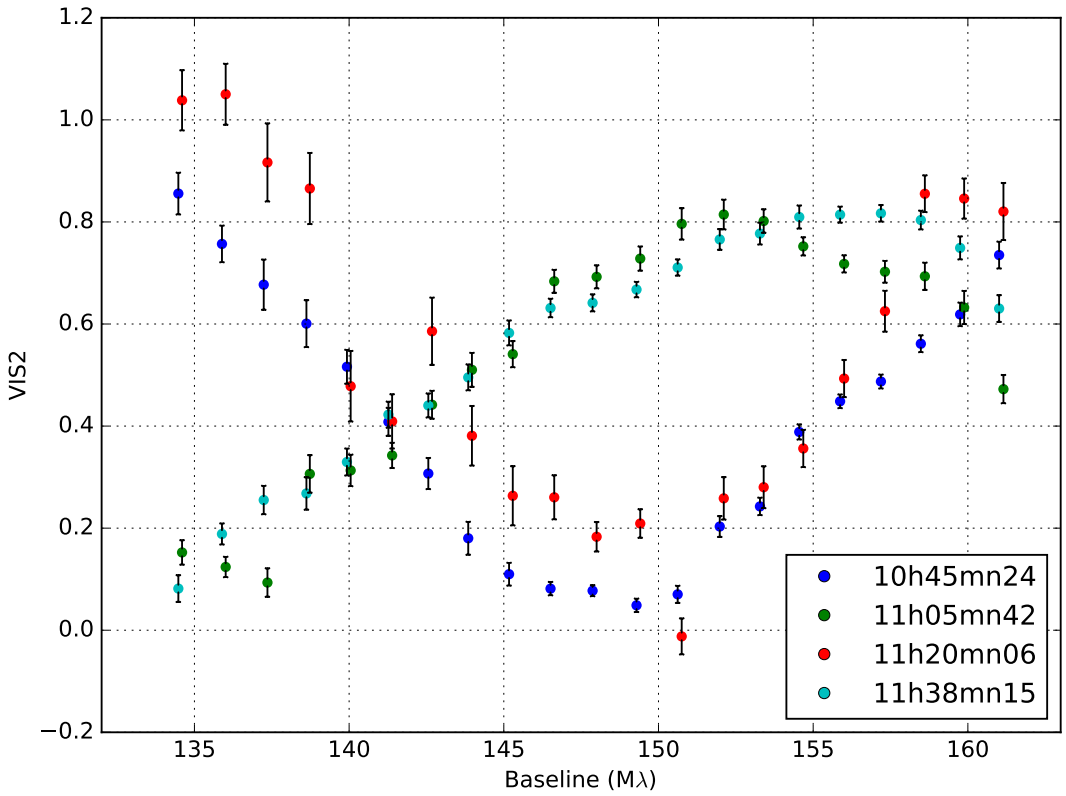

Figure A.1: VIS2 data measured with PAVO, as a function of the spacial frequencies. The third position angle acquired suffered from high noise and calibration issue due to the difficulty to find and track fringes during the data acquisition.

(i.e. when the fringe-tracker (precisely a group-delay for PAVO) is able to stabilize the fringes on the detector, and the visibility measurement can be performed), whichever is shortest. During the third acquisition, only 36 sec of tracked-fringes were acquired in 7 mn time. For this reason, the third position angle data is much noisier compared to the others, see Figure A.1. It is discarded in the data-processing. Figure A.2 illustrates the expected VIS2 values for the binary configuration at the epoch of observation, as a function of the (u,v) field; similarly to Figure A.1, it highlights the extreme timing constraint on the acquisition.

The data processing was carried using the standard PAVO pipeline. The calibration of MWC-361 was done using HD 204770 (spectral type B7, diameter Φ=0.198 mas) and HD 197950 (A8, Φ=0.339 mas); diameters were obtained with SearchCal[1], maintained by the JMMC. These calibrators were chosen to be as close as possible in coordinates, brightness and spectral type to MWC-361.

[1] http://www.jmmc.fr/searchcal_page.htm

A.3 VIS2 modelling and spectral types

The maximum VIS2 values at 1.35 and 1.55 Mλ equals 0.8, see Figure A.1. They correspond to the "envelope" of the oscillation signal due to the binary. This envelope can be modelled in different ways, and in all cases it is caused by either an over-resolved structure (flat decrement envelope) or a marginally-resolved structure (top-part of a "Gaussian"-like envelope).

The simplest unitary-model which can reproduce this decrement is a flat background value, i.e. a fully over-resolved structure introducing a constant VIS2 decrement over the spatial frequencies of the data. In order to perform a preliminary exploration, a simple model is used: it is composed of two point-sources in addition to a constant background. The contrast ratio between each unitary-model is assumed constant over the spectral range.

The initial hypothesis and fitting results are shown in Table A.2; the average and RMS of residuals are $\langle$residuals$\rangle$=-0.04 and $RMS(residuals)$=1.007, respectively, see Section 2.3.3. Figure A.3 shows the comparison between the VIS2 data, and the model fitted. The fact that the red lines is the furthest from the data can be explained by 1) calibration issues on the data, or 2) using a background unitary-model to account for the VIS2 decrement, while the decrement is only ~ 0.15 on the "crest" of the binary wave recorded on the red line, i.e. not flat decrement. Hypothsis 1) is supported by the fact that the red data records a "trough" of the binary wave, i.e. the detector was measuring a "null" which created a very low photon-count on the detector; a VIS2 mis-calibration might have introduced a systematic effect.

Table A.2: Initial (2PS+Back column) and black-body (2UD+Back) fit parameters for MWC-361 spectroscopic binary.

Parameter	Unit	Range	2PS+Back.	2UD+Back.
Prim. Ang.Sep.	mas	–	0 *	0 *
Prim. PA	°	–	0 *	0 *
Prim. CR	Arb. Unit	–	1 *	1 *
Prim. diam.	mas	–	–	0.159±0.011 (3)
Prim. Teff.	K	–	–	18600 *
Sec. Ang.Sep.	mas	[1,30]	11.82±0.04	11.83±0.05
Sec. PA	°	[0,180]	165.2±0.2 (1)	165.2±0.2 (1)
Sec. CR	F_{Prim}/F_{Sec}	[1,15]	1.98±0.09 (2)	1.97±0.08 (2)
Sec. diam.	mas	–	–	0.155±0.019 (3)
Sec. Teff.	K	[9000,19000]	–	13200^{+1000}_{900}
Back. CR	F_{Prim}/F_{Back}	[1,15]	5.85±0.25	7.23±0.4
$\sigma_{systematic}$	–	[0,0.1]	0.023±0.006	0.022±0.006

* : set values

(1) VIS2 degeneracy, 165.2° and 345.2° are both possible solutions, although the orbital fitting in next section showed that only 165.2° is valid.

(2) VIS2 degeneracy, 1.98 and 1.98^{-1} are both possible solutions.

(3) Obtained from the effective temperature, R band total magnitude (extinction corrected) and respective brightness of unitary models (i.e. contrast ratios), assuming black-body behavior.

CR≡Contrast Ratio, ie. (relative flux)$^{-}$1. CR=F_{prim}/F_{sec}.

The binary parameters are determined with great precision, and are independent of the particular choice of unitary-model which accounts for the max-VIS2 decrement. However, assuming that the stars are unresolved by the data is not accurate. Indeed, a rough approximation of the stellar diameters can be achieved using the known R band magnitude of the target, the respective contrast ratio of the unitary models and their effective temperatures, assuming a black-body behavior.

For this, one estimates the R band magnitudes of the primary and secondary stars using Contrast Ratio (CR) into the relations:

$$\begin{aligned} Rmag_{primary} &= Rmag_{object} - 2.5 * np.log10\Big(\frac{1}{1 + CR^{-1}_{secondary} + CR^{-1}_{back}}\Big) \\ Rmag_{secondary} &= Rmag_{object} - 2.5 * np.log10\Big(\frac{CR^{-1}_{secondary}}{1 + CR^{-1}_{secondary} + CR^{-1}_{back}}\Big), \end{aligned} \tag{A.1}$$

where $Rmag_{object}$ is the total R band magnitude of the object, corrected for extinction (2.2 mag in average within the R bandwidth, given A_v =3.0 and R_v =5.0). One yields ~ 0.15 mas for an effective temperature of 18600 K (primary) and ~ 0.13 mas for 15000

K ($\sim$ secondary). The VIS2 decrement due to marginally resolving the photosphere of both companion of is ~ 0.05

The R band magnitude estimation requires to assume that the total R band flux arises solely from both companions and the "background", i.e. that PAVO shows an interferometric field of view larger than the object-extension. The background flux in R band may either be stellar flux refracted by gas or dust, or high-temperature thermal emission from dust; in both cases, for this background flux to play a significant role in the total R band magnitude budget, the circumstellar material causing it must be in the very close vicinity of the binary (e.g. the circumprimary disk located at $\sim$ 2-5 mas). Given that PAVO's interferometric field of view is $B\lambda^2/\Delta\lambda \sim 74$ mas, assuming that the VIS2 data "sees" all of the R band flux is an acceptable hypothesis, and the inferred R band magnitudes of each component of the model are expected to be well-constrained.

A new global-fit is performed, where the two companions are replaced by uniform disks. A black-body behavior is assumed for the stars, which states that their magnitudes, apparent diameters and effective temperatures are mutually constrained. Note that since the angular diameters are considered, the distance to the system is marginalized and does not appear in the calculations. Their diameters are processed as preliminary steps of each MCMC-iteration, using their "MCMC-proposed" contrast ratio (i.e. respective brightness hence R_{mag}) and effective temperatures. Two hypothesis are used in the fit: the expected total brightness in R band is 6.8 magnitudes (5.6 after correction for extinction), and the contrast ratio between the companions in H band is 1.65±0.3 (John Monnier, private conversation).

The effective temperature of the primary is set to 18600 K (Alecian et al. 2008), while the effective temperature of the companion is left free for fitting, together with its angular separation, contrast ratio and position angle. The diameter of the two uniform disks are also left free for fitting.

The initial hypothesis and results of the fitting are tabulated in Table A.2, and its corner-plot is shown in Figure A.4. The average and RMS of residuals are $\langle$residuals$\rangle$=-0.04 and $RMS(residuals)$=0.996, respectively, see Section 2.3.3. One sees that the binary parameters are nearly identical to the exploratory model with two point-sources and the background, and well within the exploratory model confidence domains. The black-body uniform-disk diameters are found to be 0.159±0.011 mas and 0.155±0.019 mas for the primary and secondary, respectively. Their radii are estimated to 5.5±1.0 $R_\odot$ and 5.3±1.1 $R_\odot$ given a distance of 320±51 pc.

According to this method, the spectral type of the binary is B7±1. This spectral type estimate depends on several hypothesis:

- The primary effective temperature of 18600 K,
- The H band contrast ratio of F_{prim}/F_{sec}=1.65±0.3,
- The R band extinction-corrected magnitude of 5.4,

- The fact that the brightest star in H band (primary) is also the brightest in R band.

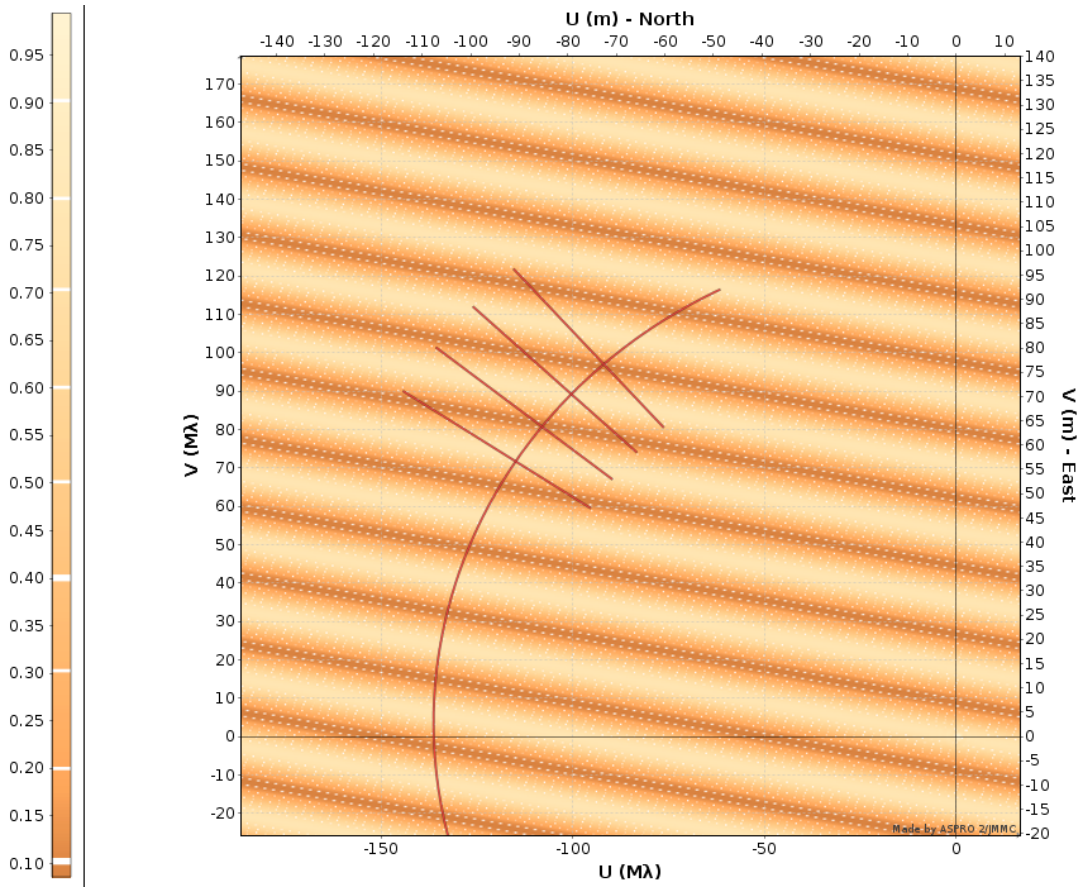

Figure A.2: Expected VIS2 values (color-coded) of the spectroscopic binary system at the epoch of observation, as a function of the (u,v) coordinates in meter (top and right axes) or in spatial frequencies (bottom and left axes). The red curve shows the (u,v) sampling as a function of time through the night as the sky rotates, for the central wavelength of PAVO. The four red straight lines show the (u,v) sampling of a single observation at a given time, with PAVO spectral dispersion. The red-end of PAVO sensitivity (0.881 μm) samples lower spatial frequencies (i.e. (u,v) coordinates closer to (0,0)); the blue-end (0.63 μm) samples higher spatial-frequencies (i.e. the outer end of the red straight line). The time increment between two successive red lines is 20 mn. This figure highlights the fact that the VIS2 value measured by PAVO on this object varies on very short time-scale, and thus must be measured as fast as possible. Image obtained with Aspro2 (JMMC, http://www.jmmc.fr/aspro_page.htm).

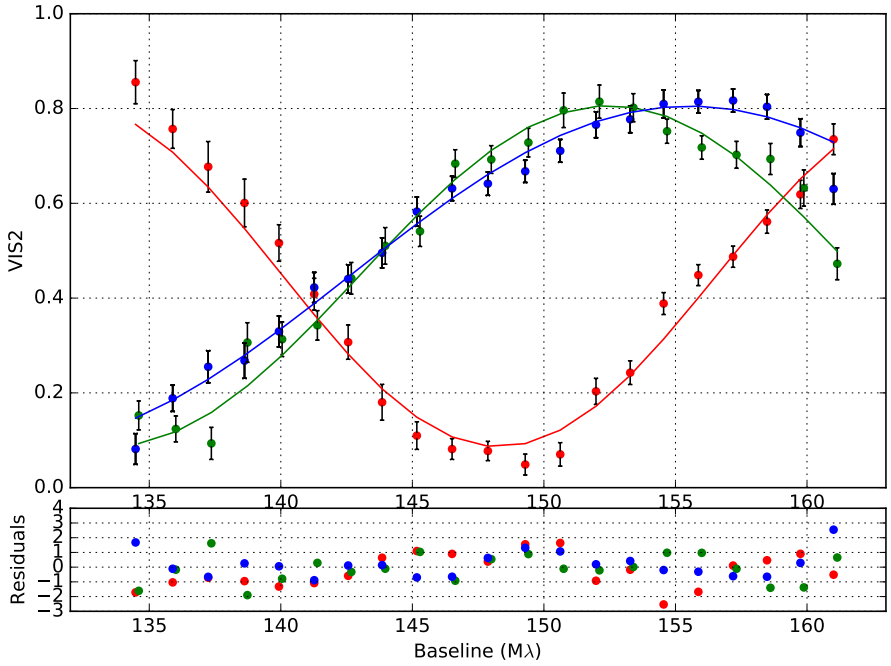

Figure A.3: MWC-361 VIS2 data (dots and error-bars) and the maximum-likelihood model (lines) for the model made of 2 point-sources and a background; residuals span ±2.

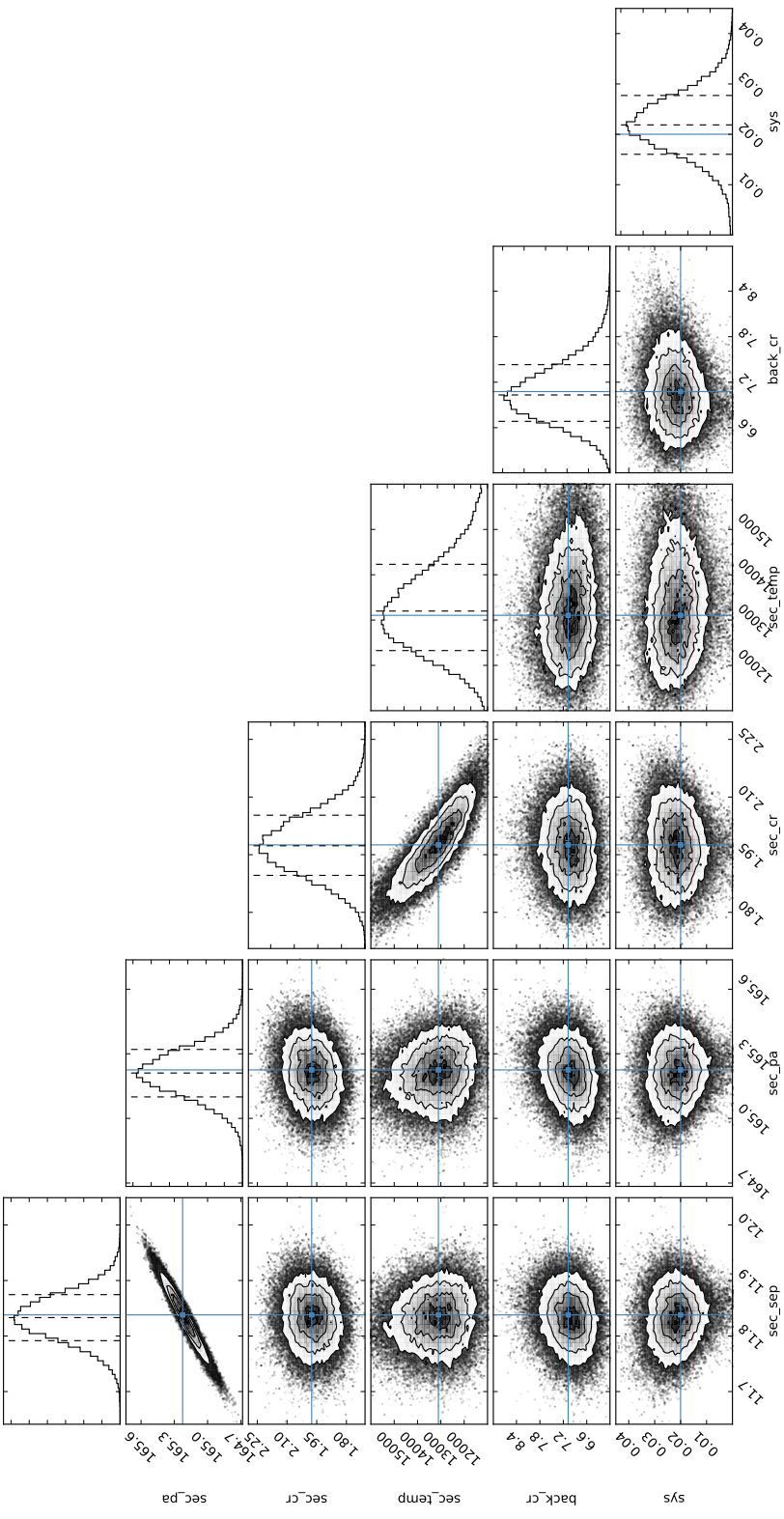

Figure A.4: Corner-plot of the fit for the model with two black-body uniform disks and a constant background. Refer to Section 2.3.2 for how to read this graph.

Table A.3: Astrometry positions used in the fit

MJD	Sep (mas)	PA (°)	Source
50981	17.9±2.60071827	2.7±9.6	Monnier06
51085	18.0±1.11305287	9.4±9.75	Monnier06
52811	11.9±4.3280936	73.0±14.84	Monnier06
52971	8.2±1.37182453	134.8±19.36	Monnier06
53162	11.4±1.21020537	171.6±12.96	Monnier06
53349	3.9±1.1414786	239.8±26.26	Monnier06
53545	12.8±0.81418582	348.3±8.8	Monnier06
57190	11.83±0.05	165.2±0.2	TW

A.4 Fitting of orbital parameters

The binary parameters obtained in the previous section are used in an orbital fitting exercise, in addition to the astrometric measurement obtained by Monnier et al. (2006). The binary positions are listed in Table A.3. The data spans ~ 4.5 orbital period (6209 days, 17 years (exactly!)), since the first measurement on June, 17 1998. This enables a substantial refinement of the orbital parameters, even though only one data point is added to the previous measurements.

Both position angles found in the VIS2 modelling (PA=165.2° and its point-symmetry at PA=345.2°) fall reasonably close to the known orbit, see Figure A.5: none of these two locations can be a priori discarded. In order to remove the degeneracy, two orbital fitting, one with each location, is performed, and the consistency of the results is compared to the orbital parameters in the literature. While the PA=165.2° is fully compatible with the literature parameters and provides an improvement over several values, the fit with PA=345.2° fails to converge. The degeneracy is solved; the value PA=165.2° is adopted.

A fitting-code based on a MCMC-sampler (*emcee* library) is used, and allows to fit directly the orbital parameters, namely the semi-major axis (a), the eccentricity (e), the inclination (i), the argument at periapsis (w) and the ascending node (O). The sixth and last independent orbital parameter fitted is called "d3M": the distance (in pc) to the cube divided by the total mass of the system (M_p+M_s) in $M_\odot$. This parameter is defined as:

$$T = \frac{distance^3}{M_p + M_s} = \sqrt{d3M \times 10^{-9} \times a^3}, \tag{A.2}$$

where T is the orbital period in years and (a) the semi-major axis in mas. Using this parametrization allows to marginalize the orbital period T, the time at periapsis t_{peri} and the distance, and combine them together with the total system-mass. This approach however forbids the use of radial velocities data in the fit, which require another orbital parametrization.

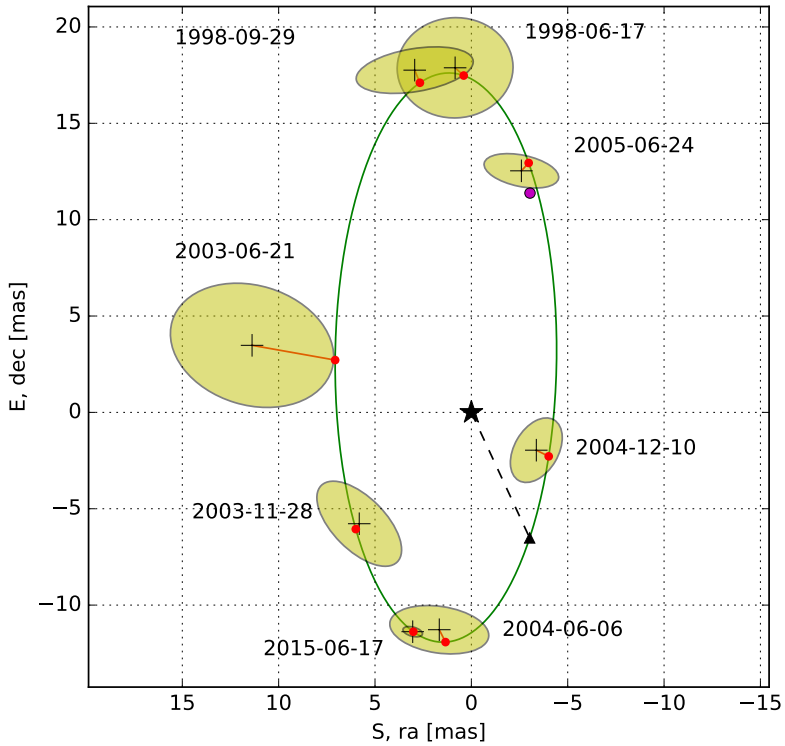

Figure A.5: Sky chart of the astrometric positions, see Table A.3, and best-fit of the orbital solution, see Figure A.6 and Table A.4. The black crosses are the astrometric locations of the secondary star with respect to the primary and the yellow ellipses the one-sigma error location. The red dots are the corresponding orbital locations from the best-fit orbit (green line). The black triangle and dotted-line represent the periastron of the orbit; the purple dot is the point-symmetry of the 17, June 2016 astrometric location, for which the orbital fitting does not converge.

Figure A.6 shows the corner-plot of the result of the orbital fitting. Parameters d3M and semi-major axis show a high correlation due to their intrinsic definition, see Eqn. (A.2); other parameters are mostly independent from each-others. The new orbit is found to be fully consistent with previous literature, see Table A.4, and brings further improvements on the determination of the inclination, semi-major axis, eccentricity and ascending node, and the confirmation of Bisyarina et al. (2015) values for the orbital period, time at periapsis and argument at periapsis.

From the fitted parameter d3M=$3.95\times10^6\pm0.33\times10^6$ and the distance d=320±51 pc, one can get back to the total system mass using Eqn. (A.2). It is estimated to $M_p+M_s=7.0^{+6.5}_{-2.3}$. This value is slightly lower than Benisty et al. (2013) (9.8 $M_\odot$) and Alecian et al. (2008) (9.2 $M_\odot$), although consistent within the one-sigma confidence domains.

Applying the mass ratio of 1.23±0.08 (Benisty et al. 2013) yields $M_p=3.85^{+3.6}_{-1.3}$ $M_\odot$ and $M_s=3.15^{+2.9}_{-1.05}$ $M_\odot$ for the primary and secondary, respectively. One needs a

distance of 335 pc – well within the distance confidence level – to obtain a total system mass of 9.5 $M_{\odot}$ and match previous literature values. One can say that the d3M value fitted from astrometric position is fully consistent with the mass and distance estimates of the MWC-361 system.

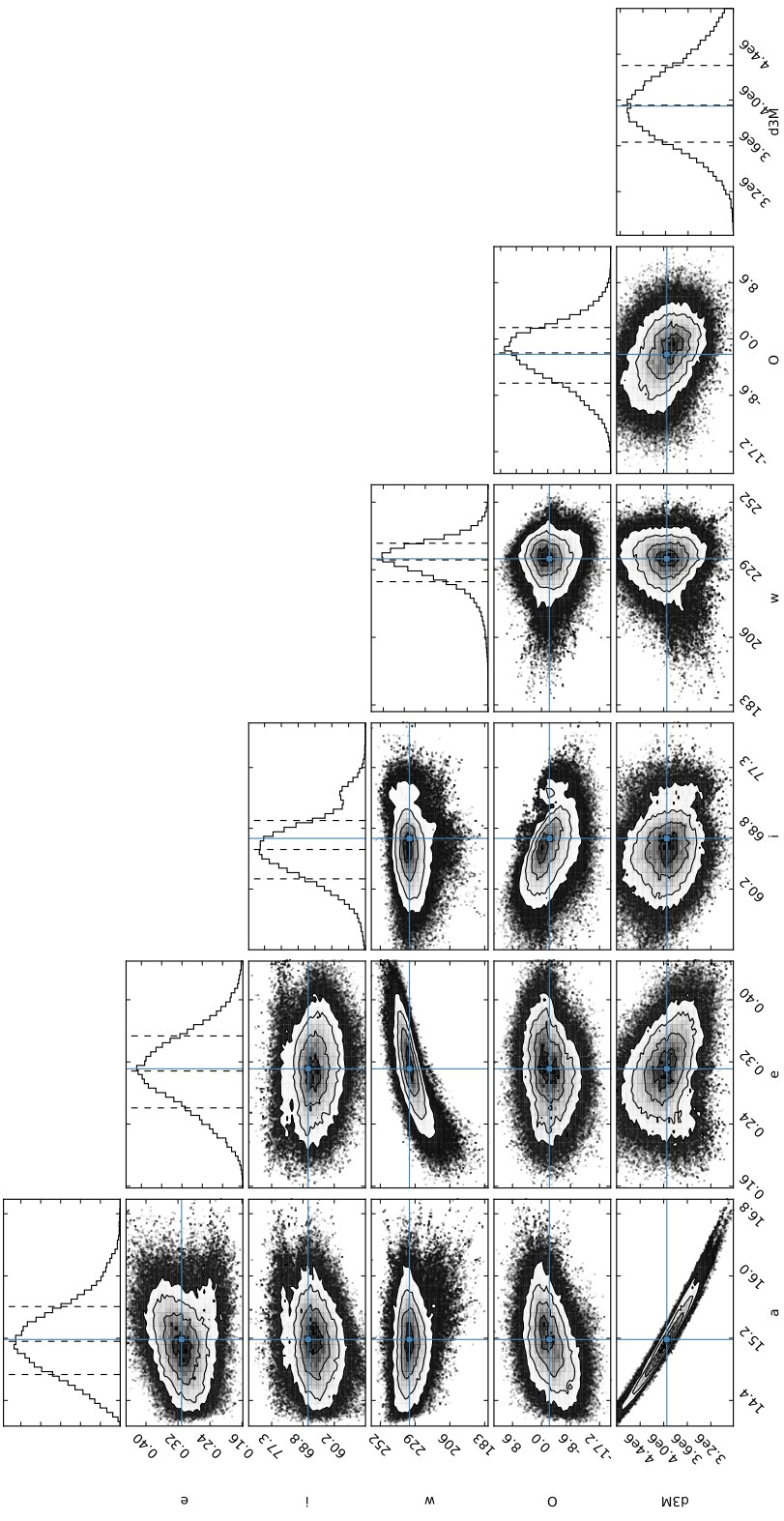

Figure A.6: Corner-plot of the orbital parameters fitting. a is displayed in mas; i, w and O in degrees; d3M in $pc^3/M_\odot$. Refer to Section 2.3.2 for how to read this graph.

Table A.4: Orbital parameters of MWC-361.

	Symbol	B15	B13	A08	M06	P04	TW
Method		RV	RV, lines	Synth. spectrum	Astrometry	RV	Astrometry
Period (days)	T	1361.3±2.2	1433±17	1412±54	1377±25	1341±23	1360±9
Time at periapsis (JD)[(1)]	t_{peri}	49241±14	48962±55	48991±152	49152±90	49149±87	49217±35
Semi-major Axis (mas)	a	–	15.9±0.7	16±9	15.14±0.7	–	15.2±0.4
Inclination (°)	i	–	66±7	48^{+17}_{-13}	65±8	–	65.5±4.0
Eccentricity	e	0.295±0.025	0.3±0.02	0.32±0.06	0.3±0.06	0.29±0.07	0.31±0.04
Argument at peri. (°)	ω	234±4	224±1	216±12	224±16	203±22	232±6
Ascending node (°)	Ω	–	-7.7±6	–	-0.2±7.6	–	-2±4
Mass ratio	M_p/M_s	1.21	1.23±0.08	$(0.81 \pm 0.22)^{-1}$	–	–	–
Primary mass ($M_\odot$)	M_p	0.8 [(3)]	5.37±1.9 [(3)]	6.8±3.3 [(3)]	–	–	$3.85^{+3.6}_{-1.3}$ [(2)]
Secondary mass ($M_\odot$)	M_s	0.7 [(3)]	4.4±1.7 [(3)]	5.5±2.8 [(3)]	–	–	$3.15^{+2.9}_{-1.05}$ [(2)]
Total mass ($M_\odot$)	M_t=M_p+M_s	1.5 [(3)]	9.8±3.6 [(3)]	12.5±7 [(3)]	–	–	$7.0^{+6.5}_{-2.3}$

B15=Bisyarina et al. (2015), B13=Benisty et al. (2013), A08=Alecian et al. (2008), M06=Monnier et al. (2006), P04=Pogodin et al. (2004), TW=This Work

RV≡Radial Velocities

(1) JD-2400000

(2) Calculated with M_p/M_s=1.23±0.08

(3) Recalculated for i =66°, given their respective mass ratio

A.5 Perspectives

This work proposed a model to understand the LBI data on June, 16 2016 obtained from PAVO at the CHARA Array observatory. It is composed of two black-body uniform disks and a background flux which accounts for the ~ 0.2 VIS2 decrement and binary wave signal encoded in the data. Is proposed a solution to the spectral types of the two stars. This will allow a precise characterization of the stellar parameters, including the age of the system. This will open a new window on the object, allowing precise modelling of its complex structure and better understanding of why 1) only the primary still shows a circumstellar disk, 2) the H_α emission on the scale of a few AU and centered on the primary varying subsequently with the orbit.

Appendix B

Thoughts on Instrumentation

I have had the chance to work on instrumentation and observation proposals for the first year and a half of my PhD, and actively took part in several engineering runs at the SUBARU Telescope in Hawaii, and observing runs on the CHARA Array either remotely or at the Mount Wilson Observatory, near Los Angeles. This work does not fit in the dust-, planetary-formation- and disk-storyline of this manuscript; I include it nonetheless in an appendix. Working on Vampires instrument (PI: Peter Tuthill, concept and design: Barnaby Norris; refer to Appendix E for the description article), an observing mode of the new Extreme AO system of the SUABRU Telescope, SCExAO. I learnt that there are many ways to build an instrument right, but there is even more possibilities to build it wrong. I witnessed and/or took part a few of them and will report the essence of some lessons-learnt.

B.1 Big data handling

Most of the time, interferometry relies on short-exposures to freeze the turbulence: this produces a lot of raw data. A typical 512*512 pixels detector produces 0.5 Mb single-frames when the data is saved as unsigned 16-bits integers. A typical 20 ms exposure-time setup will produce 180 000 frames per hour (usually stored in "cubes" of several hundreds of frames), which corresponds to 88 Gb per hour. In these conditions and including calibration and engineering tests during daylight, a successful observing run – which generally spans several nights – generates at least 500 Gb of data per night/day 24 hours period.

This raises the questions of storage and archival of data since most observatories hold public data-archival services, and of the means to transfer this data to a faster machine on which to perform the data-reduction.

Indeed, a consequence of the Zernike-Van Citter theorem stating that the visibility of the fringes is linearly related to the Fourier transform of the fringes, see Eq. (2.15). The direct consequence is that interferometric data requires heavy data-processing. A Fast-Fourier-Transform (FFT) operation on a 512*512 pixel image takes ~ 32 ms to perform on a single CPU – longer than the typical integration time –. However the FFT step is only one of the many steps of a long pipeline of data-reduction (bad pixel and cosmic rejection, flat-fielding, rotation of image due to sky rotation, summation, etc).

Moreover, this crude CPU-time estimation does not account for the human intervention during data-reduction. This intervention is extremely necessary, especially

in engineering, so that one can 1) check the quality of the data and make sure the measurement is consistent, 2) control the correct processing of the data (no code is bug-proof), 3) extract the required science or engineering outputs from the raw-data.

Interferometry produces a lot of raw data, on which the processing is extremely cumbersome. Having a robust process and code to reduce the data is utmostly mandatory.

B.2 Code recipes

A "black-box pipeline" might be adequate for a mature instrument, where only one or few different observing modes are offered and a lot of data has already been processed and published to compare and cross-check the consistency of any new data-cube being processed. Such end-to-end pipeline is however not appropriate for any other case.

The Gemini Planet Imager (GPI) team talks about data-reduction "recipes where each step of it – an "ingredient" – is an elementary operation on a frame, i.e. flat-fielding, correcting dispersion, rotating, etc. Each of these elementary steps is coded into a function taking inputs and outputs that are standardized, hence recognized and understood by other elementary steps functions.

This approach combines the short-term needs of the engineering phase, when the processing of the data requires a lot of flexibility and trial-and-error, and the long-term coding of a pipeline which re-uses of the elementary "ingredient" functions in the adequate order. There might be a small overhead of creating functions rather than copy-pasting bits of code in a kilometer-long script, however this rather small time invested in (half-decent) coding will pay off as soon as the kilometer-long script needs to be modified to cover another processing need.

Another utmostly necessary everyday tool, is code version control. Developing the control-software of an instrument, or its processing "ingredients", is a complex and time-consuming task, which is often shared between several people, and several computers. During an engineering run, many IT issues arise and one often need to reboot, re-install, or swap computers to perform new tests. Being able to try different versions of the same code, reverting to an earlier version, developing new features without breaking the latest stable version, merging the contributions of several people, or easily importing the code on a fresh install or computer are among the daily tasks of a instrumentation scientist, for which version control is critical.

Many different systems exist, such as Git, SVN, Mercurial, etc. Git is a recent yet fully-featured system, which brings key benefits over others. First, it is decentralized, meaning that the Git system will still be able to save, merge or create branches if the developer is, e.g., sitting on a plane without internet access. Second, it is in essence optimized for branching and merging, whereas SVN best works for a single incremental version of a code. Finally, it comes with countless logistic advantages, such as 1) automated (de-)registering of (deleted) new files, 2) simple and powerful file-ignoring rules and the possibility to have user-specific ones (vs. team-global one), 3) a "clean" command to optimized branch-memory usage, etc.

B.3 Information management

The data-reduction requires to know many acquisition parameters (e.g. timestamp, integration time, camera gain, instrument mode, filter wheel position, focus, etc) as well as some telescope or observatory parameters (RA-DEC, airmass, field de-rotators, weather conditions, etc). For many obvious clarity and robustness reasons, these critical acquisition parameters must lie in the same file as the data they correspond to, not a separate text- or log-file. However, some camera sofware development kits do not allow the instrument control-program to take over the recording of a frame, and its saving to the disk. This makes it in practice impossible to add such acquisition parameters in the header of the data before it is saved to the disk.

B.3.1 Headers of FITS

The code snippet below takes advantage of the FITS library of Python language, which do not require to read the whole existing file to append data to it: it adds the acquisition parameters at the end of the file, once it has already been saved. This code is able to append 100 acquisition parameters in the form of `PARAM_i: value_i / comment_i` into a 800 Mb data-file in 60±15 ms time. It can be used both as a Python function, or as a command-line bash script. The raw data is usually recorded as a cube of hundreds of single frames, meaning that only one file every many seconds is generated; under these conditions, the processing time needed to add the acquisition parameters to a data-file is negligeable.

Usage in bash command-line (provided that the file "addfitsheader" containing the code is in the PATH):

```
>>> addfitsheader ./datafile.fits "TARGET:IRS-48&TINT:60&GAIN:12& \
    TEMP:-34:Temperature of the Camera"
```

or

```
>>> addfitsheader ./datafile.fits TARGET:IRS-48 TINT:60 GAIN:12 \
    "TEMP:-34:Temperature of the Camera"
```

Usage in Python:

```
>>> addfitsheader("./datafile.fits", "TARGET:IRS-48& \
    TINT:60&GAIN:12&TEMP:-34:Temperature of the Camera")
```

or

```
>>> addfitsheader("./datafile.fits", ['TARGET:IRS-48', \
    'TINT:60', 'GAIN:12', 'TEMP:-34:Temperature of the Camera'])
```

```
#!/usr/bin/env python

from numpy import array
try:
```

```
    from astropy.io.fits import open, PrimaryHDU, Header
except ImportError:
    from pyfits import open, PrimaryHDU, Header

def _number(s):
    try:
        return float(s) if '.' in s else int(s)
    except:
        return s

def addfitsheader(filename, args, CARDsep='&', VALsep=':'):
    """args ~ 'CARD:val:comment 1&CARD2:val2:comment 2&...'"""
    fln = open(filename, mode='append')
    hd = []
    if not hasattr(args, "__iter__"): args = args.split(
       CARDsep)
    for item in args:
        dum = (item + VALsep*2).split(VALsep)
        hd.append((dum[0].strip().upper(), _number(dum[1].
            strip()), dum[2].strip()))
    fln.append(PrimaryHDU(data=array([0]), header=Header(hd)))
    fln.flush()

if __name__ == '__main__':
    from sys import argv
    addfitsheader(filename=argv[1], args=argv[2:])
```

B.3.2 Logging

Telescope systems (pointing, weather conditions, AO, etc) broadcast their status into logs. While acquisition parameters are set by the observer and can be recorded only once per data-cube, a lot of planned and un-planned events can happen during the acquisition of a cube. A logging system is among the very first things an instrument should implement, particularly in the engineering phase where the occurence of un-planned events is far larger than that of planned ones. This is particularly relevant for instruments which provide simultaneous observing modes such as SCExAO, that may send interfering or even clashing commands. Such information is critical when processing data as it gives clues on why and how some frames might look inconsistent or noisier.

The code snippet below provides a simple and robust system-wide logging mechanism for both control-software and human-comments; it was implemented on SCExAO in its engineering phase. It is based on three bash script (two for writing, one for

reading) which accept input paramters; they should be called from within the control-softwares or used by observers to log the status of their observing.

Bash scripts I developed, which implement a simple and robust system-wide logging mechanism for both control-software and human-comments. Each log entry takes ~ 20 ms to write; it should not be used for high-frequency logging. For robustness and safety reasons, the script checks the existence of the folder and log file for each entry, and creates them if they do not exist. The script could be slightly fastened by removing these checks, however this would defeat the purpose of having a fully-robust logging mechanism.

The user needs to define a base-folder for the logging, using
`logdir=/path/to/the/logging/folder/`.
The script will create a subfolder "YYYYMMDD" (base on UT time) within this logging-folder, in which to record the logs. When creating a log-entry, one must give two input paramters: the text to log, and the logging-key, i.e. the system from which originates the log-line (control-software of the instrument, human-comment, controle-software of AO, etc). The logging-key is limited to 10 characters. The log-line will be stored in
`/path/to/the/logging/folder/YYYYMMDD/logging-key.log`,
together with a date and timestamp in the format
`YYYY/MM/DD HH:MM:SS.SSSSSSSSS key log-line`.
The logging-key is added to the log-file so that log-files can be concatenated together and sorted on timestamp without loosing the information on the system from which the log-line originates.

The main logging script is `logdo` which takes two parameters: the logging-key and the log-line. A convenience script `log` is provided for the human-comments, it takes only one parameter: the log-line; the logging-key is forced to "human" (hence, then human-comments are stored in "human.log"). A script to display the logs in real-time, `logdisp`, takes one input parameter: the logging-key, which points to the log-file to eavesdrop. These scripts shall obvisouly be in the PATH of the machine where they are called.

Usage of `log`

```
>>> log This is a log-line that will end in human.log
```

Will produce the line:

```
2016/07/14 10:17:58.586123044 human      This is a \
log-line that will end in human.log
```

in the `human.log` file.

Usage of `logdo`

```
>>> logdo camera Taking a pretty image
```

Will produce the line:

```
2016/07/14 10:21:05.167564497 camera     Taking a pretty image
```

in the `camera.log` file.

Usage of `logdisp`

```
>>> logdisp camera
```

Will print:

10:21:05 -Taking a pretty image

and stay on hold, ready to print further log-lines as they are recorded to the `camera.log` file. Note that

```
>>> logdisp *
```

will print the log-lines for all logs.

Content of file `logdo`:

```
#!/bin/bash
logdir=/path/to/the/logging/folder/$(date -u +'%Y%m%d')
mkdir -p $logdir
touch $logdir/$1.log || exit
tolog=$(echo ${@:2} | sed -e "s/ / /")
printf "%s %-10s %s\n" "$(date -u +'%Y/%m/%d %H:%M:%S.%N')" "
    $1" "$tolog" >> $logdir/$1.log
```

Content of file `log`:

```
#!/bin/bash
logdo human "$@"
```

Content of file `logdisp`:

```
#!/bin/bash
logdir="/home/gschworer/$(date -u +'%Y%m%d')"
if [ $# -eq 0 ];
  then filedisp="$logdir/human.log"
  else filedisp="$logdir/$1.log"
fi
tail -q -f $filedisp | sed -e "s/[0-9/]* /`printf "\033[33m
    "`/;s/\.[0-9]* [a-zA-Z0-9]* */`printf "\\033[0m - \\033[34m
    "`/;s/$/`printf "\\033[0m"`/"
```

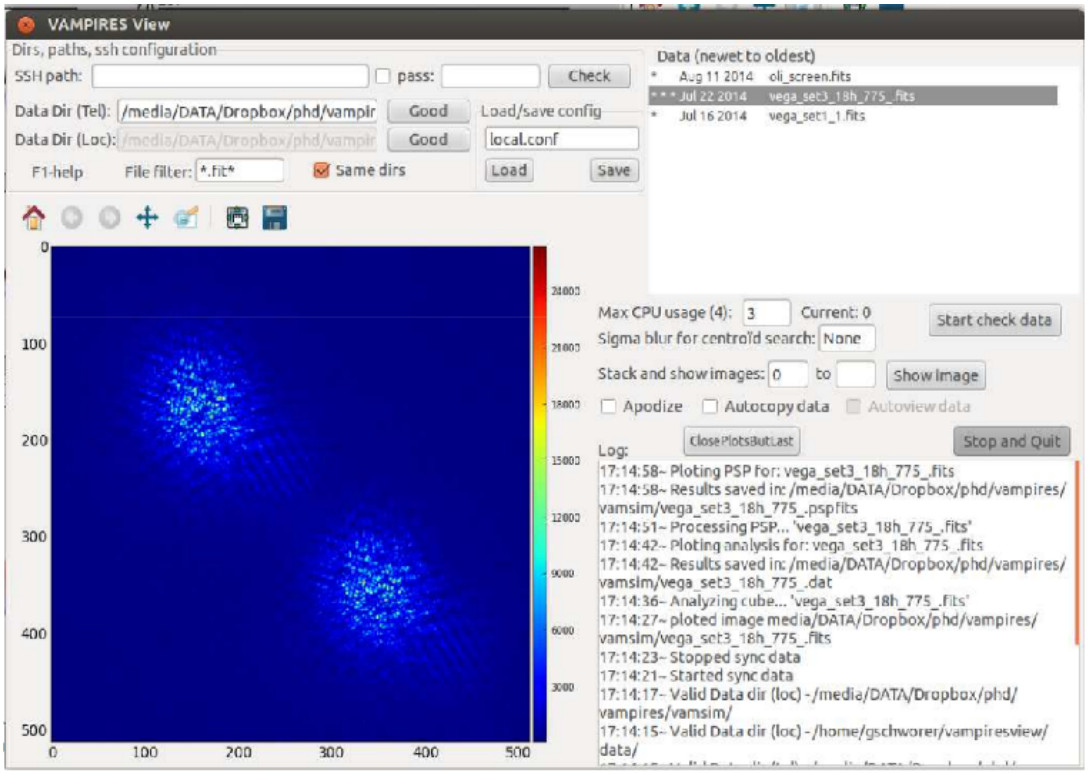

Figure B.1: Screenshot of the Vampires quickview software. Top-left panel relates to paths, ssh access and file-filters. Top-right panel shows the list of data-files, it is eavesdropping the folder where the data is being saved. Middle-right panel relates to display and quick-processing options. Bottom-right panel shows the quickview log. Bottom-left panel shows single-frames; this image shows two interference patterns because of the use of a wollaston prism, in order to measure polarization.

B.4 Quickviewing

A software allowing the instrumentalist to preview the data acquired, measure statistics on it, and apply basic data-reduction routines is necessary to perform so-called "sanity check" on the data, while it is acquiring. This is especially true for interferometric data which is highly-structured, hence not directly understandable, unlike a classical image, and needs some pre-processing before being human-analyzed. Without it, the observer is blind to issues that may compromise a large slice of data if not immediately detected and fixed. Additionally, with the help of logs, a quickview software provides some statistics on the frames in order to diagnose the origin of the problem.

Figure B.1 shows the quickview software I developed in Python during my instrumental work of the first half of my PhD. It automatically checks for new data-cubes and performs simple operations on them, such as calculate the power-spectrum, or the statistics (see Figure B.2). On this latter Figure, one sees on the FWHM bottom-left sub-plot that the FWHM value undergoes a cyclic drift of period $\sim$ 1 sec. This was

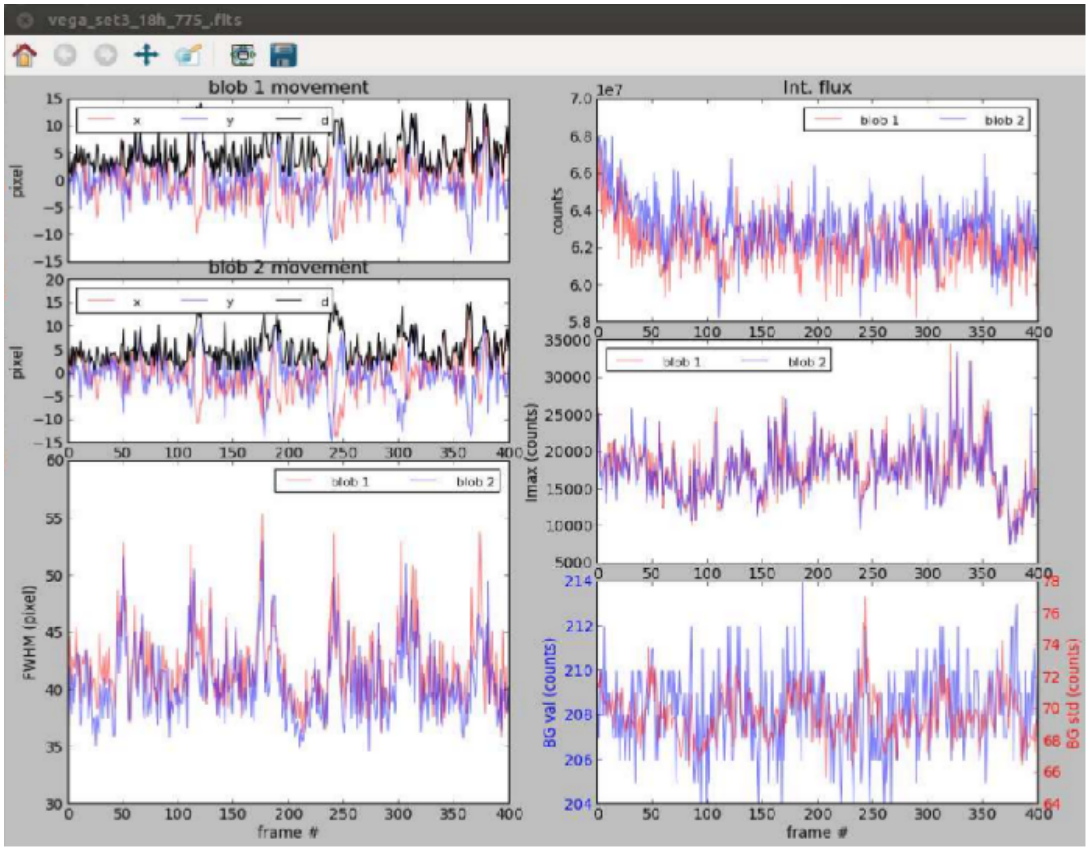

Figure B.2: Statistics on a data-cube calculated by the quickview program. All plots show a parameter as a function of the frame number in the data-cube (or as a function of time, given the integration time of 18 ms per frame). Top- and middle-left plots show the displacement in x, y and d=$\sqrt{x^2+y^2}$ of both interferograms (see bottom-left panel on Figure B.1). Bottom-left plot shows the FWHM of each blob. Bottom-right plot shows the background mean and standard deviation values. Top-right and middle-right plots show the sum and max of the frame after background removal.

found to correspond to the calibration of the deformable mirror of the extreme-AO system, which required to imprint shapes on the deformable mirror such that the PSF reference star splits in a varying amount of speckles. During this calibration phase, taking any data is worthless (apart from the deformable mirror calibration data).

Appendix C

MCFOST input file

Example of a MCFOST input-file.

```
  2.20                          mcfost version

#Number of photon packages
  20000.0                     nbr_photons_eq_th  : T computation
  5e2             nbr_photons_lambda : SED computation
  20000.0                     nbr_photons_image  : images
     computation

#Wavelength
  450  0.05 3000.0             n_lambda, lambda_min, lambda_max [
     mum] Do not change this line unless you know what you are
      doing
  T T T        compute temperature?, compute sed?, use default
     wavelength grid for ouput ?
  IMLup.lambda       wavelength file (if previous parameter is
     F)
  F F        separation of different contributions?, stokes
     parameters?

#Grid geometry and size
  1         1 = cylindrical, 2 = spherical, 3 = Voronoi
     tesselation (this is in beta, please ask Christophe)
  150 100 1 10                n_rad (log distribution), nz (or
     n_theta), n_az, n_rad_in

#Maps
  601 601 <img_au>              grid (nx,ny), size [AU]
  18   1   1                 MC : N_bin_incl, N_bin_az
  50.3   50.3   1  F            RT: imin, imax, n_incl, centered
      ?
  0    0   1                RT: az_min, az_max, n_az angles
  121.0         distance (pc)
```

```
  2.0         disk PA

#Scattering method
  0                   0=auto, 1=grain prop, 2=cell prop
  1                   1=Mie, 2=hg (2 implies the loss of
     polarizarion)

#Symetries
  T                   image symmetry
  T                   central symmetry
  T                   axial symmetry (important only if N_phi
     > 1)

#Disk physics
  1     0.0   1.0     dust_settling (0=no settling, 1=parametric
     , 2=Dubrulle, 3=Fromang), exp_strat, a_strat (for
     parametric settling)
  F                       dust radial migration
  F         sublimate dust
  F                       hydostatic equilibrium
  F  0.8       viscous heating, alpha_viscosity

#Number of zones : 1 zone = 1 density structure +
    corresponding grain properties
  3

#Density structure
  1                       zone type : 1 = disk, 2 = tappered-
     edge disk, 3 = envelope, 4 = debris disk, 5 = wall
  8e-10     10.0        dust mass,  gas-to-dust mass ratio
  14   60.0   2            scale height, reference radius (AU),
     unused for envelope, vertical profile exponent (only for
     debris disk)
  1  0     50   300   Rin, edge, Rout, Rc (AU) Rc is only used
     for tappered-edge & debris disks (Rout set to 8*Rc if
     Rout==0)
  1.3                     flaring exponent, unused for envelope
  -1   -1                 surface density exponent (or -gamma
     for tappered-edge disk or volume density for envelope),
     usually < 0, -gamma_exp (or alpha_in & alpha_out for
     debris disk)

  1                       zone type : 1 = disk, 2 = tappered-
```

```
    edge disk, 3 = envelope, 4 = debris disk, 5 = wall
  1e-05    100.0       dust mass,  gas-to-dust mass ratio
  14  60.0  2           scale height, reference radius (AU),
    unused for envelope, vertical profile exponent (only for
    debris disk)
  30.0  0.5    100.0  300  Rin, edge, Rout, Rc (AU) Rc is only
     used for tappered-edge & debris disks (Rout set to 8*Rc
    if Rout==0)
  1.3                    flaring exponent, unused for envelope
  -1  -1                 surface density exponent (or -gamma
    for tappered-edge disk or volume density for envelope),
    usually < 0, -gamma_exp (or alpha_in & alpha_out for
    debris disk)

  1                        zone type : 1 = disk, 2 = tappered-
    edge disk, 3 = envelope, 4 = debris disk, 5 = wall
  8e-12    100.0       dust mass,  gas-to-dust mass ratio
  14  60.0  2           scale height, reference radius (AU),
    unused for envelope, vertical profile exponent (only for
    debris disk)
  0.4  0    1.0  300  Rin, edge, Rout, Rc (AU) Rc is only used
     for tappered-edge & debris disks (Rout set to 8*Rc if
    Rout==0)
  1.3                    flaring exponent, unused for envelope
  -1  -1                 surface density exponent (or -gamma
    for tappered-edge disk or volume density for envelope),
    usually < 0, -gamma_exp (or alpha_in & alpha_out for
    debris disk)

#Cavity : everything is empty above the surface
 F              cavity ?
 15. 50.       height, reference radius (AU)
 1.5         flaring exponent

#Grain properties
  2  Number of species
  Mie    1    1    0.0000    0.5    0.0000
  PAHionProDiMo.dat  1
  2
  0.000487  0.000487  3.50000  1

  Mie    1    1    0.0000    0.5    0.0000
  PAHneuProDiMo.dat  1
```

```
  2
  0.000487   0.000487   3.50000   1

  1  Number of species
  Mie  2 1  0  1.0  0.9 Grain type (Mie or DHS), N_components,
       mixing rule (1 = EMT or 2 = coating),  porosity , mass
      fraction , Vmax (for DHS)
  dlsi_opct.dat  0.7  Optical indices file , volume fraction
  ac_opct.dat  0.3  Optical indices file , volume fraction
  1                   Heating method : 1 = RE + LTE, 2 = RE +
      NLTE, 3 = NRE
  0.03  2000.0 3.5 100     amin, amax [mum], aexp, n_grains (
      log distribution)

  1  Number of species
  Mie  2 1  0  1.0  0.9 Grain type (Mie or DHS), N_components,
       mixing rule (1 = EMT or 2 = coating),  porosity , mass
      fraction , Vmax (for DHS)
  dlsi_opct.dat  0.01  Optical indices file , volume fraction
  ac_opct.dat  0.99  Optical indices file , volume fraction
  1                   Heating method : 1 = RE + LTE, 2 = RE +
      NLTE, 3 = NRE
  0.03  30.0 3.5 100     amin, amax [mum], aexp, n_grains (log
      distribution)

#Molecular RT settings
  T T T 15.           lpop, laccurate_pop, LTE, profile width
      (km.s^-1)
  0.2          v_turb (delta)
  1       nmol
  co@xpol.dat 6           molecular data filename, level_max
  10.0 200            vmax (km.s^-1), n_speed
  T 1.e-6 abundance.fits.gz    cst molecule abundance ?,
      abundance, abundance file
  T  3                      ray tracing ?,  number of lines
      in ray-tracing
  1 2 3        transition numbers

#Star properties
  1 Number of stars
  9250.0   1.8  2.0  0.0  0.0  0.0  F Temp, radius (solar radius),M
       (solar mass),x,y,z (AU), is a blackbody?
  Kurucz9250-3.5.fits.gz
```

```
0.0  2.2   fUV, slope_fUV
```

Appendix D

Sparse-Aperture Masking @ Home

At the end of the building 5 in Observatoire de Paris, one finds a 10 m dome built in the 1930es, see Figure D.1. The 60 cm Schmidt telescope inside is on an equatorial mount; it can be used through the Astronomical Association[1] of the Observatoire de Paris.

I initiated a Sparse-Aperture Masking project within this association. The aim was to reproduce such masking experiment as amateur astronomer, with the most limited means. The camera used is a Nikon D3200 with 6016×4000 photosites, each being a square of 3.85 μm. Like all color DSLR, it has a Bayer Matrix in order to recover the color information for the "usual use", see Figure D.2. This 6016×4000 pixels camera (24 Mpx) only has 6 Mpx sensitive to red, 6 Mpx to blue and 12 Mpx to green. The illusion of "color" is only created in (automatic) post-processing of the raw image. However, this is an issue with interferometry, because each pixel will be alternatively sensitive to blue, green or red. Fringes being wavelength-dependent, the final "color-interpolated" image would be nothing more than a wavelength smear.

In order to overcome this issue, we read images as "raw" files, where each photosite photon-count is accessible separately, and generate four different images: a red, blue, and two green "monochromatic" layers, which can be processed separately. In some ways, the Bayer matrix replaces here the need for a monochromatic filter.

Given the focal length of 9 m, and the photosite size of 3.85*2 μm (*2 because only one photosite every two is sensitive to a given wavelength), one can not properly sample baselines longer than 23 cm for wavelengths of 0.42 μm. This prevents us from using the full 60 cm aperture of the telescope. We decide to discard the blue layer of the Bayer matrix (blue wavelengths are also more affected by turbulence), and work with the green and red layers only; this gives us the possibility to sample baselines up to 28 cm. In order to use the full aperture of the telescope, one would need to use a black and white camera with a pixel size of $\sim$ 4 μm, and use an additional monochromatic filter to avoid a too large bandwidth smearing.

First, a mapping of the defaults of the primary was achieved, with the main conclusion that pigeons should not be allow in the dome. A five-holes mask is designed (see Table D.1) such that the longest baseline is within the 28 cm limit, and that all the holes fall on a usable area of the optics, see Figure D.3.

The mask is mounted in front of the telescope using the spider of the secondary mirror. The size of the holes is set to 2.5 cm as being a trade-off between sensitivity and spatial coherence of the light.

[1] http://clubastro.obspm.fr/

x (cm)	y (cm)
0	0
0	-6
-5.19	-3
-5.19	9
5.19	9

Table D.1: Holes coordinates for the five holes mask.

Figure D.5 shows the PSF of the mask (focused) where on sees the first Airy ring, and unfocused where one sees the five holes of the mask creating fringes in their Airy rings. One notices here the chromaticity of fringes and speckles.

An sequence is acquired, with maximum ISO and an integration time of 20 ms (1/50e). The post-processing consists of reading the raw frames, splitting the Bayer matrix layers, and adding the modulus of the Fourier Transform of each layer, in order to display a power-spectrum. Figure D.6 shows a comparison between the measure power-spectrum of Vega, and the theoretical one.

One sees that most spatial frequencies are visible on the measured power-spectrum. A slight elongation of the spots suggests bandwidth smearing – the green filer of the Bayer matrix has a bandwidth $\sim 0.15\ \mu m$ –. A visibility loss as baseline increases suggests a bad focusing or a high turbulence. Dispersion (i.e. higher visibility loss on a specific direction) is also visible; indeed, at this time and date, the target was at $\sim 50°$ elevation. Given the dynamic range between the central spot and the other ones compared to the theoretical power-spectrum, one can suppose that turbulence dramatically affected the observation. As a reference value, an aperture size of 2.5 cm produces $\sim 10\%$ of visibility loss for r_0 =15 cm.

The next step would be to 1) use a black and white camera with higher quantum efficiency in order to be able to sample baselines up to 60 cm (although this defeats the purpose of doing SAM with the most limited means), and 2) observe a binary star and try to measure the binary parameters, although a first check in the Washington Double-Star catalog displayed only a few possible targets, due to sensitivity constraints.

Figure D.1: Dome and telescope "Table equatoriale" by night, with Orion constellation, and light pollution from Paris.

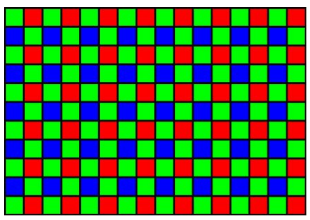

Figure D.2: Bayer matrix, which illustrates that all "pixels" (here called "photosite") of a DSLR are not sensitive to all colors.

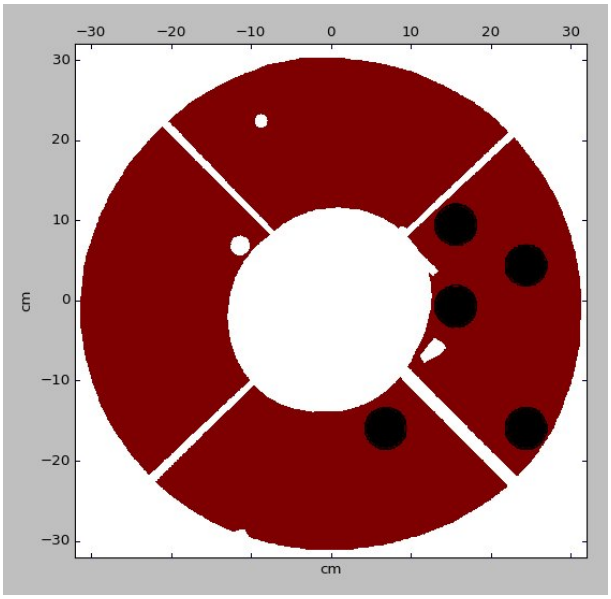

Figure D.3: Five holes mask design (black disks) and usable area of the optics (red). One sees the spiders and the secondary mirror.

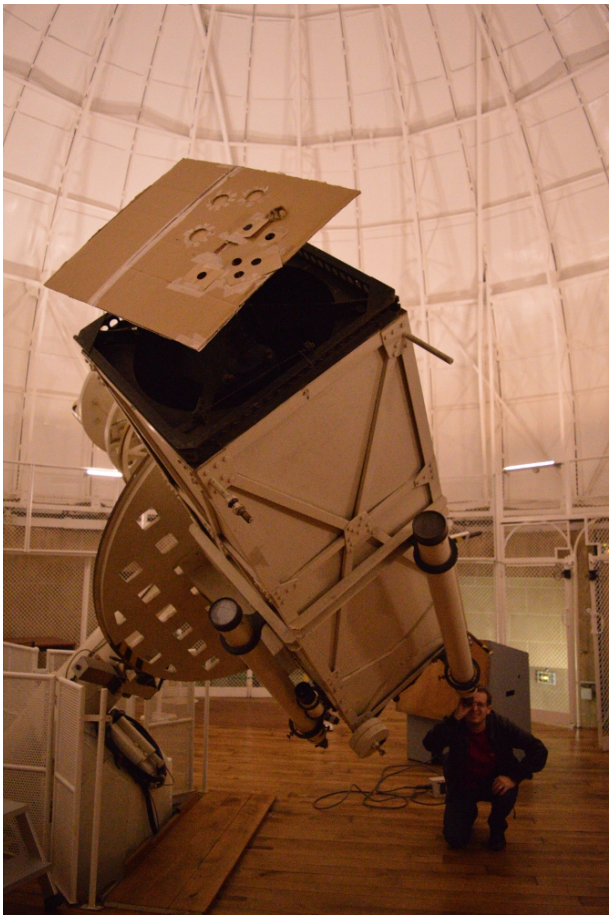

Figure D.4: Mask mounted behind the spider of the secondary mirror, and made of simple cardboard. This mask is a prototype of a 6-holes mask.

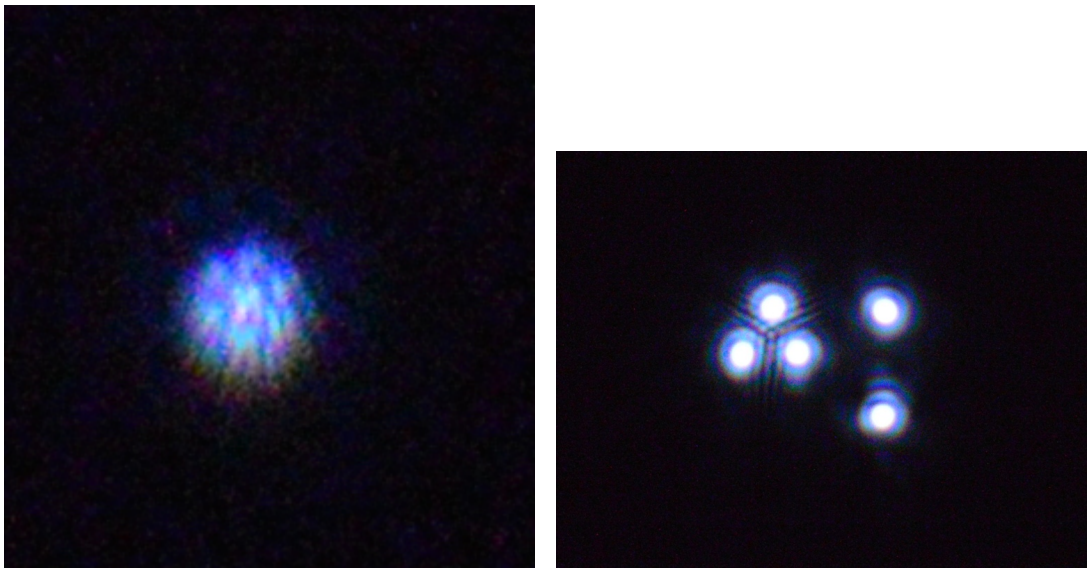

Figure D.5: PSF and non-focused PSF showing the separate mask holes.

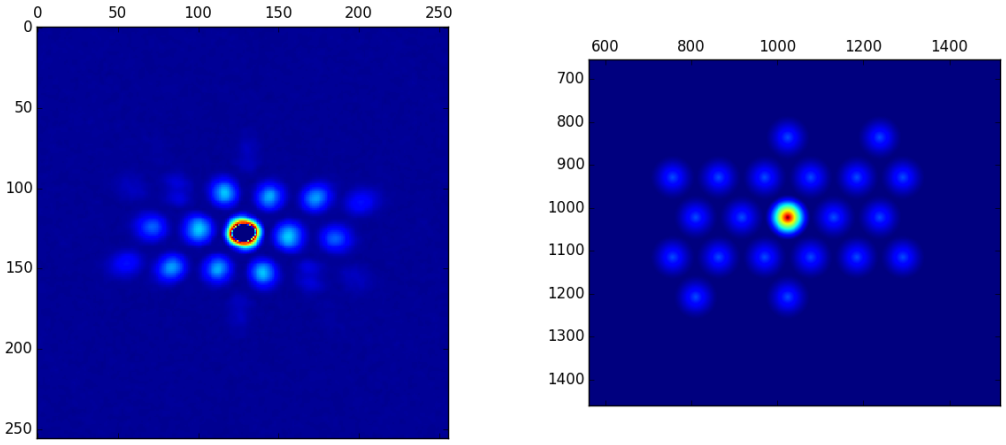

Figure D.6: Measured (left) and theoretical (right) power spectrum of the mask. The central spot of the measure was artificially removed in order to reduce the dynamical range of the image.

Appendix E

Articles

Contents

Draft version July 2, 2015
Preprint typeset using LaTeX style emulateapj v. 5/14/03

THE SUBARU CORONAGRAPHIC EXTREME ADAPTIVE OPTICS SYSTEM: ENABLING HIGH-CONTRAST IMAGING ON SOLAR-SYSTEM SCALES

N. Jovanovic[1], F. Martinache[2], O. Guyon[1,3,4], C. Clergeon[1], G. Singh[1,5], T. Kudo[1],V. Garrel[6], K. Newman[4,7], D. Doughty[1,4], J. Lozi[1], J. Males[3,8], Y. Minowa[1], Y. Hayano[1], N. Takato[1], J. Morino[9], J. Kuhn[10], E. Serabyn[10], B. Norris[11], P. Tuthill[11], G. Schworer[5,11], P. Stewart[11], L. Close[3], E. Huby[5,12], G. Perrin[5], S. Lacour[5], L. Gauchet[5], S. Vievard[5], N. Murakami[13], F. Oshiyama[13], N, Baba[13], T. Matsuo[14], J. Nishikawa[9], M. Tamura[9,15], O. Lai[1,6], F. Marchis[16], G. Duchene[17,18], T. Kotani[9], and J. Woillez[19]

Draft version July 2, 2015

ABSTRACT

The Subaru Coronagraphic Extreme Adaptive Optics (SCExAO) instrument is a multipurpose high-contrast imaging platform designed for the discovery and detailed characterization of exoplanetary systems and serves as a testbed for high-contrast imaging technologies for ELTs. It is a multi-band instrument which makes use of light from 600 to 2500 nm allowing for coronagraphic direct exoplanet imaging of the inner 3 λ/D from the stellar host. Wavefront sensing and control are key to the operation of SCExAO. A partial correction of low-order modes is provided by Subaru's facility adaptive optics system with the final correction, including high-order modes, implemented downstream by a combination of a visible pyramid wavefront sensor and a 2000-element deformable mirror. The well corrected NIR (y-K bands) wavefronts can then be injected into any of the available coronagraphs, including but not limited to the phase induced amplitude apodization and the vector vortex coronagraphs, both of which offer an inner working angle as low as 1 λ/D. Non-common path, low-order aberrations are sensed with a coronagraphic low-order wavefront sensor in the infrared (IR). Low noise, high frame rate, NIR detectors allow for active speckle nulling and coherent differential imaging, while the HAWAII 2RG detector in the HiCIAO imager and/or the CHARIS integral field spectrograph (from mid 2016) can take deeper exposures and/or perform angular, spectral and polarimetric differential imaging. Science in the visible is provided by two interferometric modules: VAMPIRES and FIRST, which enable sub-diffraction limited imaging in the visible region with polarimetric and spectroscopic capabilities respectively. We describe the instrument in detail and present preliminary results both on-sky and in the laboratory.

Subject headings: Astronomical Instrumentation, Extrasolar Planets

1. INTRODUCTION

The field of high-contrast imaging is advancing at a great rate with several extreme adaptive optics systems having come online in 2014, including the Gemini Planet Imager (GPI) (Macintosh 2014), the Spectro-Polarimetric High-contrast Exoplanet REsearch instrument (SPHERE) (Beuzit *et al.* 2008), and the focus of this work, the Subaru Coronagraphic Extreme Adaptive Optics (SCExAO) system which join the already running P1640 (Dekany *et al.* 2013). These systems all share a similar underlying architecture: they employ a high order wavefront sensor (WFS) and a deformable mirror (DM) to correct for atmospheric perturbations enabling high Strehl ratios in the near-infrared (NIR) ($> 90\%$), while a coronagraph is used to suppress on-axis starlight downstream. The primary motivation for such instrumentation is the direct detection of planetary mass companions at contrasts of 10^{-5}–10^{-6} with respect to the host star, at small angular separations (down to 1–5 λ/D) from the host star.

The era of exoplanetary detection has resulted in $\sim$ 1500 planets so far confirmed (Han *et al.* 2014). The majority of these were detected via the transit

[1] National Astronomical Observatory of Japan, Subaru Telescope, 650 North A'Ohoku Place, Hilo, HI, 96720, U.S.A.
[2] Observatoire de la Cote d'Azur, Boulevard de l'Observatoire, Nice, 06304, France
[3] Steward Observatory, University of Arizona, Tucson, AZ, 85721, U.S.A.
[4] College of Optical Sciences, University of Arizona, Tucson, AZ 85721, USA
[5] LESIA, Observatoire de Paris, Meudon, 5 Place Jules Janssen, 92195, France.
[6] Gemini Observatory, c/o AURA, Casilla 603, La Serena, Chile
[7] NASA Ames Research Center, Moffett Field, CA 94035, USA
[8] NASA Sagan Fellow
[9] National Astronomical Observatory of Japan, 2-21-1 Osawa, Mitaka, Japan
[10] Jet Propulsion Laboratory, California Institute of Technology, 4800 Oak Grove Dr, Pasadena, CA 91109, USA
[11] Sydney Institute for Astronomy (SIfA), Institute for Photonics and Optical Science (IPOS), School of Physics,
University of Sydney, NSW 2006, Australia
[12] Dpartement d?Astrophysique, Gophysique et Ocanographie, Universit de Lige, 17 Alle du Six Aot, 4000 Lige, Belgium
[13] Division of Applied Physics, Faculty of Engineering, Hokkaido University, Kita-13, Nishi-8, Kita-ku, Sapporo, Hokkaido 060-8628, Japan
[14] Kyoto University, Kitashirakawa-Oiwakecho, Sakyo-ku, Kyoto 606-8502 Japan
[15] Department of Astronomy, University of Tokyo, 7-3-1 Hongo, Bunkyo, Tokyo 113-0033, Japan
[16] Carl Sagan Center at the SETI Institute, Mountain View, CA 94043, USA
[17] Astronomy Department, University of California, Berkeley, CA 94720-3411, USA
[18] University Grenoble Alpes & CNRS, Institut de Planetologie et d'Astrophysique de Grenoble (IPAG), Grenoble F-3800, France
[19] European Southern Observatory (ESO), Karl-Schwarzschild-Str. 2, Garching 85748, Germany
Electronic address: jovanovic.nem@gmail.com

technique with instruments such as the Kepler space telescope (Borucki *et al.* 2010). The radial velocity method (Mayor & Queloz 1995) has also been prolific in detection yield. Both techniques are indirect in nature (the presence of the planet is inferred by its effect on light from the host star) and hence often deliver limited information about the planets themselves. It has been shown that it is possible to glean insights into atmospheric compositions via techniques such as transit spectroscopy (Charbonneau 2001), whereby star light from the host passes through the upper atmosphere of the planet as it propagates to Earth, albeit with limited signal-to-noise ratio. The ability to directly image planetary systems and conduct detailed spectroscopic analysis is the next step towards understanding the physical characteristics of their members and refining planetary formation models.

To this end, so far < 50 substellar companions have been directly imaged (see Fig. 3 in (Pepe *et al.* 2014)). The challenge lies in being able to see a companion, many orders of magnitude fainter, at very small angular separations (< 1"), from the blinding glare of the host star. Indeed, the Earth would be $> 10^9\times$ fainter than the sun if viewed from outside the solar system in reflected light. Although these levels of contrast can not be overcome from ground based observations at small angular separations (< 0.5"), it is possible to circumvent this by imaging the thermal signatures instead and targeting bigger objects. Indeed, all planets imaged thus far were large Jupiter-like planets (which are brightest) detected at longer wavelengths (in the near-IR H and K-bands and the mid-IR L and M-bands) in thermal light (a subset of detections include (Kraus & Ireland 2012; Lagrange *et al.* 2009; Marois *et al.* 2008)). To overcome the glare from the star which results in stellar photons swamping the signal from the companion, adaptive optics systems (AO) are key (Lagrange *et al.* 2009). Although angular differential imaging is the most commonly used technique for imaging planets thus far (Marois *et al.* 2008), coronagraphy (Lafreniere *et al.* 2009; Serabyn *et al.* 2010*a*) and aperture-masking interferometry (Kraus & Ireland 2012) have also been used to make detections. With the direct detection of the light from the faint companion itself, spectroscopy becomes a possibility and indeed preliminary spectra have been taken for some objects as well (Barman *et al.* 2011; Oppenheimer *et al.* 2013).

In addition to planetary spectroscopy, how disks evolve to form planetary systems is a key question that remains unanswered. Thus far coronographic imagers like HiCIAO at the Subaru Telescope have revealed intricate features of the inner parts of circumstellar disks using polarization differential imaging (under the SEEDS project (Tamura *et al.* 2009)). These solar-system scale features include knots and spiral density waves within disks like MWC758 and SAO 206462 (Grady *et al.* 2013; Muto *et al.* 2012). How such features are affected by or lead to the formation and evolution of planets can only be addressed by high-contrast imaging of the inner parts (up to 15 AU from the star) of such disks. To address the lack of information in this region, high-contrast imaging platforms equipped with advanced wavefront control and coronagraphs are pushing for smaller inner working angles (IWA). In the limit of low wavefront aberrations, currently achieved with AO systems operating in the near-IR, coronagraphs are the ideal tool for imaging the surrounding structure/detail as they are unrivaled in achievable contrast. Both the contrast and IWA are dependent on the level of wavefront correction available. With wavefront corrections typically offered by facility adaptive optics (AO) systems on 5–10 m class telescopes ($\sim 30-40\%$ in H-band) previous generations of coronagraphic imagers, such as the Near-Infrared Coronagraphic Imager, NICI on the Gemini South telescope (Artigau 2008) were optimized for an IWA of $5-10\ \lambda/D$. However, with extreme AO (ExAO) correction offering high Strehl ratio and stable pointing, GPI and SPHERE have been optimized for imaging companions down to angular separations of $\sim 3\ \lambda/D$ (> 120 mas in the H-band). SCExAO utilizes several more sophisticated coronagraphs including the Phase Induced Amplitude Apodization (PIAA) (Guyon 2003) and vector vortex (Mawet *et al.* 2010), which drive the IWA down to just below $1\lambda/D$. At a distance of 100 pc, the PIAA/vortex coronagraphs on SCExAO would be able to image from 4 AU outwards (approximately the region beyond the orbit of Jupiter). Further, in the case of the HR8799 system the IWA would be 1.6 AU (the distance of Mars to our Sun) making it possible for SCExAO to image the recently hypothesized 5^{th} planet at 9 AU (mass between 1-9 Jupiter masses) (Gozdziewski & Migaszewski 2014) if it is indeed present as predicted.

Despite the state-of-the-art IWA offered by these coronagraphs in the near-IR, the structure of disks and the distribution of planets at even closer separations than $1\ \lambda/D$ will remain inaccessible with coronagraph technology alone. This scale is scientifically very interesting as it corresponds to the inner parts of the solar system where the majority of exoplanets have been found to date based on transit and radial velocity data (Han *et al.* 2014). To push into this regime SCExAO uses two visible wavelength interferometric imaging modules known as VAMPIRES (Norris *et al.* 2012) and FIRST (Huby *et al.* 2012). VAMPIRES is based on the powerful technique of aperture masking interferometry (Tuthill *et al.* 2000), while FIRST is based on an augmentation of that technique, known as pupil remapping (Perrin *et al.* 2006). Operating in the visible part of the spectrum, the angular resolution of these instruments on an 8-m class telescope approaches a territory previously reserved for long baseline interferometers (15 mas at $\lambda = 700$ nm) and expands the type of target that can be observed to include massive stars. Although the modules operate at shorter wavelengths where the wavefront correction is of a lower quality, interferometric techniques allow for sub-diffraction limited imaging (10 mas resolution using $\lambda/2D$ criteria as conventionally used in interferometry) even in this regime, albeit at lower contrasts ($\sim 10^{-3}$), making optimal use of the otherwise discarded visible light. Despite the lower contrasts aperture masking interferometry has already delivered faint companion detections at unprecedented spatial scales (Kraus & Ireland 2012). Each module additionally offers a unique capability. For example the polarimetric mode of VAMPIRES is designed to probe the polarized signal from dusty structures such as disks around young stars and shells around giant stars (Norris *et al.* 2012, 2015) at a waveband where the signal is strongest. This is a visible analog of that

offered by the SAMPol mode on the NACO instrument at the VLT (Lenzen *et al.* 2003; Norris *et al.* 2012; Tuthill *et al.* 2010). FIRST on the other hand offers the potential for broadband spectroscopy and is tailored to imaging binary systems and the surface features of large stars. Such capabilities greatly extend SCExAO beyond that of a regular ex-AO facility.

Finally, with a diffraction-limited point-spread-function (PSF) in the near-IR, and a large collecting area, SCExAO is ideal for injecting light into fiber fed spectrographs such as the Infrared Doppler instrument (IRD) (Tamura *et al.* 2012). In addition, this forms the ideal platform for exploring photonic-based technologies such as photonic lanterns (Leon-Saval *et al.* 2013) and integrated photonic spectrographs (Cvetojevic *et al.* 2012) for next generation instrumentation.

The aim of this publication is to outline the SCExAO instrument and its capabilities in detail and offer some preliminary results produced by the system. In this vein, section 2 describes the key components of SCExAO while section 3 highlights the functionalities and limitations of the instrument. Section 4 outlines plans for future upgrades and the paper concludes with a summary in Section 5.

2. THE ELEMENTS OF SCEXAO

In order to understand the scientific possibilities and limitations of the SCExAO instrument, it is important to first understand the components and their functionalities. To aid the discussion a system level diagram of SCExAO is shown in Fig. 1, and an image of the instrument at the Nasmyth platform is shown in Fig. 2. A detailed schematic of the major components is shown in Fig. 3. The components and functionalities of SCExAO have been undergoing commissioning as will be outlined throughout this publication. A summary of the commissioning status of each mode of operation or module of SCExAO can be found in Table 9.

The main aim of SCExAO is to exploit the well corrected wavefront enabled by the high order WFS to do high-contrast imaging with light across a broad spectrum: from 600 nm to 2500 nm. As such there are a number of instrument modules within SCExAO that operate in different wavebands simultaneously while the coronagraph is collecting data. This hitchhiking mode of operation enables maximum utilization of the stellar flux, which allows for a more comprehensive study of each target.

2.1. *SCExAO at a glance*

The SCExAO instrument consists of two optical benches mounted on top of one another, separated by $\sim$ 350 mm. The bottom bench (IR bench) hosts the deformable mirror, coronagraphs, and a Lyot-based low order wavefront sensor (LLOWFS) while the top bench (visible bench) hosts the pyramid WFS, VAMPIRES, FIRST and lucky imaging (see Figure 3). The benches are optically connected via a periscope.

The light from the facility adaptive optics system (AO188) is injected into the IR bench of SCExAO and is incident on the 2000 element deformable mirror (2k DM) before it is split by a dichroic into two distinct channels: light shorter than 940 nm is reflected up the periscope and onto the top bench while light longer than 940 nm is transmitted. The visible light is then split by spectral content by a range of long and short pass dichroics which send the light to the pyramid WFS (PyWFS) and visible light science instruments. The PyWFS is used for the high order wavefront correction and drives the DM on the IR bench. The VAMPIRES and FIRST modules utilize the light not used by the PyWFS. Lucky imaging/PSF viewing makes use of light rejected by the aperture masks of VAMPIRES.

The IR light that is transmitted by the dichroic on the IR bench propagates through one of the available coronagraphs. After the coronagraphs, the light reflected by the Lyot stop is used to drive a LLOWFS in order to correct for the chromatic and non-common errors (such as tip/tilt) between the visible and IR benches (Singh *et al.* 2014). The light transmitted by the coronagraphs is then incident on the science light beamsplitter which determines the spectral content and exact amount of flux to be sent to a high frame rate internal NIR camera as compared to a science grade detector such as the HAWAII 2RG in the HiCIAO instrument and soon to be commissioned CHARIS. The internal NIR camera can then be used to drive various coherent differential imaging algorithms.

2.2. *Detailed optical design*

The instrument is designed to receive partially corrected light from the facility adaptive optics system, AO188 (188 actuator deformable mirror). The beam delivered from AO188 converges with a speed of $f/14$. Typical H-band Strehl ratios are $\sim 30-40\%$ in good seeing (Minowa *et al.* 2010). The beam is collimated by an off-axis parabolic mirror (OAP1, $f = 255$ mm) creating an 18 mm beam. Details of the OAPs can be found in section 6. The reflected beam is incident upon the 2k DM, details of which are in section 3.1.1. The surface of the DM is placed one focal length from OAP1 which conjugates it with the primary mirror of the telescope (i.e. it is in a pupil plane). Once the beam has reflected off the DM it is incident upon a fixed pupil mask which replicates the central obstruction and spiders of the telescope (see Fig. 5), albeit slightly oversized. This mask is permanently in the beam (both on-sky and in the laboratory) so that response matrices collected for the various wavefront sensors with the internal light source in SCExAO can be used on-sky as well. It is positioned as close to the pupil plane as possible ($\sim$ 70 mm away from the DM) and forms the primary pupil for the instrument. The image/pupil rotator in AO188 is used to align the telescope pupil with the fixed internal mask when on-sky (i.e. SCExAO operates with a fixed pupil and rotating image when observing).

Immediately following the mask is a dichroic beamsplitter (50 mm diameter, 7 mm thick) which reflects the visible light ($<$ 940 nm) and transmits the IR ($>$ 940 nm). In the transmitted beam path, there is a mask wheel after the dichroic which hosts numerous masks including the shaped pupil coronagraphic mask. The automated mounts for the phase induced amplitude apodization (PIAA) coronagraph lenses are adjacent to the mask wheel. They too were placed as close to the DM pupil as possible. The PIAA lenses themselves will be described in detail, for now it is important to note that they can be retracted from the beam entirely. A

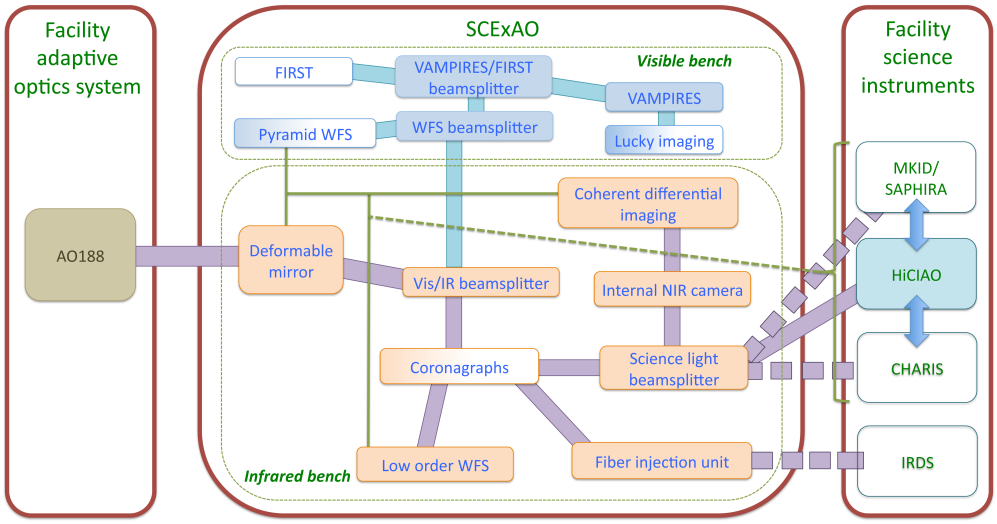

FIG. 1.— System level flow diagram of the SCExAO instrument. Thick purple and blue lines depict optical paths while thin green lines signify communication channels. Dashed lines indicate that a connection does not currently exist but it is planned for the future. Box fill indicates commissioning status. Solid boxes: commissioned, graded boxes: partially commissioned, white background: not commissioned.

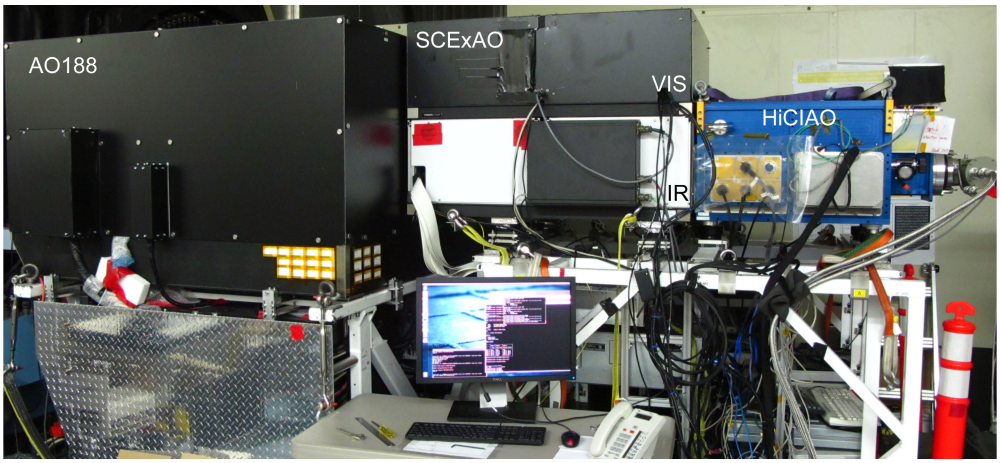

FIG. 2.— Image of SCExAO mounted at the Nasmyth IR platform at Subaru Telescope. To the left is AO188 which injects the light into SCExAO (center) and HiCIAO is shown on the right. The FIRST recombination bench is not shown for visual clarity.

flat mirror is used to steer the light onto OAP2 which focuses the beam (f = 519 mm). A variety of coronagraphic focal plane masks, used to suppress the on-axis star light are housed in a wheel which also has three axes of translation in the focal plane (the masks are outlined in sections 3.2). OAP3 recollimates the beam to a 9 mm diameter beam (f = 255 mm). A wheel with Lyot plane masks is situated in the collimated beam such that the masks are conjugated with the pupil plane. The Lyot wheel can be adjusted in lateral alignment via motorized actuators. Light diffracted by the focal plane mask and reflected from the Lyot stop is imaged onto a non-science grade (i.e. relatively high noise), high frame rate detector which is used for low order wavefront sensing. The light transmitted by the Lyot stop is next incident upon the inverse PIAA lenses (detailed in 3.2). They are mounted on stages which allow motorized control of the lateral positioning and are conjugated to the PIAA lenses upstream and can also be retracted from the beam entirely. OAP4 and OAP5 reimage the telescope pupil for the HiCIAO/CHARIS camera. On its way to the camera the beam is intercepted by the science light beamsplitter which is used to control the flux and spectral content sent to a high frame rate internal NIR camera and the facility science instruments. Detectors in a high-contrast imaging instrument are amongst the most important components and therefore the performance of those used in SCExAO is summarized in Table 1.

The light directed to the internal NIR camera passes through a filter wheel for spectral selectivity. The content of the filter wheel and the science light beamsplitter wheels are reported in Table 2. An image is formed on the internal NIR camera via a pair of IR achromatic lenses (see Section 6 for details). The sampling and field-of-view on this and other cameras is summarized in Table 3. The internal NIR camera is mounted on a translation stage allowing it to be conjugated to any location between the focal and pupil planes.

The light reflected by the dichroic on the bottom bench (which splits the visible and IR channels) is directed to-

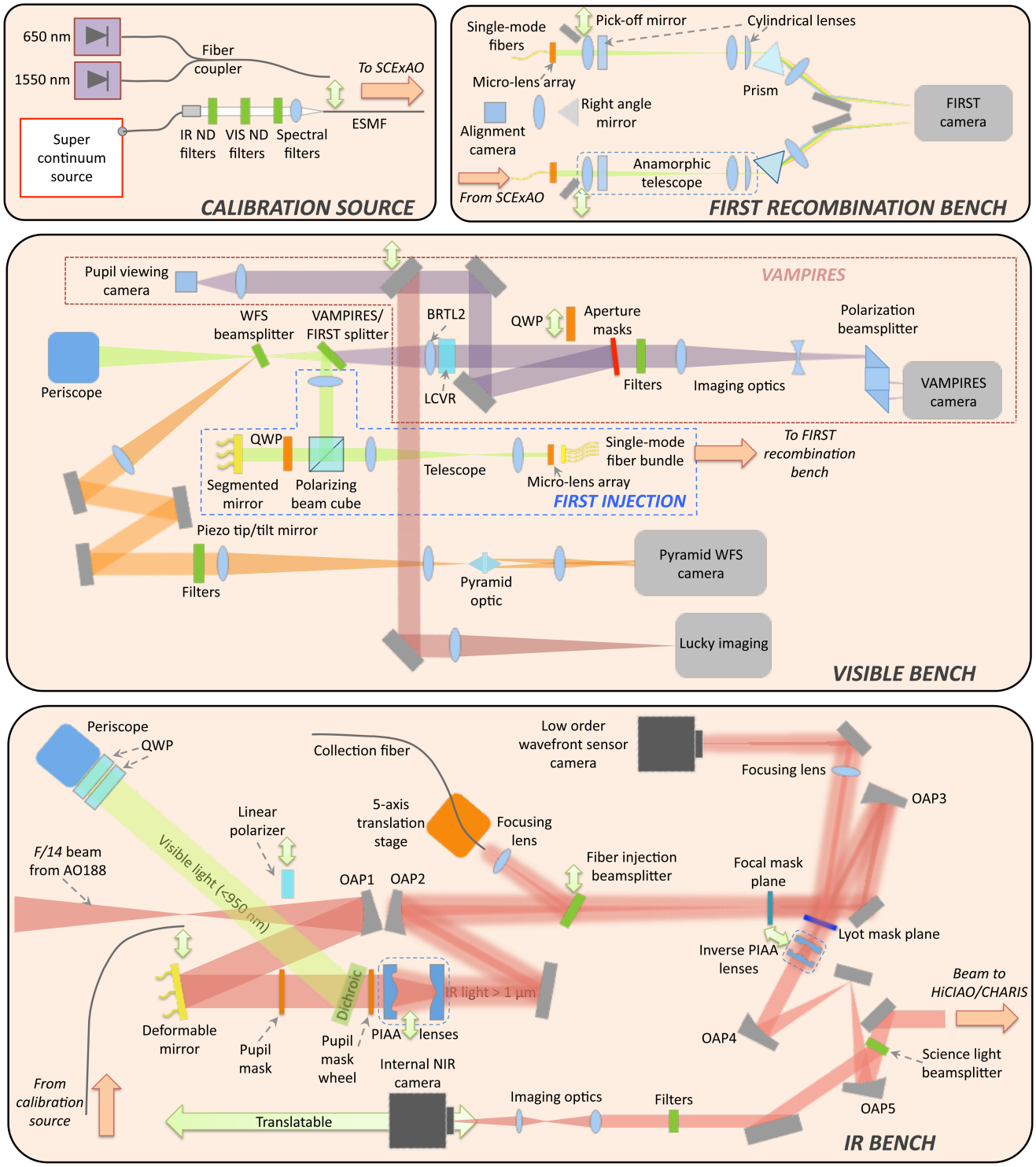

FIG. 3.— Schematic diagram of the SCExAO instrument. Top box (left): Portable calibration source layout. Top box (right): FIRST recombination bench. Middle box: layout of the visible optical bench which is mounted on top of the IR bench. Bottom box: IR bench layout. Dual head green arrows indicate that a given optic can be translated in/out of or along the beam. Orange arrows indicate light entering or leaving the designated bench at that location.

wards a periscope which transports it to the upper bench. An achromatic lens (50 mm diameter, $f = 500$ mm) is mounted in the periscope to reimage the pupil onto the top bench. A wheel hosts a range of dichroic beamsplitters at the focus of the beam on the top bench to select the spectral content to be directed towards the PyWFS (named WFS beamsplitter, content listed in Table 2). The light reflected is collimated by an achromatic lens ($f = 200$ mm) and the pupil image is located on a piezo-tip/tilt mirror used to modulate the PyWFS.

Table 1. Detector characteristics used within SCExAO.

Detector Name	Technology	Detector size (pixels)	Pixel size (μm)	Read-out noise (e^-)	Full frame (Frame-rate (Hz))	Operating Wavelengths (nm)	Manufacturer (Product name)
Internal NIR camera	InGaAs (CMOS)	320×256	30	114	170	$900 - 1700$	Axiom Optics (OWL SW1.7HS)
LOWFS camera	InGaAs (CMOS)	320×256	30	140	170	$900 - 1700$	Axiom Optics (OWL SW1.7HS)
HiCIAO/ CHARIS	HgCdTe (CMOS)	2048×2048	18	$15 - 30$	< 3	$850 - 2500$	Teledyne (HAWAII 2RG)
PyWFS (previous)	Si (sCMOS)	2560×2160 (128×128)	6.5	1.2	100 (1700)	$350 - 1000$	Andor (Zyla)
PyWFS (current)	Si (EMCCD)	240×240 (120×120)	24	< 0.3	2000 (3700)	$350 - 1000$	Firstlight Imaging ($OCAM^2K$)
Lucky imaging	Si (EMCCD)	512×512	16	< 1	35	$300 - 1000$	Andor (iXon3 897)
VAMPIRES	Si (EMCCD)	512×512	16	< 1	56	$300 - 1000$	Andor (iXon Ultra 897)
FIRST	Si (EMCCD)	512×512	16	< 1	31.9	$300 - 1000$	Hamamatsu (ImagEM C9100-13)

Note. — The values in the table are taken from manufacturer specifications/measurements. Values in parenthesis indicate the sub-framed (previous PyWFS) or binned (current PyWFS) image size and corresponding frame rate used. Read-out noise quoted for EMCCDs is with gain applied. Quantum efficiencies for these detectors are shown in Table 7.

The reflected beam is routed to focusing optics which form a converging beam with $F/\# = 40$ (a combination of achromatic lenses with focal lengths of $f = 400$ and $f = 125$ mm are used for this). A double pyramid prism shaped optic (Esposito *et al.* 2010) is placed at the focus of the beam such that the vertex is on the optical axis. An image of the resulting four pupils is generated via one additional lens ($f = 300$ mm) on the detector. The PyWFS is discussed in more detail in section 3.1.2.

The light which is not directed to the WFS is split between two modules: VAMPIRES and FIRST. The basic optical layouts are outlined here and details in regards to specifics, including calibration and performance are given in other publications (Huby *et al.* 2012; Norris *et al.* 2015). For engineering purposes a grey beamsplitter is used to divide the light between VAMPIRES and FIRST (50/50), but can be swapped for several other optics if the science demands it (contents of the VAMPIRES/FIRST splitter wheel are shown in Table 2).

The light transmitted by the splitter is used by the VAMPIRES module. It is first collimated (by BRTL2) and then passes through a series of optics including a liquid crystal variable retarder (LCVR), pupil masks, and spectral filters before being focused by a combination of a converging and diverging lens onto a low noise detector. A polarization beamsplitter, consisting of a polarizing beam cube and 3 right-angled prisms is placed in the beam after the final focusing lens and is used to spatially separate the two orthogonally polarized components on the detector. The VAMPIRES module combines aperture masking interferometry with polarimetry. The sparse aperture masks are housed in the pupil wheel where an assortment of masks with various throughputs and Fourier coverage can be found (please see Norris *et al.* (2015) for details). The module operates on 50 nm bandwidths of light selected within the 600–800 nm range, via a set of spectral filters in order to maintain fringe visibility, while maximizing the signal-to-noise ratio. At 650 nm VAMPIRES can achieve an angular resolution of 8.4 mas (Fizeau criteria) and has a field-of-view in masking mode which ranges from 80 mas to 460 mas depending on the mask selected (larger fields-of-view, $\sim$ 1–2" are possible in normal imaging mode, no mask). Rather than simply blocking the unwanted light from the pupil, the masks are reflective mirrors with transmissive sub-apertures so that the unwanted light is redirected to a pupil viewing camera (PtGrey, Flea, FL3-U3-13S2M-CS) which allows for fine alignment of the masks with the pupil. The pupil viewing mode of VAMPIRES is only used when aligning the masks. To utilize the light when pupil viewing is not being used a mirror is translated into the beam to direct the light to the Lucky imaging module/point spread function (PSF) viewer (described in detail in 3.3).

The high angular resolution imaging capability of VAMPIRES is boosted by an advanced polarimetric capability. This gains its strength from the multi-tiered differential calibration scheme which is utilized. Firstly, two quarter wave plates (HWP) mounted in front of the periscope on the bottom bench can be used to compensate for the birefringence induced by the mirrors in AO188 and SCExAO. The setting of these plates is done by careful calibration beforehand. Fast polarization modulation ($\sim$ 50 Hz) comes from the LCVR which is switched between every image. The analyzer splits the signal into two distinct interferograms on the de-

Table 2. Filter and beamsplitter wheel contents.

Slot	Internal camera filters	Science light beamsplitters	Wavefront sensor beamsplitter	VAMPIRES/FIRST splitter
1	Open	AR-coated window ($900-2600$ nm)	Open	Silver mirror
2	T=y-band	$T, R = 50\%$ ($900-2600$ nm)	Silver mirror	$T, R = 50\%$, $600-950$ nm
3	T=J-band	$T = 10\%$, $R = 90\%$ ($900-2600$ nm)	$T, R = 50\%$, $600-950$ nm	$T < 700$ nm, $R > 700$ nm
4	T=H-band	$T = 90\%$, $R = 10\%$ ($900-2600$ nm)	$T < 650$ nm, $R > 650$ nm	$T > 700$ nm, $R < 700$ nm
5	50 nm bandpass at 1600 nm	$T > 90\%$ ($1400-2600$ nm), $R > 95\%$ ($900-1400$ nm)	$T < 700$ nm, $R > 700$ nm	AR-coated window ($600-950$ nm)
6	-	$T > 90\%$ ($1900-2600$ nm), $R > 95\%$ ($900-1900$ nm)	$T < 750$ nm, $R > 750$ nm	Open
7	-	Gold mirror	$T < 800$ nm, $R > 800$ nm	-
8	-	-	$T < 850$ nm, $R > 850$ nm	-
9	-	-	$T > 750$ nm, $R < 750$ nm	-
10	-	-	$T > 800$ nm, $R < 800$ nm	-
11	-	-	$T > 850$ nm, $R < 850$ nm	-

Note. — The values in the table are based on the final measurements made by the manufacturer. T-Transmission, R-Reflection. AR-anti-reflection. Note item 5 and 6 of the science light beamsplitter have not been delivered yet.

Table 3. Plate scale and field-of-view.

Detector	Sampling (mas/pixel)	Field-of-view (")
Internal NIR camera	12.1 ± 0.1	4×3
HiCIAO	8.3 ± 0.1	$> 10 \times 10$
VAMPIRES (M)	-	0.08–0.46
VAMPIRES (NM)	6.0	2×1
FIRST	-	0.1

Note. — All values in this table were measured off-sky by moving the calibration source laterally in the input focal plane (AO188 focal plane) and determining this motion in pixels on the detector. This motion is converted to a plate scale based on the knowledge of the AO188 plate scale which is well known to be 1.865 "/mm. This method yields consistent values to those obtained by looking at astrometric binaries. M-with aperture masks, NM-no masks. Range of field-of-view is dependent on choice of mask. Please see Norris *et al.* (2015) for more details.

tector with orthogonal polarizations. Finally, a HWP positioned in front of AO188, used for HiCIAO polarimetric imaging in the NIR, was determined to work well in the visible and is used as the main polarization switching component in VAMPIRES. The quarter wave plate (QWP) before the aperture mask wheel and the polarizer on the bottom bench are used for calibrating the polarization systematics with the internal calibration source and can be swung into the beam when off-sky (they are not used on-sky). For more details about the nested differential calibration procedure please refer to Norris *et al.* (2015).

The light reflected by the beam splitter is sent to the FIRST module. It is collimated before entering a polarizing beamsplitter cube. The main beam is reflected at 90° onto a 37 element segmented mirror (Iris AO (Helmbrecht 2011)) which is conjugated to the pupil plane. A QWP placed between the polarizing beamsplitter and the segmented mirror is used to rotate the polarization so that the beam passes through the cube when reflected off the segmented mirror. A beam reducing telescope compresses the beam so that a single segment of the mirror has a one-to-one correspondance with a micro-lens in the micro-lens array (MLA) used for injecting into the bundle of single-mode polarization maintaining fibers (see Fig. 3). This architecture allows the segmented mirror to fine tune the coupling into each of the fibers with small tip/tilt control. Currently 18 of the 30 available fibers (2 sets of 9 fibers each) are used and they transport the light to a separate recombination bench (see Fig. 3) where the interferograms are formed and data collected. A description of the recombination bench is beyond the scope of this work. The instrument offers an angular resolution of 9 mas at 700 nm with a 100 mas field-of-view ($\sim 6\lambda/D$ in radius). In addition, broadband operation from 600–850 nm, with a spectral resolving power of 300, offers a new avenue to maximizing data output while using standard bispectrum analysis techniques (and hence precision/contrast) while simultaneously allowing spectra to be collected.

FIRST has had several successful observing campaigns on close binary stars at Lick Observatory. It has now made the move from the Cassegrain focus of the Shane telescope to the gravitationally invariant Nasmyth platform of Subaru Telescope, which minimizes mechanical flexure and hence instrumental instabilities. A more comprehensive description of the instrument including the recombination bench, how it works and the initial science results is presented in Huby *et al.* (2012, 2013).

Despite all the advanced wavefront control, interferometers and coronagraphs in SCExAO, the performance of the system is highly dependent on the stability of the PSF. Vibrations can plague high-contrast imaging testbeds via flexure, windshake of mirrors, or moving parts (cryocoolers for example). For this reason several key efforts have been made to address PSF stability in SCExAO. Firstly four elastomer-based vibration isolators (Newport, M-ND20-A) are used to support the SCExAO bench at the Nasmyth platform. These elastomers have a natural frequency $9-12$ Hz and are used to damp high frequency mechanical vibrations from the surrounding environment. Secondly, the mounts for the OAP-based relay optics in the instrument were custom made from a single piece to minimize the drift of the PSF. Finally, the mounting scheme for the HiCIAO cry-

ocooler was rebuilt such that the pump was connected to the dewer by springs and metal bellows only (soft connections with low spring constants for maximum damping). This reduced the tip/tilt jitter observed on the NIR internal camera by a factor of 10 at 10 Hz and up to 100 at a resonant frequency of 23 Hz (Jovanovic *et al.* 2014a). These steps have improved overall PSF stability against long term drifts and vibrations above a few Hz. However, there are small residual resonances which will be addressed with a linear quadratic Gaussian (LQG) controller (Poyneer *et al.* 2014) implemented to the LLOWFS loop in future.

2.3. *Internal calibration*

An important feature of any high-contrast testbed is the ability to internally calibrate it off-sky. The SCExAO instrument can be aligned/calibrated with its internal calibration source. The source can be seen in Fig. 3 and consists of a standalone box which houses a super continuum source (Fianium - Whitelase micro) for broadband characterization, and two fiber coupled laser diodes (675 nm and 1550 nm) for alignment. The light from the super continuum source is collimated and passes through a series of wheels which house neutral density filters for both visible and IR wavelengths as well as a selection of spectral filters. The light is coupled into an endlessly single-mode photonics crystal fiber (NKT photonics - areoGUIDE8) which transports the light to the SCExAO bench. The fiber is mounted on a translation stage and can be actuated into the focus of the AO188 beam (see Fig. 3) when internal calibration is performed or the instrument is not at the telescope. The endlessly single-mode fiber is ideal for this application as it offers a diffraction-limited point source at all operating wavelengths of the super continuum source and SCExAO ($600 - 2500$ nm).

The effects of atmospheric turbulence can also be simulated. This is achieved by using the DM to create a large phase-screen with the appropriate statistical fluctuations. A single-phase screen Kolmogorov profile is used where the low spatial frequencies can be attenuated, to mimic the effect of an upstream AO system like AO188. A 50×50 pixel sub-array (corresponding to the actuators of the DM) is extracted from the larger phase screen. By scanning the sub-array across the phase map, a continuous and infinite sequence of phase screens can be generated. The amplitude of the RMS wavefront map, the magnitude of the low spatial frequency modes and the speed of the sub-array passing over the map (i.e. windspeed) are all free parameters that can be adjusted. This simulator is convenient as it allows great flexibility when characterizing SCExAO modules. Note that due to the limited stroke of the DM (which is discussed in section 3.1.1), the turbulence simulator cannot be used to simulate full seeing conditions but provides a level of wavefront perturbation that is representative of post AO188 observing conditions. Finally, although the simulator can provide turbulence with the correct spatial structure pre or post AO, it does not take into account the temporal aspects of the correction provided by an upstream AO system (i.e. AO corrects low temporal frequencies leaving only higher frequencies).

2.4. *Instrument throughput*

To plan observing schedules and determine the limitations of the instrument, the throughput was accurately characterized. As SCExAO has many branches, Tables 4 and 5 summarize the measured internal system throughput for each. Although not explicitly listed, the throughputs include all flat mirrors required to get the light to a given module. In addition Table 6 highlights the measured throughputs of the optics upstream from SCExAO which includes the effects of the atmosphere, telescope, AO188 HWP, atmospheric dispersion compensator (ADC), AO188 optics as well as HiCIAO. To determine the total throughput to a given detector plane of the instrument, one should first use Table 2 to select the appropriate beamsplitter, and then find the corresponding throughput for that branch from Table 4 or 5. This value should then be multiplied by the relevant throughputs in Table 6. To convert to photoelectrons, the quantum efficiencies for the detectors used in SCExAO are listed in Table 7. Finally, the throughputs of the focal plane masks used for the coronagraphs are not shown in Table 4 as they are specifically designed to attenuate the light. Indeed, the throughput of these masks depends on the distance from the optic axis and for this we refer the reader to literature such as Guyon (2005).

From the tables we can determine the throughput to several focal planes within SCExAO as an example of the system performance and a demonstration of how to use the tables. One commonly used observing mode involves directing the majority of the post-coronagraphic light towards HiCIAO for H-band imaging. In this case one would select the 90% transmitting beamsplitter in the science light beamsplitter wheel (Slot 4 from Table 2). In this case the throughput of SCExAO would be 9.4% to the internal NIR camera and 58.2% to HiCIAO (from Table 4). To determine the total throughput from the top of the atmosphere, one would need to multiply the SCExAO throughputs by those listed for the atmosphere (97%), telescope (92%), HWP (94%), ADC (92%), AO188 (79%) and HiCIAO optics/filters (78%) by those listed in Table 6, which yields values of 4.5% and 27.7% respectively. From here one would need to take into account the losses of the focal plane and Lyot masks which are coronagraph specific. Finally, it is possible to use the quantum efficiencies listed in Table 7 to convert the throughput of the instrument into the number of photoelectrons on the HiCIAO detector for a given magnitude target.

In addition to flux at the detector plane, the throughput to the primary wavefront sensor is a useful piece of information for appropriate target selection. Since the PyWFS does most of its sensing at 850–900 nm, one could operate with an 800 nm short pass filter in the wavefront sensor beamsplitter wheel (slot 7 from Table 2). The throughput of SCExAO to the WFS detection plane with this splitter would be 48.7% in the z-band (from Table 5). The associated throughput as measured from the top of the atmosphere would be 23.2% (including the z-band throughputs from Table 6). This relatively low throughput is attributed to the fact the PyWFS is a long way downstream of the telescope and even within SCExAO. In the future, if SCExAO were to be rebuilt, one could imagine moving the WFS to be the first element after the telescope and ADC which would no doubt improve

Table 4. Throughput of the various arms of the IR channel of SCExAO measured in the laboratory from the internal calibration source.

Path (elements)	Band	Throughput (%)
From calibration source input to....		
Internal NIR camera		
(OAPs, DM, SLB2)	y	35.3
(OAPs, DM, SLB3)	y	60.6
(OAPs, DM, SLB4)	y	4.5
(OAPs, DM, SLB7)	y	71.1
(OAPs, DM, SLB2)	J	27.2
(OAPs, DM, SLB3)	J	53.7
(OAPs, DM, SLB4)	J	5.9
(OAPs, DM, SLB7)	J	50.4
(OAPs, DM, SLB2)	H	32.8
(OAPs, DM, SLB3)	H	56.2
(OAPs, DM, SLB4)	H	9.4
(OAPs, DM, SLB7)	H	63.4
Facility science instruments		
(OAPs, DM, SLB1)	y	72.1
(OAPs, DM, SLB2)	y	34.9
(OAPs, DM, SLB3)	y	7.6
(OAPs, DM, SLB4)	y	67.2
(OAPs, DM, SLB1)	J	66.9
(OAPs, DM, SLB2)	J	33.4
(OAPs, DM, SLB3)	J	6.2
(OAPs, DM, SLB4)	J	60.5
(OAPs, DM, SLB1)	H	65.2
(OAPs, DM, SLB2)	H	31.8
(OAPs, DM, SLB3)	H	5.0
(OAPs, DM, SLB4)	H	58.2
Single-mode injection		
(OAPs, DM, FIB)	J	77.0
(OAPs, DM, FIB)	H	78.3
Components in isolation		
(PIAA+binary Mask+IPIAA)	y	53.2
(PIAA+binary Mask+IPIAA)	J	52.2
(PIAA+binary Mask+IPIAA)	H	52.5

Note. — OAPs-refers to off-axis parabolic mirrors used to relay the light, DM-The window and mirror of the DM, SLB-science light beamsplitter, the number designates the slot (see Table 2), FIB-Fiber injection beamsplitter.

Table 5. Throughput of the various arms of the visible channel of SCExAO measured in the laboratory from the internal calibration source.

Path (elements)	Band	Throughput (%)
From calibration source input to....		
Pre-WFSBS		
(PTTB)	R	57.8
	I	65.4
	z	65.6
PyWFS camera		
(PTTB + PyWFS optics	R	43.0
WFSBS 2)	I	47.1
	z	47.6
(PTTB + PyWFS optics,	R	20.5
WFSBS 3)	I	23.0
	z	25.2
(PTTB + PyWFS optics,	R	42.4
WFSBS 4, 9, 10 or 11)		
(PTTB + PyWFS optics,	I	49.1
WFSBS 4, 5, 6 or 7)		
(PTTB + PyWFS optics,	z	48.7
WFSBS 4, 5, 6, 7 or 8)		
VAMPIRES camera		
(PTV + WFSBS 3)	R	12.6
	I	15.3
	z	15.2
(PTV + WFSBS 5, 6, 7 or 8)	R	25.3
(PTV + WFSBS 8)	I	27.5
(PTV + WFSBS 9, 10 or 11)	z	30.6)
FIRST input		
(PTF + WFSBS 3)	R	12.6
	I	15.3
	z	13.4
(PTF + WFSBS 5, 6, 7 or 8)	R	27.1
(PTF + WFSBS 8)	I	29.0
(PTF + WFSBS 9, 10 or 11)	z	28.6

Note. — OAP1-refers to the first off-axis parabolic mirror used to relay the light, DM-The window and mirror of the DM, WFSBS-Wavefront sensor beamsplitter, the number designates the slot (see Table 2), BRTL1-beam reducing telescope lens 1 which is located in the periscope. Path to top bench (PTTB): OAP1, DM, dichroic, QWP ×2, periscope mirrors, BRTL1. Path to VAMPIRES (PTV): OAP1, DM, dichroic, QWP ×2, periscope mirrors, BRTL1 & 2, 50/50 BS and focusing lenses. Path to FIRST (PTF): OAP1, DM, dichroic, QWP ×2, periscope mirrors, BRTL1, 50/50 BS and collimating lens. Note the throughput is only quoted to the input of FIRST. Also, the throughput of the aperture masks for VAMPIRES were not included, please see Norris *et al.* (2015) for these values.

the throughput by a factor of 2 at least. This would allow the PyWFS to operate with high performance on a 1 magnitude fainter star.

3. THE FUNCTIONALITIES OF SCEXAO

Key to the successful implementation of a high performance coronagraph or interferometer for high-contrast imaging is a wavefront control system to correct for both atmospheric as well as instrumental aberrations. Wavefront control comprises two primary components: sensing and correction. The former is taken care of by a wavefront sensor, a device designed to map the spatial profile of the phase corrugations while the latter by an adaptive element such as a DM. In this section we describe how the elements of SCExAO function.

3.1. *Wavefront control*

3.1.1. *Wavefront correction*

The deformable mirror is the proverbial heart of any adaptive optics system. The 2k DM used in SCExAO (Figure 4) is manufactured by Boston Micromachines Corporation based on MEMS technology. The DM is enclosed in a sealed chamber in order to control its environment. The critical parameter to control is the humidity level and is kept below 20% as advanced aging of MEMS actuators has been observed when high voltages (180 V is the maximum that can be applied), required to actuate individual elements, are applied in a moist environment (Shea *et al.* 2004). A desiccant is used to filter the compressed air of moisture. A circuit monitors both humidity and pressure and is setup to interlock the power

Table 6. Throughput of the atmosphere, telescope, AO188 HWP, atmospheric dispersion compensator (ADC), AO188 optics and HiCIAO as a percentage.

Band	Atmos.	Tele.	HWP	ADC	AO188	HiCIAO
R	91	82	93	95	68	-
I	96	75	95	95	69	-
z	97	79	95	95	69	-
y	98	80	94	95	72	-
J	95	91	96	94	77	87
H	97	92	94	92	79	78
K	92	93	92	70	82	82

Note. — The atmospheric transmission in R, I, Z bands is estimated from Buton *et al.* (2012). The throughput of the atmosphere in the y, J, H and K bands assumes an airmass of 1.5 and precipitable water vapor content of 1.6 mm (data taken from Gemini Observatory website) (Lord 1992). The throughput of the telescope is calculated from the reflectivity of the material used for the coating and does not include effects like diattenuation from M3 for example. The throughput for the HWP and ADC were measured on-sky. The throughputs for R, I, Z, and y band for AO188 have been calculated from materials. J, H and K band throughputs for AO188 were measured.

Table 7. Quantum efficiency as a function of waveband for the detectors in SCExAO as a percentage.

Detector	R	I	z	y	J	H	K
Internal NIR camera	-	-	-	58	73	73	-
LOWFS camera	-	-	-	58	73	73	-
HiCIAO/CHARIS	-	-	-	-	46	68	68
PyWFS (current)	98	96	77	-	-	-	-
Lucky imaging	93	74	47	-	-	-	-
VAMPIRES	93	74	42	-	-	-	-
FIRST	91	70	42	-	-	-	-

Note. — Values were taken from manufacturer specifications.

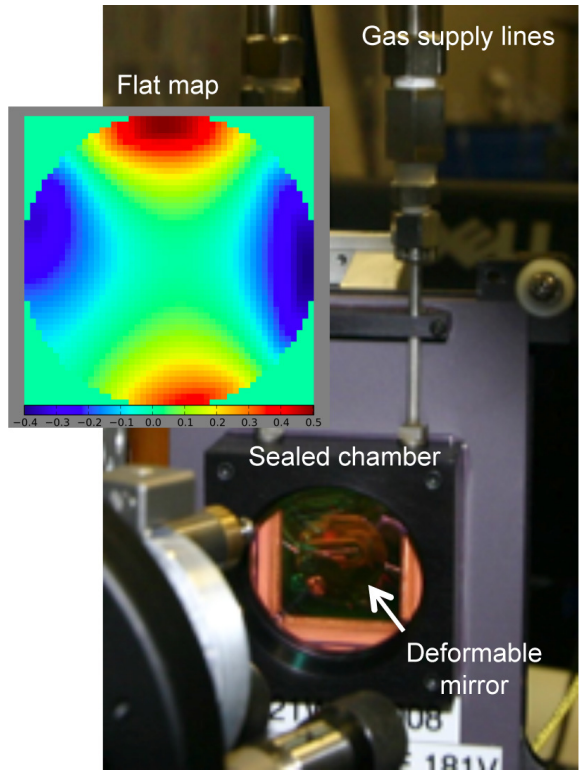

Fig. 4.— 2k DM mounted in the SCExAO instrument. The gas supply lines to the sealed chamber can be seen along with the gold surface of the DM itself. Inset: The map applied to the DM in order to compensate for the DM surface figure. The map shows the magnitude of the modulation of the actuators in microns. The window is 50 actuators in diameter corresponding to the functioning region of the DM. The map required to flatten the DM surface is dominated by the Zernike which represents astigmatism.

to the DM based on these two metrics (see Section 6).

The chamber window is optimized for transmission across the entire operating range of SCExAO, 550 – 2500 nm (anti-reflection coated, IR fused silica). The DM's silicon membrane is gold coated and hosts 2000 actuators within the 18 mm diameter beam (there are others outside the pupil but they are not connected). The membrane is bonded to the ~ 250 μm square-shaped actuators which are on a pitch of 400 μm. This means that there are 45 and 45.5 actuators across the 18 mm beam in the vertical and horizontal directions respectively. The number of actuators across the DM defines the highest spatial frequency components which can be probed/controlled by the DM and hence the region of control in the focal plane. For our case the 45 actuator pupil diameter means that the fastest modulation that can be Nyquist sampled by the DM consists of 22.5 cycles across the diameter. This means that spatial frequencies out to 22.5 λ/D from the PSF can be addressed, which defines the radius of the control region in the focal plane (0.9" in H-band, highlighted in Fig. 5). Figure 5 shows the surface of the DM, where the 5 dead actuators (actuators that cannot be modulated) are clearly visible. Fortunately, it was possible to position three of the actuators behind the secondary or outside the pupil and one is partially blocked by the spiders of the telescope, leaving only one dead segment in the illuminated pupil. Dead segments compromise the maximum contrast achievable post coronagraph as they diffract light and hence the 1–2 illuminated for SCExAO is close to ideal. Note, most coronagraph Lyot stops currently installed in SCExAO do not mask out the actuators, but there are plans to include such masks in the future. In addition the resolution of the DM can be qualitatively examined in Fig. 5 where a bit map image of the PI, Guyon's face and the bat symbol have been imprinted in phase. The camera used to capture the image is not conjugated to the plane of the DM so that phase information gets recorded as amplitude information on the camera. The resolution of the images generated by the DM demonstrates the high level of sophistication MEMS technology has reached.

The surface of the unpowered DM is not flat. The inset to Figure 4 shows the voltage map that needs to be applied to obtain a flat DM in units of microns of stroke, known as a flatmap. The distortion of the surface of the DM is clearly dominated by astigmatism. Images of the PSF of SCExAO taken without and with the flat map applied are shown in the top left panels of Fig. 5. The image without the flatmap is consistent with the presence of strong astigmatism. The PSF post flatmap

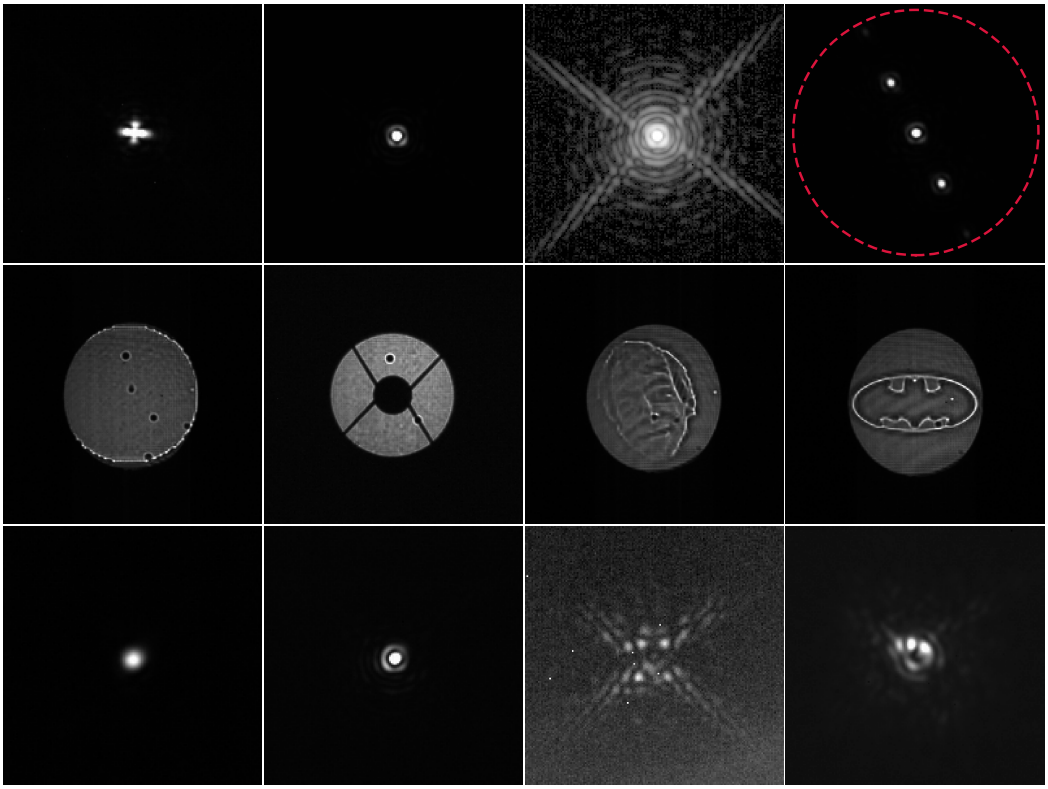

FIG. 5.— Top row: PSF of SCExAO at 1550 nm with the unpowered DM surface (left). Strong astigmatism is clearly visible. An image of the instrument PSF taken with the optimum flat map applied with linear (middle-left) and logarithmic (middle-right) scaling. The image is diffraction limited and numerous Airy rings can be seen. Image with several artificial speckles applied (right). The dashed ring designates the edge of the control region of the DM corresponding to a radius of 22.5 λ/D or 900 mas at 1550 nm. Second row: Pupil images showing the unmasked surface of the DM with 5 dead actuators (left), the internal spider mask in place masking several actuators (middle-left), an image of the PI Guyon (middle-right) and the bat symbol (right). These two images demonstrate the resolution of the DM. Bottom row: Image of the PSF taken in the laboratory with a laser at 1550 nm, after the conventional PIAA lenses (left), with the IPIAA lenses (middle-left) as well as with the achromatic focal plane mask (AFPM) (1.9 λ/D IWA) (middle-right). (right) An image with the PIAA, IPIAA and AFPM is shown taken on-sky on the night of the 25^{th} of July 2013 with the full H-band.

is diffraction-limited. It is clear that the maximum stroke required for correction near the edges approaches 0.5 μm. This means that 25% of the 2 μm stroke of the actuators is used up to flatten the DM.

3.1.2. *Wavefront sensing*

Wavefront correction within the SCExAO instrument comes in two stages: low spatial and temporal frequencies are partially corrected by AO188 prior to being injected into SCExAO where a final correction including higher order modes is implemented. In good seeing conditions AO188 can offer $30-40$% Strehl ratios in the H-band. The high-order wavefront correction, which is the focus of this section is facilitated by a pyramid wavefront sensor (PyWFS). The PyWFS is chosen because of its large dynamic range and its sensitivity properties (Guyon 2005). In its standard implementation, a tip/tilt mirror modulates the location of the PSF in a circular trajectory which is centered on the apex of the pyramid. This implementation has been used to correct seeing-limited light to Strehl ratios as high as 90% in very good seeing on LBTAO (Esposito *et al.* 2011) and MagAO (Close *et al.* 2013). By removing modulation however, the range over which the sensor responds linearly to aberrations is greatly reduced. Hence to utilize a PyWFS without modulation the wavefronts must be partially corrected by another sensor initially. With AO188 providing such a correction upstream, this implementation is possible with the PyWFS on SCExAO. SCExAO incorporates a piezo-driven mirror mount (shown in Fig. 3) to provide the modulation functionality, with the driver carefully synchronized to the frame rate of the camera. The implementation allows for continuous changes of the modulation radius (see Fig. 6). Such an architecture enables the possibility to start with a modulated PyWFS that has a larger range of linearity and slowly transition to a non-modulated sensor for maximum sensitivity and the highest Strehl ratio, as wavefront errors are gradually reduced.

The PyWFS has undergone laboratory and initial testing on-sky. In its initial format it exploited a micro-lens array instead of a pyramid optic as it was easier to obtain (pyramid optics need to be custom made). However, it was determined that although small micro-lenses have good inter-lens quality, which keeps diffraction effects at a minimum, they have a limited field-of-view which limits their use with modulation. On the other hand, larger micro-lenses remove this limitation but the inter-lens quality is poor and results in strong diffraction. Hence it was not possible from the 2 micro-lens ar-

rays tested to simultaneously obtain a large field-of-view and low diffraction (there may indeed be micro-lenses on the market that can achieve both) (Clergeon 2014). For this reason a dedicated pyramid optic was obtained. The pyramid optic presented here is a double pyramid, as shown in Figure 6 and is a replica of the one used on MagAO (Close *et al.* 2013; Esposito *et al.* 2010). The pyramid optic segments the PSF and generates 4 images of the pupil on the camera (see Fig. 6). The OCAM^{2}k from FirstLight imaging (see full specs. in Table 1), is used as the detector and is capable of photon counting, with low read noise, high frame rate, and low latency (< 1 frame) which enables the correction of high temporal frequencies and allows operation on faint guide stars. To facilitate full speed PyWFS loop operation (limited by camera frame rate), fast computations are required and for this a bank of GPUs is utilized. Details of the control loop architecture for the PyWFS are beyond the scope of this work. Here we focus on the recent performance of the loop.

In laboratory testing, the PyWFS successfully closed the loop with modulation (amplitude of 1.7 λ/D) on up to 830 modes. Our modal basis consisted of linearly-independent modes obtained by singular value decomposition of an input basis consisting of 5 Zernike coefficients (tip, tilt, focus, astigmatisms) and the remainder Fourier modes (sine waves) up to a given spatial frequency of the DM. Non-orthogonality between input modes was addressed by rejecting (not controlling) low-eigenvalue modes. This basis set was chosen purely for convenience. This was achieved with the turbulence simulator generating 300 nm RMS wavefront error maps with a wind speed of 5 m/s and the low order spatial frequencies scaled to 30% of the Kolmogorov power spectrum value to simulate upstream low order wavefront correction. Light with wavelengths between 800 and 940 nm was used for the tests and the loop was run at 1 kHz. The Strehl of the images captured by the internal NIR camera was measured in the open and closed-loop regime and the results depicted in Fig. 6. The average Strehl in the open-loop regime was 23% which is consistent with the value predicted from Marechal's approximation (Hardy 1998) (22.7%) given 300 nm of wavefront error at 1550 nm. When the loop is closed on 830 modes, the Strehl improved to $> 90\%$ on average confirming that given realistic post-AO correction, the PyWFS can indeed achieve extreme AO performance as required.

The non-modulated mode was also tested with the turbulence simulator in the laboratory. However, due to the smaller linear range of the sensor without modulation the amplitude of wavefront errors was reduced. For the purposes of the test it was set to 60 nm (windspeed 5 m/s and low order Kolmogorov frequencies set to 30%). The loop was successfully closed at 1.5 kHz on the turbulence simulator on 1030 modes (which include 5 Zernikes). In this regime, it was clear that the speckles in the halo surrounding the PSF were held very static. The loop speed is constantly being improved by optimizing the code and removing delays. An operational speed as high as 3.5 kHz with minimal delay should be possible in the near future. Since the WFS detector operates in photon-counting mode, the loop will be able to run at full speed (3.5 kHz) even on faint targets (I-mag $\sim$ 10) albeit at lower loop gain. Fainter targets still will require lower

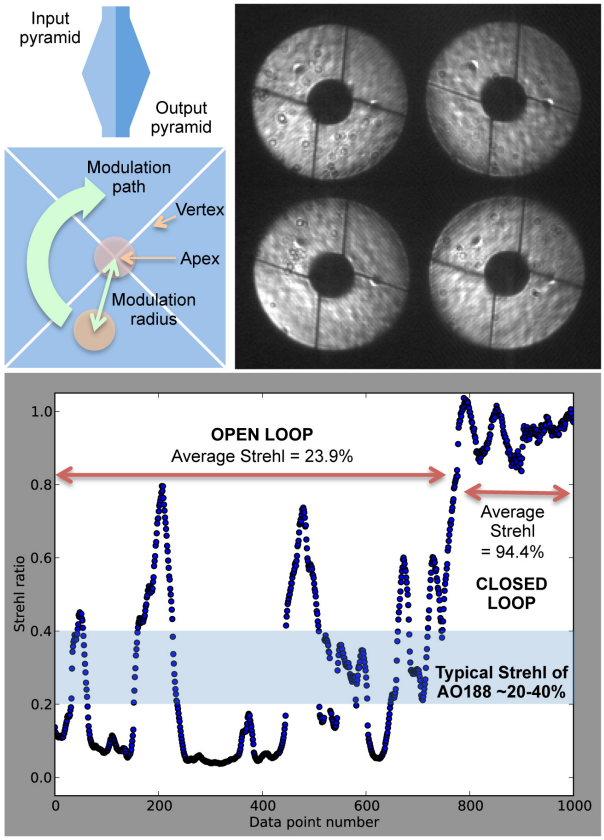

FIG. 6.— (Top left) A side view of the double pyramid. A very shallow angle ($\sim 1°$) is required which is hard to produce so two steeper pyramids are used such that the cumulative effect of refraction between them is equivalent to a single shallower sloped pyramid optic (Esposito *et al.* 2010). Below this a front view of the pyramid is shown. The circles represent the PSF position without modulation (red spot) and with modulation (orange spot). The green arrow shows the path of the PSF across the front face of the pyramid optic when modulation is applied. (Top right) An image of the four pupils generated by the pyramid optic taken with modulation applied. (Bottom image) Strehl measured for the internal source with 300 nm RMS wavefront error applied to the turbulence simulator and the PyWFS loop open and then closed. NB, the Strehl ratio calculation procedure has a limited accuracy of about $5-7\%$ when the Strehl ratio is $> 90\%$. Hence values > 1 are possible in this regime as shown in the above chart and should simply be interpreted as regions of high Strehl, with no emphasis put on the exact value.

loop speeds. An optimal modal gain integrator will also be implemented soon.

Thus far the PyWFS has undergone some initial on-sky testing and has performed well on up to 130 modes (with modulation, 1.7 λ/D radius). However as the speed of the loop was the same as AO188 (i.e. 1 kHz) and there were less modes than are corrected by AO188 a negligible improvement in Strehl was observed. Most of the gain came in the form of reduced tip/tilt jitter which was clearly visible in long integration time images. With further improvements in the AO loop code, the PyWFS should perform as demonstrated in the laboratory more recently, on-sky.

Non-common path and chromatic low-order errors between the visible PyWFS and the IR coronagraphs, are measured with the LLOWFS on the IR channel. The

LLOWFS utilizes the light diffracted by the focal plane masks of the coronagraphs (discussed in detail in sections 3.2), which is otherwise thrown away. A reflective Lyot stop is used to direct the diffracted light to the LOWFS camera (Singh *et al.* 2014). In this way a reimaged PSF formed on the camera can be used to drive low-order, including tip/tilt, corrections by looking at the presence of asymmetries in the image. It has been tested thoroughly both in the laboratory and on-sky. Indeed it was used on-sky in conjunction with the vector vortex coronagraph on Vega, on the nights of the $14/15^{th}$ April, 2014, and produced residual RMS tip/tilt wavefront errors of $0.01\lambda/D$ (Singh *et al.* 2015).

In addition to the PyWFS and LLOWFS we are testing other wavefront sensing techniques. One such technique is known as focal plane wavefront sensing which exploits eigenphase imaging techniques (Martinache 2013). The focal plane wavefront sensor relies on establishing a relationship between the phase of the wavefront in the pupil plane and the phase in the Fourier plane of the image. Although it has a limited range of linearity ($\sim \pi$ radians), which means that the wavefront must first be corrected to the 40% Strehl ratio level before this sensor can be utilized, it can boost the Strehl ratio to $> 95\%$ in the H-band by correcting low order modes. In addition, it operates just as effectively in the photon noise regime and is extremely powerful as non-common path errors are eliminated. This wavefront sensor is currently under development and has been successfully tested on both the internal calibration source, in which case the aberrations due to the internal SCExAO optics were corrected as well as on-sky, where the static aberrations due to the telescope, AO188 optics and SCExAO were all corrected. Some additional detail of this work can be found in Martinache *et al.* (2014a).

3.1.3. *Coherent speckle modulation and control*

As a booster stage to the primary wavefront control loops, SCExAO makes use of coherent speckle modulation and control to both measure and attenuate residual starlight in the instrument's post-coronagraph focal plane. The 2k DM actuators are used to remove starlight from a pre-defined region, referred to as the dark hole (Malbet *et al.* 1995). Active modulation, induced by the 2k DM, creates coherent interferences between residual speckles of unknown complex amplitude and light added by modifying the DM's shape (this component's complex amplitude is known from a model of the DM response and the coronagraph optics). By iterating cycles of measurement and correction, starlight speckles that are sufficiently slow to last multiple cycles are removed from the dark hole area. This approach, developed and perfected in the last 20 yrs (Borde & Traub 2006; Codana & Kenworthy 2013; Give'on *et al.* 2007; Guyon *et al.* 2010; Malbet *et al.* 1995), is well suited to high-contrast imaging as it effectively targets slow speckles, which are the dominant source of confusion with exoplanets. It also allows coherent differential imaging (CDI), a powerful post-processing diagnostic allowing true sources (incoherent with the central starlight) to be separated from residual starlight (Guyon *et al.* 2010). Compared to passive calibration techniques, such as angular differential imaging, CDI offers more flexibility, and achieves faster averaging of speckle noise. This is especially relevant at small angular separations, where ADI would require very long observation time to achieve the required speckle diversity. An example of a pair of speckles being generated by a periodic corrugation applied to the DM and used for starlight suppression is shown in the top right inset of Fig. 5.

In SCExAO, coherent speckle control is implemented as discrete speckle nulling: the brightest speckles are identified in the dark hole region, and simultaneously modulated by the 2k DM, revealing their complex amplitudes. The 2k DM nominal shape is then updated to remove these speckles, and successive iterations of this loop gradually remove slow and static speckles. While discrete speckle nulling is not as efficient as more optimal global electric field inversion algorithms, it is far easier to implement and tune and thus more robust for ground-based systems which have much larger wavefront errors than laboratory testbeds or space systems. This approach has been validated on SCExAO both in the laboratory (Martinache *et al.* 2012) and on-sky (Martinache *et al.* 2014b) and is a means of carving out a dark hole on one side of the PSF to boost contrast in that region. A recently taken image demonstrating the successful implementation of speckle nulling without a coronagraph on RX Boo is shown in the lower panel of Fig. 7. The region where the nulling process was performed is outlined by the dashed white line and spans from $5-22.5\ \lambda/D$. An image without the nulling applied is shown in the top panel of Fig. 7 for comparison. This result was obtained on the 2^{nd} of June 2014 in favorable seeing conditions (seeing < 0.7"). The nulling process reduced the average flux over the entire controlled area by 30% and by 58% in the region between $5-12\ \lambda/D$, where the nulling was most effective. With better wavefront correction and the use of a coronagraph, the improvement in the contrast will grow.

The current limitations to achieving high-quality speckle nulling on-sky are: wavefront correction, readout noise and loop speed. As high sensitivity cameras in the NIR are currently limited in regards to maximum frame rate (the Axiom cameras used are amongst the fastest commercially available at the time of writing), it is not possible for the active speckle nulling algorithm to pursue atmospherically induced speckles as they change from frame-to-frame. Hence, the current implementation of speckle nulling on SCExAO aims at removing the static and quasi-static speckles induced by diffraction from the secondary and spiders as well as optical aberrations. For this reason it is important to have a high level of atmospheric wavefront correction on-sky so that the persistent speckles due to static and quasi-static aberrations can be easily identified. As the speckles are $\sim 1000\times$ fainter than the PSF core, a magnitude limit for speckle nulling of 3–4 in the H-band is imposed by the current cameras used due to the high readout noise ($114e^-$). This places a severe limitation on potential targets of scientific interest. To alleviate these issues SCExAO is acquiring a Microwave Kinetic Inductance Detector (MKID) which is a photon counting, energy discriminating NIR array (Mazin *et al.* 2012). The MKID array will offer almost no readout noise or dark current and is capable of high frame rates (> 1 kHz). This enables speckle nulling to be performed on fainter more scientifically relevant targets and for non-common speckles due to chro-

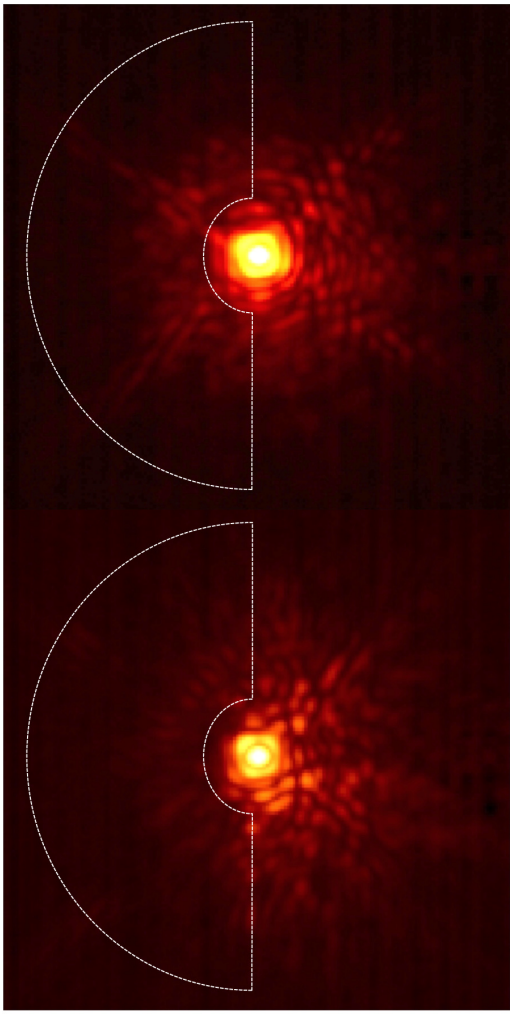

FIG. 7.— Top: RX Boo with no speckle nulling applied. Bottom: RX Boo with speckle nulling performed on the region enclosed by the white dashed line. Each image is a composite of 5000, 50 μs frames which have been shifted and added together. Each panel has a square root stretch applied to it and the maximum and minimum values are clipped for optimum viewing contrast.

matic dispersion in the atmosphere to be corrected for the first time, allowing for a significant improvement in detectability of faint companions. As the developmental time for the MKID array is several years, speckle control is being tested with a SAPHIRA (SELEX) array of avalanche photodiodes in the interim (Atkinson *et al.* 2014).

In contrast to speckle suppression, the addition of artificial speckles to the focal plane image can be utilized for precision astrometry when the on-axis starlight has been suppressed post-coronagraph. Further, by modulating the phase of the speckles during an exposure they can be made incoherent with the speckles in the halo offering superior astrometric performance. In addition, by carefully calibrating the flux ratio between the PSF core and speckles it is also possible to use these speckles for photometry and hence retrieving the contrast of companions as well (Martinache *et al.* 2014b). As opposed to diffractive grids utilized by other high-contrast imagers (Wang *et al.* 2014), the adaptive nature of the DM allows the speckle position, and brightness to be carefully tailored to each science case.

TABLE 8. DETAILS OF SCEXAO CORONAGRAPHS.

Coronagraph type	Inner working angle (λ/D)	Waveband(s)
PIAA	1.5	y-K
PIAACMC	0.8	y-K
Vortex	2	H
MPIAA + Vortex	1	H
MPIAA + 8 Octant	2	H
4 quadrant	2	H
Shaped pupil	3	y-K

3.2. *Coronagraphs*

The advanced wavefront control techniques utilized on SCExAO build the foundation for high-contrast (10^{-5}–10^{-6}) imaging of faint companions with the onboard coronagraphs. The coronagraphs available in SCExAO are listed in Table 8. The performance of the coronagraphs used in SCExAO is limited by the level of wavefront control achieved. The PIAA/PIAACMC and the Vortex offer the lowest IWA and highest throughput but are more sensitive to wavefront error. On the other hand the shaped pupil has a larger IWA and lower throughput but is less sensitive to residual wavefront error. Hence, the coronagraphs available are designed to span a large range of residual wavefront error and should be chosen accordingly.

The two key coronagraphs are the Phase induced amplitude apodization (PIAA) and the vector vortex types. PIAA refers to the act of remapping a flat-top pupil to a soft edged pupil in order to remove the diffraction features associated with a hard edged aperture (i.e. Airy rings) (Guyon 2003). These diffraction features make it difficult to suppress all of the light via a coronagraphic mask in the focal plane without blocking a close, faint companion. A combination of aspheric lenses are used to achieve the remapping in SCExAO and are referred to as PIAA lenses. SCExAO offers several types of remapping lenses. The first type is referred to as the conventional PIAA design and was presented in Lozi *et al.* (2009). Conventional PIAA lenses offer the most aggressive remapping, eliminating the secondary and converting the post-PIAA pupil into a prolate spheroid (a near-Gaussian which is finite in extent). An image depicting the remapping process between the two PIAA lenses in the laboratory is shown in Fig. 8, while a radial profile of the apodization function is shown in Fig. 9.

To complete the softening of the edges of the beam a binary mask is used which has a radially variant attenuation profile. Note that the binary mask is used, to reduce the demand on the curvature changes across the aspheric surfaces of the PIAA lenses and it is possible to eliminate it at the expense of increased manufacturing complexity of the PIAA lenses. As outlined in Guyon (2003), once the on-axis star has been suppressed with a focal plane mask, it is important to reformat the pupil to its original state in order to preserve the field-of-view. This can be done by using another set of PIAA lenses in

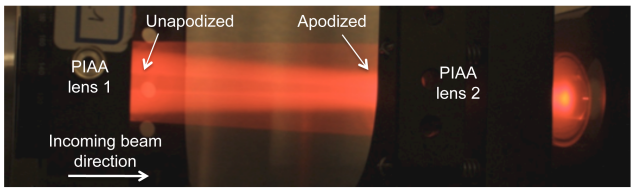

FIG. 8.— Picture of a visible beam being apodized by the conventional PIAA lenses in the laboratory (side view). The image is taken between the two lenses. The beam enters from the left of the image where the intensity across the beam is uniform except for the faint part in the middle of the beam (behind the secondary) and at the right hand side of the image, the beam is concentrated in the middle (i.e. apodized).

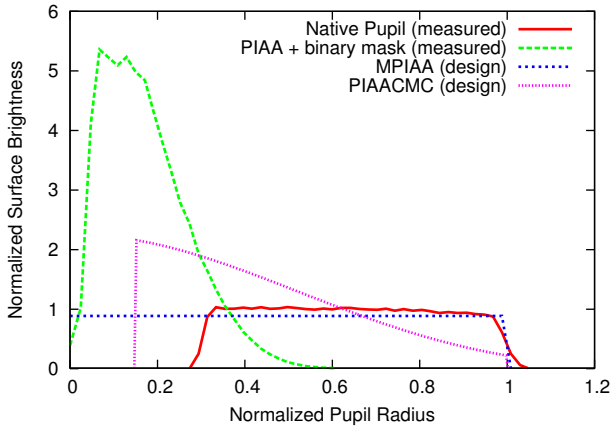

FIG. 9.— The figure shows a comparison of the radial apodization profiles of the various PIAA lenses as compared to the Subaru telescope pupil. The PIAA (green line) pulls the light inwards most aggressively, almost entirely removing the secondary and softens the edges of the beam. The PIAACMC (pink line) pulls some of the light inwards but does not entirely remove the presence of the secondary or soften the edges completely. The MPIAA (blue line) removes the presence of the secondary but does not soften the edges at all.

reverse and the ensemble of lenses are referred to as the inverse PIAA lenses (IPIAA). The position of the PIAA and inverse PIAA lenses can be seen in Figure 3. Due to the low material dispersion of CaF_2, the conventional PIAA lens design used in SCExAO is achromatic across the NIR (y-K bands). However, an appropriate focal plane mask must be chosen to achieve this. If an ordinary opaque mask is used, then the size of the mask is wavelength dependent, and so is the IWA. To circumvent this issue, SCExAO uses focal plane masks that consist of a central cone surrounded by a ring of pits periodically positioned around the cone, made from a transmissive material on a substrate which refracts rather than reflects the on-axis star light (Newman *et al.* 2015). In this way a variable focal plane mask which is achromatic across H-band can be achieved. In addition, since the light is strongly diffracted outwards by the focal plane masks, it can be redirected towards the LLOWFS via a reflective Lyot mask (Singh *et al.* 2014).

Despite the fact that the conventional PIAA offered in SCExAO has an IWA of 1.5 λ/D, due to the aggressive remapping which causes an abrupt phase step in the central part of the beam post-PIAA, the contrast at 1.5 λ/D is limited to 1×10^{-5} and is very sensitive to tip/tilt. To alleviate these issues a modified version of the PIAA coronagraph can by used. It is referred to as the PIAA complex mask coronagraph (PIAACMC) and is outlined in greater detail in Guyon *et al.* (2010). The major difference is that the PIAA lenses used for the PIAACMC are less aggressive which means the remapped pupil has soft edges but the secondary is still present as shown in Fig. 9. The lenses themselves are in the same mounts as those for the PIAA so they can be replaced on the fly. The focal plane mask is now replaced with a partially transmissive, phase shifting mask which is manufactured via electron beam etching. The IWA of the coronagraph can be tuned by varying the opacity of the focal plane mask and in the limit when the mask is fully transmissive, the IWA is minimized at the expense of sensitivity to tip/tilt. Nonetheless, the PIAACMC offers a contrast of 1×10^{-6} at 1 λ/D, is less sensitive to tip/tilt than the PIAA and is fully achromatic from y-K band. It is scheduled to be installed and commissioned in the near future.

A third and final type of PIAA is used to remap the pupil into a flat top without a central obstruction for an 8-octant coronagraph which is discussed in the following section (Oshiyama *et al.* 2014). The lenses are referred to as MPIAA lenses and reside in the same mounts as the other two. Despite the remapping these optics are not apodizers as the pupil retains its hard edge post remapping. A comparison of the various apodization schemes is shown in Fig. 9.

Other coronagraphs include the vortex (Mawet *et al.* 2009, 2010), 4-quadrant (Rouan *et al.* 2000), 8-octant (Murakami *et al.* 2010) and shaped pupil (Carlotti *et al.* 2012) versions. The vortex, 4-quadrant and 8-octant coronagraphs are phase-mask coronagraphs as opposed to occulting coronagraphs and consist of two primary elements; a focal plane and Lyot stop mask. All focal plane masks are situated in a wheel in the focal plane while the Lyot stop masks are located in the Lyot mask wheel and the positions of both are shown in Fig. 3.

The vortex coronagraph in SCExAO uses a H-band optimized, topographic charge 2 focal plane mask. This mask is constructed from a birefringent liquid crystal polymer material, i.e. a waveplate where the optical axis (fast axis) orientation is spatially dependent and in this case a function of the azimuthal coordinate (Mawet *et al.* 2009). Although an IWA of 0.9 λ/D is achievable with an unobstructed pupil with non-manufacturing defects, it is limited to 2.0 λ/D with the pupil geometry at the Subaru Telescope. However, the vector vortex on SCExAO could be used in conjunction with the MPIAA lenses to circumvent this issue and regain the inherent IWA. The vector vortex mask is more achromatic than a scalar mask and hence can operate across the full H-band (Mawet *et al.* 2009). As the nulling process is based on interference of light from different parts of the mask, best performance is achieved with higher Strehl ratios and stable centering of the PSF on the mask (5 mas tip/tilt error or below in this case).

The 8-octant coronagraph focal plane mask employed on SCExAO is based on photonic crystal technology (Murakami *et al.* 2010). It consists of 8 triangular segments that comprise half-wave plates where the optical axes of a given segment is always orthogonal to its two nearest neighbors. This creates a π phase shift between

adjacent segments for the transmitted beam which destructively interferes in the reimaged focal plane to null out the on-axis star. The 8 octant itself is not achromatic but broadband operation can be realized by placing a polarizer and analyzer before and after the mask respectively (Murakami *et al.* 2008) (note this is also true for the vortex coronagraph). This coronagraph exploits the pupil-reformatting MPIAA lenses described above to achieve an IWA of $\sim 2\ \lambda/D$ and offers very high-contrasts at these angular scales. Similar to the vector vortex it is also sensitive to tip/tilt and hence active control is preferred mode of operation.

The 4-quadrant focal plane mask is a scalar mask which consists of segments that phase shift the light by π with respect to the neighboring segments. Although a perfectly manufactured 4-quadrant mask could offer an IWA of as low as $1\ \lambda/D$ if used in conjunction with the MPIAA lenses mentioned above, the mask in SCExAO has manufacturing defects and so can not achieve such performance. The 4-quadrant in SCExAO is a prototype which serves its purpose for internal testing only.

The Lyot stop masks for the vector vortex, 4-quadrant and 8 octant coronagraphs are designed to reflect rejected light towards the LOWFS camera for fine tip/tilt guiding which is discussed in the subsequent section. The vector vortex and 4-quadrant Lyot stop masks consist of a replica mask to the Subaru Telescope pupil geometry with slight modifications. Both masks have a slightly oversized secondary and spiders for better rejection, however, the 4-quadrant has a square secondary instead of a circular one. On the other hand, as the secondary is eliminated thanks to the MPIAA lenses, then the Lyot stop for the 8-octant is simply a slightly undersized circular aperture.

Finally, shaped pupil coronagraphs can also be tested on SCExAO. These coronagraphs are located in the pupil plane mask wheel and any focal or Lyot plane masks required are placed in the appropriate wheel. For further details please see Carlotti *et al.* (2012).

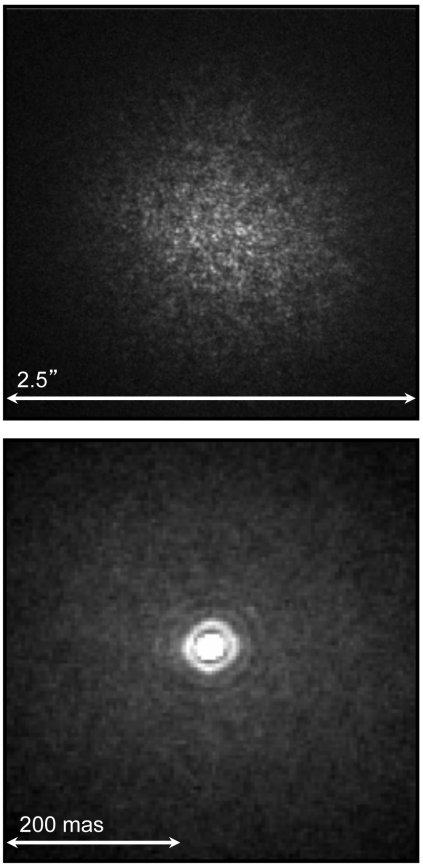

FIG. 10.— Top image: Vega in 2” seeing at 680 nm. Bottom image: Synthesized image of Vega at 680 nm in the presence 2” seeing. Image was reconstructed from a 1% selection of Fourier components across the 10^4 frames collected. A diffraction-limited PSF with a FWHM of 17 mas is obtained post-reconstruction (note: the scale of the bottom image differs from the top one). The data was acquired on the 5^{th} and 6^{th} of February, 2012.

3.3. *Lucky Fourier Imaging*

An important element of all adaptive optics systems is a real-time PSF monitoring camera. This is depicted as the Lucky imaging camera in Fig. 3, the specifications of which are listed in Table 1. Currently a narrowband of light ($\sim 30-50$ nm) is steered towards this camera from the pupil plane masks of VAMPIRES and the PSF imaged. The camera runs at a high frame rate, sub-framed and collects images rapidly which are primarily used for monitoring the PSF. The frames can subsequently also be used for traditional lucky imaging. However, a more advanced version of this technique named Lucky Fourier Imaging is commonly utilized (Garrel *et al.* 2012). The technique relies on looking for the strongest Fourier components of each image, and then synthesizing a single image with the extracted Fourier information. In this way diffraction-limited images at 680 nm of targets like Vega (bottom image in Fig. 10) and Betelgeuse have been synthesized in 2” seeing (Garrel 2012). This is clearly an extremely powerful tool and we propose to advance this imaging capability by adding multiple spectral channels.

3.4. *Fiber injection unit*

In addition to direct imaging, long baseline interferometry and high precision radial velocity both stand to gain significantly from a stable and 90% Strehl PSF on an 8-m class telescope. For example, long baseline interferometers like the Optical Hawaiian Array for Nano-radian Astronomy (OHANA) combine beams from multiple telescopes once it has been transported to the combination room via single-mode optical fibers (Woillez *et al.* 2004). However, coupling efficiently into single-mode fibers is no mean feat, but with access to a stable PSF with 90% Strehl, it can be achieved. Indeed this is already being exploited for the purposes of nulling interferometry on P1640 (Serabyn *et al.* 2010*b*). Once the light has been coupled into a single-mode fiber, it could be used as an alternative feed for a conventional multimode fiber-fed spectrograph. The non-temporally and spatially varying PSF provided by a single-mode fiber can be used in precision radial velocity measurements to eliminate modal-noise, a limiting factor in achieving high precisions. For these reasons we are developing a single-mode injection unit on the SCExAO platform.

To inject light into the fiber, it is tapped off with a retractable dichroic on its way to focus after OAP2 (see Fig. 3). A dichroic which reflects y, J and H-short

Table 9. Commissioning status of SCExAO modes of operation and modules.

Module/mode	Commissioning status (completion date)
Wavefront control	
LLOWFS	Complete
SN	Complete
PyWFS	Partially complete (fall 2015)
PyWFS+LLOWFS	Partially complete (fall 2015)
SN+PyWFS+LLOWFS	Incomplete (late 2015)
Coronagraphs	
PIAA	Complete
Vortex	Complete
4 quadrant	Complete
Shaped pupil	Complete
PIAACMC	Incomplete (fall 2015)
MPIAA+Vortex	Incomplete (late 2015)
MPIAA+8 octant	Incomplete (fall 2015)
Visible imagers	
VAMPIRES	Complete
Lucky imaging	Partially complete (late 2015)
FIRST	Incomplete (late 2015)
NIR fiber injection	Complete
NIR science imagers	
CHARIS	Expected delivery early 2016 (mid 2016)
MKID	Expected delivery late 2016 (2017)

Note. — + signifies that these modes/modules are operating in conjunction, SN-speckle nulling, PIAA will be replaced by the PIAACMC.

bands is currently used for this. An achromatic lens (f = 10 mm) is used to adjust the $F/\#$ of the beam before it is injected into the fiber which sits atop a stage. The 5-axis stage allows for XYZ translation via precise stepper motor actuators and course alignment of tip/tilt. The stage can be scanned through focus to maximize coupling into the fiber. A further advantage of implementing such a module on SCExAO is that we can use the conventional PIAA lenses to more closely match the intensity distribution of the collection fiber and hence boost the coupling to a theoretical value of 100%. To make this useful on-sky, this injection system relies on the PyWFS delivering a high Strehl beam. The fine tip/tilt control is provided by the LLOWFS by using the transmitted H-band light. This unit is currently operational and may be utilized by instruments such as the high precision spectrograph IRD for the survey it will undertake (Tamura *et al.* 2012). In addition, by developing such a unit, it becomes possible to exploit numerous other photonics technologies on-sky (Cvetojevic *et al.* 2012; Marien *et al.* 2012). The injection unit is described in more detail in Jovanovic *et al.* (2014b).

4. COMMISSIONING STATUS AND FUTURE EXTENSIONS

SCExAO is clearly a complex instrument with modules at various stages of commissioning. Table 9 summarizes the commissioning status/plan of the various modes of operation and modules of SCExAO.

Table 9 shows that the integral field spectrograph known as CHARIS will replace the HiCIAO imager from mid 2016. This instrument segments the focal plane with an array of micro-lenses, before dispersing each PSF and then reimaging onto a detector (see Table 1) (Peters *et al.* 2012). This allows for spatially resolved spectral information albeit at low resolving powers. Such an instrument has three key advantages. Firstly, background stars in a given image can quickly be identified. Secondly, owing to the fact that the instrument operates over a very broadband (J-K bands), the presence of a planet can be inferred by detecting the fixed speckle within a spectral data cube. Finally, low resolution spectra of gas giants can be taken enabling the atmospheres of these planets to be constrained and better understood (Brandt *et al.* 2014; McElwain *et al.* 2012). Indeed, presently operating integral field spectrographs such as OSIRIS at the Keck Telescope, the units in P1640 and GPI have been used to characterize the atmospheres of known planetary systems like HR8799 (Barman *et al.* 2011; Ingraham *et al.* 2014; Oppenheimer *et al.* 2013).

Although not included in the table, it has been proposed to outfit the IR arm of SCExAO with a polarimetric mode of operation to study scattered dust in circumstellar disks. This mode known as polarization differential imaging (PDI) has been hugely successful for the HiCIAO imager (Grady *et al.* 2013), and we aim to preserve this capability while offering a superior IWA. This IR polarimetric mode will complement the one of VAMPIRES offered in the visible, albeit on different spatial scales.

5. SUMMARY

The SCExAO instrument is a versatile high-contrast imaging platform which hosts advanced wavefront control systems, IR coronagraphs and visible interferometers, that are ideal for imaging at $< 3\ \lambda/D$ (solar-system scales). The extreme adaptive optics system delivers the necessary wavefront correction to be able to push detection limits for ground-based observations at small angular separations and interferometer precisions. Such instruments will be critical to understanding the inner structure of circumstellar disks and planetary systems and how they form. In addition, they will provide the appropriate avenue to collecting spectra from planetary candidates and determining their physical properties for the first time. Further, the SCExAO platform is an ideal testbed for demonstrating and prototyping technologies for future ELTs and space-missions. SCExAO is the only high-contrast imager of its kind and will be uniquely positioned to contribute to exoplanetary science.

6. APPENDIX

6.1. *Off-axis parabolic mirrors*

All OAPs in the SCExAO instrument were manufactured via diamond turning of aluminum and overcoating with gold, are 50 mm in diameter and were designed to work at a nominal off-axis angle of 17°. OAPs 1, 3, 4, & 5 have a f = 255 mm while OAP2 has a f = 519 mm. Although, there is no data on the wavefront error of these optics, each optic was initially used to form an image in the visible and it was determined from this that the RMS wavefront error was $< \lambda/20$ at 630 nm over a 20 mm beam size corresponding to that which is used in SCExAO.

6.2. *Internal NIR camera lenses*

The focusing lenses for the science camera include a $f = 150$ and 50 mm converging, achromatic doublet which are AR-coated for the NIR region ($1 - 1.65$ μm). The distance between the lenses is set to be just larger than the sum of their focal lengths so that a slow beam is formed ($F/\# = 65$).

6.3. *Deformable mirror environmental controls*

An interlock system which monitors the environmental conditions in the DM chamber (pressure, humidity) was put in place to prolong the life of the DM as they are known age rapidly in high humidity environments (Shea *et al.* 2004). A low pressure regulator (Fairchild-M4100) was used to offer fine control of the injected dry air pressure to the DM chamber at the < 1 psi level (with respect to ambient). The pressure is set to 0.4 psi above ambient when operating and monitored by a precise pressure sensor (FESTO - SDE1). Such low-pressure differentials are used so that the chamber does not deform significantly and hence induce any extra errors to the wavefront. A 1 psi pressure differential relief valve is used as a hard limit in case of over pressure in the circuit. The humidity in the circuit is measured with a moisture probe (Edgetech - HT120). The alarms for both the pressure and humidity sensors are used to control the power supplied to the DM electronics. When the humidity is below 15% and the pressure between $0.2-0.8$ psi, the DM electronics will be powered and the actuators can be driven. However, if the humidity rises above 15% and/or the pressure goes above 0.8 psi or below 0.2 psi, then the alarms on the sensors will trigger a relay switch, to which the DM electronics are connected to, to trip and cut the power to the DM. As a final level of reassurance, a low flow rate (250 mL/min) flow controller is connected to the end of the line to insure that there is a very slow flow over the DM membrane and no turbulence in the chamber. A rapid flow could tear the thin silicon membrane (3 μm) and or cause turbulence in the chamber which would be equivalent to seeing. The window to the chamber is 50 mm in diameter, made from a 12 mm thick piece of IR fused silica which is AR-coated across the operating range.

We are grateful to B. Elms for his contributions to the fabrication of parts for the SCExAO rebuild. The SCExAO team thanks the Subaru directorate for funding various grants to realize and develop the instrument.

Facilities: Subaru.

REFERENCES

Artigau, E., Biller, B. A., Wahhaj, Z., Hartung, M., Hayward, T. L., Close, L. M., Chun, M. R., Li, M. C., Trancho, G., Rigaut, F., Toomey, D. W., & Ftaclas, C., 2008, Proc. of the SPIE, 70141Z

Atkinson, D., Hall, D., Baranec, C., Baker, I., Jacobson, S., & Riddle, R., 2014, Proc. of the SPIE, 915419A

Barman, T. S., Macintosh, B., Konopacky, Q. M., & Marois, C., 2011, ApJ, 733, 65B.

Beuzit, J.-L., Feldt, M., Dohlen, K., Mouillet, D., Pugeta, P., Wildi, F., Abee, L., Antichif, J., Baruffolof, A., Baudozg, P., Boccaletti, A., Carbillet, M., Charton, J., Claudi, R., Downing, M., Fabron, C., Feautrier, P., Fedrigo, E., Fusco, T., Gach, J.-L., Gratton, R., Henning, T., Hubin, N., Joos, F., Kasper, M., Langlois, M., Lenzen, R., Moutou, R., Pavlov, A., Petit, C., Pragt, J., Raboua, P., Rigal, F., Roelfsema, R., Rousset, G., Saisse, M., Schmid, H.-M., Stadler, E., Thalmann, C., Turatto, M., Udry, S., Vakili, F., and Waters, R., 2008, Proc. of SPIE, 701418

Borde, P. J., & Traub, W. A., 2006, ApJ, 638, 488B

Borucki, B., Koch, D., Basri, G., Batalha, N., Brown, T., Caldwell, D., Caldwell, J., Christensen-Dalsgaard, J., Cochran, W. D., DeVore, E, Dunham, E. W., Dupree, A. K., Gautier, T. N., III, Geary, J. C., Gilliland, R., Gould, A., Howell, S. B., Jenkins, J. M., Kondo, Latham, D. W., Marcy, G. W., Meibom, S., Kjeldsen, H., Lissauer, J. J., Monet, D. G. Morrison, D., Sasselov, D., Tarter, J., Boss, A., Brownlee, D., Owen, T., Buzasi, D., Charbonneau, D., Doyle, L., Fortney, J., Ford, E. B., Holman, M. J., Seager, S., Steffen, J. H., Welsh, W. F., Rowe, J., Anderson, H., Buchhave, L., Ciardi, D., Walkowicz, L., Sherry, W., Horch, E., Isaacson, H., Everett, M. E., Fischer, D., Torres, G., Johnson, J. A., Endl, M., MacQueen, P., Bryson, S. T., Dotson, J., Haas, M., Kolodziejczak, J., Cleve, J. V., Chandrasekaran, H., Twicken, J. D., Quintana, E. V., Clarke, B. D., Allen, C., Li, J., Wu, H., Tenenbaum, P., Verner, E., Bruhweiler, F., Barnes, J., and Prsa A, 2010, Science, 327, 977

Brandt, T., McElwain, M., Janson, M., Knapp, G., Mede, K., Limbach, M., Groff, T., Burrows, A., Gunn, J., Guyon, O., Hashimoto, J., Hayashi, M., Jovanovic, N., Kasdin, J. Kuzuhara, M., Lupton, R., Martinache, F., Sorahana, S., Spiegel, D., Takato, N., Tamura, M., Turner, E., Vanderbei, R., & Wisniewski, J., 2014, Proc. of SPIE, 9148-49

Buton, C., *et al.* 2012, A&A, 549A, 5B

Carlotti, A., Kasdin, N. J., Martinache, F., Vanderbei, R., J., Young, E. J., Che, G., Groff, T. D., & Guyon, O., 2012, Proc. of the SPIE, 84463C.

Charbonneau, D., Brown, T. M., Noyes, R. W., and Gillilna, R. L., 2001, ApJ, 568, 377

Clergeon, C., PhD dissertation, 2014

Close, L. M., Males, J. R., Morzinski, K., Kopon, D., Follette, K., Rodigas, T. J., Hinz, P., Wu, Y.-L., Puglisi, A., Esposito, S., Riccardi, A., Pinna, E., Xompero, M., Briguglio, R., Uomoto, A., & Hare, T., 2013, ApJ,774, 94C

Codana, J. L., & Kenworthy, M., 2013, ApJ, 767, 100C

Cvetojevic, N., Jovanovic, N., Betters, C., Lawrence, J. S., Ellis, S., Robertson, G., Bland-Hawthorn, J., 2012, A&A, 544, L1

Dekany, R., Roberts, J., Burruss, R., Antonin, T., Baranec, C., Guiwits, S., Hale, D., Angione, J., Trinh, T., Zolkower, J., Shelton, C., Palmer, D., Hemming, J., Croner, E., Troy, M., McKenna, D., Tesch, J., Hildebrandt, S., Milburn, J., 2013, ApJ, 776, 130D

Esposito, S., Riccardi, A., Fini, L., Puglisi, A. T., Pinna, E., Xompero, M., Briguglio, R., Quirs-Pacheco, F., Stefanini, P., Guerra, J. C., Busoni, L., Tozzi, A., Pieralli, F., Agapito, G., Brusa-Zappellini, G., Demers, R., Brynnel, J., Arcidiacono, C., & Salinari, P., 2010, Proc. of SPIE, 7736-09F.

Esposito, S., Riccardi, A., Pinna, E., Puglisi, A., Quirs-Pacheco, F., Arcidiacono, C., Xompero, M., Briguglio, R., Agapito, G., Busoni, L., Fini, L., Argomedo, J., Gherardi, A., Brusa, G., Miller, D., Guerra, J. C., Stefanini, P., & Salinari, P., 2011, Proc. of SPIE, 8149-02E

Garrel, V., Guyon, O., & Baudoz, P., PASP, 124, 861

Garrel, V., PhD dissertation, 2012

Give'on, A., Kern, B., Shaklan, S., Moody, D. C., & Pueyo, L., 2007, Proc. of SPIE, 66910A

Gozdziewski, K., & Migaszewski, C., 2014, MNRAS, 440, 3140.

Grady, C. A. Muto, T., Hashimoto, J., Fukagawa, M., Currie, T., Biller, B., Thalmann, C., Sitko, M. L., Russell, R., Wisniewski, J., Dong, R., Kwon, J., Sai, S., Hornbeck, J., Schneider, G., Hines, D., Martn, A. M., Feldt, M., Henning, Th., Pott, J.-U., Bonnefoy, M., Bouwman, J., Lacour, S., Mueller, A., Juhsz, A., Crida, A., Chauvin, G., Andrews, S., Wilner, D., Kraus, A., Dahm, S., Robitaille, T., Jang-Condell, H., Abe, L., Akiyama, E., Brandner, W., Brandt, T., Carson, J., Egner, S., Follette, K. B., Goto, M., Guyon, O., Hayano, Y., Hayashi, M., Hayashi, S., Hodapp, K., Ishii, M., Iye, M., Janson, M., Kandori, R., Knapp, G., Kudo, T., Kusakabe, N., Kuzuhara, M., Mayama, S., McElwain, M., Matsuo, T., Miyama, S., Morino, J.-I., Nishimura, T., Pyo, T.-S., Serabyn, G., Suto, H., Suzuki, R., Takami, M., Takato, N., Terada, H., Tomono, D., Turner, E., Watanabe, M., Yamada, T., Takami, H., Usuda, T., and Tamura, M., 2013, ApJ,762, 48

Guyon, O., 2003, A&A, 404, 379

Guyon, O., 2005, ApJ, 629, 592

Guyon, O., Matsuo, T., & Angel, R. 2009, ApJ, 693, 75

Guyon, O., Martinache, F., Belikov, R., and Soummer, R. 2010, ApJS, 190, 220

Guyon, O., Pluzhnik, E., Martinache, F., Totems, J., Tanaka, S., Matsuo, T., Blain, C., & Belikov, R., 2010, PASP, 122, 71G

Han, E., Wang, S., Wright, J. T., Feng, Y., K., Zhao, M., Fakhouri, O., Brown, J., I., & Hancock, C., 2014, PASP, 126, 827

Hardy, J. W., 1998, Adaptive optics for astronomical telescopes, Oxford University Press, New York

Helmbrecht, M. A., Min H., Carl K., & Marc B., 2011, Proc. of SPIE 793108.

Huby, E., Perrin, G., Marchis, F., Lacour, S., Kotani, T., Duchene, G., Choquet, E., Gates, E. L., Woillez, J. M., Lai, O., Fedou, P., Collin, C., Chapron, F., Arslanyan, V., and Burns, K. J., 2012, A&A, 541A, A55

Huby, E., Duchene, G., Marchis, F., Lacour, S., Perrin, G., Kotani, T., Choquet, E., Gates, E. L., Lai, O., Allard, F., 2013, A&A, 560, A113

Ingraham, P., *et al.*, 2014, ApJ, 794L, 15I.

Jovanovic, N., Guyon, O., Martinache, F., Clergeon, C., Singh, G., Kudo, T., Newman, K., Kuhn, J., Serabyn, E., Norris, B., Tuthill, P., Stewart, P., Huby, E., Perrin, G., Lacour, S., Vievard, S., Murakami, N., Fumika, O., Minowa, Y., Hayano, Y., White, J., Lai, O., Marchis, F., Duchene, G., Kotani, T., Woillez, J., 2014, Proc. of SPIE, 9147-1Q.

Jovanovic, N., Guyon, O, Martinache, F., Schwab, C., & Cvetojevic, N., 2014, Proc. of SPIE, 9147, 9147-287

Kraus A., & Ireland M. J., 2012, ApJ, 745, 1

Lafreniere, D., Marois, C., Doyon, R., & Barman, T., 2009, ApJ, 694L, 148L.

Lagrange, A.-M., Gratadour, D., Chauvin, G., Fusco, T., Ehrenreich, D., Mouillet, D., Rousset, G., Rouan, D., Allard, F., Gendron, ., Charton, J., Mugnier, L., Rabou, P., Montri, J., & Lacombe, F., 2009, A&A, 493, 21L.

Lenzen, R., Hartung, M., Brandner, W., Finger, G., Hubin, N., Lacomber, F., Lagrange, A.-M., Lehnert, M., Moorwood, A., & Mouillet, D., 2003, Proc. of SPIE, 4841-944L

Leon-Saval, S. G., Argyros, A., & Bland-Hawthorn, J., 2013, Nanophot., 2, 429.

Lord, S. D., 1992, NASA Technical Memorandum 103957

Lozi, J., Marinache, F., and Guyon, O., 2009, PASP, 121, 1232

Macintosh, B. et. al., 2014, PNAS, 111, 12661.

Malbet, F., yu, J. W., & Shao, M., 1995, PASP, 107, 386M

Marien, G., N., Jovanovic, Cvetojevic, N., Williams, R., Haynes, R., Lawrence, Parker, Q., & Withford, M., 2012, MNRAS, 421, 3641

Marois, C., Macintosh, B., Barman, T., Zuckerman, B.; Song, I., Patience, J., Lafrenire, D., & Doyon, R., 2008, Science, 322, 1348M.

Martinache, F., Guyon, O., Clergeon, C., and Blain, C., 2012, PASP, 124, 1288

Martinache, F., 2013, PASP, 125, 422M

Martinache, F., Guyon, O., Jovanovic, N., Clergeon, C., Singh, G., Kudo, T., Currie, T., Thalmann, C., McElwain, M., & Tamura, M., 2014, Proc. of the SPIE, 9148, 914870

Martinache, F., Guyon, O., Jovanovic, N., Clergeon, C., Singh, G., Kudo, T., Currie, T., Thalmann, C., McElwain, M., & Tamura, M., 2014, PASP, 126, 565

Mawet, D., Serabyn, E., Liewer, K., Hanot, Ch., McEldowney, S., Shemo, D., & O'Brien, N., 2009, Opt. Exp., 17, 1902

Mawet, D., Serabyn, E., Liewer, K., Burruss, R., Hickey, J., & Shemo, D., 2010, ApJ, 709, 53

Mayor, M., and Queloz, D., 1995, Nature, 378, 355

Mazin, B. A., Bumble, B., Meeker, S. R., O?Brien, K., McHugh, S., & Langman, E., 2012, Opt. Exp., 20, 1503.

McElwain, M. W., Brandt, T. D., Janson, M., Knapp, G. R., Peters, M. A., Burrows, A. S., Carlotti, A., Carr, M. A., Groff, T., Gunn, J. E., Guyon, O., Hayashi, M., Kasdin, N. J., Kuzuhara, M., Lupton, R. H., Martinache, F., Spiegel, D., Takato, N., Tamura, M., Turner, E. L., & Vanderbei, R. J., 2012, Proc. of SPIE, 84469C

Minowa, Y., Hayano, Y., Oya, S., Watanabe, M., Hattori, M., Guyon, O., Egner, S., Saito, Y., Ito, M., Takamia, H., Garrel, V., Colley, S., Golota, T., & Iye, M., 2010, Proc. of SPIE, 77363N

Murakami, N., Uemura, R., Baba, N., Nishikawa, J., Tamura, M., Hashimoto, N., & Abe, L., 2008, PASP, 120, 1112

Murakami, N., Nishikawa, J., Yokochi, K., Tamura, M., Baba, N., & Abe, L., 2010, ApJ, 714, 772

Muto, T., Grady, C. A., Hashimoto, J., Fukagawa, M., Hornbeck, J. B., Sitko, M., Russell, R., Werren, C., Cura, M., Currie, T., Ohashi, N., Okamoto, Y., Momose, M., Honda, M., Inutsuka, S., Takeuchi, T., Dong, R., Abe, L., Brandner, W., Brandt, T., Carson, J., Egner, S., Feldt, M., Fukue, T., Goto, M., Guyon, O., Hayano, Y., Hayashi, M., Hayashi, S., Henning, T., Hodapp, K. W., Ishii, M., Iye, M., Janson, M., Kandori, R., Knapp, G. R., Kudo, T., Kusakabe, N., Kuzuhara, M., Matsuo, T., Mayama, S., McElwain, M. W., Miyama, S., Morino, J.-I., Moro-Martin, A., Nishimura, T., Pyo, T.-S., Serabyn, E., Suto, H., Suzuki, R., Takami, M., Takato, N., Terada, H., Thalmann, C., Tomono, D., Turner, E. L., Watanabe, M., Wisniewski, J. P., Yamada, T., Takami, H., Usuda, T., Tamura, M., 2012, ApJ Letters, 748, L22

Newman, K., Guyon, O., Balasubramanian, K., Belikov, R., Jovanovic, N., Martinache, F., & Wilson, D., 2015, PASP, 127, 437

Norris, B., Tuthill, P. G., Ireland, M. J., Lacour, S., Zijlstra, A. A., Lykou, F., Evans, T. M., Stewart, P., Bedding, T. R., Guyon, O., & Martinache, F., 2012, Proc. of SPIE, 844503N.

Norris, B., Tuthill, P. G., Ireland, M. J., Lacour, S., Zijlstra, A. A., Lykou, F., Evans, T. M., Stewart, & P., Bedding, 2012, Nature, 484, 220

Norris, B., Schworer, G., Tuthill, P., Jovanovic, N., Guyon, O., Stewart, P., & Martinache, F., 2015, MNRAS, 447, 2894N.

Oppenheimer, B. R., Baranec, C., Beichman, C., Brenner, D., Burruss, R., Cady, E., Crepp, J. R., Dekany, R., Fergus, R., Hale, D., Hillenbrand, L., Hinkley, S., Hogg, David W., King, D., Ligon, E. R., Lockhart, T., Nilsson, R., Parry, I. R., Pueyo, L., Rice, E., Roberts, J. E., Roberts, L. C., Jr., Shao, M., Sivaramakrishnan, A., Soummer, R., Truong, T., Vasisht, G., Veicht, A., Vescelus, F., Wallace, J. K., Zhai, C., Zimmerman, N., 2013, ApJ, 768. 24O.

Oshiyama, F., Murakami, N., Guyon, O., Martinache, F., Baba, N., Matsuo, T., Nishikawa, J., & Tamura, M., 2014, PASP, 126, 270

Pepe, F., Ehrenreich, D., & Meyer, M. R., 2014, Nature, 513, 358.

Perrin, G., Lacour, S., Woillez, J., & Thiebaut, E., 2006, MNRAS, 373, 747P

Peters, M. A., Groff, T., Kasdin, N. J., McElwain, M. W., Galvin, M., Carr, M. A., Lupton, R., Gunn, J. E., Knapp, G., Gong, Q., Carlotti, A., Brandt, T., Janson, M., Guyon, O.,

Poyneer, L. A., De Rosa, R. J., Macintosh, B., Palmer, D. W., Perrin, M. D., Sadakuni, N., Savransky, D., Bauman, B., Cardwell, A., Chilcote, J. K., Dillon, D., Gavel, D., Goodsell, S. J., Hartung, M., Hibon, P., Rantakyr, F. T., Thomas, S., Veran, J.-P., 2014, Proc. of SPIE, 9148E, 0KP.

Rouan, D., Riaud, P., Boccaletti, A., Clenet, Y., & and Labeyrie, A., 2000, PASP, 112, 1479

Serabyn, E., Mawet, D., & Burruss, R., 2010, Nature, 464, 1018.

Serabyn, E., Mennesson, B., Martin, S., Liewer, K., Mawet, D., Hanot, C., Loya, F., Colavita, M. M., & Ragland, S., 2010, Proc. of SPIE 77341E.

Shea, H. R., Gasparyan, A., Chan, H. B., Arney, S., Frahm, R. E., Lopez, D., Jin, S., & McConnell, P., 2004, Trans. on Dev. & Mat. Rel., 4, 198

Singh, G., Martinache, F., Baudoz, P., Guyon, O., Matsuo, T., Jovanovic, N., & Clergeon, C., 2014, PASP, 126, 586

Singh, G., Lozi, J., Guyon, O., Jovanovic, N., Baudoz, P., Martinache, F., Kudo, T., Serabyn, E., & Kuhn J., G., 2015, in preparation.

Tamura, M., 2009, Proc. of AIPC, 1158, 11T
Tamura, M., Suto, H., Nishikawa, J., Kotani, T., Sato, B., Aoki, W., Usuda, T., Kurokawa, T., Kashiwagi, K., Nishiyama, S., Ikeda, Y., Hall, D., Hodapp, K., Hashimoto, J., Morino, J., Inoue, S., Mizuno, Y., Washizaki, Y., Tanaka, Y., Suzuki, S., Kwon, J., Suenaga, T., Oh, D., Narita, N., Kokubo, E., Hayano, Y., Izumiura, H., Kambe, E., Kudo, T., Kusakabe, N., Ikoma, M., Hori, Ya., Omiya, M., Genda, H., Fukui, A., Fujii, Y., Guyon, O., Harakawa, H., Hayashi, M., Hidai, M., Hirano, T., Kuzuhara, M., Machida, M., Matsuo, T., Nagata, T., Ohnuki, H., Ogihara, M., Oshino, S., Suzuki, R., Takami, H., Takato, N., Takahashi, Y., Tachinami, C., & Terada, H., 2012, Proc. of SPIE, 84461T
Tuthill, P., Monnier, J. D., Danchi W. C., Wishnow E. H., Haniff C. A., 2000, PASP, 112, 555
Tuthill, P., Lacour, S., Amico, P., Ireland, M., Norris, B., Stewart, P., Evans, T., Kraus, A., Lidman, C., Pompei, E., & Kornweibel, N., 2010, Proc. of the SPIE, 77351OT
Vogt, F., Martinache, F., Guyon, O., Yoshikawa, T., Yokochi, K., Garrel, V., & Matsuo, T., 2011, PASP, 123, 1434
Wang, J. J., *et al.*, 2014, Proc. of SPIE, 9147-195.
Woillez, J. M., Perrin, G., Guerin, J., Lai, O., Reynaud, F., Wizinowich, P. L., Neyman, C. R., Le Mignant, D., Roth, K., & White, J., 2004, Proc. of SPIE, 5491, 1425

Astronomy & Astrophysics manuscript no. exospoc˙arxiv
May 13, 2015

Predicting exoplanet observability in time, contrast, separation and polarization, in scattered light

Guillaume Schworer[1,2] & Peter G. Tuthill[2]

[1] LESIA, Observatoire de Paris, CNRS/UMR 8109, UPMC, Universit Paris Diderot, 5 place J. Janssen, 92195 Meudon, France
e-mail: guillaume.schworer@obspm.fr
[2] Sydney Institute for Astronomy (SIfA), School of Physics, The University of Sydney, NSW 2006, Australia

Received January 1, 2014; accepted January 1, 2014

ABSTRACT

Context. Polarimetry is one of the keys to enhanced direct imaging of exoplanets. Not only does it deliver a differential observable providing extra contrast, but when coupled with spectroscopy, it also reveals valuable information on the exoplanetary atmospheric composition. Nevertheless, angular separation and contrast ratio to the host-star make for extremely challenging observation. Producing detailed predictions for exactly how the expected signals should appear is of critical importance for the designs and observational strategies of tomorrow's telescopes.
Aims. We aim at accurately determining the magnitudes and evolution of the main observational signatures for imaging an exoplanet: separation, contrast ratio to the host-star and polarization as a function of the orbital geometry and the reflectance parameters of the exoplanet.
Methods. These parameters were used to construct polarized-reflectance model based on the input of orbital parameters and two albedo values. The model is able to calculate a variety of observational predictions for exoplanets at any orbital time.
Results. The inter-dependency of the three main observational criteria – angular separation, contrast ratio, polarization – result in a complex time-evolution of the system. They greatly affect the viability of planet observation by direct imaging. We introduce a new generic display of the main observational criteria, which enables an observer to determine whether an exoplanet is within detection limits: the Separation-POlarization-Contrast diagrams (SPOC).
Conclusions. We explore the complex effect of orbital and albedo parameters on the visibility of an exoplanet. The code we developed is available for public use and collaborative improvement on the python package index, together with its documentation. It is another step towards a full comprehensive simulation tool for predicting and interpreting the results of future observational exoplanetary discovery campaigns.

Key words. planets and satellites: atmosheres, planets and satellites: detection, methods: obsevational

1. Introduction

Observational technologies for detecting the light reflected from an exoplanet are reaching a level of precision that makes direct imaging of exoplanets a realistic possibility in about the coming decade. Because of the very challenging contrast ratio between exoplanets and host-stars in the optical, there is great interest in differential methods, such as polarimetry, to deliver an extended reach to imaging instruments (Hough et al. (2006), Keller (2006), Schmid et al. (2006)). Built upon previous detections of polarized signals from exoplanets Berdyugina et al. (2008), Wiktorowicz (2009), Lucas et al. (2009), Berdyugina et al. (2011), the polarimetric imaging modules that are currently being integrated on the 10m class telescopes (SPHERE-ZIMPOL on the VLT Thalmann et al. (2008), GPI on Gemini Wiktorowicz et al. (2012), and VAMPIRES on SUBARU Telscope Norris et al. (2015)) promise to achieve a differential polarized contrast down to $approx10^{-6}$ in the visible or near- infrared. It is therefore an opportune moment to produce detailed predictions for exactly how the expected signals should appear, which will be of critical importance for the designs and observational strategies of these instruments. We aim at accurately determining the magnitudes and evolution of the main observational signatures as a function of the basic parameters of the exoplanetary system: the star-exoplanet orbital parameters and the optical properties of the planet. We incorporate the complexity arising from effects such as polarization based on Rayleigh scattering. Additionally and as a first-order observability estimator, the absolute flux in photon per unit time and surface received from the exoplanet target is computed assuming a black-bodied star. We finally provide a querier and parser of the `http://exoplanet.eu/` exoplanet database for searching and importing any star-planet target.

Several models were already developed to predict the light signature of an exoplanet as it should appear to an observer, for example see Cahoy et al. (2010), Buenzli & Schmid (2009), or for the case of Earth-like planets with varying atmospheric parameters, see Karalidi & Stam (2012) and Zugger et al. (2010). However, to the best of our knowledge, the inter-dependency of the main observational criteria is never taken carefully into account. The relative evolution of angular separation, polarization, and contrast ratio is of critical importance because their respective maxima do not occur at the same time in the general case: this makes the best-case scenario for detection very unlikely. We correct for this by showing the relative evolution of the angular separation, contrast ratio, and polarization as a function of the orbital and reflectance parameters of the planet. The findings resulting from this integrated treatment highlight dependencies that are much more complex than previously reported. The three main observational criteria – angular separation, contrast ratio, and polarization – in general do not exhibit a strong positive cor-

relation and must be analyzed separately to determine the direct visibility of a potential planet target.

2. Model

We developed a polarized reflectance model. Its algorithm relies on the orbital parameters of the exoplanet and the linear combination of two albedo values; it is briefly described below.

As our prime observables are in any event differential between the star and exoplanet (such as the contrast ratio) or inherent to the planet (such as the polarization fraction), absolute fluxes are not described in detail. A simple black-body modeling of the host stars is used to give a first-order idea on the absolute fluxes that are expected from a exoplanet. For the sake of conciseness, "polarization" is used instead of "polarization fraction".

2.1. Orbital parameters

Each exoplanet orbit is defined by the usual parameters listed in Table 1. Note that the shape of the orbit as seen by the observer is solely defined by e, i, and ω_p.

Symbol	Name	Unit
T	Period	days
t_p	Time at periapsis	Julian date
a	Semi-major axis	AU
e	Eccentricity	∅
i	Inclination to the observer	degrees
ω_p	Argument of periapsis	degrees
Ω	Longitude of ascending node	degrees

Table 1. Orbital parameters for an exoplanet. i=90° corresponds to an edge-on orbit (transiting), i¿90° corresponds to a retrograde orbit.

The phase angle of the exoplanet and the distance between the star and the planet are obtained from these orbital parameters. The phase angle $\alpha$is defined as the vector angle between the star, an exoplanet, and the observer, as seen from the exoplanet. It is 0° when the planet is at full phase (superior conjunction) and 180° when the exoplanet is at new phase (inferior conjunction, transiting).

2.2. Rayleigh scattering polarization

For the sake of conciseness, in the following discussions we use the quantity called phased albedo, which is defined as the product of the phase function and the geometric albedo of a planet, for a given wavelength:

$$A_\alpha(\alpha) = A_g \cdot \phi(\alpha) = \frac{I(\alpha)}{\pi F}, \tag{1}$$

for an incident flux πF, with $I(\alpha)$ the emerging flux from a body at the phase angle α. It represents the fraction of the incident irradiance that is reflected by the planet when it is seen at phase angle $\alpha$by the observer, so that $E_{Planet,\ out} = A_\alpha(\alpha) \cdot E_{Planet,\ in}$, with E being the spectral irradiance arriving at or leaving the planet.

The polarization induced by an exoplanet on a reflected beam of light is described by many different models, such as Mie, Rayleigh, or Raman scattering. It is assumed here that single Rayleigh scattering is the predominant source of polarization

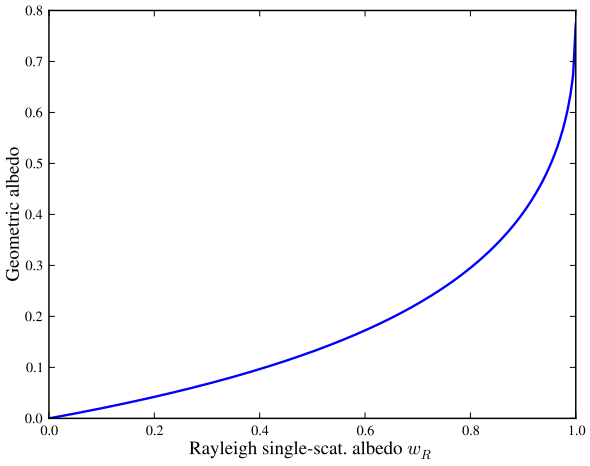

Fig. 1. The geometric albedo $A_{g,Rayleigh}$arising from single-scattering as a function of the Rayleigh single-scattering albedo w_R.

in planetary atmospheres. This is a good approximation as long as Mie scattering (and especially the primary rainbow polarizing effect of liquid droplets in clouds, see Bailey (2007) remains lower than Rayleigh scattering. This scenario is usually achieved for wavelengths shorter than approximately $1\mu m$, which also corresponds to the most favorable wavelengths for Rayleigh polarization measurements of scattered light, as it is function of λ^{-4}. Integrated over the stellar disk, the flux from the star can be considered to be unpolarized (Kemp et al. (1987). Hence, only the light from the exoplanet carries polarization.

The results of Madhusudhan & Burrows (2012) for the Stokes parameters Q/I and U/I were adopted as input data to carry out more polarization and reflectance computations. Their model assumes an unresolved semi-infinite homogeneous atmosphere (hence cloud free), dominated by Rayleigh scattering. The atmosphere is assumed to be spherical, which is a satisfactory assumption when the planetary rotation remains slow. Given the strong depolarizing effect of multiple scattering, they used the single-scattering albedo as a unique reflectance parameter from which a geometric albedo $A_{g,Rayleigh}$arising from the Rayleigh single-scattering albedo was calculated; their result is reproduced in Figure 1.

Stokes-V is found to be zero for Rayleigh scattering in planet atmospheres. Hence, the degree of polarization $Pz_{Rayleigh}$ is defined by

$$Pz_{Rayleigh} = \frac{\sqrt{Q_{out}^2 + U_{out}^2}}{I_{out}}, \tag{2}$$

and it depends on the phase angle $\alpha$of the planet and the single-scattering albedo w_R, which represents the amount of absorption versus scattering in a given atmosphere. The existing literature provides solutions to several phase functions. Madhusudhan & Burrows (2012) provided an analytical solution for scattering models for Lambertian, Rayleigh, isotropic, and asymmetric scattering. Zugger et al. (2010) addressed the liquid surface scattering model. Some phase functions are reproduced in Figure 2. Given the symmetry of the phase angle αalong the orbit, only $\alpha = [0, 180]°$ values are represented. The illuminated fraction values are also plotted for comparison.

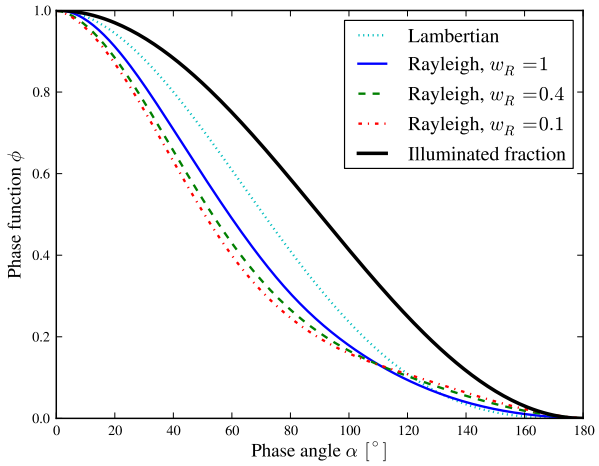

Fig. 2. Phase functions ϕas a function of phase angle $\alpha$for several scattering models. The illuminated fraction is also displayed (thick line). The Rayleigh-scattering model corresponds to a vectorial Rayleigh phase matrix.

Rayleigh and Lambertian surface models follow the same general S-curve shape between zero flux and full flux. A Lambertian or Rayleigh planet is faint at small αbecause the illuminated fraction f_I is small, hence fewer photons are reflected.

2.3. Polarized and unpolarized albedo

It is now apparent that clouds and condensates are very common in planet atmospheres. An atmosphere solely described by a single-scattering albedo could only take into account Rayleigh scattering of the atmosphere in the optically thick case, which is quite restrictive. Indeed, clouds, rocky surfaces or liquid surfaces do not follow Rayleigh scattering, but they often strongly contribute to the reflectivity of the exoplanet.

In this section we describe a novel approach to the reflectance properties of an exoplanet atmosphere to include effects of a greater atmospheric variety.

We assumed that any non-Rayleigh single-scattering from the atmosphere follows Lambertian scattering. This assumption is discussed below. A planet is better defined by two combined albedo quantities:

- a total geometric albedo $A_{g,Total}$that represents the total fraction of incoming irradiance reflected by the exoplanet, taking into account all scattering processes,
- a Rayleigh single-scattering albedo w_R that represents the fraction of incoming irradiance that is scattered by the atmosphere according to Rayleigh single-scattering alone, from which arises a Rayleigh geometric albedo $A_{g,Rayleigh}$. Only this part of reflected light carries a defined degree of polarization in this model. This albedo can be approximated by the single-scattering albedo of the exoplanet multiplied by the fraction of Rayleigh-scattered emerging light.

These albedo values can be added linearly so that

$$A_{g,Total} = A_{g,Lambertian} + A_{g,Rayleigh}. \quad (3)$$

Following this, we can express the outgoing irradiances using the phased albedo A_α:

$$A_{\alpha,Rayleigh} = \phi_{Rayleigh} \cdot A_{g,Rayleigh} \quad (4)$$

$$A_{\alpha,Total} = \phi_{Lambertian} \cdot (A_{g,Total} - A_{g,Rayleigh}) + \phi_{Rayleigh} \cdot A_{g,Rayleigh}. \quad (5)$$

The total emerging spectral irradiance of the exoplanet $I_{Total,out}$ including thermal emission is

$$I_{Total,out} = E_{Rayleigh,out} + E_{Lambertian,out} + E_{Thermal,out}. \quad (6)$$

Note that this thermal emission is much weaker than the reflected light from the host-star unless the exoplanet is a hot Jupiter and the observing wavelength lies in the infrared. Below, we assume that $E_{Thermal,out}$ is negligible for $\lambda_{Obs} \lesssim 1\mu m$.

The different Stokes parameters and polarization degree can be easily obtained with

$$Q/I = \frac{(\frac{Q}{I_{Rayleigh,out}}) \cdot E_{in} \cdot A_{\alpha,Rayleigh}}{I_{Total,out}} \quad (7)$$

$$U/I = \frac{(\frac{U}{I_{Rayleigh,out}}) \cdot E_{in} \cdot A_{\alpha,Rayleigh}}{I_{Total,out}} \quad (8)$$

$$V/I = 0 \quad (9)$$

$$Pz_{Total} = \frac{Pz_{Raylgeigh}}{1 + \frac{A_{\alpha,Lambertian}}{A_{\alpha,Rayleigh}}}, \quad (10)$$

where $Q/I_{Rayleigh,out}$ and $U/I_{Rayleigh,out}$ are the Stokes ratios from the Rayleigh-scattering polarization section of this model; they are used to calculate $Pz_{Raylgeigh}$ using Equation 2.

According to previous sections, the following complete relation for the exoplanet reflected irradiance, given the host-star surface irradiance, is

$$E_{Planet,Distance} = E_{Star,Surface} \cdot (\frac{R_*}{r_{orbit}})^2 \cdot (\frac{R_{Planet}}{d})^2 \cdot A_\alpha, \quad (11)$$

where R are radii. The observer-exoplanet distance is here approximated by the distance observer-star d. The contrast ratio CRbetween a planet and its host-star is then obtained from Equation 11:

$$CR = (\frac{R_{Planet}}{r_{orbit}})^2 \cdot A_\alpha. \quad (12)$$

We highlight here that the polarization of the exoplanet Pz_{Total} and the contrast ratio CRdo not depend on the incoming irradiance from the host-star, they are intrinsic to the planet. However, they are strongly dependent on the observation wavelength λ_{Obs}through Rayleigh single-scattering and geometric albedo, even though for clarity of notation, λ was not explicitly written in the relations.

Thanks to the separation of the contributions from the different scattering processes on an exoplanet, an original model for planetary polarized reflectance has now been set up. It yields the phased albedo A_α, which indicates the fraction of reflected irradiance from an observed planet, as a function of geometric albedo A_g, phase angle α, and Rayleigh single-scattering albedo w_R. While αcan be easily determined as described in the orbital computations part of the model, the albedo parameters $A_g$and $w_R$depend on factors too numerous to be modeled here: they therefore need prior computation. If $A_g$and $w_R$are obtained separately, the albedo and phase functions previously defined are successful in describing the emerging irradiance that is reflected

by a planet. Its most accurate results are obtained for wavelengths shorter than approximately $1\mu m$ unless thermal emission and Mie scattering are also added to the model.

We assumed a polarized-reflectance model that incorporates Rayleigh and Lambertian scattering as two linear scattering phenomena. The approximation made is that any scattering that does not relate to Rayleigh single-scattering is assumed to be Lambertian. As a consequence, a beam of light undergoing multiple-Rayleigh scattering or a combination of Lambertian and Rayleigh scattering is assumed to be multiple Lambertian scattered. This approximation mainly affects the angle at which a photon emerges from the exoplanet and in turn the phase-function of integrated emerging light. In our model, this integrated phase function is a linear combination of Rayleigh and Lambertian phase functions. Adding these second-order scattering phenomena to the computation of the integrated phase function adds terms to its computation: a multiple Rayleigh phase function term and a coupled Rayleigh-Lambertian phase function term. We assumed that these second-order phase functions are similar to the Rayleigh and Lambertian phase functions, which differ only slightly (see Figure 2). Furthermore, we assumed that the weight of these additional phase functions in the computation of the integrated phase function is smaller than Rayleigh single-scattering and Lambertian single or multiple scatterings. Note also that the lower the albedo values, the less likely multiple-scattering becomes and the smaller the errors induced by this approximation.

The results were benched-marked against several other models providing photopolarimetric curves as a function of one or several orbital parameters, such as models developed by Buenzli & Schmid (2009), Madhusudhan & Burrows (2012), Fluri & Berdyugina (2010), and Zugger et al. (2010). The locations of the polarization peaks and minima were reproduced with very good agreement; they mostly depend on the phase functions and the processing of orbital parameters. The intensity of the polarization peaks were reproduced with good accuracy; they mostly depended on the fine-tuning of the two albedo values. More specifically, the shift of the polarization peak to phase angles greater than 90° reported in the last bench-mark reference was also observed.

2.4. Model completeness

The calculation code that implements this model takes up to 11 input parameters and N orbital positions for which the calculations are performed. It generates N-element vectors for up to 11 output parameters, listed in Table 2. Table 3 shows the mapping between the input and output parameters, where the input parameters are listed as column headers and output parameters are row headers of Table 3.

In the way the code is written, the only mandatory input is the eccentricity, the inclination, and the argument at periapsis. When compared with exoplanetary detections reported in the literature, these three orbital parameters are rarely known with any precision. This is currently the case for 132 exoplanets out of the 1790 (≈7.4%, source: `http://exoplanet.eu/`). However, where more complete data exist, reasonably good estimates can be made.

Output	Name	Unit
α	Phase angle	degrees
f_T	Period fraction since last periapsis	%
ν	True anomaly	degrees
r_{orbit}	Star-planet distance	AU
θ	Angular separation with star	arcsec
$date$	Julian Date	JD
CR	Contrast ratio with star	∅
Pz	Polarization degree	%
Φ_{Pz}	Polarization angle	degrees
φ_{North}	Angle with the north	degrees
υ_{orb}	Apparent orbital velocity	mas/hour

Table 2. Output parameters from the calculation code. Their processing depends on the availability of input parameters, refer to Table 3. "mas" stands for milli-arcsecond.

	e, i, ω_p	a	d	T	t_p	R_P, A_g	w_R	Ω
α, f_T, ν r_{orbit}[1], θ[1]	x							
$date$ [1]	x			x				
$date$ [2]	x			x	x			
r_{orbit}[2], θ[2]	x	x	x					
CR[1]	x					x		
CR[2]	x	x				x		
Pz, Φ_{Pz}[1]	x					x	x	
Φ_{Pz}[2]	x					x	x	x
φ_{North}	x							x
υ_{orb}	x	x	x	x				x

[1] relative values
[2] absolute values

Table 3. Mapping between the input (columns) and output (lines) parameters of the model. An "x" indicates that the given input parameter(s) is required for computing that output parameter(s). Example: calculating the relative angular separation (line 4) and the absolute contrast ratio (line 7) only requires six input parameters: e, i, ω_p, a, R_{Planet}, and A_g.

3. Results

3.1. SPOC diagrams

An important tool introduced here is the Separation-POlarization-Contrast (SPOC diagram) which presents all the useful information to enable an observer to evaluate whether a planet target is observable at given instrumental limits and how this signal will evolve with orbit and time. Perhaps most importantly, in the event of a detection, SPOC diagramsprovide a powerful mechanism to constrain exoplanet properties given observational imaging data.

Figure 3 shows an example of a SPOC diagramapplied to Alpha Centaury Bb, an Earth-mass planet discovered in 2012 Dumusque et al. (2012) that was later debated Hatzes (2013). Its probable orbital parameters are shown in Table 4. The exoplanet was discovered with the radial velocities method, hence its inclination and argument of ascending node are unknown. For i, values in [15, 35, 60, 85]°were explored, whereas Ωwas neglected because it does not change the shape of the orbit: it only defines a rotation of the orbit locus as seen by an observer along the line of sight (i.e., it is only useful for projecting the exoplanet location around the star onto RA-DEC axes). Its radius was calculated from its mass$\cdot sin(i)$ = 0.0036 $\cdot M_{Jupiter}$ assuming the same density as Earth, which leads to M = [4.42,

2.00, 1.32, 1.15] M_{Earth} and R = [1.64, 1.26, 1.10, 1.05] R_{Earth} for the four previous i. In this example, the light from objectAlpha Centaury A received by the exoplanet is neglected because it is roughly 2.10^5 fainter than that from Alpha Centaury B. Reflectance parameters were chosen to be similar to those of a Venus-like planet (A_g=0.67, ω_p=0.85) in V-band.

Set	T [day]	ω_p [°]	a [AU]	e	t_p [JD]
$Cen_{\alpha,0}$	3.2357	0	0.04	0	55280.17
$Cen_{\alpha,0.34}$	3.2357	246	0.04	0.34	55282.53

Table 4. Two sets of probable orbital parameters for Alpha Centaury Bb, see section 9 of the supplementary information of Dumusque et al. (2012). The inclination is choosen from [15, 35, 60, 85]°, which leads to M = [4.42, 2.00, 1.32, 1.15] M_{Earth} and R = [1.64, 1.26, 1.10, 1.05] R_{Earth} respectively (assuming Earth density).

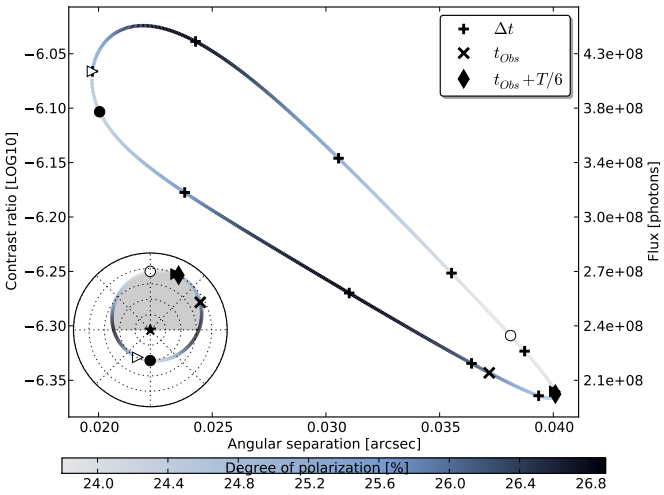

Fig. 3. SPOC diagramfor $Cen_{\alpha,0.34}$ with i=15°, see Table 4, assumed to be Venus-like regarding its reflectance parameters. It represents the polarization values as gray scale, plotted against the angular separation and the contrast ratio axes. The exoplanet's orbit is therefore displayed in a separation-contrast phase diagram. The wavelength is the V-band. The "**x**" indicates the position of the exoplanet at an arbitrary observation time. The 'diamond indicates the position of the planet one sixth of the orbital period Tlater (giving the forward direction of time). The 10 plus signs indicate the evolution of the planet along the curve; they are linearly spaced in time. The empty and filled triangles are periapsis and apoapsis: r_{min} = 0.026AU and r_{max} = 0.054AU. The empty and filled circles are minimum and maximum phase angle: α_{min} = 75° and α_{max} = 105°. The bottom left panel shows the orbit as seen by the observer, where the shaded area corresponds to the portion of the orbit that is behind the plane of the paper. The dashed lined corresponds to the limit of the same instrument sensitivities as in the preceding example. The right-hand side y-axis is given in photons per VLT collecting area per hour integrated over V-band. Two successive plus signs correspond to 7h46min.

In Figure 3, $Cen_{\alpha,0.34}$ is shown with i=15°. This figure displays the polarization encoded with color, while the two axes plot the separation against contrast ratio; finally, a set of different markers give temporal information. The first striking feature of the plot is that the exoplanet does not run a "back and forth" locus in the separation-contrast ratio phase diagram. This is because the apparent symmetry of the orbit is broken. When the orbital parameters $i$and $e$are non-zero and $\omega_p$is different from [0,90,180,270]°, the geometry of the orbit as it appears to the observer has no symmetry. In other words, the star is not at a focal point of the apparent elliptical locus of the orbit. Note that the semi-major axis $a$does not play a role in the shape of the orbit; it acts as a simple scaling factor. The photon flux on the right-hand side y-axis is given in photons per collecting-area per hour, integrated over V-band. It was calculated assuming that Alpha Centaury B is a black-body, T_{eff} = 5214 and M_v = 1.33. The collecting area is 51.7m^2, which corresponds to a diameter of 8.2 meter with a central obstruction of 2% (same as VLT telescopes).

Figure 3 shows that the lowest and highest contrast ratios are reached close to the maximum and minimum phase angle (black and white disks). This corresponds to the inferior and superior conjunction of the exoplanet with its star. We note that the periapsis and apoapsis are not reached at these phase angle extrema because of the non-null value of ω_p, which re-orients the orbit with respect to its host star. Polarization reaches two maxima near α=90°(the limit between the shaded and the bright area in the bottom left subplot of the same figure). This is linked to the fact that polarization is observed from Rayleigh scattering, which has a peak polarization for 90°. However, in the case of non-entirely Rayleigh planets, the peak polarization occurs at slightly different phase angles.

An even more interesting diagram is shown in Figure 4. It represents the apparent orbital motion in mas per hour plotted against the angular separation as x-axis and the polarized contrast ratio as y-axis. The apparent orbital motion is found to be an important factor to take into account here because the period of Alpha Centaury Bb is only 3.24 days: it reaches 1.8 to 3.5 mas per hour, which limits the observer to a few hours of exposures, depending on the plate scale of its detector. The photon flux is extremely high as a result of the brightness of the star (1.3mag in V) and the large bandwidth of the V filter (550 ± 44nm). The SPHERE-ZIMPOL performance curve for 1h exposure time using a V-filter with the double-difference polarization calibration was added to the plot (see Fig. 4 in Roelfsema et al. (2014)). It shows that this instrument could observe Alpha Centaury Bb during ≈ 35% of its orbit if i=15°. Longer integrations could increase the sensitivity at the expense of larger apparent orbital motion on the detector, which will significantly limit the angular differential imaging (ADI) processing capability.

Figure 5 shows SPOC diagramsfor the two sets of orbital parameters $Cen_{\alpha,0.34}$ and $Cen_{\alpha,0}$, and for all four i.

This figure shows that for higher orbital inclinations, the radius inferred from the orbital velocity profile decreases, which leads to a smaller reflecting surface and consequently, a lower contrast ratio. The effect of eccentricity is clearly seen: curves for $Cen_{\alpha,0}$ all run a "back and forth locus" because of their orbital symmetry. Eccentric orbits display an increasingly complex shape as the inclination increases: this is due to the projection of the orbit locus on the sky as an observer would see it.

We refer to Appendix A for more detailed studies of diverse SPOC diagramsthat are based on known exoplanets.

3.2. Separations and contrast ratios for the solar system

An interesting illustration of the usefulness of the SPOC diagramsis provided by our solar system as viewed by an external observer.

Planet	Diameter to Earth	$a[AU]$	e	$i[^\circ]$	$\omega_p[^\circ]$	A_g
Mercury	0.382	0.3870	0.205	7.00	77.45	0.142
Venus	0.948	0.7233	0.006	3.39	131.53	0.67
Earth	1	1.000	0.016	0.00	102.94	0.367
Mars	0.532	1.523	0.093	1.85	336.04	0.170
Jupiter	11.2	5.203	0.048	1.30	14.75	0.52
Saturn	9.44	9.537	0.054	2.48	92.43	0.47
Uranus	4.00	19.19	0.047	0.76	170.96	0.51
Neptune	3.88	30.06	0.008	1.76	44.97	0.41

Table 5. Planetary and orbital parameters for the planets of the solar system, in the V-Band. Source: `http://nssdc.gsfc.nasa.gov/planetary/factsheet/`. Inclinations is this table are measured from the plane of the ecliptic.

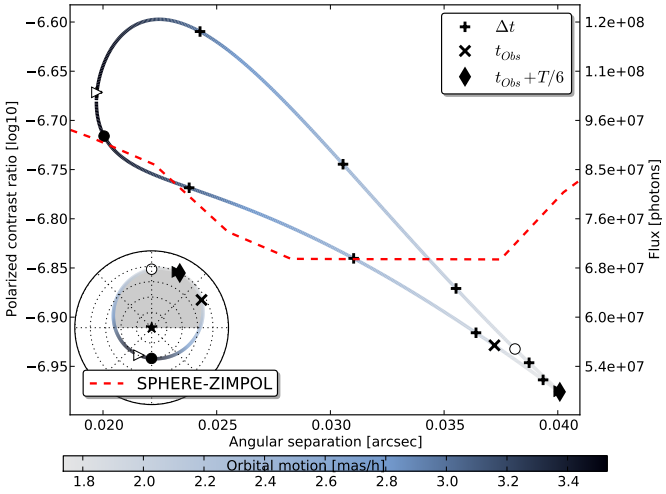

Fig. 4. Same caption as Figure 3 except that it represents the apparent orbital motion in mas per hour as gray scale, plotted against the angular separation and the polarized contrast ratio axes. The red dotted line corresponds to the SPHERE-ZIMPOL performance for 1 hour exposure (observability domain being above the line).

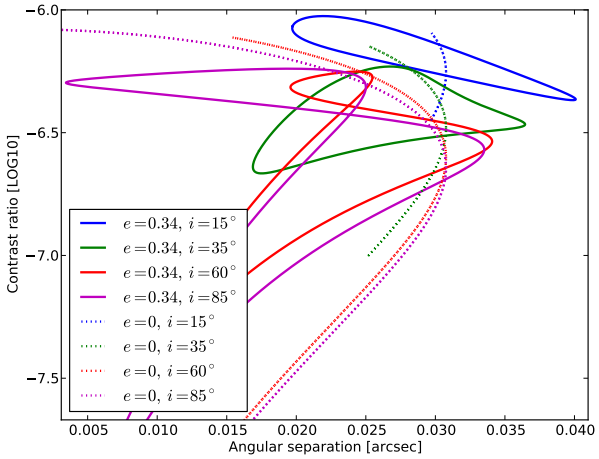

Fig. 5. Contrast ratio versus angular separation plots for both orbital parameters of Alpha Centaury Bb as described in Figure 3 and for inclinations in [15, 35, 60, 85]°. Dotted lines correspond to e=0 and ω_p=0°and full lines to e=0.34 and ω_p=246°. A color version is available in the online journal.

Figure 6 gives the contrast-separation diagram for the planets of the solar system, whose parameters are listed in Table 5. In this figure, polarization is not shown (for clarity). It displays values for two different angles of inclination for the observer, 0°and 45°. The observational wavelength is visible light. Note that no rings were modeled for Saturn; they are anticipated to have a variable effect on both contrast ratio and polarization (see discussion in Sect. 3.3).

Note that the angular separation of Earth to the Sun is $\approx$ 1arcsec when the ecliptic inclination is 0°, consistent with the definition of a parsec. Earth's average angular separation decreases as the orbit appears more inclined to the observer.

Figure 6 highlights the strong dependency of the contrast ratio and angular separation on inclination, argument at periapsis, and eccentricity. Mercury especially, but also Mars and Saturn do not follow a "back and forth locus" because the symmetry of their orbit as it appears to the observer is broken.

Venus is seen to be the second brightest planet in the solar system (for a ringless Saturn). Significantly brighter than Earth, but fainter than Jupiter. A rule of thumb can explain this easily: Venus receives twice as much solar flux as Earth and has an albedo nearly twice as high. Because the diameters of the two planets are close to each other, they present almost the same reflective area (Venus has ≈90% of that of Earth): Venus is therefore on average nearly four times brighter than Earth to an external observer. The same rules can be applied to compare the relative brightness of Jupiter and Venus': Jupiter is only twice as bright as Venus to the observer. The same rule of thumbs can explain the surprising faintness of Mars, Uranus, and Neptune. They show a relatively small reflective area because of their distance to the Sun, which makes them receive little flux; furthermore, Mars has a significantly low albedo. Note that these comparative values are averaged over the entire orbits.

Finally, this same figure highlights once more that focusing the discussion on averaged contrast ratios and separation is futile: depending on the respective configuration of the planets, Earth might easily become the brightest planet in the solar system at some epochs. As an example, let us consider the case when the observer sees the Solar System with an inclination of 45°. Figure 7 shows the contrast ratios of Jupiter, Venus, and Earth as a function of time during a whole Jovian orbit.

It can be calculated that, during the Jovian revolution (11.9 years):

- CR(Earth) ¿ CR(Venus) for 2.55 years (21.53% of T_{Jup}),
- CR(Earth) ¿ CR(Jupiter) for 1.04 years (8.82%),
- CR(Venus) ¿ CR(Jupiter) for 3.16 years (26.61%),
- Venus is the brightest of the 3 planets for 3.11 years (26.16%),
- Earth is the brightest of the 3 planets for 4.83 months (3.39%),

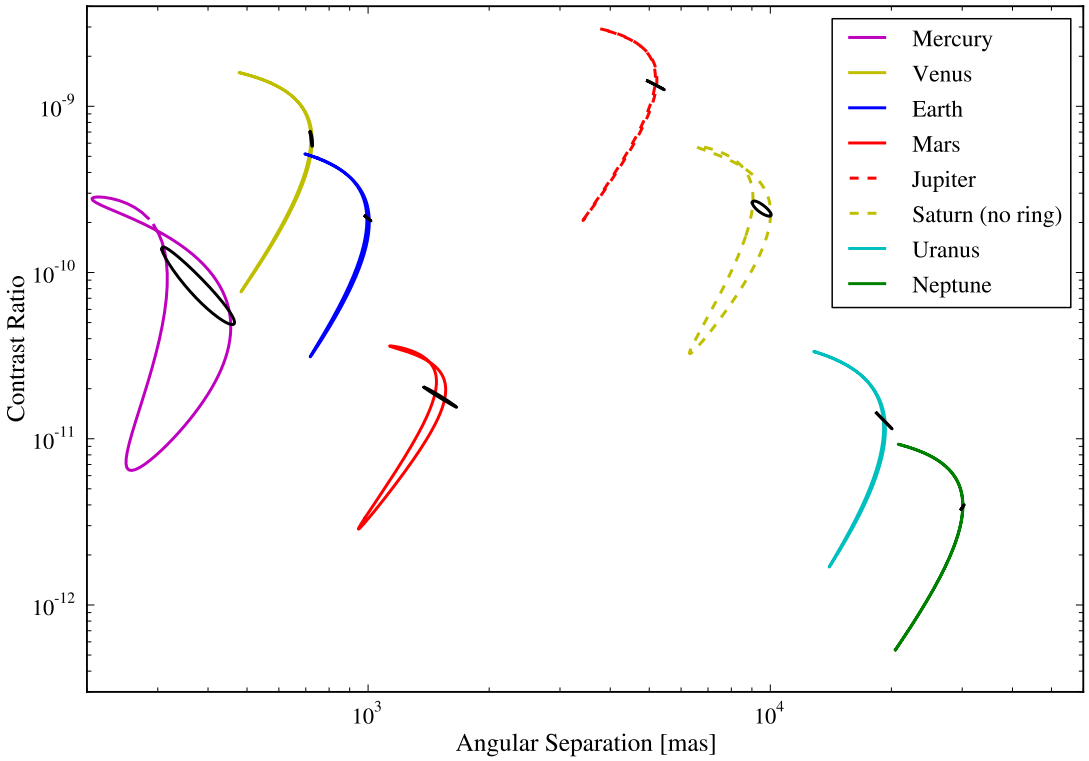

Fig. 6. Contrast-separation diagram for the planets of the solar system as seen from 1pc distance in visible light. Small black curves correspond to an inclination of the ecliptic of 0°(observer reference frame); colored curves show the solar system at an inclination of 45°. Note that both axes have logarithmic scales. A color version is available online.

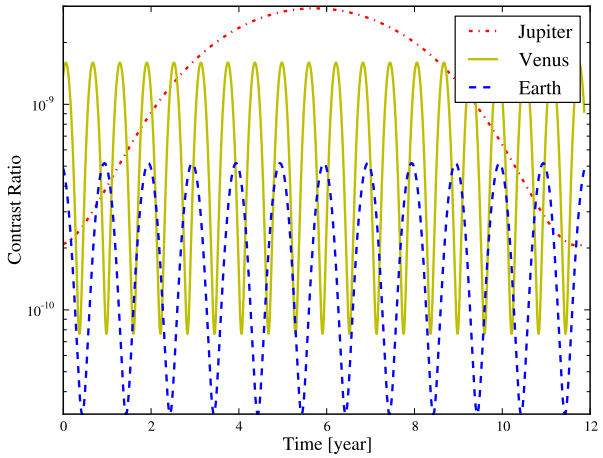

Fig. 7. Evolution of the contrast ratio to the Sun for Venus, Jupiter and the Earth, during an entire Jovian revolution (11.9 years).

– Jupiter is the brightest of the 3 planets for 8.36 years (70.44%),

where CR stands for contrast ratio. These values become 28.28%, 18.89%, 32.14%, 30.30%, 4.83%, and 64.86% respectively when the observer sees the solar system at an inclination of 75°. Note also that for an inclination of 45°, Mercury is brighter than Jupiter during 1.75% of T_{Jup}. This duration increases to 11.62% for an inclination of 75°.

Despite the large variability in apparent brightness, it remains true that all solar system planets are extremely challenging: Earth's relative magnitude to the Sun is about ≈ +23mag, at best. Gas giant planets at the snow line such as Jupiter do not always offer dramatic gains in observability, as might naively be thought.

3.3. Effect of extensive planetary rings

Rings were not included in this model. To do so would at least double the number of parameters describing a planet (exoplanet obliquity, obliquity at periapsis, ring radii (inner and outer), reflectance parameters, etc). The ring orientation to the observer is critical for determining reflected light from the host-star. Beyond the model of our own solar system, there is little observational data to constrain the speculative range of ring properties. However, their presence around an exoplanet would significantly change the observable properties of planets. Rings can either act as reflectors with a potential polarized enhancement or obstruct of the exoplanet illumination or irradiance, depending on their apparent inclination to the star, the observer and their polarized-reflectance characteristics. Both reflection and obstruction effects are coupled for extensive systems of rings that project shadows onto the exoplanet atmosphere. We refer to Dyudina et al. (2005) or Arnold & Schneider (2006) for a more detailed discussion of the impacts of rings on light curves.

3.4. Distinguishing radius and albedo with polarization

Knowing both the contrast ratio (or absolute flux) of the planet and its polarization degree, preferably at several orbital positions, allows the observer to distinguish between several atmospheric models of the atmosphere and finally determine its radius and albedo. For a given exoplanet atmosphere and the same unpolarized flux measured, a planet with large radius and low albedo will exhibit a higher polarization degree than a small exoplanet with high albedo. We refer to the relation between peak polarization and single-scattering albedo in Madhusudhan & Burrows (2012). Such radius-albedo measurements were carried out in Berdyugina et al. (2008) and Berdyugina et al. (2011).

4. Conclusions

4.1. Model and calculation code

We have constructed a model to fully describe the emerging radiation field from an exoplanet with given orbital geometry and reflectance parameters. This model aclculates the three main observables that are relevant for direct imaging of an exoplanet: polarization, contrast ratio, and angular separation as a function of date. A key strength of this model is the relatively restricted number of free input parameters despite the complex processes addressed. Only 3 of these input parameters – eccentricity, inclination, and argument of periapsis – are mandatory for performing a first assessment of the variability over time of the exoplanet observability.

The calculation code developed is available for public use and collaborative improvement on the python package index `https://pypi.python.org/pypi` under "exospoc", together with its documentation. This code is implemented on the `http://exoplanet.eu/` exoplanet database (see Schneider et al. (2011)), where SPOC diagramsare accessible in the exoplanet information sheets at the link "Observability Predictor".

4.2. SPOC diagrams

We have introduced a novel tool - the SPOC diagram. It highlights the interdependency of polarization, contrast ratio, and angular separation to the host star for an input exoplanet and gives the observer critical information for predicting expected exoplanetary signal from a minimum set of parameters. The complex shape of the SPOC diagramcurves highlights the fact that in the general case (inclination higher than $\approx 10^{\circ}$), the critical observables strongly depend on the geometry of the orbit as it appears to the observer. As a consequence, we stress that restricting consideration to values averaged along the entire orbit for angular separation, contrast ratio, or polarization may be a misleading oversimplification in many applications. An illustration of this is that an external observer would report Earth to be the brightest of the eight planets for a significant fraction of random observations.

The variation of the main observational criteria is critical in timing a direct observation of an exoplanet. This variation mainly relies on the combined effect of the inclination, the eccentricity and the argument of periapsis, hence the shape of the orbit as it appears to the observer. This latter parameter has a surprisingly important role to play in the visibility prediction for a planet in acting to either amplify or cancel the effects of inclination and eccentricity over the contrast ratio and angular separation values over time. The albedo parameters only shifts the lowest and highest values of the contrast ratio; however they do not significantly change the span of its minimum and maximum. The planet radius, semi-major axis and, observer-host-star distance parameters simply scale all observables to higher or lower contrast ratios and angular separations.

The simultaneity of the maxima of three main observational criteria can also be studied with SPOC diagrams. The simultaneity of contrast ratio and polarization (or of contrast ratio and angular separation) maxima is unlikely (or very unlikely) in the $t_{CR,max} \pm (20\% \text{ of } T)$ temporal window. Therefore, the best-case scenario for detection, maxima of contrast, separation, and polarization, is extremely unlikely.

Acknowledgements. We thank Vincent Coud du Foresto and Sylvestre Lacour for their comments and advice. We acknowledge that this work was partly supported by the French National Agency for Research (ANR-13-JS05-0005-01). We thank the exoplanet.eu team and especially Marco Mancini, who adapted this work to the online database.

References

Arnold, L. & Schneider, J. 2006, in IAU Colloq. 200: Direct Imaging of Exoplanets: Science and Techniques, ed. C. Aime & F. Vakili, 105–110
Bailey, J. 2007, Astrobiology, 7, 320
Berdyugina, S. V., Berdyugin, A. V., Fluri, D. M., & Piirola, V. 2008, ApJ, 673, L83
Berdyugina, S. V., Berdyugin, A. V., Fluri, D. M., & Piirola, V. 2011, ApJ, 728, L6
Buenzli, E. & Schmid, H. M. 2009, A&A, 504, 259
Cahoy, K. L., Marley, M. S., & Fortney, J. J. 2010, ApJ, 724, 189
Dumusque, X., Pepe, F., Lovis, C., et al. 2012, Nature, 491, 207
Dyudina, U. A., Sackett, P. D., Bayliss, D. D. R., et al. 2005, ApJ, 618, 973
Fluri, D. M. & Berdyugina, S. V. 2010, A&A, 512, A59
Hatzes, A. P. 2013, ApJ, 770, 133
Hough, J. H., Lucas, P. W., Bailey, J. A., et al. 2006, PASP, 118, 1302
Karalidi, T. & Stam, D. M. 2012, A&A, 546, A56
Keller, C. U. 2006, in Society of Photo-Optical Instrumentation Engineers (SPIE) Conference Series, Vol. 6269, Society of Photo-Optical Instrumentation Engineers (SPIE) Conference Series, 0
Kemp, J. C., Henson, G. D., Steiner, C. T., & Powell, E. R. 1987, Nature, 326, 270
Lucas, P. W., Hough, J. H., Bailey, J. A., et al. 2009, MNRAS, 393, 229
Madhusudhan, N. & Burrows, A. 2012, ApJ, 747, 25
Norris, B., Schworer, G., Tuthill, P., et al. 2015, MNRAS, 447, 2894
Roelfsema, R., Bazzon, A., Schmid, H. M., et al. 2014, in Society of Photo-Optical Instrumentation Engineers (SPIE) Conference Series, Vol. 9147, Society of Photo-Optical Instrumentation Engineers (SPIE) Conference Series, 3
Schmid, H. M., Beuzit, J.-L., Feldt, M., et al. 2006, in IAU Colloq. 200: Direct Imaging of Exoplanets: Science and Techniques, ed. C. Aime & F. Vakili, 165–170
Schneider, J., Dedieu, C., Le Sidaner, P., Savalle, R., & Zolotukhin, I. 2011, A&A, 532, A79
Thalmann, C., Schmid, H. M., Boccaletti, A., et al. 2008, in Society of Photo-Optical Instrumentation Engineers (SPIE) Conference Series, Vol. 7014, Society of Photo-Optical Instrumentation Engineers (SPIE) Conference Series
Wiktorowicz, S. J. 2009, ApJ, 696, 1116
Wiktorowicz, S. J., Millar-Blanchaer, M., Perrin, M. D., et al. 2012, in Society of Photo-Optical Instrumentation Engineers (SPIE) Conference Series, Vol. 8446, Society of Photo-Optical Instrumentation Engineers (SPIE) Conference Series
Zugger, M. E., Kasting, J. F., Williams, D. M., Kane, T. J., & Philbrick, C. R. 2010, ApJ, 723, 1168

Appendix A: Observability predictor examples

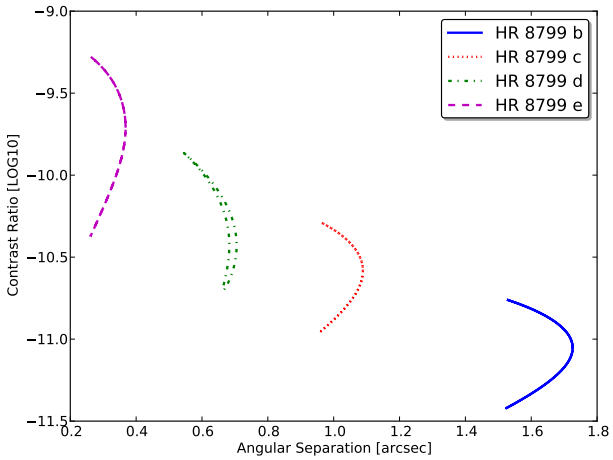

Fig. A.1. Contrast-separation diagram for V-band reflectance parameters (no polarization information added for clarity reasons) showing the famous HR 8799 exoplanetary system with its four confirmed candidates. The planet e was assumed to be the same size as the three other planets ($1.2R_{Jupiter}$). All four planets but planet d follow a "back and forth" locus because of their null eccentricity. Despite their large reflecting area, the contrast ratios are extremely low because of their distance to the host star.

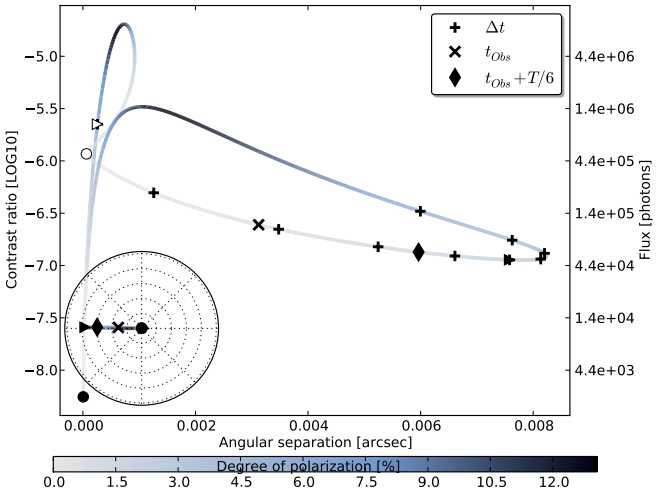

Fig. A.2. SPOC diagram for HD 80606 b, for which all orbital parameters are known down to a very high accuracy. The very high eccentricity (0.93) of this transiting planet gives a peculiar phase diagram. The higest contrast ratio is not reached at periapsis because of the combination of i, e, and $\omega_p$orbital parameters. Photon count is given per hour per VLT collecting area. The reflectance parameters were assumed to be Jupiter-like, in V-band.

Monthly Notices
of the
ROYAL ASTRONOMICAL SOCIETY

MNRAS **447,** 2894–2906 (2015) doi:10.1093/mnras/stu2529

The VAMPIRES instrument: imaging the innermost regions of protoplanetary discs with polarimetric interferometry

Barnaby Norris,[1⋆] Guillaume Schworer,[1,2] Peter Tuthill,[1] Nemanja Jovanovic,[3] Olivier Guyon,[3] Paul Stewart[1] and Frantz Martinache[4]

[1]*Sydney Institute for Astronomy, School of Physics, Physics Road, University of Sydney, NSW 2006, Australia*
[2]*LESIA, Observatoire de Paris, Section de Meudon, 5 place Jules Janssen, F-92195 Muedon, Cedex, France*
[3]*National Astronomical Observatory of Japan, Subaru Telescope, 650 N. AOhoku Place, Hilo, Hawaii 96720, USA*
[4]*Laboratoire Lagrange, CNRS UMR 7293, Observatoire de la CÃ te dAzur, Bd de lObservatoire, F-06304 Nice, France*

Accepted 2014 November 28. Received 2014 November 4; in original form 2014 April 26

ABSTRACT

Direct imaging of protoplanetary discs promises to provide key insight into the complex sequence of processes by which planets are formed. However, imaging the innermost region of such discs (a zone critical to planet formation) is challenging for traditional observational techniques (such as near-IR imaging and coronagraphy) due to the relatively long wavelengths involved and the area occulted by the coronagraphic mask. Here, we introduce a new instrument – Visible Aperture-Masking Polarimetric Interferometer for Resolving Exoplanetary Signatures (VAMPIRES) – which combines non-redundant aperture-masking interferometry with differential polarimetry to directly image this previously inaccessible innermost region. By using the polarization of light scattered by dust in the disc to provide precise differential calibration of interferometric visibilities and closure phases, VAMPIRES allows direct imaging at and beyond the telescope diffraction limit. Integrated into the SCExAO (Subaru Coronagraphic Extreme Adaptive Optics) system at the Subaru telescope, VAMPIRES operates at visible wavelengths (where polarization is high) while allowing simultaneous infrared observations conducted by HICIAO. Here, we describe the instrumental design and unique observing technique and present the results of the first on-sky commissioning observations, validating the excellent visibility and closure-phase precision which are then used to project expected science performance metrics.

Key words: instrumentation: high angular resolution – instrumentation: interferometers – instrumentation: polarimeters – techniques: interferometric – planet-disc interactions – protoplanetary discs.

1 INTRODUCTION

The mechanism by which planets are formed within circumstellar discs is a key question in current astronomy. Flattened, cool discs of gas and dust surround most low-mass stars for their first several millions of years of existence, during which they gradually dissipate via photoevaporation, mass outflow, assimilation by the star, and condensation into planetisimals and eventually planets (Williams & Cieza 2011). Of particular interest are so-called transition-discs – protoplanetary discs exhibiting a partially evacuated gap, first identified via a distinctive dip in their infrared spectral energy distributions (e.g. Calvet et al. 2002). An exciting possibility is that these gaps are indicative of planetary formation (Bryden et al. 1999) and detailed observational characterization is of particular importance.

Although our understanding of the evolutionary processes involved is incomplete, in recent times spatially resolved observations have provided great insight into the structure and evolution of such protoplanetary discs, including the gaps, knots, and other density modulations that provide evidence of planetary formation. Sub-millimetre observations have resolved the inner cavities of transition discs (Andrews et al. 2011), as has long-baseline optical interferometry (Olofsson et al. 2011). Furthermore, infrared observations using coronagraphy and polarimetry have revealed fine substructure within protoplanetary discs. Spiral arms and complicated asymmetrical structure has been imaged using these techniques in several discs, such as those surrounding AB Aurigae (Fukagawa et al. 2004; Hashimoto et al. 2011) and MWC 758 (Grady et al. 2013).

While such infrared observations are extremely productive, the imaging of the innermost region (within ∼100 mas) is highly challenging, due to the high contrast and angular resolution required as

⋆E-mail: bnorris@physics.usyd.edu.au

well as the area occulted by the coronagraphic mask in traditional coronagraphs. However, this inner region is critical for the understanding of disc structure and planet formation (Williams & Cieza 2011). The main disc inner rim, the partially evacuated cavity (such as that characteristic of transition discs), and an inner-disc may all lie within this region. Here, we introduce a new instrument, the Visible Aperture-Masking Polarimetric Interferometer for Resolving Exoplanetary Signatures (VAMPIRES), specifically designed to directly observe this key inner region. Using a unique combination of aperture-masking interferometry and differential polarimetry, VAMPIRES will directly image the structure of the inner disc region in scattered starlight at visible wavelengths, revealing rim structure, disc geometry, and asymmetric density perturbations betraying the presence of an accreting planetesimal. Furthermore, polarimetric measurements reveal the distribution of dust grain sizes and species. Integrated into the SCExAO (Subaru Coronagraphic Extreme Adaptive Optics) system (Guyon et al. 2011; Jovanovic et al. 2013) at the Subaru 8 m telescope, it will enable observations at the telescope diffraction limit. The observational parameter space explored by VAMPIRES is distinct from – and complementary to – that of a coronagraphic polarimetric imager; it has no limitation on inner working angle (limited only by its resolving power, around 10 mas) and offers diffraction-limited imaging of this inner region while being robust against seeing and imperfect AO correction.

The remainder of this section will outline the technical background to the technique employed by VAMPIRES. Section 2 will describe the instrument itself. Section 3 describes the unique triple-differential interferometric calibration used by VAMPIRES. The results from the first on-sky observations are presented in Section 4. A qualitative demonstration of the expected data from science observations is given in Section 5 and a summary is included in Section 6. Appendix A explains the calibration procedure used for residual instrumental polarization not removed during the differential process.

1.1 Non-redundant aperture masking

Non-redundant aperture masking (Readhead et al. 1988; Tuthill et al. 2000), segments the pupil of a single telescope into a number of sub-apertures by placing an opaque metal mask with a carefully designed pattern of holes at a pupil plane upstream of an imaging instrument. This causes a diffraction pattern to form on the detector, with each set of fringes corresponding to a particular pair of sub-apertures (holes) in the aperture mask. Thus, each pair of sub-apertures forms a baseline of a Fizeau interferometer, with the visibilities and phases recovered by Fourier analysis of the diffraction pattern.

The key to the technique's performance is that the layout of sub-apertures must be *non-redundant* – that is, the vector separation of every hole pair must be unique. This allows for the noise-process arising from seeing to be largely eliminated (see Readhead et al. 1988 for more detail). The power (or squared visibility) recorded for fringes on any baseline is intrinsically robust against phase errors caused by seeing, and this observable alone provides powerful constraint for diffraction-limited imaging from terrestrial telescopes. However, visibilities do not preserve any of the phase information of the image. Ideally, the phases recorded for each baseline would also be utilized, however these are completely dominated by random error from seeing. However, an alternate observable – the closure phase (Baldwin et al. 1986) – can be derived, which in the limit of small sub-apertures and short exposures, is immune to the effects of seeing. When starlight entering each sub-aperture is corrupted by a random phase error, then by taking the sum of phases around three baselines forming a closing triangle, phase errors cancel out and the resultant observable, the closure phase, is a function only of the source intensity distribution. The use of non-redundant masking along with these two observables has been highly successful in producing diffraction-limited, high-contrast images of such targets as stellar surfaces and atmospheres of evolved stars (Haniff et al. 1987; Tuthill, Haniff & Baldwin 1999a; Woodruff et al. 2008), dusty plumes surrounding Wolf–Rayet stars (Tuthill, Monnier & Danchi 1999b) and, most recently, protoplanetary discs (Eisner et al. 2009; Huélamo et al. 2011), and even suspected sub-stellar companions undergoing formation within (Arnold et al. 2012; Kraus & Ireland 2012).

Both visibilities and closure phases are subject to systematic errors arising from imperfections and instabilities in the instrumental point spread function (PSF). To combat this, the conventional approach in interferometry is to interleave observations of the science targets with observations of a calibrator star, usually an unresolved point-source (or sometimes an object with well-known structure). The calibrated visibilities are formed from the ratio of the science target's visibilities to those of the calibrator star, and the calibrated closure phases are the difference between those of the science and calibrator stars. The success of this calibration assumes that aberrations encountered by the calibrator star are a good statistical representation of those for the science target. This can be a poor assumption if the two are at different airmasses or if conditions change between observations.

Current masking interferometry programmes usually deploy the aperture-mask in a beam corrected by an adaptive optics system. For such experiments (Tuthill et al. 2006), the AO system acts as a fringe-tracker, stabilizing the fringe phase so that visibility information is preserved for exposure times longer than the atmospheric coherence time (a fraction of a second). The precision calibration provided by non-redundant masking then allows the PSF of the AO-corrected imaging system to be accurately calibrated.

1.2 Astronomical polarimetry

Polarimetry and polarimetric imaging are well-established techniques in astronomy. Earlier polarimetric studies measured the overall polarization of light from a star using a polarimeter with a single pixel detector such as a photomultiplier tube (e.g. Hall & Mikesell 1950; Hiltner 1956; Gehrels & Teska 1960; Mathewson & Ford 1970). These instruments had polarization precisions as good as 0.01 per cent when used over narrow bands, with subsequent developments extending this precision to wide bandwidths (e.g. Tinbergen 1973.) Later, imaging polarimeters were developed that could measure the polarization of a spatially resolved field, using both photographic (Woltjer 1957) and electronic (Scarrott et al. 1983) methods. General-purpose imaging instruments on 8 m telescopes such as NACO on the VLT and AO188/HICIAO on the Subaru telescope offer polarization modes, wherein the emphasis is on polarimetric differential imaging (PDI) – using the difference in polarization between starlight and scattered light to solve the contrast-ratio problem of imaging circumstellar discs – rather than high polarization precision (which is of the order of 1 per cent for NACO (Witzel et al. 2011). Newly developed polarimeters such as SPHERE/ZIMPOL (Thalmann et al. 2008) promise sensitivities of the order of 1 part in 10^5.

As in conventional imaging, all these polarimeters operate by forming an image of the science target on an array detector (such as a CCD), but with the addition of polarization optics which convert the polarization properties of the signal into intensity variations. In

the simplest case, this could be an analyser (linear polarizer), but in practice more complex systems are used to achieve the desired sensitivity and mitigate the effects of systematic errors resulting from instrumental polarization. Dual beam methods (where orthogonal polarizations are measured simultaneously using a polarizing beam-splitter) are often used, originally designed to improve polarimetric precision by removing the effect of seeing (Hiltner 1951). A related technique, channel switching (where polarizations are switched upstream with a rotating half-wave plate, HWP, or similar) is often used in combination with dual beam methods (Appenzeller 1967). Here, the channel-switching device is placed as far upstream as possible (before polarization-modifying elements just as mirrors and filters) allowing these systematic errors to be cancelled. Using either or both of these techniques, the differences or ratios of the intensities in the channels can be used to mitigate the effects of seeing and of instrumental polarization (Bagnulo et al. 2009).

High-precision instruments may use fast polarization switching (using a liquid crystal device or similar) to modulate the polarization on time-scales equal to or faster than atmospheric turbulence (Tinbergen 1973). Initially restricted to use with single-pixel detectors, advances have subsequently allowed this technique to be used with array detectors via some form of de-modulation at the detector, using an optical demodulator (Stenflo & Povel 1985) or an on-detector charge-shuffling technique (Thalmann et al. 2008; Bazzon et al. 2012). A particular challenge is the changing instrumental polarization at the Nasmyth focus of modern alt-az telescopes due to the changing angle of the M3 mirror with respect to the Nasmyth platform – a challenge that can be addressed by using a rotating compensator plate system (Tinbergen 2007). In all cases, proper characterization of and calibration for instrumental polarization is necessary.

In terms of exoplanet and protoplanetary disc studies, single-pixel polarimeters rely on detecting the small perturbations made to the overall polarization of the stellar system by the presence of a planet or other asymmetric body. They therefore need to be extremely sensitive to small polarizations; even systems with a close-in giant planet are expected to exhibit polarizations of only 10^{-5} or so (Seager, Whitney & Sasselov 2000). However, if the planet or disc is spatially resolved (as in an imaging polarimeter), then a much lower polarimetric sensitivity is required, assuming the surface polarization of the object is high. This methodology has been used successfully in the imaging of protoplanetary discs and the sub-structure therein, including around AB Aurigae (Perrin et al. 2009), HD100546 (Quanz et al. 2011) and HD142527 (Avenhaus et al. 2014), in which fractional (surface) polarizations from several per cent up to several tens of per cent were observed in the near-IR. These adaptive optics observations provided imaging of the disc to within an inner working angle of (in the best case) 100 mas from the star.

1.3 A new approach: polarimetric differential non-redundant masking

The VAMPIRES instrument is based upon a recent extension to the aperture-masking technique: *polarimetric* non-redundant masking, initially demonstrated using the NACO instrument on the VLT to image the dust shells around asymptotic giant branch stars (Norris et al. 2012). This technique – and the VAMPIRES instrument – leverage the aforementioned switching and modulation methods from conventional polarimetry and recast them in an interferometric context. In contrast to proposed methods for full Stokes optical interferometry (Elias 2001), we take a different, differential approach. Rather than calibrating the instrumental transfer function using a nearby reference star, this technique instead records two orthogonal polarisations of the science target simultaneously. Differential polarized observables can then be extracted by calibrating these observations against one another. In practice, extreme care must be taken to avoid systematic errors which would otherwise overwhelm the science signal – see Sections 2 and 3. This technique offers three distinct advantages in imaging circumstellar regions which emit even a modest degree of polarized flux.

First, it allows direct observations of polarized circumstellar structures at very small separations from the star, at contrasts which are unachievable with conventional non-redundant masking. Dusty structures such as mass-loss shells and circumstellar discs scatter unpolarized light from their host star, a process which yields a polarized signal. The differential polarimetric observables produced by this technique describe the spatially resolved polarized intensity distribution, allowing faint, polarized structures to be clearly imaged in isolation despite the immediate proximity of the very bright (but unpolarized) stellar photosphere.

Secondly, imaging data for the two orthogonal polarizations are recorded simultaneously, as opposed to many minutes apart for more conventional stellar interferometry (the time taken to slew from science target to reference star). For the interferometric calibration, this is a profound difference. Rather than attempting calibration of the statistical properties of the telescope–atmosphere transfer function, starlight recorded simultaneously traversed identical optical paths (with the exception of a small instrumental leg immediately prior to the detector discussed later). Exact, frame-by-frame calibration then makes it possible to eliminate errors arising from temporal-variation such as seeing, imperfect AO correction, changing airmass, and flexure of the optics.

Thirdly, the polarimetric data produced can reveal important information about the scattering medium. By using multiwavelength studies of the degree of fractional polarization, quantities such as dust grain size and even chemical makeup can be accurately constrained.

It is also important to compare polarimetric aperture masking to conventional imaging polarimetry. The key distinction in technique is that the differential calibration – performed by subtraction or division of intensities in conventional polarimetry – is instead performed in the Fourier domain by the calibration of interferometric visibilities. The goal of this technique is analogous to that of PDI – to exploit the difference in polarization between a star and the surrounding circumstellar dust (such as a protoplanetary disc) to overcome the contrast ratio problem and directly image the circumstellar region.

However, the parameter space in which polarimetric aperture masking operates is quite distinct from that of conventional polarimetric imaging/PDI. High-contrast, high angular-resolution imaging polarimeters generally employ a coronagraph to block out the light from the star to help achieve the desired contrast ratio between star and disc. This technique is thus limited by the coronagraph's inner working angle, with the two newest instruments – SPHERE and Gemini Planet Imager (GPI) – having an inner working angle of ∼100 and ∼200 mas, respectively (Martinez, Aller-Carpentier & Kasper 2010). This puts the innermost regions of circumstellar discs – critical for proper understanding of the planetary formation process – out of reach for conventional imaging polarimeters. A polarimetric aperture-masking instrument such as VAMPIRES, however, has an effective inner working angle limited only by its resolving power, approximately 10 mas (with a field of view of only ∼300 mas). Additionally, the spatial resolution of an imaging polarimeter

is limited by the performance of its adaptive optics system, while aperture masking can provide diffraction-limited performance even with high levels of wavefront error. Thus, this technique can explore a unique parameter space, unreachable with – but complementary to – conventional imaging or imaging polarimetry.

In the comparison between conventional polarimetry and polarimetric aperture masking, it is also important to note that the residual systematic errors in the differential visibilities (as shown in Section 4.1) do not represent the absolute polarization precision of the instrument. Rather, they arise from the difficulties in precisely calibrating visibilities common to all optical interferometry. Conventional aperture masking exhibits errors in calibrated visibilities of the order of 5–10 per cent (Monnier et al. 2004), while the polarimetric technique described here produces errors more than an order of magnitude better than this (see Section 4.1).

Polarimetric non-redundant masking offers one other advantage over a conventional imaging polarimeter: the Fourier transform of each interferogram is normalized with respect to the zero-baseline power, so the resulting visibilities are not a function of the total flux in the channel. This means that the derived observables are intrinsically immune to many forms of instrumental polarization systematic error, such as differing levels of transmission through the two channels of the polarizing optics. This automatically sidesteps a large fraction of instrumental challenges arising in more orthodox polarimeters, with the remainder being calibrated as described in Appendix A.

2 THE VAMPIRES INSTRUMENT

VAMPIRES is a purpose-designed instrument for performing polarimetric differential non-redundant masking. It is integrated into the SCExAO Extreme-AO system at the 8 m Subaru telescope, first tested on-sky in 2013 July. The concept grew from experience with the SAMPol mode commissioned by our group on the NACO instrument at the VLT (Norris et al. 2012) which enables near-infrared polarimetric masking interferometry. However, the new purpose-built VAMPIRES instrument offers a number of major advantages. While SAMPol relies on a strategy of slow-switching (every few minutes) of an HWP to swap polarization channels and thereby calibrate non-common path error, VAMPIRES features a fast-switching liquid-crystal variable retarder (LCVR) which allows channel switching every ∼10 ms. This is part of a three-tiered differential calibration scheme that demonstrated on-sky polarized visibilities calibrated to a precision of 1 part in 10^3 and polarized closure phases calibrated to a fraction of a degree, as detailed in Section 4.

A Wollaston prism (first tier) provides simultaneous measurements of orthogonal polarizations, allowing precise calibration of all time-varying components (e.g. due to seeing) but introduces non-common path errors. The fast-switching LCVR (second tier) works in concert, calibrating non-common path errors and variability on time-scales longer than the switch time. Finally, an HWP (third tier) which is placed further upstream calibrates out residual instrumental polarization and non-common path error of all optics downstream, particularly the non-ideal performance (e.g. chromaticity) of the LCVR. The entire instrument has been designed with precision instrumental polarization calibration in mind, incorporating a polarization state injector and rotating quarter-wave plate (QWP) for instrumental characterization.

Whereas NACO/SAMPol operates in the near-infrared $J - K$ bands, the visible/IR region (from 0.6 to 1.0μm) explored by VAMPIRES exploits the fact that the degree of polarization induced by scattering is a strongly rising function with shorter wavelengths. At the limit of small particle sizes, this can be seen in the λ^{-4} term in Rayleigh scattering. Moreover, at shorter wavelengths, the dependence of scattering cross-section on particle-size (for Mie scattering) is more pronounced, allowing greater discrimination between grain sizes. Stronger scattered-light signals yield more benign contrast ratios between circumstellar material and bright unpolarized host stars, allowing a wider range of astrophysical targets to be observed. Furthermore, wavelengths shorter than 1 μm are favoured from the perspective of detector technology as sensitive, relatively inexpensive EMCCD cameras are available providing rapid-exposure frames that are essentially free of readout noise.

VAMPIRES operates in a 'hitch-hiker' mode, taking data concurrently with infrared observations. The SCExAO system delivers wavelengths longer than 1 μm to its coronagraphs and IR science instruments (such as the HICIAO camera). Meanwhile, wavelengths shorter than 1 μm are routed to a second 'visible' optical bench where the available band is further divided between SCExAO's pyramid wavefront-sensor (PyWFS), VAMPIRES, and potentially other instruments. Therefore, VAMPIRES offers the opportunity to perform polarimetric aperture-masking observations simultaneously with HICIAO imaging during observations of protoplanetary discs and other suitable targets, delivering a supporting data stream without cost in additional observing time.

The parameter space explored by VAMPIRES is highly complementary to that of coronagraphs. VAMPIRES can deliver extremely high angular resolutions (of the order of 10 mas) over a limited field of view (∼300 mas depending of choice of mask and wavelength). Thus, the *outer working angle* of VAMPIRES complements the *inner working angle* of traditional coronagraphs, which typically have occulting spots of a few hundred milliarcseconds (Grady et al. 2013). VAMPIRES small inner working angle (effectively defined by the telescope diffraction limit) is in line with SCExAOs core mission of small inner-working angle wavefront control and coronagraphy, as implemented by its PIAA coronagraph (Guyon et al. 2010, whose inner working angle is as small as 50 milliarcseconds in the near-infrared). This inner region also plays into the nature of expected astrophysical signals, in which scattered starlight is expected to exhibit a strong fall-off with disc radius.

Although the primary design driver for VAMPIRES is the differential polarized masking mode, the instrument does allow a more versatile set of observational configurations. For example, it is entirely possible to treat VAMPIRES as a standard masking interferometer and employ a separate PSF reference star (as in Section 1.1). This would then deliver standard complex visibility imaging data (rather than polarization-differential data), enabling normal interferometry science to be performed and sacrificing the exceptional differential calibration. The outcome of operational testing of this mode is briefly discussed in Section 4.2. An even more straightforward operational mode is to employ VAMPIRES as an imaging polarimeter. Reconfiguring so that the mask is removed from the beam, and an image-plane field stop deployed to prevent polarized-field overlap, then rapid exposure differential imaging polarimetry data can be recorded. However, the focus of this paper is on the novel interferometric polarimetry and further discussion of these more orthodox strategies is limited.

2.1 Instrument design description

A schematic diagram of the instrument is given Â in Fig. 1. VAMPIRES is integrated into the SCExAO extreme adaptive optics

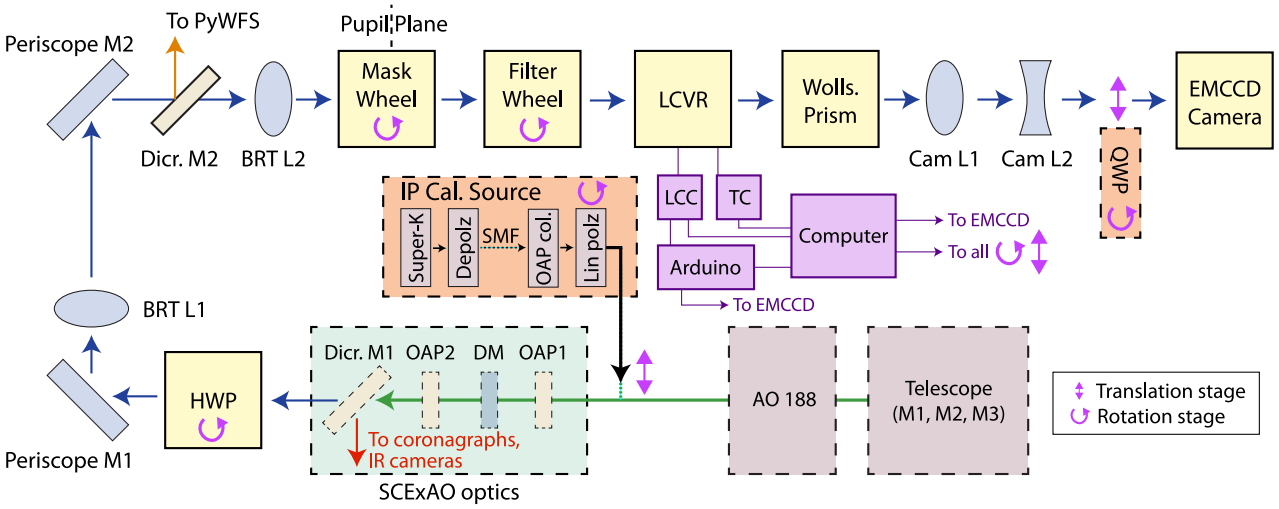

Figure 1. A schematic diagram of VAMPIRES as configured on-sky in 2013 July, with all items relevant to the VAMPIRES beam train shown. Operation of each sub-system is described in the text. Abbreviations: M – Mirror; L – Lens; OAP – Off Axis Parabola; DM – Deformable Mirror; Dicr.M – Dichroic Mirror; HWP – Half-wave plate; BRT – Beam Reducing Telescope; LCVR – Liquid-Crystal Variable Retarder; LCC – LCVR Controller; TC – Temperature Controller; Cam – Camera; QWP – Quarter-Wave Plate; Depolz – Depolarizer; OAP col. – OAP Collimator; Lin polz – Linear polarizer. In an alternative configuration, the HWP can be replaced with a pair of QWP to allow birefringence to be corrected as needed.

system which consists of two optical tables mounted one above the other, with the lower bench dedicated mainly to the near-infrared channel and the upper bench dedicated to the visible. The beam path from the telescope and AO 188 system passes into SCExAO, where high-order AO correction takes place. Wavelengths shorter than 1 μm are split off via a long-pass dichroic mirror and sent to the top 'visible' bench via a periscope and beam-reducing telescope (BRT). VAMPIRES' HWP is mounted in a Newport CONEX-AG-PR100P piezo-motor rotation stage which is positioned in the reflected beam immediately after the dichroic mirror and prior to the periscope mirror. This places it as far upstream as possible, sampling the greatest possible number of optics which could potentially induce instrumental polarization and therefore delivering the best possible calibration via channel switching (see Section 3). The HWP is a custom-designed achromatic wave-plate manufactured by Casix, with $\lambda/2$ retardance from 600 to 1000 nm. An alternative configuration is also being investigated wherein the HWP is replaced by two QWP. In this case, moving the QWPs together rotates the polarization as per the HWP, but moving one QWP relative to the other allows birefringence in the system to be compensated for.

The beam diameter at the HWP is 18 mm, but this reduces to 7.2 mm as it travels to the top bench through a periscope that also contains a BRT which consists of a Thorlabs AC508-500-B lens and AC508-200-B lens. A band-pass dichroic mirror is placed at the focus of the BRT to divert part of the spectrum to SCExAO's PyWFS. This dichroic can be exchanged under automated control to select the band directed to the PyWFS, and hence also the complementary band entering VAMPIRES. The BRT re-images the telescope pupil on to the non-redundant aperture mask. The aperture masks available are shown in Fig. 2, and are located in a custom wheel (mounted on a CONEX-AG-PR100P rotation stage) allowing masks to be changed at will. Factors governing choice of mask can be complicated, but often boil down to achieving the best balance between Fourier coverage and throughput for a given science target. Following the mask, a wheel populated with filters ranging from 600 to 800 nm with bandwidths of 50 nm is used to select the observing band.

Next, the beam encounters the LCVR, a Thorlabs LCC1111T-B device controlled by a Thorlabs LCC25 liquid crystal controller. The LCVR acts as variable wave-plate, switching its retardance between 30 nm and $\lambda/2$ depending on the applied voltage. This switching takes place rapidly, with a rise time of ∼10 ms and fall time of ∼250 μs. The retardance is also a function of temperature, and specified values are required for successful calibration. Therefore, the temperature of the device is actively controlled (using a Thorlabs TC200 temperature controller) to a temperature 45°C (higher temperatures allow faster switching times). The two orthogonal polarizations are then separated using a custom-designed Wollaston prism (manufactured by Altechna), and focused on to the detector using a pair of lenses (Thorlabs AC254-200-B and ACN254-075-B) in a telephoto configuration. The detector is an Andor Ixon 897 Ultra EMCCD camera.

The system is controlled by custom software written in MATLAB on a LINUX-based Intel i7 computer. This software allows control and scripting of all aspects of data acquisition (interfacing with the EMCCD camera, Arduino, and LCVR controller) as well as reconfigurable optomechanics. The software allows control of all functions via single graphical user interface, allowing simple remote operation and permitting the automation of lengthy calibration procedures.

A separate sub-system allows off-line characterization of the LCVR and calibration of residual polarization errors throughout the internal instrumental optical path. A calibration source (common to SCExAO and VAMPIRES) can remotely inject a simulated telescope beam into SCExAO with a specified polarization state. This consists of a supercontinuum source coupled into a single-mode fibre via a Thorlabs DPU-25-B achromatic depolarizer to remove any prior intrinsic polarization. The light is then collimated and passed through an achromatic linear polarizer (Thorlabs LPVIS100-MP) mounted in a CONEX-AG-PR100P rotation stage to allow linear polarized light at any specified orientation to be injected. A QWP (Thorlabs AQWP10M-980), also in a rotation mount, is also moved into the beam allowing a complete Mueller matrix of the instrument to be constructed as described in Appendix A.

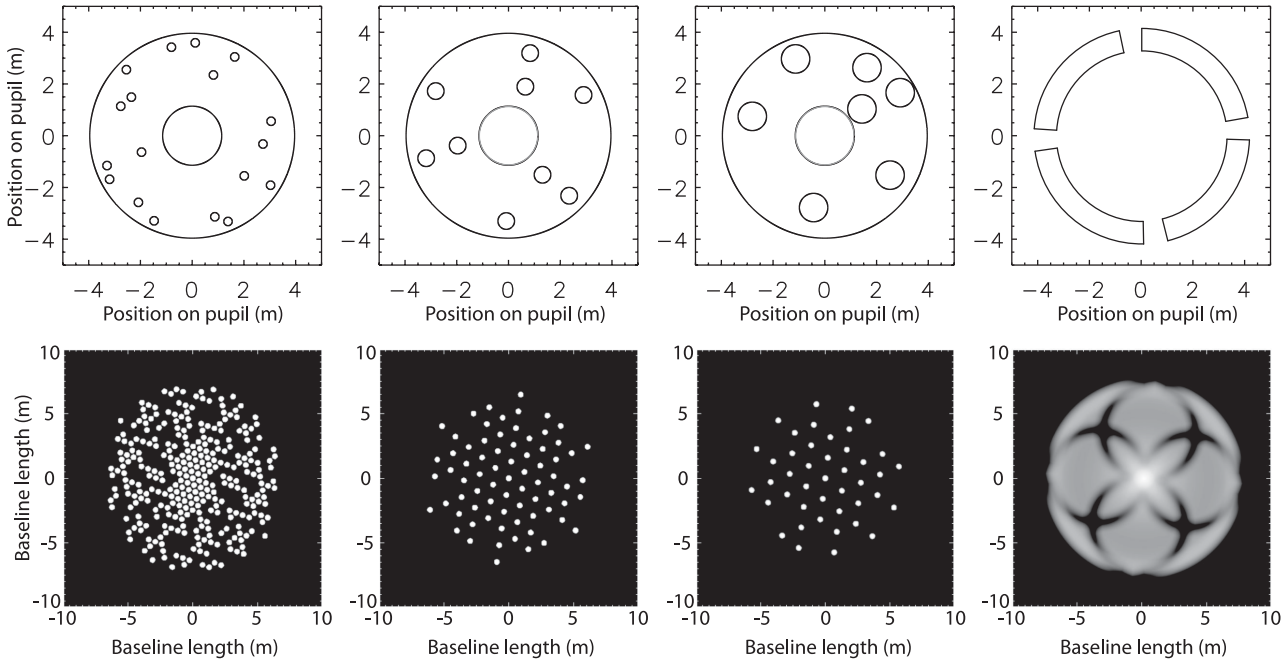

Figure 2. The non-redundant aperture mask designs installed in VAMPIRES (top) and their corresponding Fourier coverage (bottom). Masks with a greater number of holes boast better Fourier coverage at the expense of throughput. Masks are all non-redundant (the vector separation of all hole pairs is unique), with the exception of the annulus mask (right). This is doubly redundant, sacrificing non-redundancy for high throughout and full Fourier coverage. The gaps in Fourier coverage for this mask are due to the missing portions of the annulus needed to screen out the secondary-mirror supports (spiders).

As described in Section 3, VAMPIRES employs three tiers of differential calibration, one of which is rapid channel switching using the LCVR. This requires alternate frames acquired by the camera to have the incident beam polarization rotated by 90°, thus swapping the state probed by the two Wollaston channels. Due to the high acquisition rate and short integration times used (∼17 ms in order to maintain high visibilities despite residual seeing after AO correction), it was not possible to directly control the LCVR switching and camera exposures using the computer, due to the non-realtime operating system and variable USB latency. Instead, the timing signals were generated by a dedicated Arduino Uno microcontroller. When a data acquisition cycle is initiated at the computer, the desired timing parameters and commands are sent to the Arduino. The Arduino sends the appropriate timing signals based on its internal clock (via 5V TTL pulses) to the LCVR controller and camera. The computer software and Arduino remain in communication to allow further user interaction. Other settings, such as the desired LCVR voltages, temperature, camera readout patterns, and gain, are sent directly to the devices over USB cables.

3 DIFFERENTIAL DATA ANALYSIS

They key to VAMPIRES' performance is its differential measurement process, which is based on a calibration strategy adapted from conventional masking interferometry (see Section 1.1). However, rather than employing a separate PSF reference star, calibration is performed between Fourier observables extracted from images in simultaneously recorded orthogonal polarizations. This differential multitiered calibration process removes most sources of spatially and temporally dependent systematic error, producing a purely polarimetric set of observables.

Because calibration takes place on Fourier domain observables, the first step is the extraction of the two interferograms arising from each Wollaston channel in every camera frame to be windowed and Fourier transformed. The visibilities are then extracted from the power spectrum, and accumulated over a data cube (corresponding to a given LCVR and HWP state) consisting of around 200 frames. The bispectrum (the triple-product of the complex amplitudes of three baselines forming a closing triangle) is also accumulated, and the argument of the accumulated bispectrum gives the closure phase. For the non-redundant aperture masks, the complex visibility data are extracted at the *uv* coordinates corresponding to the set of known baselines formed by the mask. For the partially redundant annulus, discreet baselines are not present, so instead the Fourier domain is sampled uniformly while avoiding the regions of low power associated with gaps in the annulus (covering the secondary-mirror support structures as depicted in Fig. 2).

An overview of the calibration process is depicted in Fig. 3. The Wollaston prism allows measurements of orthogonal polarizations to be taken simultaneously and calibrated against each other, resistant to time-varying errors but subject to non-common path error. Conversely, the fast channel-switching LCVR allows the two channels of the Wollaston prism to be switched, and calibration performed between channel-switched states. This removes the effect of non-common path in the Wollaston, although with switching time-scales longer than τ_0 (the atmospheric coherence time, due to seeing) it is subject to some time-varying error. The calibration of these two calibrated quantities against one another – forming a second tier of calibration – provides resistance against both these error types. Finally, channel-switching of the bulk of the instrument takes place via a rotating HWP upstream. This calibrates out spatially dependent systematic errors due to the intervening optics. The rotating HWP also allows both linear Stokes parameters (Q and U) to be measured by rotating the polarization 45°.

For example, the visibilities from the two channels of the Wollaston prism ($V_{\rm Ch1}$, $V_{\rm Ch2}$) may be calibrated against one another

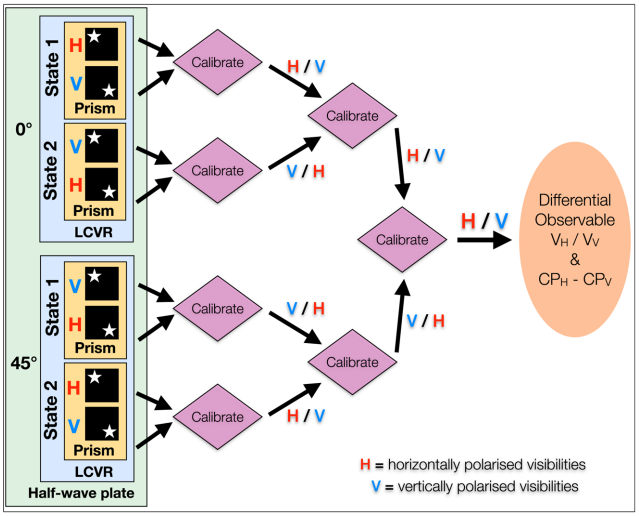

Figure 3. A pictorial depiction of our three-tiered calibration procedure. Calibration is performed between orthogonal polarizations rather than between a target and PSF calibrator star, to yield a polarimetric differential observable. The star in the black squares represents the interferogram as it appears on the detector. The 'H' or 'V' next to the black square indicates whether this polarization is Horizontal or Vertical, as determined by the combination of LCVR state, HWP position, and Wollaston prism channel. The top-most image is denoted 'horizontal' for purposes of demonstration. A series of divisions of visibilities create the final differential observable whilst systematic errors are cancelled out; an analogous process is performed with the closure phases using differences rather than ratios.

to produce

$$\frac{V_{\rm Ch1}}{V_{\rm Ch2}} = \frac{V_{\rm Horiz}}{V_{\rm Vert}}. \tag{1}$$

This is repeated but with polarizations rotated by 90° using the LCVR, yielding

$$\frac{V'_{\rm Ch1}}{V'_{\rm Ch2}} = \frac{V_{\rm Vert}}{V_{\rm Horiz}}. \tag{2}$$

These two differential quantities are then calibrated against one another, and raised to the power of 1/2 to maintain units:

$$\left(\frac{V_{\rm Ch1}}{V_{\rm Ch2}} \Big/ \frac{V'_{\rm Ch1}}{V'_{\rm Ch2}}\right)^{1/2} = \left(\frac{V_{\rm Horiz}}{V_{\rm Vert}} \Big/ \frac{V_{\rm Vert}}{V_{\rm Horiz}}\right)^{1/2} \tag{3}$$

$$= \left(\frac{V^2_{\rm Horiz}}{V^2_{\rm Vert}}\right)^{1/2} \tag{4}$$

$$= \frac{V_{\rm Horiz}}{V_{\rm Vert}}. \tag{5}$$

This is repeated for all other states and HWP positions, as depicted in Fig. 3, resulting in a final, calibrated $V_{\rm Horiz}/V_{\rm Vert}$ observable cleaned of almost all temporal and non-common-path errors. The same process takes place for the closure phases, but with differences rather than ratios, to produce a final calibrated $CP_{\rm Horiz} - CP_{\rm Vert}$. Note that the 'horizontal' and 'vertical' polarization angles referred to here are arbitrary (ultimately mapping to a known position angle on sky), and conceptually represent any two orthogonal states. The entire process is repeated for both Stokes Q and U by offsetting the angle of the HWP.

4 ON-SKY RESULTS

The VAMPIRES instrument was tested on-sky in 2013 July during SCExAO engineering time which allowed the calibration precision to be measured under real observing conditions. These tests were conducted with the standard AO 188 system. The system configuration at the time had relatively low throughput, with the visible beam being split between several different instruments both spectrally and with a 50/50 grey beam-splitter. Therefore, we expect the precisions shown here to improve in subsequent observations. The goal is to demonstrate differential visibility precision of the order of 10^{-3} (or 0.1 per cent).

4.1 On-sky differential visibilities and closure phases

Two unresolved bright stars, Vega and Altair, were observed as part of the SCExAO engineering schedule, while the VAMPIRES instrument was able to obtain simultaneous observations in the visible. This provided an ideal test of VAMPIRES' calibration precision, since these point-source[1] stars should ideally exhibit a polarized-differential visibility of 1.0 on all baselines, and zero closure phases. This also allowed the evaluation of VAMPIRES' multiple tiers of differential calibration, both individually and in combination.

The results of observing Vega with the 18 hole mask at $\lambda = 775$ nm (FWHM = 50 nm) with a total integration time of 109 s are shown in Fig. 4. The standard deviation of the differential visibilities is seen to increase with successive tiers of differential calibration. The Wollaston prism in (a) removes time-varying errors (e.g. due to seeing) so small random-errors are reflected in the error-bars, but non-common path error leads to large (up to 10 per cent) systematics. Conversely, the LCVR (b) removes non-common path error but is subject to time-varying error, resulting in a mean of ∼1 but large random error. Double-differential calibration (c) with the LCVR and Wollaston mitigates both time-varying and non-common path error. Triple-differential calibration (d) with the HWP further removes static systematic errors (such as those arising from instrumental effects, and non-uniform retardance across the aperture of the LCVR due to thermal gradients). The resulting differential visibilities have a standard deviation of 4.2×10^{-3}, which is approaching our desired performance levels. At this point, the precision is limited by random noise processes (such as photon and Electron Multiplying (EM) gain noise) and would improve with longer integrations. It should also be noted that these data were taken without the Extreme-AO correction anticipated from SCExAO in the future, which will lead to further improvement (increased fringe visibility and hence increased signal/noise). A similar observational sequence on Altair was conducted with the 9 hole mask (which trades more sparse Fourier sampling for the gain of higher throughput) at $\lambda = 750$ nm (FWHM = 40 nm). Here, the triple-differential visibilities had a standard deviation of 2.4×10^{-3}.

The annulus mask was also tested while observing Vega at $\lambda = 775$ nm, but performed poorly due to a misalignment between the mask and telescope pupil (due to chromatic effects upstream). This mask is especially susceptible to such misalignments since the annulus is oversized, relying on the edge of the telescope pupil to define the outer edge of the masked aperture. One side of the annular opening was almost completely occluded, causing large errors at longer baselines (see Fig. 5). Performing the same analysis considering only baselines with lengths shorter than 4 m, then

[1] The known disc around Vega is significantly too large to be seen with VAMPIRES.

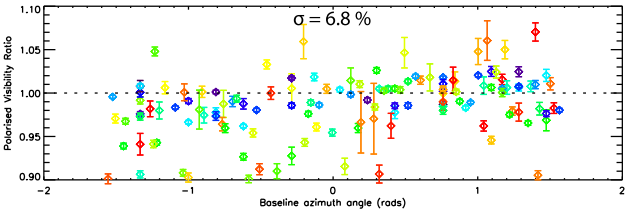

(a) 1 tier - Wollaston prism only. No temporal variation leads to small error bars, but strong systematic errors (from non-common path) dominate.

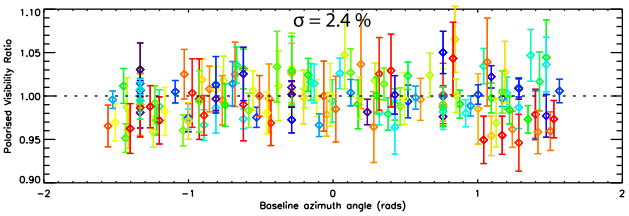

(b) 1 tier - LCVR only. No non-common path error, and the mean is ∼1.0. However since switching is slower than seeing temporal errors lead to large error bars.

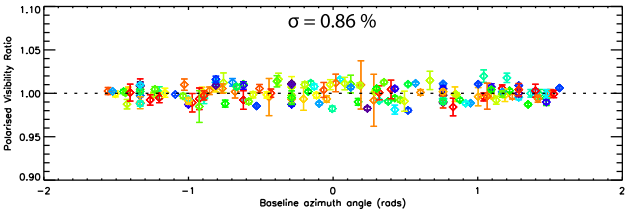

(c) 2 tiers - Wollaston + LCVR. The Wollaston and LCVR cancel each others errors. Systematic errors are still visible.

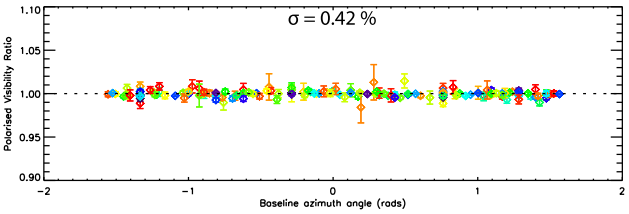

(d) 3 tiers - Wollaston + LCVR + HWP. The HWP cancels out static systematic errors (such as those arising from instrumental effects). Here precision is limited by random error; additional integration time would improve precision further.

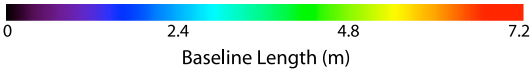

Figure 4. The on-sky differential visibilities from an observation of Vega at 775 nm with the 18 hole mask, showing the effect of different tiers of calibration. Ideally, the visibility ratio should be unity on all baselines, since the source is unresolved. Baseline azimuth is plotted on the horizontal axis, while baseline length is represented by colour. The precision is seen to increase with successive layers of calibration, as discussed in the text. Data were taken without Extreme-AO correction.

the performance dramatically improves with the standard deviation of the triple-differential visibilities dropping to 1.7×10^{-3} (see Fig. 5b). VAMPIRES is being upgraded to allow complete remote mask positioning and pupil viewing, eliminating the potential for such a misalignment problem in future observations.

Multiple differential calibration was found to provide improvements in closure-phase precision similar to those described for visibilities. For an unresolved star, the closure phases on all triangles should be zero. Therefore, for the ensemble of all closure phases should ideally have a mean of zero and standard deviation of zero.

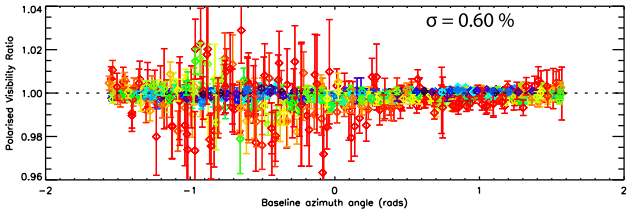

(a) Annulus mask, all baselines. Errors from long baselines due to pupil misalignment dominate.

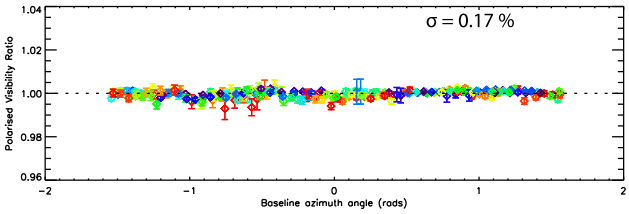

(b) Only baselines shorter than 4 m (unaffected by pupil mislagniment).

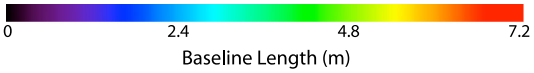

Figure 5. The on-sky triple differential visibilities from Vega at 775 nm, with the annulus mask. Due to a misalignment between the mask and pupil, many longer baselines have extremely low visibilities, resulting in large errors (panel a). If these affected baselines are eliminated by only plotting shorter baselines, excellent precision (0.17 per cent) is observed (panel b).

A set of histograms of closure phases (for the same Vega observation as in Fig. 4) at varying levels of differential calibration are given in Fig. 6. As found for the visibilities, the precision – represented by a small mean and width of the distribution – improves with increasing levels of calibration. With the full triple-calibration applied, the closure-phase distribution has a standard deviation of 0.°72 and a mean of 0.°009. However, examination of the random error for each triangle (based on the error encountered across the set of all integrations) is large compared to the standard error of the ensemble of closure phases, indicating that statistical errors set the present limitation and precision will improve further with larger volumes of data.

4.2 Non-polarimetric on-sky results

As previously mentioned, VAMPIRES can also operate in a non-polarimetric mode, wherein it works the same way as conventional aperture masking (albeit at shorter wavelengths). In this case, signals from orthogonal polarization channels are simply combined together, thus discarding the polarization information. Calibration was now performed with respect to a separate observation of an unresolved reference star. During the 2013 July observations, VAMPIRES had the opportunity to observe χ Cygni, an S-type star expected to be spatially resolved, and the binary star η Pegasi.

χ Cygni was observed by VAMPIRES with the 18 hole mask at $\lambda = 750$ nm, and was resolved, allowing its angular diameter to be measured. The V magnitude was ∼6 at time of observation,[2] and total integration time was 54 s. No polarized signal was detected from this target during these observations within the sensitivity achieved in this observation (differential visibility precision of ∼2 per cent due to the relatively short integration time and faintness of the

[2] Observations from the AAVSO International Database, http://www.aavso.org.

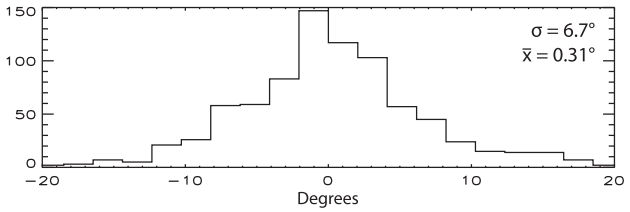

(a) Raw closure phases (no calibration).

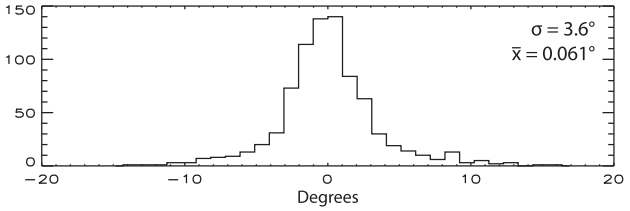

(b) 1 tier - Wollaston prism only. The mean now close to zero.

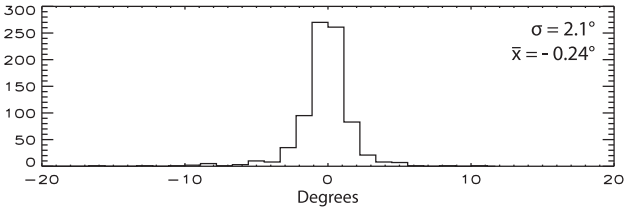

(c) 1 tier - LCVR only. CP distribution improves but a large offset remains.

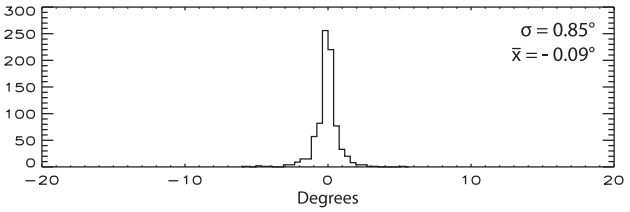

(d) 2 tiers - Wollaston + LCVR. Both the width of the distribution and the mean improve.

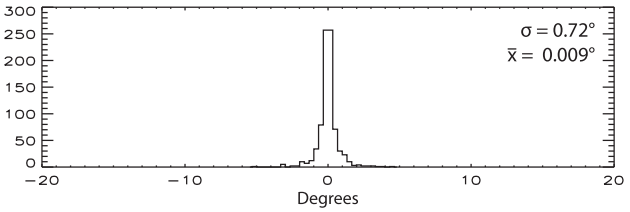

(e) 3 tiers - Wollaston + LCVR +HWP. The offset improves by an order of magnitude. The standard deviation is still dominated by random noise, so will improve with longer integration / greater throughput.

Figure 6. Histograms of the on-sky differential closure phases recorded on Vega (same data as presented in Fig. 4), showing the effect of different calibration levels. Since the star is unresolved, ideally both the mean and standard deviation would be zero.

target). However, non-polarimetric measurements were made using the previously observed star Altair (discussed above) as a PSF reference, although this was not an ideal calibrator since it was observed at a different airmass and time of the night. Despite this, accurate complex visibility data were recovered, constraining a uniform disc fit yielding a diameter of 32.2 ± 0.1 mas. This is in close agreement with the literature values tabulated in the CHARM2 catalogue (Richichi, Percheron & Khristoforova 2005), which gives the uniform disc diameter as 32.8 ± 4.1 mas in *V* band.

The binary system η Pegasi was observed with the 18 hole mask at $\lambda = 775$ nm, again for a total integration time of 54 s. Vega was again used as a calibrator (with the same reservations). The binary was detected, and its separation and position angle constrained. A Monte Carlo simulation was used to determine the statistical confidence of the detection, which was found to be better than 99.9 per cent. The separation was measured to be 48.9 ± 0.6 mas. This is consistent with the predicted separation based on the orbital parameters measured by Hummel et al. (1998) of 49.9 mas. The slight discrepancy is probably a result of imperfect knowledge of the mapping between the sky and instrumental field orientations, which is presently based only on values from the optical system model. Further studies of several stellar systems with known structure are planned to precisely calibrate both orientation and plate scale of VAMPIRES. The contrast ratio was measured to be 3.55 ± 0.06 mag, again in good agreement with the value measured by Hummel et al. (1998) of 3.61 ± 0.05 mag.

5 SIMULATED DATA AND PERFORMANCE PREDICTIONS

The differential Fourier visibilities (e.g. $V_{\rm Horiz}/V_{\rm Vert}$) obtained from VAMPIRES are not directly equivalent to the differential intensities (or fractional polarizations) obtained in techniques such as polarized differential imaging. Rather, the magnitude of each of these differential visibilities (i.e. of their departure from $V_{\rm Horiz}/V_{\rm Vert} = 1$) describes the amount of correlated polarized flux at the corresponding spatial frequency, and the differential closure phases describe the corresponding phase. Since these quantities are less intuitive than polarized intensities, simulated VAMPIRES data have been produced using a radiative transfer model of a representative flared axisymmetric protoplanetary disc, in order to give a qualitative example. This particular model demonstrates the ability of VAMPIRES to precisely observe the inner rim of such discs. The model was created using the HYPERION radiative transfer code (Robitaille 2011) using a parametric density function, with a power-law surface density profile and Gaussian vertical structure (Andrews et al. 2011). The disc density is given by

$$\rho(R, z, \phi) = \rho_0 \left(\frac{R_0}{R}\right)^{\beta - p} \exp\left(-\frac{1}{2}\left(\frac{z}{h(R)}\right)^2\right), \quad (6)$$

where

$$h(R) = h_0 \left(\frac{R}{R_0}\right)^{\beta}. \quad (7)$$

Parameters were set to typical values, with an inner radius of 25 au and an outer radius of 300 au, and a disc mass of 0.01 $M_\odot$, from which ρ_0 is calculated automatically. The surface density exponent p was set to −1 and the scaleheight exponent β set to 1.125. H_{100}, the scaleheight of the disc at 100 au, was set to 20 au. The inclination and position angle are 57° and 30°, respectively. The model disc surrounds an A0-type star with $T_{\rm eff} = 9000$ K. The dust in the disc is a mix of silicate and carbon species based on the KMH distribution (Kim, Martin & Hendry 1994). The observational wavelength is 800 nm and the disc is placed at a distance of 500 pc.

Polarized images produced by the HYPERION code, together with the corresponding polarized differential visibilities, are shown in Fig. 7. In this model scenario, starlight scattered by the inner wall dominates, and the VAMPIRES data are seen to be extremely sensitive to the structure of the inner region. A strong modulation of the differential visibilities as a function of azimuth and baseline length is apparent in Fig. 7(c). Along with the associated differential closure phases (not plotted here), these encode the detailed polarized

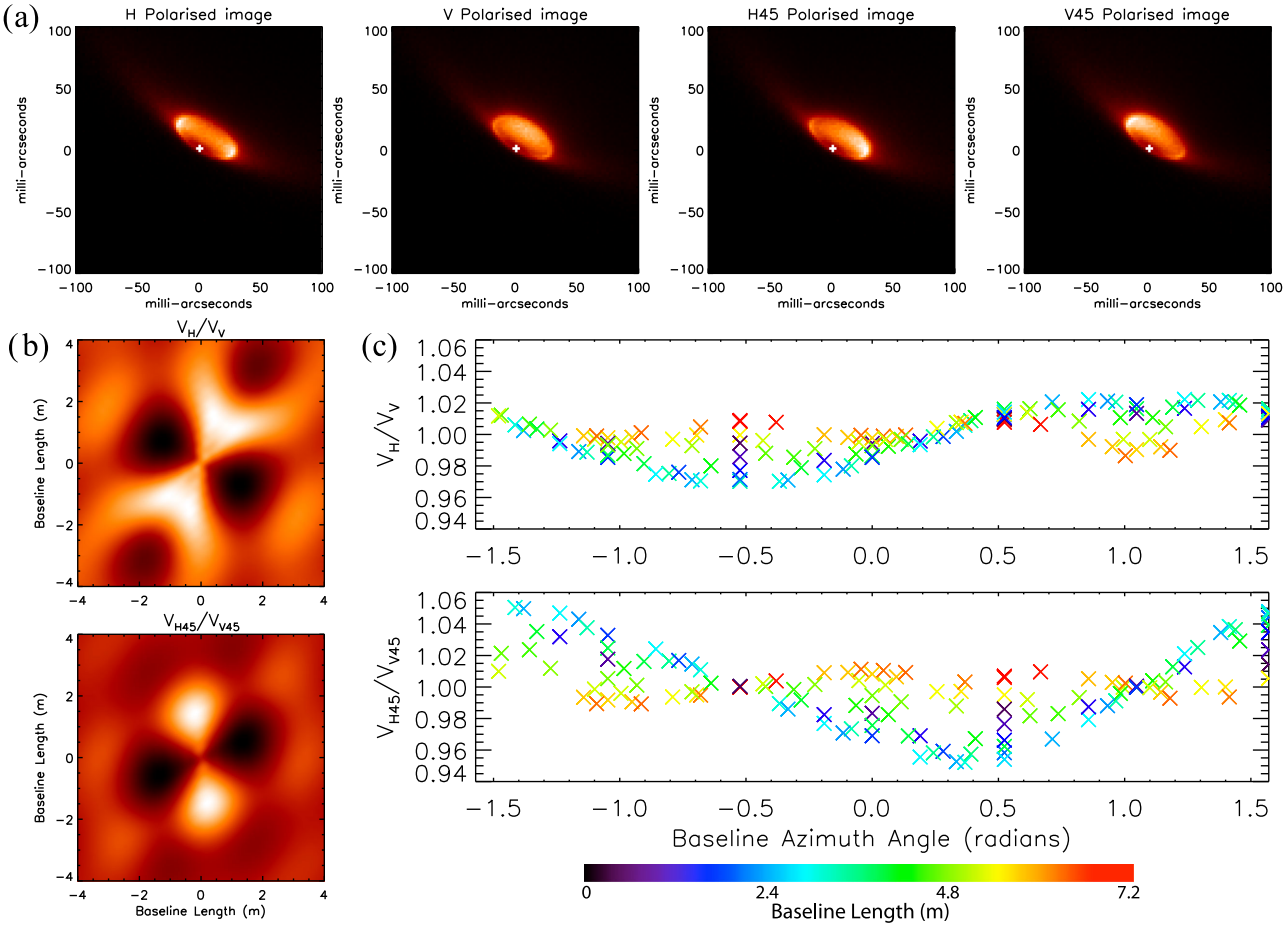

Figure 7. A modelled protoplanetary disc at 500 pc (see Section 5) and the derived VAMPIRES data for $\lambda = 800$ nm. (a) Image of the inner region of the disc, shown with a non-linear intensity mapping, in four polarizations: horizontal H and vertical V corresponding to Stokes Q, while H45 and V45 are the two orthogonal polarizations rotated 45° corresponding to Stokes U. (b) The differential power spectra for the two pairs of orthogonal polarizations. (c) Expected differential visibility signals as seen by VAMPIRES with an 18 hole mask.

structure of the inner 100 mas or so. If more complex structures were present, such as asymmetrical clumps or an inner disc, they would be clearly evident in these signals.

The on-sky sensitivity of VAMPIRES has been quantified based on laboratory testing, wherein flux levels matching various stellar magnitudes were used along with simulated atmospheric turbulence. The turbulence was simulated by reproducing a AO-corrected Kolmogorov screen (based on typical seeing and wind speeds) via active modulation of the wavefront using the 2K deformable mirror within SCExAO. Visibility precisions of the order of 10^{-3} were reliably obtained for targets as faint as fourth magnitude using the 18 hole mask for integration times of 15 min (plus overhead for wave-plate switching), or 5.5 mag in 1 h integration. For fainter targets, a mask with higher throughput is advantageous. The laboratory test data indicated that the 9 hole mask will achieve this precision in 1 h for 6.5 mag stars and the 7 hole mask will achieve it in 1 h for eighth magnitude. The annulus should theoretically achieve order 10^{-3} precision in 1 h integration for stars as faint as 8.5 mag; however, as discussed in Section 4.1, this is currently only realized on the shorter (<4 m) baselines due to pupil alignment drift, a problem that is currently being addressed. Additional overhead must be allowed for due to time taken for wave-plate switching – this can be anywhere between 25 and 100 per cent of the integration time depending on switching frequency.

The representative model presented in this section has differential visibilities with an average magnitude (deviation for unity) of approximately 2 per cent. With the demonstrated on-sky precision using the 18 hole mask of 0.4 per cent, the $V_{\rm Horiz}/V_{\rm Vert}$ of each baseline can be measured to 5σ. However, the actual uncertainties on a fitted model would be much smaller due to the relatively small number of free parameters involved.

6 SUMMARY

By combining non-redundant aperture-masking interferometry with differential polarimetry, the VAMPIRES instrument will directly image the innermost region of protoplanetary discs, providing critical insight into the processes of disc evolution and planet formation. Non-redundant aperture masking provides diffraction-limited performance by way of the established interferometric visibility and closure-phase observables. VAMPIRES' triple-differential polarimetric calibration strategy exploits the polarization of scattered starlight, utilizing simultaneous differential measurements with a Wollaston prism, fast channel-switching with an LCVR and slow-switching with a rotating HWP to better remove instrumental systematics. The resulting signal encodes the resolved, polarized structure of the inner disc. These observables are largely immune to the effects of instrumental polarization, with the remainder being

removed by precise calibration of the instrumental Mueller matrix using an in-built characterization system.

VAMPIRES records data at visible wavelengths (where polarization from scattering is typically higher) in a hitch-hiker mode that does not affect simultaneous science operation of other (infrared) instruments. On-sky demonstrations of the VAMPIRES instrument yielded a differential-visibility precision approaching 10^{-3} and closure-phase standard-deviation better than 1°. Limitations to both performance metrics are presently provided by restricted statistical sample size and therefore further improvement is expected with longer on-sky integration times. Precise visibilities and closure phases will be used to accurately constrain disc models, and to detect the presence of asymmetries and density enhancements which reveal the presence of embedded gravitating companions. The instrument is now integrated into the SCExAO system and is ready for its first science observations, planned for mid to late 2014. Eventually, the instrument will be largely autonomous and capable of entirely remote operation, allowing simultaneous measurements with standard facility instruments SCExAO/HICIAO when required.

REFERENCES

Andrews S. M., Wilner D. J., Espaillat C., Hughes A. M., Dullemond C. P., McClure M. K., Qi C., Brown J. M., 2011, ApJ, 732, 42
Appenzeller I., 1967, PASP, 79, 136
Arnold T. J., Eisner J. A., Monnier J. D., Tuthill P., 2012, ApJ, 750, 119
Avenhaus H., Quanz S. P., Schmid H. M., Meyer M. R., Garufi A., Wolf S., Dominik C., 2014, ApJ, 781, 87
Bagnulo S., Landolfi M., Landstreet J. D., Landi Degl'Innocenti E., Fossati L., Sterzik M., 2009, PASP, 121, 993
Baldwin J. E., Haniff C. A., Mackay C. D., Warner P. J., 1986, Nature, 320, 595
Bazzon A. et al., 2012, in McLean I. S., Ramsay S. K., Takami H., eds, Proc. SPIE Conf. Ser. Vol. 8446, SPHERE/ZIMPOL: Characterization of the FLC Polarization Modulator. SPIE, Bellingham, p. 844693
Bryden G., Chen X., Lin D. N. C., Nelson R. P., Papaloizou J. C. B., 1999, ApJ, 514, 344
Calvet N., D'Alessio P., Hartmann L., Wilner D., Walsh A., Sitko M., 2002, ApJ, 568, 1008
Clarke D., 1973, A&A, 24, 165
Eisner J. A., Monnier J. D., Tuthill P., Lacour S., 2009, ApJ, 698, L169
Elias N. M., II, 2001, ApJ, 549, 647
Fukagawa M. et al., 2004, ApJ, 605, L53
Gehrels T., Teska T. M., 1960, PASP, 72, 115
Goldstein D., 2011, Polarized Light, Revised and Expanded, Optical Engineering. Marcel Dekker, New York
Grady C. A. et al., 2013, ApJ, 762, 48
Guyon O., Martinache F., Belikov R., Soummer R., 2010, ApJS, 190, 220
Guyon O., Martinache F., Clergeon C., Russell R., Groff T., Garrel V., 2011, in Tyson R. K., Hart M., eds, Proc. SPIE Conf. Ser. Vol. 8149, Wavefront Control with the Subaru Coronagraphic Extreme Adaptive Optics (SCExAO) System. SPIE, Bellingham, p. 814908
Hall J. S., Mikesell A. H., 1950, Publ. U.S. Nav. Obs. Second Ser., 17, 3
Haniff C. A., Mackay C. D., Titterington D. J., Sivia D., Baldwin J. E., 1987, Nature, 328, 694
Hashimoto J. et al., 2011, ApJ, 729, L17
Hauge P., 1980, Surf. Sci., 96, 108
Hiltner W. A., 1951, The Observatory, 71, 234
Hiltner W. A., 1956, ApJS, 2, 389
Huélamo N., Lacour S., Tuthill P., Ireland M., Kraus A., Chauvin G., 2011, A&A, 528, L7
Hummel C. A., Mozurkewich D., Armstrong J. T., Hajian A. R., Elias N. M., II, Hutter D. J., 1998, AJ, 116, 2536
Jovanovic N. et al., 2013, in Esposito S., Fini L., eds, Proc. Third AO4ELT Conf., SCExAO as a Precursor to an ELT Exoplanet Direct Imaging Instrument. Available at: http://ao4elt3.sciencesconf.org/
Kim S.-H., Martin P. G., Hendry P. D., 1994, ApJ, 422, 164
Kraus A. L., Ireland M. J., 2012, ApJ, 745, 5
Martinez P., Aller-Carpentier E., Kasper M., 2010, The Messenger, 140, 10
Mathewson D. S., Ford V. L., 1970, MNRAS, 74, 139
Monnier J. D. et al., 2004, ApJ, 605, 436
Norris B. R. M. et al., 2012, Nature, 484, 220
Olofsson J. et al., 2011, A&A, 528, L6
Perrin M. D., Schneider G., Duchene G., Pinte C., Grady C. A., Wisniewski J. P., Hines D. C., 2009, ApJ, 707, L132
Quanz S. P., Schmid H. M., Geissler K., Meyer M. R., Henning T., Brandner W., Wolf S., 2011, ApJ, 738, 23
Readhead A. C. S., Nakajima T. S., Pearson T. J., Neugebauer G., Oke J. B., Sargent W. L. W., 1988, AJ, 95, 1278
Richichi A., Percheron I., Khristoforova M., 2005, A&A, 431, 773
Robitaille T. P., 2011, A&A, 536, A79
Scarrott S. M., Warren-Smith R. F., Pallister W. S., Axon D. J., Bingham R. G., 1983, MNRAS, 204, 1163
Seager S., Whitney B. A., Sasselov D. D., 2000, ApJ, 540, 504
Stenflo J. O., Povel H., 1985, Appl. Opt., 24, 3893
Thalmann C. et al., 2008, in McLean I. S., Casali M. M., eds, Proc. SPIE Conf. Ser. Vol. 7014, SPHERE ZIMPOL: Overview and Performance Simulation. SPIE, Bellingham, p. 70143F
Tinbergen J., 1973, A&A, 23, 25
Tinbergen J., 2007, PASP, 119, 1371
Tuthill P. G., Haniff C. A., Baldwin J. E., 1999a, MNRAS, 306, 353
Tuthill P. G., Monnier J. D., Danchi W. C., 1999b, Nature, 398, 487
Tuthill P. G., Monnier J. D., Danchi W. C., Wishnow E. H., Haniff C. A., 2000, PASP, 112, 555
Tuthill P. et al., 2006, in Ellerbroek B. L., Calia D. B., eds, Proc. SPIE Conf. Ser. Vol. 6272, Sparse-Aperture Adaptive Optics. SPIE, Bellingham, p. 62723A
Williams J. P., Cieza L. A., 2011, ARA&A, 49, 67
Witzel G. et al., 2011, A&A, 525, 130
Woltjer L., 1957, Bull. Astron. Inst. Neth., 13, 301
Woodruff H. C., Tuthill P. G., Monnier J. D., Ireland M. J., Bedding T. R., Lacour S., Danchi W. C., Scholz M., 2008, ApJ, 673, 418

APPENDIX A: CALIBRATION OF INSTRUMENTAL POLARIZATION

The differential calibration of VAMPIRES mitigates the effect of many instrumental polarization effects. Moreover, since the visibilities for each polarization channel are normalized with respect to the total flux in that channel, simple diattenuation has no effect on the measured observables (unlike the case for standard polarimetry). However, this does not take into account cross-terms in the instrumental Mueller matrix (which describes the polarization properties intrinsic to the instrument and how they alter each of the Stokes parameters of the incoming light (Goldstein 2011)). $Q \rightarrow U$ and $U \rightarrow Q$ mixing will lead to incorrect measurement of the relative magnitude of Stokes Q and U measurements. The $Q \leftrightarrow V$ and $U \leftrightarrow V$ cross-terms are even more problematic – since VAMPIRES does not measure Stokes V, it thus appears to the instrument that part of the Stokes Q and U components have 'disappeared', leading to an underestimation of the magnitude of the polarization. Since VAMPIRES itself is behind the pre-existing systems AO 188 (which includes a k-mirror image rotator) and SCExAO, significant instrumental polarization cannot be avoided, and instead must be mitigated by careful calibration and the tripe-differential measurement process.

To resolve these problems, a careful full characterization of the instrumental Mueller matrix is performed immediately before or after astronomical observations, which is then used to correct data during processing. This characterization procedure is fully automated and can be performed remotely. First, a linear polarizer on

a rotation stage is driven into the beam upstream of the SCExAO optical path, and a rotating QWP is positioned immediately before the Wollaston prism inside VAMPIRES – see Fig. 1. Any residual polarized structure in the light incident upon the linear polarizer is removed by first passing it (as a large-diameter beam) through an achromatic wedge depolarizer, allowing an arbitrary linear polarization to be generated. Alternatively, the halogen flat-field lamp, linear polarizer and HWP which already exist within the AO188 adaptive optics system may be used to inject the linearly polarized reference, which has the advantage of characterizing the optics within AO188 itself as well. By using the Wollaston prism as the analyser, a rotating-polarizer/rotating-compensator+fixed-analyser (RP/RCFA) type Mueller matrix polarimeter (Hauge 1980) is created. Data from such a setup can specify the first three columns of the Mueller matrix of the instrument. While the fourth column cannot be determined, if the assumption is made that the astrophysical source has a negligible circular polarization component, then the missing fourth column is inconsequential.

If the QWP and linear polarizer are rotated synchronously such that the angle of the QWP is three times that of the polarizer, then the first three columns of the Mueller matrix can be directly determined by Fourier analysis of the resulting intensity variation (Hauge 1980). Alternatively, to provide more physical insight into the origin of the polarization effects, a polarization model of the instrument can be created, and then fine-tuned by fitting it to the measured calibration data (Witzel et al. 2011). In this case, the Mueller matrix of the instrument is created by combining the Mueller matrices of the individual components, with the appropriate rotations. The linear polarizer (and the Wollaston prism channels), with their polarization axis at angle θ, are represented by the matrix $M_{\rm LP}$:

$$M_{\rm LP} = M_{\rm r(\theta)}^{-1} \times M_{\rm LP(h)} \times M_{\rm r(\theta)}, \tag{A1}$$

where $\times$ signifies matrix multiplication, $M_{\rm LP(h)}$ represents the matrix of an ideal horizontal linear polarizer, i.e.

$$M_{\rm LP(h)} = \frac{1}{2}\begin{pmatrix} 1 & 1 & 0 & 0 \\ 1 & 1 & 0 & 0 \\ 0 & 0 & 0 & 0 \\ 0 & 0 & 0 & 0 \end{pmatrix} \tag{A2}$$

and $M_{\rm r(\theta)}$ is the rotation matrix in Stokes space for angle θ:

$$M_{\rm r(\theta)} = \begin{pmatrix} 1 & 0 & 0 & 0 \\ 0 & \cos 2\theta & \sin 2\theta & 0 \\ 0 & -\sin 2\theta & \cos 2\theta & 0 \\ 0 & 0 & 0 & 1 \end{pmatrix}. \tag{A3}$$

Similarly, the Mueller matrix for a wave-plate (retarder) can be represented as

$$M_{\rm WP} = M_{\rm r(\theta)}^{-1} \times M_{\rm WP(h)} \times M_{\rm r(\theta)}, \tag{A4}$$

where $M_{\rm r(\theta)}$ is as before and $M_{\rm WP(\mathit{h})}$ is the matrix of a wave-plate with retardance ϕ:

$$M_{\rm WP(h)} = \begin{pmatrix} 1 & 0 & 0 & 0 \\ 0 & 1 & 0 & 0 \\ 0 & 0 & \cos\phi & \sin\phi \\ 0 & 0 & -\sin\phi & \cos\phi \end{pmatrix}. \tag{A5}$$

Combinations of these matrices can represent VAMPIRES' HWP, LCVR, and Wollaston prism, as well as the linear polarizer and QWP used for calibration. Instrumental polarization arises mostly from reflections off various mirrors in the system. Reflections from a metallic mirror cause both a change in transmission between linear polarization components and a change in phase between these components. The Mueller matrix for a metallic mirror can thus be constructed by combining the matrices for a partial-linear polarizer with a wave-plate, resulting in the following matrix (Clarke 1973):

$$M = \frac{1}{2}\begin{pmatrix} r_\perp + r_\parallel & r_\perp - r_\parallel & 0 & 0 \\ r_\perp - r_\parallel & r_\perp + r_\parallel & 0 & 0 \\ 0 & 0 & \sqrt{r_\perp r_\parallel}\cos\delta & \sqrt{r_\perp r_\parallel}\sin\delta \\ 0 & 0 & -\sqrt{r_\perp r_\parallel}\sin\delta & \sqrt{r_\perp r_\parallel}\cos\delta \end{pmatrix}, \tag{A6}$$

where $r_\perp$ and $r_\parallel$ are the coefficients of reflection for the perpendicular and parallel polarizations, respectively, and δ is the retardance between the components. For each metallic surface in the VAMPIRES optical model, these values are in turn calculated from the metal's known complex refractive index $\widetilde{n_2}$ using the amplitude Fresnel equations (where $\widetilde{n_1} \approx 1$ is the refractive index of air). The complex amplitudes of the perpendicular and parallel reflected components, respectively, are given by

$$\widetilde{r_\perp} = \frac{\widetilde{n_1}\cos\theta_{\rm i} - \widetilde{n_2}\cos\theta_{\rm t}}{\widetilde{n_1}\cos\theta_{\rm i} + \widetilde{n_2}\cos\theta_{\rm t}} \tag{A7}$$

$$\widetilde{r_\parallel} = \frac{\widetilde{n_2}\cos\theta_{\rm i} - \widetilde{n_1}\cos\theta_{\rm t}}{\widetilde{n_1}\cos\theta_{\rm t} + \widetilde{n_2}\cos\theta_{\rm i}}, \tag{A8}$$

where $\theta_{\rm i}$ is the angle of incidence and $\theta_{\rm t}$ is nominally the angle of transmission, and is calculated using Snell's law, but in the case of a metallic reflection it is complex. The coefficients of reflection are then simply

$$r_\perp = |\widetilde{r_\perp}|^2, \quad r_\parallel = |\widetilde{r_\parallel}|^2 \tag{A9}$$

and the relative retardance is just

$$\delta = \arg(\widetilde{r_\perp}) - \arg(\widetilde{r_\parallel}). \tag{A10}$$

A Mueller matrix for the entire instrument is thus created by combining the matrices of all polarizing elements, with the appropriate rotations. Using the Levenberg–Marquardt algorithm (or a simple parameter grid), a fit of the model to the measured calibration data is performed, in which the free parameters are the complex refractive indices of the metallic surfaces (starting at the tabulated value[3] for the specific metal comprising the mirror coating). This fitting process also allows the dichroic mirror (of poorly known reflection characteristics) to be characterized. To reduce the number of free parameters, the SCExAO focusing mirror and the DM (which are both in the same plane of reflection) are combined into one component.

Finally, the instrumental polarization contribution from the telescope itself and the AO 188 system must be taken into account. In principle, it should be straightforward to probe this portion of the optical system with observations of polarized standard stars, but until such data can be obtained, detailed optical modelling must serve. Fortunately, a precise ZEMAX model of the system was made available to us, yielding precise knowledge of position and angle of all optical surfaces. Alternatively, the contribution from AO 188

[3] Complex refractive indices obtained from http://refractiveindex.info/. Optics suppliers unfortunately do not provide this level of characterization.

can be measured by using its own flat-field lamp, linear polarizer and HWP. Exploiting this, an accurate matrix $M_{\rm tel}$ can be calculated using the methods discussed above.

Thus, a final Mueller matrix for the instrument is constructed:

$$\begin{aligned} M_{\rm VAMPIRES} = {} & M_{\rm Woll} \times M_{\rm QWP} \times M_{\rm LCVR} \times M_{\rm PerM2} \\ & \times M_{\rm r(\theta_{Per})} \times M_{\rm HWP} \times M_{\rm PerM1} \\ & \times M_{\rm OAP+DM} \times M_{\rm LP} \times M_{\rm tel}, \end{aligned} \tag{A11}$$

where each matrix term incorporates its appropriate rotation matrix. $M_{\rm OAP+DM}$ represents the combined in-plane mirrors on the bottom bench, $M_{\rm PerM1\&2}$ are the periscope mirrors, $M_{\rm r(\theta_{per})}$ is the beam rotation of the periscope and $M_{\rm Woll}$ the Wollaston prism, which in fact exists in two instances (with $\pm 45^\circ$ rotations corresponding to the two channels). The calibration polarizer and wave-plate ($M_{\rm QWP}$ and $M_{\rm LP}$) are included for fitting the model to the calibration data. An alternative configuration under investigation replaces the HWP with a pair of QWP, which allows the polarization to be rotated (as with the HWP) but also the system birefringence to be compensated for (by differential rotation of these wave-plates). In this case, the $M_{\rm HWP}$ term above is replaced by two $M_{\rm QWP}$ terms.

A sample Mueller matrix for the instrument is given below – in this case, the matrix for the instrument at 775 nm in the dual-QWP configuration, for zero polarization rotation, Wollaston prism ordinary beam and LCVR retardance set to $\pi/2$.

$$M = \begin{pmatrix} 1 & -0.026 & -0.062 & -0.015 \\ -0.022 & 0.706 & 0.225 & -0.668 \\ 0.059 & 0.130 & -0.973 & -0.189 \\ 0.026 & -0.693 & 0.045 & -0.717 \end{pmatrix}. \tag{A12}$$

Substantial off-diagonal terms are seen (while noting that this matrix includes the beam rotation by the periscope between benches), and as described in Section 3 the bulk of these effects are mitigated by the triple-differential measurement process and the inherent robustness of interferometry against diattenuation (since the signal in each polarization channel is normalized with respect to the total flux in that channel). (This full matrix, however, is still used for correction during data reduction to ensure any residual effects are calibrated for.) The effect of birefringence is most strongly seen in the $Q \leftrightarrow V$ terms rather than the $U \leftrightarrow V$ terms, due largely to the rotation of the beam by the periscope. This matrix includes the contribution of AO 188, which makes a sizeable contribution to the instrumental polarization due to its image rotator (k-mirror).

Polarized light of Stokes vector S incident on the telescope is transformed by the instrument to emerge as S', where

$$S' = M_{\rm VAMPIRES} \times S. \tag{A13}$$

To determine the signal measured by the camera (which only measures intensity), we apply the detector operator D, which is the row vector [1, 0, 0, 0]. The intensity measured is then

$$I = D \times M_{\rm VAMPIRES} \times S. \tag{A14}$$

To correct for instrumental polarization in the intensity domain, the inverse instrumental Mueller matrix $M^{-1}_{\rm VAMPIRES}$ could simply be applied to the measured Stokes vector. However, VAMPIRES' calibration precision relies on immediately transforming each frame of fringes into the Fourier domain and conducting all subsequent operations in this domain, making such a strategy impractical. Therefore, rather than applying the instrumental polarization correction to the data, instead we apply $M_{\rm VAMPIRES}$ directly to the astrophysical model (e.g. a radiative transfer model) or image reconstruction before fitting to the data, which is the technique we will employ in future science observations.

This paper has been typeset from a TEX/LATEX file prepared by the author.

Appendix F

Proposals

Contents

F.1 Notes on individual proposals

F.1.1 PAVO @ CHARA, Binarity and Circumstellar Matter in Formation of Bright Intermediate Mass Stars

The PAVO @ CHARA, YSO proposal was granted two nights (June 12-13, 2015: technical issues leading to CHARA Array shutdown; some data was finally acquired on June 16, 2015 during a generously granted backup-night as "secondary observer"). This 2015 proposal is an updated resubmission of the 2014 YSO proposal (PI: Schworer) which was granted four nights (September 15-16 2014: weathered out and poor seeing/technical issues, December 7-8 2014: weathered out). The 2014 YSO program was itself an updated resubmission of the 2013 YSO (PI: Tuthill) which was granted two nights (November 9-10, 2013: technical issues, bad weather and observation of a target of opportunity (novae)).

F.1.2 GPI @ Gemini South, Mapping the dust in planet-forming disks using polarimetric masking interferometry

Accepted as part of a 4-days commissioning + science observation run from March, 28 to 31 2015. It was canceled at the last minute because floods and mudflows in the Atacama desert cut the roads to go to the telescopes https://en.wikipedia.org/wiki/2015_Northern_Chile_floods_and_mudflow. PI: Schworer.

F.1.3 SCExAO @ SUBARU Telescope, A high-angular-resolution study of the inner regions of proto-planetary discs

Refused due to unusually high competition in this category this round. PI: Schworer (even though, for proposal submission technical reasons, the PI in the document is Julien Lozi, staff member of the SUBARU Telescope).

F.1.4 NACO&SPHERE @ VLT, Detecting circum-planetary discs around young stars with SPHERE/ZIMPOL and NACO/SAM

Accepted in semester 95A, the NACO observations could not be done due to NaCo technical failures. The proposal was resubmitted in semester 97A (same NaCo issues), and in semester 98A where it was accepted again to perform the remaining NaCo observations (currently pending). PI: Mendigutia-Gomez.

Request for Observing Time at the CHARA Array

For the Period

April 1 – August 30, 2015

Type only within boxed areas immediately after hyphens

P.I. Name - G Schworer **PhD Research?** – yes

Co-P.I. Names - P. Tuthill, M. Ireland, R. Morgan, V. Coudé du Foresto

Observing Participants - P. Tuthill, M. Ireland, R. Morgan, V. Coudé du Foresto

Proposal Title – Binarity and Circumstellar Matter in Formation of Bright Intermediate Mass Stars.

Is this a new or continuing project? – continuing

Abstract - The Herbig Ae/Be stars are believed to be the high-mass analog of the T Tauri stars: systems still undergoing active accretion and with a host of unexplored and compelling astrophysics including jet launch, inflow, winds and (potentially) planetary system assembly. To date, there have been a handful interferometric observations made with sufficient angular resolution to image the immediate (~several R*) circumstellar environment. Such an endeavor requires the full resolution of the CHARA array operating in the visible, as delivered by the PAVO instrument. Here we propose to continue a first pilot study, targeting a handful of the brightest Herbig stars, to widen this new observational window. Our primary scientific target is the known binary MWC 361 for which a first flux ratio was measured with PAVO. Taking more robust measurements, at different epochs, will pin the spectral types of both components, resolving the major source of uncertainty in the models. In addition, we propose to explore the immediate circumstellar environments of a small sample of Herbigs which are within reach of PAVO's superior sensitivity. This will settle the (often contentious) question of binarity among these much-studied objects, and will prospect for the signatures of circumstellar matter associated with the ongoing accretion and wind phenomena known to be driven by physical processes operating at these spatial scales.

Summary of Requested Observing Run(s)

Run	Optimal No. of Nights	Minimal No. of Nights	Optimal Dates	Acceptable Dates	Beam Combiner	Telescopes
1	3-4 (depending on night duration)	2	Mid-Jun => Mid-Jul	Beg-Jun => Mid-Aug	PAVO	Any W.S.E. Triangle

Unacceptable Observing Dates (for non-astronomical reasons) **–** N/A

2015 – Submission Deadline: 19 Jan 2015, midnight EST (Monday night)– Submit to proposals@chara-array.org

Scientific Justification -

In contrast to the case for low-mass stars, which are commonly accepted to form in the gravitational collapse of a dusty cloud, the formation of massive stars remains an area of active debate. The difficulty arises from a set of related circumstances: the objects are intrinsically rare, therefore distant and the key physics happens on a short timescale whilst the star is still heavily embedded within their nascent molecular clouds. Within this scenario, Herbig Ae/Be stars, which are believed to be very young objects of intermediate mass, form a critical bridge with the lower-mass Herbig Ae stars exhibiting much common phenomenology with the low-mass T Tauri stars (Vink et al. 2005), whereas the Herbig Be stars are similar to the more embedded massive young stellar objects (MYSOs; e.g. Drew et al. 1997). To make significant headway understanding the physics governing formation across the mass scale, it is necessary to (1) probe the (circum-) stellar environments at small scales, where many important features for the further evolution such as discs, outflows and binaries are found; and (2) survey objects at the epoch of formation, where dynamical configurations remain in their primordial state.

Dramatic recent progress in the understanding of stellar and planetary system assembly has been driven, in part, by the availability of the first resolved image data at spatial scales sufficient to reveal the action taking place in the immediate stellar environment. Such observational campaigns, almost entirely in the infrared, have delivered truly revolutionary astrophysics, such as the establishment of the size-luminosity relationship (Monnier et al. 2005) and the understanding that the inner rim of circumstellar disks is set by dust sublimation physics (Tuthill et al. 2001). In the optical, serious work has only very recently commenced, with important exploration of the emission-line wind by differential interferometry across spectral lines by VEGA/CHARA (e.g. Rousselet-Perrault et al., 2010) at <100m baselines.

Our primary target, MWC 361, is a known binary which now, thanks to recent MIRC observation, has an exquisitely-well constrained orbit (Figure 1). Given the obvious compelling nature of finding a young system such as this in which there is the potential to obtain model-independent mass and distance directly from interferometry, it is therefore critical to remove all remaining degeneracies in the interpretation. The outstanding one of these is the spectral type of each component; a result notoriously difficult to extract from the blended spectrum. Given that the infrared flux ratio has been tightly constrained by MIRC and IOTA, all that remains to pin the temperature of both component stars is our requested second flux ratio measurement in the optical with PAVO.

The wider sample of Herbig Ae/Be stars requested below encompasses a list of 8 of the brightest examples available to CHARA (in order, (AB Aur), (MWC 480), (HD 45677), (MWC 158), MWC 614, MWC 275, MWC 239 and MWC 361 – targets in brackets are only observable in winter). Of these, new detections of binarity have recently been reported in three (AB Aur, HD 45677, MWC 158) in a widely cited paper (Baines et al. 2006) utilizing a long-slit spectroastrometry method. However, few of these objects have been unambiguously confirmed with follow-up long baseline interferometry. In addition to determining the state of binarity, we also aim (somewhat more speculatively) to explore our data for signatures of gas in the immediate circumstellar environments. To do this we will exploit PAVO's ability to deliver multi-wavelength Fourier imaging data, including closure phases, and search for subtle differential signals corresponding to likely emission lines in the gas.

Observing Methodology (How will your observations be made? Which beam combiner and baselines do you need? What special needs do you have? How will you analyze your data?)

Observations of MWC 361 and our secondary survey targets will require use of the PAVO beam combiner. Although the targets are faint, they should be within PAVO's ability to find and track fringes, provided conditions are at least moderately favorable. One run is required mid-year. For the binary science, any triangle spanning the 3 different arms should be sufficient for our purposes.

The objects are certainly observable with routine PAVO settings, and indeed (as described in section L below), have been briefly observed in an earlier program. Unfortunately this earlier work did not yield scientifically competitive data due to a combination of weather and technical issues.

Data reduction and analysis should be relatively routine using established software and procedures.

Figures

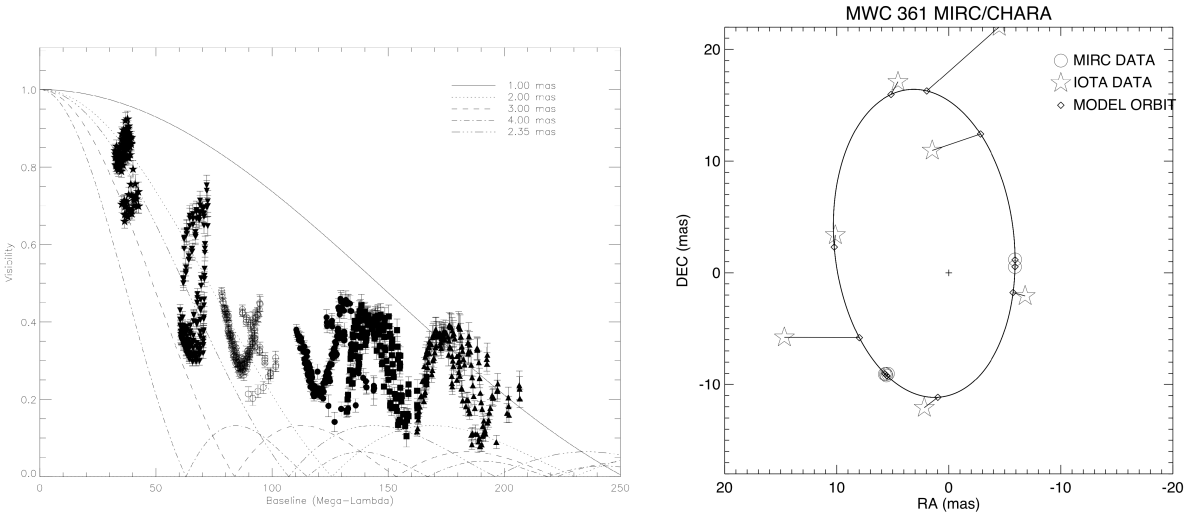

Figure 1. Left Panel: Plot of raw MIRC visibility data on MWC 361. Overplotted models are indicative of visibility function from differing size uniform disks (not intended as fits to data). Strong sinusoidal signals betray the presence of the binary star. Right Panel: Best fit orbit to MIRC and IOTA data (note the exceptional precision of the MIRC points).

References:
Baines et al. 2006, MNRAS, 367, 737
Drew et al., 1997, MNRAS, 286, 538
Monnier et al., 2005, ApJ, 624, 832
Rousselet-Perrault et al., 2010, A&A, 516, L1
Tuthill et al. 2001, Nature, 409, 1012
Vink et al., 2005, MNRAS, 359, 1049

Object Catalog – Double click on the table below and enter relevant data on the Excel spreadsheet. Click outside the table when completed.

HD	Obj/Cal	V mag	K mag	RA (hr)	RA (min)	RA (sec.xx)	Dec (º)	Dec (′)	Dec (″)
142983	Obj	4.87	4.83	15	58	11.36	-14	16	45.68
163296	Obj	6.85	4.78	17	56	21.29	-21	57	21.87
179218	Obj	7.4	6	19	11	11.25	15	47	15.63
200775	Obj	7.4	4.6	21	1	36.92	68	9	47.8

Status of Unpublished Data (Detail your intentions and schedule regarding any unpublished data you already have in hand. Because of observing time pressure, a record of productive use of prior data will play a determining role in scheduling decisions.) -
Same YSO program in 2014:
Sept and Dec runs - 2*2 nights runs (small amount of good data on primary science target obtained due to weather, see below)

New observation time with new baselines on 5 targets already observed (among which MWC 361, the primary science target), and 2 new targets (HD142983, HD179218) should lead to good quality publications.

If you observed at CHARA in 2014, how successful were those observations?
Observations made for the same program:
On-site observing: 16-17 Sept 2014 – first night was median, second night mostly weathered out (primary science target unobservable during the clear part of the night)
Remote observing: 8-9 Dec 2014 – first night was weathered out, second night some (low quality) data acquired

F.1.5 TAC report

Referee 1: 3.00
This project has the potential to answer a lot of questions about the nature of Herbig Ae/Be stars. Some explanation describing the expected results when characterizing the circumstellar environments would have been helpful.

Referee 2: 3.75
Goal to observe Herbig binaries with PAVO to determine flux ratios in the visible and explore circumstellar environments. Well describes science plan and motivation.

Referee 3: 3.00
The proposal aims to continue a PAVO campaign to observe intermediate mass binaries with circumstellar discs. The prospect of interferometric observations of YSO's to the optical is exciting, with potential for high impact CHARA results, making the science case very compelling. The project is new and hence the acquisition of additional data is justified. There is some concern, however, that the proposal relies rather heavily on PAVO 3-telescopes visibility and closure phase calibration capabilities, which have so far not been demonstrated (in particular given the faintness of the most of the targets). More detailed comments about the feasibility of these observations with PAVO would help to strengthen this proposal.

Referee 4: 2.60
Pilot study of binarity of Herbig stars. Interesting proposal on measuring the flux ratio between MWC-361 components. Are we sure that this flux ratio is stable over the orbit?

Subaru Telescope
National Astronomical Observatory of Japan

Semester	S15B
Proposal ID	S15B0165N
Received	03/10/2015

Application Form for Telescope Time (Normal+Intensive Programs)

1. Title of Proposal

A high-angular-resolution study of the inner regions of proto-planetary discs

2. Principal Investigator

Name: Lozi Julien

Institute: NAOJ

Mailing Address: 650 North A Ohoku Place, Hilo, 96720, HI, USA

E-mail Address: lozi@naoj.org Phone: +1-808-934-5949

3. Scientific Category

- ☐ Solar System
- ☐ Normal Stars
- ☐ Extrasolar Planets
- ☑ Star and Planet Formation
- ☐ Metal-Poor Stars
- ☐ Compact Objects and SNe
- ☐ Milky Way
- ☐ Local Group
- ☐ ISM
- ☐ Nearby Galaxies
- ☐ AGN and QSO Activity
- ☐ QSO Abs. Lines and IGM
- ☐ Cosmology
- ☐ Gravitational Lenses
- ☐ Proto-Clusters and Galaxy Environment
- ☐ Clusters of Galaxies
- ☐ High-z Galaxies(LAEs, LBGs)
- ☐ High-z Galaxies(others)
- ☐ Miscellaneous

4. Abstract *(approximately 200 words)*

Intense interest has been focused upon a handful of young stellar objects believed to be in a transitional state between embedded Class II pre-main-sequence stars and more evolved Class III systems hosting a debris disk: the so-called transition disks. The confirmation of the disk-gap architecture revealed by sub-millimetre measurements and optical interferometry has inspired a number of mechanisms to explain these gaps: extensive grain growth, photo evaporation, binarity and most excitingly a tidal barrier created by dynamical interaction with low-mass disk objects (such as exoplanets). These different mechanisms can be distinguished by studying the distribution of the gas and dust within the gaps. We propose here to make a multi-wavelength survey in the Visible and Near-Infrared of 9 of the most promising transition disk candidates, using a novel differential polarimetric observing mode which offers unique science reach and a high contrast detection threshold at the required spatial scales.

5. Co-Investigators

Name	Institute	Name	Institute
Guillaume Schworer	U. Sydney + Obs. de Paris	Sylvestre Lacour	Paris Obs.
Barnaby Norris	Saitama Univ.	Vincent Coude du Foresto	Paris Obs.
Thayne Currie	NAOJ		
Peter Tuthill	University of Sydney		
Nemanja Jovanovic	NAOJ		
Olivier Guyon	NAOJ		
Garima Singh	NAOJ		
Tomoyuki Kudo	NAOJ		
Motohide Tamura	NAOJ		
Timothy Brandt	Institute for Advanced Study		

6. Thesis Work

☑ This proposal is linked to the thesis preparation of Guillaume Schworer

Long-Baseline Interferometry and Non-Redundant Masking observations to understand planetary formation

7. Subaru Open Use Intensive Programs

☐ This is a proposal for Intensive Programs.

8. List of Applicants' Related Publications *(last 5 years)*

Norris, B., et al. (2015), *The VAMPIRES instrument: imaging the innermost regions of protoplanetary discs with polarimetric interferometry*, MNRAS, 447, 3.
Jovanovic, N., et al. (2014), *Development and recent results from the Subaru coronagraphic extreme adaptive optics system*, Volume 9147, id. 91471Q.
Norris, B., et al. (2012), *A close halo of large transparent grains around extreme red giant stars*, Nature, 484, 7393.
Cheetham, A., et al (2015) *Near-IR imaging of T Cha: evidence for scattered-light disk structures at solar system scales*, MNRAS in press.
Huelamo, N., et al. (2015) *High-resolution observations of the outer disk around T Chamaeleontis: the view from ALMA*, A&A, 575, 5
Rizzuto, A.C., et al. (2013) *Long-baseline interferometric multiplicity survey of the Sco-Cen OB association*, MNRAS, 436, 1694
Absil, O., et al., (2013) *A near-infrared interferometric survey of debris-disc stars. III. First statistics based on 42 stars observed with CHARA/FLUOR*, A&A, 555, 104
Cieza, L., et al., (2013) *Sparse Aperture Masking Observations of the FL Cha Pre-transitional Disk*, ApJ, 762, 12
Biller, B., et al., (2012) *A Likely Close-in Low-mass Stellar Companion to the Transitional Disk Star HD 142527*, ApJ, 753, 38
Tuthill, P., et al. (2010), *Sparse aperture masking (SAM) at NAOS/CONICA on the VLT*, Volume 7735, id. 77351O.

9. Condition of Closely-Related Past and Scheduled Observations

Please fill in here, if this proposal is a continuation of (or inextricably related with) the previously accepted proposals. This is to describe what kind of relevant/similar proposals have existed in the past. If your scheduled observation exists, please describe it.

Proposal ID	Title (may be abbreviated)	Observational condition	Achievement (%)
S14B-035	(abridged) Searching for Planets in Disks with SC	bad weather	0
S15A-112	Directly Imaging Exoplanets/Asteroid Belts With S	TBD	TBD

10. Post-Observation Status and Publications

Please report the status or outcome of your main Subaru observations carried out in the past. All observations relevant to this proposal should be included here. Similarly, all those within last 3 years with which you were involved as P.I. must be reported.

Year/Month	Proposal ID	PI name	Status: data reduction/analysis	Status: publication
2009-2014	SEEDS	M. Tamura	published	35 refereed publications

11. Experience

The observing team includes PIs from all SCExAO, HiCIAO and VAMPIRES instruments. This team is highly experienced in performing observations with the Subaru telescope, and specifically with all modules and modes supported by extreme Adaptive Optics. Over the design, testing and commissioning phases of SCExAO and VAMPIRES instrument, our team has performed many engineering observations, and are therefore familiar with the operation, limitations and unique data analysis methods required. More broadly, members of this team have spent the majority of their careers building advanced instrumentation at a range of modern large observatory facilities, including VLT, Gemini and Keck, and therefore have wide experience across observational and instrumental astronomy, allowing optimal risk-mitigation when turning a capability with entirely novel performance to the skies for first science, as proposed here.

Title of Proposal

A high-angular-resolution study of the inner regions of proto-planetary discs

12. Observing Run

Instrument	#Nights	Moon	Preferred Dates	Acceptable Dates	Observing Modes
SCExAO+NGS-AO	0.5	any	1st-21th August	1st Aug. - 5th Sept.	imaging/VAMPIRES+HiCIAO
SCExAO+NGS-AO	0.5	any	1st-21th August	1st Aug. - 5th Sept.	imaging/VAMPIRES+HiCIAO
SCExAO+NGS-AO	2	any	1st-23rd November	15st Oct. - 15th Dec.	imaging/VAMPIRES+HiCIAO

2nd choice: SCExAO alone is capable of achieving our goals: this proposal is not appropriate for Gemini or Keck time exchanges.

comments:

Total Requested Number of Nights [3] Minimum Acceptable Number of Nights [2]

13. Scheduling Requirements

Request Remote Observation ☐ at Hilo ☐ at Mitaka

14. List of Targets

Target Name	RA	Dec	Magnitude (Band)
HD 163296 (1)	17 56 21.29	-21 57 21.87	R = 6.86, H = 5.531
HD 169142 (1)	18 24 29.78	-29 46 49.37	R = 8.2, H = 6.911
MWC 361 (1)	21 01 36.92	68 09 47.76	R = 6.8, H = 5.44
HD 179218 (1)	19 11 11.25	15 47 15.64	R = 7.25, H = 6.65
49 Cet (1,2)	01 34 37.78	-15 40 34.90	R = 5.6, H = 5.528
MWC 480 (2)	4 58 46.26	29 50 36.98	R = 7.76, H = 6.26
MWC 758 (2)	5 30 27.53	25 19 57.98	R = 8.3, H = 6.56
AB Aur (2)	4 55 45.85	30 33 4.29	R = 6.96, H = 5.06
HD 45677 (2)	6 28 17.42	-13 03 11.14	R = 8.11, H = 6.34
alf Ari (cal)	02 07 10.406	+23 27 44.703	R = 1.15, H = -0.52
Altair (cal)	19 50 46.999	+08 52 05.956	R = 0.62, H = 0.24
Sirius (cal)	06 45 08.917	-16 42 58.017	R = -1.46, H = -1.33

Our target selection consists of two sets referred as (1) and (2) in the target listing above. It groups 9 well-known young stellar objects having active circumstellar discs. With the addition of southern targets to be observed by GPI this semester, a large sample of young discs will be observed, at various stages of youth. The statistical weight of such a sample size will enable the study disk-gaps as a new object class, immediately enabling unique studies of the diversity of cavity architectures.
PSF calibrators (denoted (Cal)) are unresolved targets required for PSF characterization, employed in the calibration of interferometric data for VAMPIRES. For HiCIAO images, they should allow us to obtain the total intensity maps (Grady, Currie et al. 2015 in prep). Calibrators have been selected to be somewhat brighter than targets to minimise calibration time. No known bias is known to be introduced by such a choice.

15. Observing Method and Technical Details

Please describe in detail about instrument configuration, exposure time, required sensitivity, and so on.

Our proposal exploits the ability of SCExAO to perform simultaneous observations in the infrared and visible. The observing strategy and basic configuration for the various modules is given below.

AO188: Since all targets are much brighter than R = 16.5, AO-188 will be used in natural guide star mode referenced on the target itself. Even though some extended structure surrounds them, the contrast ratio is high (of order 100:1 or 1000:1) so that AO-188 should treat them as point-source for NGS purposes. (Nonetheless we do have the known morphologies' FWHM available if required by the operator). There is no minimum Strehl requirement as such since science can be performed in poor conditions if necessary (see Section 17). Targets are not within 30° of the moon on most of the suitable nights.

SCExAO PIAA coronagraph: The coronograth will be used to suppress the stellar PSF while maintaining high contrast measurements with a narrow inner working angle in the NIR. HiCIAO will directly benefit from high order correction provided by SCExAO.

SCExAO Low-order WFS: This will be operated in the normal mode, to provide both precise alignment of the coronagraphic focal-plane mask and fringe stabilisation in VAMPIRES.

SCExAO High-order WFS: The high-order Py-WFS will be used to enhance the PSF for NIR imaging and to stabilise the fringes in the VAMPIRES interferometer (a similar role to low-order WFS). We understand this module is offered in shared-risk mode, and our science will proceed without this module (albeit with potentially reduced sensitivity).

HiCIAO: HiCIAO will be used in Direct Imaging mode, using Y-, J- and H- band filters. Our observing time request is mostly driven by the requirements of VAMPIRES, as even very short HiCIAO observations of bright targets are contrast limited. In each filter we will take 150 1.5s exposures (225s on source), resulting in 21 minutes of observing time, including read-out time, per filter. This sequence will be repeated multiple times for targets where multiple VAMPIRES masks are used. This will result in a sensitivity in J-band of 15 mag.arcsec^{-2}, with contrast better than 10^{-5} at 1" from the central star after PSF subtraction.

VAMPIRES: VAMPIRES will be operated in non-redundant mask mode. All 5 filters (650 nm to 775 nm) and both the *9Hole* and *annulus* masks are requested for, respectively, high calibration precision and extensive fourier coverage. Standard 0.018 s exposure times and fast Frame Transfer timing mode will be used, with standard four-position waveplate sequence. A VAMPIRES data-block (8 sets of 4 HWP angles) takes 22 minutes. Total time on target is determined both by absolute brightness and also the requirement for a sufficient amount of sky rotation on a single data-set to mitigate baseline-dependant systematics. Since VAMPIRES filter or mask changes are instant, changes are interleaved between data sub-sets. Each target will be observed following the pattern: 3(filters) x 22 minutes x 2 sets = 132 mins per data-set. Brightest targets will be observed with 2 masks (9holes and annulus) while faintest ones only with one. These observing block times have been demonstrated to produce a 5σ visibility precision of 5×10^{-3} on a single baseline. Total time requested is based on the observation of the 9 requested targets (4 with 2 masks and 5 with only 1 mask), 3 filters, as well as 2 PSF calibrators per night and finally allowing 15 minutes AO overhead per target.

16. Instrument Requirements *Specify the number of masks (MOIRCS/MOS) or the set of filters to use (S-Cam and HSC).*

These observations are built around the AO188+SCExAO AO systems, using the coronagraph and VAMPIRES modules of SCExAO and the HiCIAO NIR imager. AO188 is required to track targets and provide wavefront correction, SCExAO for its coronagraphic modes and high-order wavefront correction, VAMPIRES for high angular resolution polarimetric interferometry (for inner circumstellar region imaging and dust-grain property analysis) and HiCIAO for NIR imaging of the circumstellar extended sctructure.

17. Backup Proposal in Poor Conditions *(specify object names)*

In poor conditions, observations of the most promising targets can proceed with reduced AO and ExAO performance. The conventional imaging modes of HiCIAO will be used (without the advanced coronagraphy). VAMPIRES will continue to operate successfully, however the integration time will need to be increased to achieve adequate signal/noise ratio. This will necessitate a reduction in the number of targets observed, but good science will still be produced.

18. Public Data Archive of Subaru

☒ *Yes, I have checked SMOKA.*

If your targets have already been observed by Subaru in the past, please describe why you need to observe them again.

Several targets have been observed by SUBARU before, however SCExAO offers completely new capabilities. VAMPIRES and HiCIAO explore spectral and contrast-ratio ranges, inner working angles and polarimetric differential modes that have not been explored by any telescope. This program does not replicate any program with public or proprietary data.

19. Justify Duplications with the HSC SSP *(for HSC proposers)*

An ultra-high-angular-resolution polarimetric study of the innermost regions of proto-planetary discs (Science Justification)

Science background and aim

In recent years, intense interest has been focused upon a handful of young stellar objects believed to be in a transitional state between embedded Class II pre-main-sequence stars and more evolved Class III systems hosting an already old debris disc. These objects, known as transition discs, are characterized by a distinctive dip in their infra-red SED which suggests that a partially evacuated gap exists in the inner region of the protoplanetary disc (e.g. Wahhaj et al. 2007). The profound implications for studies of planetary formation have become increasingly apparent with the confirmation of the disc-gap architecture by sub-millimetre measurements (e.g. Perez et al. 2014) and optical interferometry (e.g. Oloffson et al. 2011, Benisty et al. 2009). A number of mechanisms have been proposed to cause these gaps, including extensive grain growth (Dullemond & Dominik 2005), photo evaporation (Clarke et al. 2001) and binarity (Ireland & Kraus 2008), however most exciting for exoplanetary science is the potential for such systems to arise from the tidal barrier created by dynamical interaction with low-mass disc objects (e.g. Bryden et al. 1999, Papaloizou et al. 2007). These different mechanisms can be distinguished by studying the distribution of the gas and dust within the gaps. For example, a large (stellar) companion or photoevaporation would almost completely evacuate the inner regions while a less massive planetary companion would allow gas and small dust grains to exist within its orbit (Lubow et al. 1999). Furthermore, in the latter case, the measurement of the size and distribution of this material would allow the orbit and mass of the planetary companion to be constrained (Andrews et al. 2011).

Here, using an innovative new observational technique we propose to characterize the inner-most regions (within 100 mas) of 5 of the most favorable targets which show evidence of a young and active transition disc, at slightly different stages. This region – unexplored in conventional observations due to the limited inner-working-angle of traditional coronagraphs – is of critical importance to the understanding of planetary evolution. For nearby systems this lies within the snow-line and corresponds to inner-solar-system scales. Simulations constrained by representative disk models show that our data will enable us to recover the first polarized dust density imaging of these important inner regions of the discs (see Figure 1 for example data). A wealth of topical astrophysics is directly addressed by this, including the presence of sub-structure (e.g. density waves) within the discs, the geometrical extent of cavities, and the critical dust density profiles (both vertical and radial). This campaign lays the groundwork for future detailed multi-wavelength imaging, enabling full characterization of the dust grain size as a function of spatial position in the disc. This proposal builds upon our successful legacy of non-redundant masking discoveries in this area and extends it with the implementation of 1) a differential polarimetric-interferometric observing mode offered by SCExAO/VAMPIRES in the red-visible light and 2) a very-high contrast capability offered by SCExAO/HiCIAO (using the PIAA coronagraph) in the near-infrared, which can both run simultaneously. We therefore have substantial experience in construction of experiments to exploit these complex modes.

VAMPIRES as an explorer of the inner-most scattering regions

Directly imaging the faint, tenuous dust in the disc which exists in such close proximity to the bright central star has proven to be observationally challenging in the near-infrared, with previous direct imaging efforts relying on the thermal emission from the disc and/or conventional coronagraphs with limited inner-working-angle. Here, however, using SCExAO/VAMPIRES we employ an entirely new technique. Using non-redundant masking and high acquisition speeds, we perform interferometric observations of the targets to produce precise visibilities and closure phases. By exploiting the polarisation of the starlight scattered by dust grains in the disk, we effectively suppress the unpolarised flux from the central star and also provide an unprecedented level of calibration precision for the interferometric observables, resulting in diffraction-limited imaging of the dust distribution, with an inner-working-angle limited only by the angular resolution ($\sim$ 8.5 mas). By operating at shorter wavelengths (650 to 775nm), where the scattered signal is strong, we can achieve angular resolutions $\sim$3 times higher than images of thermal emission, as good as $\sim$8.5 mas (Fizeau criteria). Furthermore, since scattering is a strong function of dust grain size and wavelength, observations at 3 wavelengths within the 600-800 nm window will yield a first-order measurement of the dust grain size as a function of spatial position in the disc, providing critical insight into the planetary formation process and groundwork for future many-wavelength measurements. We have successfully demonstrated this technique in observations of the dust shells surrounding AGB stars (Norris et al., 2012, Nature), wherein we observed the circumstellar shells and placed accurate constraints on the size of the shells and the size of the constituent dust grains.

HiCIAO as a NIR dusty structures probe

While VAMPIRES takes advantages of polarimetry and interferometry to image to within < 10 mas of the host star, HiCIAO will be used in coronagraphic mode, delivering high-contrast direct imaging of the disc further from the star. Thanks to the extreme-AO system on SCExAO, HiCIAO will benefit from a 5 - 10 times improvement in contrast ratio over AO-188 alone. The final contrasts for 1-hour integration time are expected to yield ΔH 5×10^{-6} and 10^{-4} at r = 600 mas and 200 mas, respectively, for 5-σ SNR level. **The field-of-view in the NIR is perfectly complementary to that of VAMPIRES**, $\sim$80 to 460mas, depending mask choice. Thus, HiCIAO will 1) uncover the more extended structure of the young disc targets in the NIR, allowing optimal spatial and spectral coverage, and 2) provide VAMPIRES with critical boundary conditions in the range r = 0.04 to 0.2 arcsec to further constrain model-fitting and 3) set good limits on young jovian planets at wide separations (e.g. 0.5-2 Mj at 25-50 AU).

Observation and Analysis

The primary observations delivered by this ambitious proposal will be linear Stokes imaging of the scattered polarized

light in the inner disc and gap regions of our target sample (to within ~ 10 mas of the star, as well as NIR images of the structures beyond r = 0.2 arcsec. Our derived scattered-light distribution and NIR surface brightness will then constrain (1) the distribution and (2) the grain size and composition of the dust in the inner regions of our sample of transition discs. Features such as gaps, clumps and density waves will be clearly identified. The transition disc phase represents a small fraction of the lifetime of a star, and relatively few are known. Our target list represents the closest and brightest of these systems. Providing images of these targets at higher angular resolutions than previous studies, represents a significant step forward in understanding their formation and evolution. Data analysis will be performed using the suite of data analysis and modeling software written by the co-I research group in Sydney, specifically designed to analyze this differential polarimetric non-redundant masking and NIR surface brightness data.

Case study of a typical disk target

Young stars exhibit a massive, dense disc at large radii, with our program targeting those at the transitional disc phase, Sitko et al. (2008). Using CO line measurements obtained with ALMA on one of our primary targets, HD 163296, Rosenfeld et al (2013) demonstrated a vertical gradient in temperature, creating a cold midplane composed of grains (from 150AU) and warm atmosphere composed of gas. Figure 1 (left panel) shows the result of their hydrostatic modeling of such a complex disc.

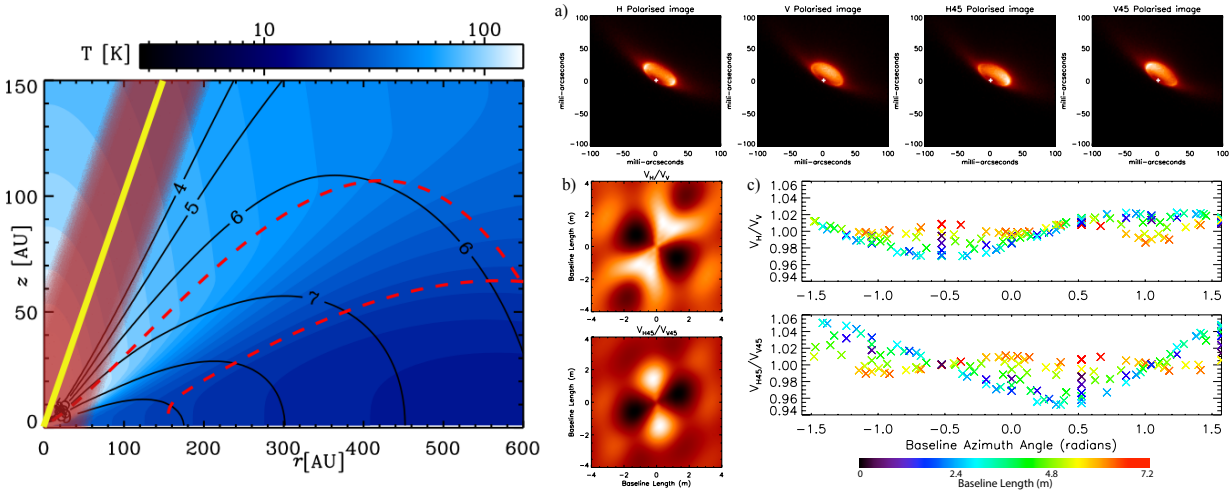

Figure 1: **Left:** Temperature (color scale) and gas density structure (black contours; log $n_{gas} = [4, 5, 6, 7, 8, 9]$ cm^{-3}) of the hydrostatic model. The dashed red curves mark the photo dissociation boundaries, for $\sigma_s = 5 \times 10^{-20}$ cm^{-2}. The lower red curve indicates the upper boundary of the cold midplane where the gas phase CO densities are reduced due to freezeout onto grains. The solid yellow line shows the line of sight on the disc, the red-shaded area show VAMPIRES field of view. For clarity, the HiCIAO field-of-view of was not added to the figure: it starts where VAMPIRES' one ends, r = 50 AU. **Right:** A modelled representative protoplanetary disk at 500 pc and the derived VAMPIRES data for $\lambda = 800$ nm. a) Image of the inner region of the disk, shown with a non-linear intensity mapping, in four polarisations: horizontal H and vertical V corresponding to Stokes Q, while H45 and V45 are the two orthogonal polarisations rotated 45° corresponding to Stokes U. b) The differential power spectra for the two pairs of orthogonal polarisations. c) Expected differential visibility signals as seen by VAMPIRES with an 18 hole mask.

Benisty et al (2009) used VLTI AMBER in K and H bands and showed a significant deviation from point-symmetry, revealing an asymmetry in the very inner disc (0.1-1.5 AU unprojected). This deviation may possibly be caused by an inner rim at ∼0.5 AU, or any asymmetric brightness distribution, such as a symmetric flared disc with a stellar contribution that is off-centered by a few percent of the inner disc radius with respect to the disc. A well-constrained model could not be obtained due to the lack of high-resolution interferometric (u,v) coverage.

Previous measurements reported in Fukagawa et al (2010) using a 1 arcsec coronagraph with CIAO on SUBARU Telescope, reported contrast ratios L_{scat}/L_{total} of the order 5×10^{-4} for several of our targets, in scattered light at 1.6 μm for the extened outer ring . Due to the large r^{-2} increase in stellar flux at closer separations and the mostly gray spectra of Herbig and T-tauri stars (Schneider et al 2003, Weinberger et al 2002), such discs will be well within VAMPIRES' demonstrated sensitivity of 10^{-3} in R-I bands. In addition, Figure 1 shows that a higher gas density is to be expected in the inner part of the disc, allowing a larger scattering cross-section, hence more favorable contrast ratio in reflected light. For example, HiCIAO will be able to image HD 163296 disc from 25AU and VAMPIRES from 1.5 to 50AU, in several narrow-band filters from 0.6 to 0.8 μm and in several NIR bands, where no other instrument was ever able to produce simultaneous and consistent observations.

Key Scientific Return

With our uniquely incisive study of our selected sample of transitional disks, this program will 1) constrain the prevalence and spatial scales of gaps in protoplanetary disks, 2) help differentiate between competing models of physical mechanisms of disk feature formation (and potentially planetary evolution), and 3) constrain the dust grain size and species, and their spatial distribution throughput the disk. Answering these questions will provide key insights into ongoing debate on mechanisms for planetary system assembly.

F.1.6 TAC report

In the assigned category of your proposal, "Star & Planet Formation" and "ISM", 5 proposals were approved for time allocation out of 15 proposals. (Grouping of similar categories was done by TAC. Combination of categories may vary from semester to semester depending on the number of submitted proposals in each category.)

Your proposal was ranked in the top 1/3 among 10 unsuccessful proposals in this category group. Although we could not fulfill your wish this time given the limited amount of telescope time available, we would like to encourage you to try again on the next occasion. The averaged scores of your proposal rated by referees, and comments by referees and TAC if any are given below for your reference.

Referees Scores:

Overall relative score (normalized and averaged) [10(top)–0(last)]: <S> = 6.0
Absolute scores for 4 check points (averaged) [3(high)-1(low)]

- <a1> = 2.8 (Scientific importance/Originality)
- <a2> = 2.4 (Clarity of scientific justification)
- <a3> = 2.4 (Feasibility to achieve the proposed goal)
- <a4> = 2.8 (Use of telescope capability)

Scoring Description:
Each referee is asked to assign the rank value r (1 for the highest and N for the lowest) for each of the N proposals which he/she sees, by sorting them according to the order of priority (as judged from a comprehensive point of view). And this rank (r) is converted to the score (S) as S = 10 - 10(r-1)/(N-1) (i.e., S = 10.0 highest priority and S = 0.0 for the lowest). These score values from each of the referees are averaged to make the final score <S>. Meanwhile, a1, a2, a3, and a4 are the "absolute" grades, for which any of A(high=3), B(middle=2), or C(low=1) are given by referees in terms of the four check points.

Referee Comments:

1. The proposers request 3 nights of SCExAO observations to probe the inner disk regions of 9 stellar targets. As this uses new instrumentation, it is somewhat higher risk, but also has a potentially very high reward as it will explore a relatively unexplored region of these disks, so the potential for unforeseen discoveries is high. The large angular dynamic range which will be observed (from $\sim$ 10 mas with VAMPIRES to a few hundred mas with HiCIAO) is a compelling feature. The complexity of the data analysis appears daunting, but the large team appears experienced enough to deal with it.

2. The authors propose to utilize a new technique to obtain close insight of the inner region of transition disk that was unreachable with previous observational

methods. The advantages of the new technique and expected scientific outcomes are described in detail so that I am convinced that their proposed observations are vetch much worth conducting.

3. It is an interesting and unique proposal to see the innermost region of transitional disks.

4. This observation potentially give meaningful contribution to our understanding of disk evolution.

TAC Comments:
The scientific case is made strong and the observations are feasible. We wish we could allocate 2 nights as requested, but could not do so unfortunately, due to unusually high competition in this category this round. We strongly encourage the PI and the team to re-submit next round. A reviewer is a little concerned that the data analysis of SCexAO is challenging. Please be well prepared by the next semester.

European Organisation for Astronomical Research in the Southern Hemisphere

OBSERVING PROGRAMMES OFFICE • Karl-Schwarzschild-Straße 2 • D-85748 Garching bei München • e-mail: opo@eso.org • Tel.: +49 89 320 06473

APPLICATION FOR OBSERVING TIME PERIOD: **95A**

Important Notice:

By submitting this proposal, the PI takes full responsibility for the content of the proposal, in particular with regard to the names of CoIs and the agreement to act according to the ESO policy and regulations, should observing time be granted.

1. Title Category: **C–4**

Detecting circum-planetary discs around young stars with SPHERE/ZIMPOL and NACO/SAM.

2. Abstract / Total Time Requested

Total Amount of Time: 0.7 nights VM, 0 hours SM

The increasing number of known exoplanets contrast with the lack of robust detections of proto-planets around young stars. We aim to detect disks around forming sub-stellar companions surrounding two best-candidates, young intermediate-mass (Herbig Ae/Be) stars. NACO will be used to detect the dusty counterpart in the near-IR, by image reconstruction using Sparse Aperture Masking (SAM). SPHERE will be used to observe the gaseous counterpart by detecting the Hα (un-polarized) emission from planet accretion using ZIMPOL. The **combination of both instruments** will allow to confirm and improve previous detections (for HD 142527), as well as to provide the strongest observational support for possible new companions (HD 142527 and HD 100546). This is feasible by **covering a wide wavelength range** (from the optical to the near-IR), **at a similar high contrast and spatial resolution** (a minimum Δmag ~ 5 at $\lesssim 30$ mas).

3.

Run	Period	Instrument	Time	Month	Moon	Seeing	Sky	Mode	Type
A	95	SPHERE	0.3n	may	n	0.8	PHO	v	
B	95	NACO	0.4n	may	n	0.8	PHO	v	

4. Number of nights/hours Telescope(s) Amount of time

a) already awarded to this project:

b) still required to complete this project:

5. Special remarks:

This is a pilot study aiming to test the combined capabilities of SPHERE/ZIMPOL and NACO/SAM to provide robust detections of forming sub-stellar companions around two best-candidate young stars.

6. Principal Investigator: Ignacio Mendigutia, I.Mendigutia@leeds.ac.uk, UK, School of Physics and Astronomy,The University of Leeds

6a. Co-investigators:

R.D.	Oudmaijer	School of Physics and Astronomy,The University of Leeds,UK
G.	Schworer	LESIA,,F
N.	Huélamo	Centro de Astrobiologia (CSIC-INTA),E
P.	Tuthill	University of Sydney,School of Physics A28,AU

Following CoIs moved to the end of the document ...

7. Description of the proposed programme

A – Scientific Rationale: Planets are formed in circumstellar disks around low and intermediate-mass young pre-main sequence (PMS) stars (classical T Tauri -CTT, and Herbig Ae/Be -HAeBe, respectively). While there is debate on the specific process and timescale of their formation, there is consensus that planetary systems should be completely formed before $\sim$ 10 Myr, when circumstellar disks are dissipated (Haisch et al. 2001, ApJ, 553, L153). Therefore, planetary accretion rates of $\sim 10^{-10}$-10^{-9} $M_\odot$ yr^{-1} are necessary to form planets of $\sim$ 1-10 M_J on that timescale. Indeed, theoretical works indicate that protoplanets grow from circumplanetary accretion disks, providing estimates on different parameters such as the planet accretion rate decay with time, evolution of the dust disk temperature, and others (see e.g. Sabrham & Boley 2013, ApJ, 767, 63; Zhu, 2014, ApJ, preprint arXiv:1408.6554, and references therein). Despite the increasing number of observations regarding already formed planets around MS stars (e.g. http://exoplanet.eu/catalog/), there is a lack of robust detections of proto-planets around PMS objects. The observational characterization of gas and dust circumplanetary disks is therefore crucial to test our understanding of planet formation. **The advent of the new instrument SPHERE, combined with the capabilities of NACO, provide the necessary tools for a robust detection of both the accretion (gas) and dust properties of circumplanetary disks in young PMS stars.**

Most sub-stellar (planetary) companion candidates have been detected through spatially resolved observations in the near-IR -mainly from Sparse Aperture Masking (SAM)/NACO, coming from dust condensations around a few PMS stars (Húelamo et al. 2011, A&A, 528, L7). Many of these detections surround central HAeBe stars (e.g. Quanz et al. 2013,ApJ, 766, L1; Biller et al. 2014, ApJ, 792, L22; Reggiani et al. 2014, ApJ, 792, L23), since their higher brightness and relative disk sizes compared with CTTs make them the ideal candidates for high spatial resolution observations. In addition, detections of specific dust structures in circumstellar disks have been associated with ongoing planetary formation (e.g.; Boccaletti et al. 2013, A&A, 560, A20). Given it well tested performance, **we will use SAM/NACO to characterize the dusty counterpart of disks surrounding sub-stellar companions.** It is noted however that the detection of dust condensations or structures cannot be considered themselves as solid proofs of ongoing planet formation, since those could have different origins like background sources, scattered light from disk features, stellar companions, and others (see e.g. Comerón, 2012, A&A, 537, A97; Quanz et al. 2013). In principle, polarimetric analysis are not helpful in these cases, since the dust in disks around sub-stellar companions does not have a strong enough polarization signature distinctive from the surrounding circumstellar disk (e.g. Zapatero Osorio et al. 2011, ApJ, 740, 4). **A defining characteristic of circumplanetary disks is the presence of accretion, which is the second ingredient for their characterization.**

Observations of circumplanetary accretion disks have been claimed mainly from spatially resolved Hα excess emission (Zhou et al. 2014, ApJL, 783, 1). Therefore, the Hα emission is not only a quantitative accretion tracer for CTTs (Muzerolle et al. 1998, AJ, 116, 455) and HAeBe stars (Mendigutía et al. 2011, A&A, 535, A99), but has also been proposed to be the best tracer of ongoing planet formation (Close et al. 2014, ApJL, 781, L30). The only object with a characterization of both a near-IR dust condensation (through NACO/SAM, Fig. 1, Biller et al. 2012, APJL, 753, L38) spatially coincident with an excess of optical emission in Hα (through MagAO, Fig. 2, Close et al. 2014) is the late-type HAeBe star HD 142527 (Mendigutía et al. 2014, ApJ, 790, 21), which can be considered the most robust detection of a circumplanetary disk to date. A main objection is that an Hα excess spatially coincident with a dust condensation could also be optical light reflected (i.e., not related with circumplanetary accretion), since there is no guarantee that the emission arises directly from the dust condensation. The new instrument SPHERE provides the way to circumvent this problem by using **ZIMPOL polarimetric imaging with a narrow Hα filter**: an excess of Hα emission coming from an accretion circumplanetary disk should be unpolarized, in contrast with reflected, polarized light. **The spatial resolution achieved this way is the same as with NACO/SAM aperture masking in the near-IR.**

B – Immediate Objective: This pilot study aims to combine the capabilities of SPHERE/ZIMPOL and NACO/SAM to simultaneously detect possible gas and dust circumplanetary disks around two HAeBes selected to be best candidates to host sub-stellar companions (Sect. 11). SPHERE/ZIMPOL differential polarimetric imaging in Hα will provide direct information on possible ongoing planetary accretion. Image reconstruction through NACO/SAM at $\sim$ 4 μm will provide information on the dusty counterpart of the possible circumplanetary disks. **Both instruments are complementary not only in the wavelength range covered, from the optical to the near-IR, but also in their high contrasts and similar spatial resolutions (A minimum of Δmag $\sim$ 5 at $\lesssim$ 30 mas). Spatially coincident detections with both instruments will constitute the best proof of ongoing sub-stellar (planetary) formation.**

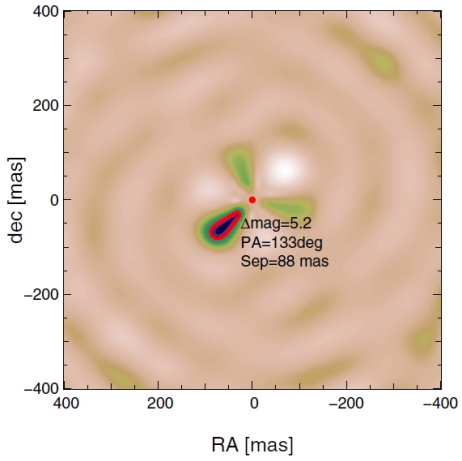

Fig. 1: Taken from Biller et al. (2012): L' band χ^2 surface as a function of RA and DEC around HD 142527, obtained from the best fit binary model to the closure phases. the minimum indicates the position of the companion (Δ mag $\sim$ 5), at 88 $\pm$ 5 mas (13 $\pm$ 2 AU at 145 pc). the red contours correspond to 3σ and 5σ error bars in the detection. It is noted that these results were obtained from the "7 holes" mask, which provide strongly model-dependent results. We aim to improve the detections by using complete image reconstruction from the "18 holes" mask.

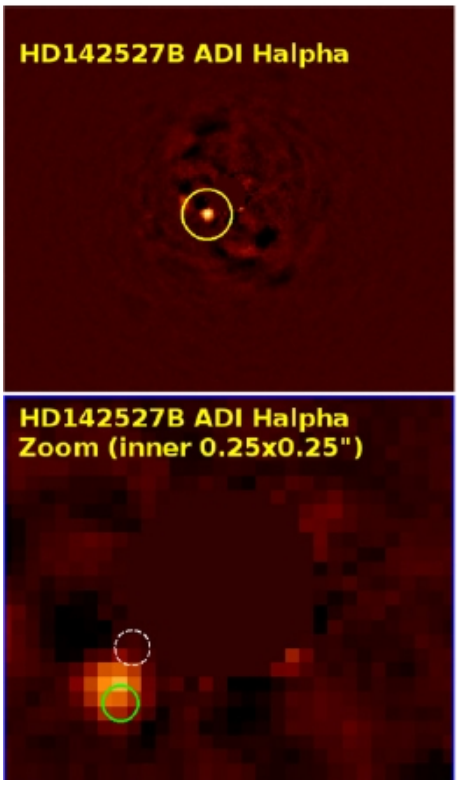

Fig. 2: Taken from Close et al. (2014): Hα Angular differential imaging around HD 142527. The 10.5σ detection (Δ mag $\sim$ 6) is spatially close with the one by Biller et al. (Fig. 1), indicated here with a green circle (note that observations were not simultaneous). The Hα detection is inconsistent with a background star position (white circle).

8. Justification of requested observing time and observing conditions

Lunar Phase Justification: The observations can be taken in bright time.

Time Justification: (including seeing overhead)

SPHERE: We plan to use ZIMPOL in polarimetric mode ("P1", without derotation), with the narrow-band Hα filter. The goal is to obtain a minimum contrast of ~ 5 magnitudes at the closest distance from the star (around 30 mas), and higher contrasts at longer distances (up to ~ 9.5 mag at ~ 100 mas). This way we can confirm and improve the previous detections for HD 142527, and find similar ones for HD 100546. To achieve this goal, the ESO Exposure Time calculator (ETC) provides exposure times of $\sim$ 1+1 hours for HD 142527 and HD 100546. The R-magnitudes in Sect. 11, a median seeing (0.8-1.2 arcsecs), and "1.2fastPOL" DIT were assumed. According with the manual, ~ 30 mins overheads should be considered for each star, including telescope preset and AO loop closing. Therefore a total of $\sim$ 3h is required with SPHERE/ZIMPOL.

NACO: In this case we will use SAM aiming to carry out image reconstruction with the filters NB3.74 and NB4.05. The sources are bright enough to use of the 18-holes mask. In addition, those bands are more important than others at shorter wavelengths, in order to disentangle the nature of possible sub-stellar companions (Zhu, 2014). The manual provides exposure times of ~ 10 s for both HD 142527 and HD 100546 (L mag ~ 4, see Sect. 11), to obtain peak counts of ~ 250 with each filter. The ETC indicates that SNR above 200 are obtained in this way. The observing time is dominated by the overheads. Our previous experience with SAM indicates that typically 2 hours time per target yields a well calibrated dataset, taking into account the overheads of telescope slewing time and optical settings of adaptive optics and dithering. Therefore, a total of ~ 4 hours is required with NACO/SAM.

8a. Telescope Justification:

This proposal requires the highest spatial resolution and contrast in the optical and the near-IR, for which the use of ZIMPOL/SPHERE and SAM/NACO is necessary.

8b. Observing Mode Justification (visitor or service):

SPHERE/ZIMPOL observations can be carried out both in visitor and service mode. Only visitor mode is offered for NACO/SAM.

8c. Calibration Request:

Standard Calibration

9. Report on the use of ESO facilities during the last 2 years

Mendigutía et al. "Multi-epoch observations of intermediate-mass pre-main sequence stars: accretion rates and accretion tracers." XShooter-VLT-088.C-0218. Observations completed at the beginnig of 2013. Data reduced and under analysis, partial results published.

Oudmaijer et al. "HD 100546: Star and planet formation at the same time - zooming in on the gas properties inside the gap." AMBER-VLT-092.D-064. Data reduced. Paper to be submitted.

Norris et al. "Sparse Aperture Masking Polarimetry of Massive Young Stellar Objects". 091.C-0806 SAMpol, weathered out.

9a. ESO Archive - Are the data requested by this proposal in the ESO Archive (http://archive.eso.org)? If so, explain the need for new data.

The data requested in this proposal is not available in the ESO archive. SPHERE is offered in P95 for the first time. 18-holes mask NACO/SAM data is not available for the stars in the sample.

9b. GTO/Public Survey Duplications:

10. Applicant's publications related to the subject of this application during the last 2 years

Ilee et al. 2014, MNRAS (accepted, see arXiv:1409.4897): Investigating the inner discs of Herbig Ae/Be stars with CO bandhead and Br Gamma emission

Mendigutía et al. 2014, ApJ, 790, 21: Stellar parameters and accretion rate of the transition disk star HD 142527 from X-Shooter

Lacour et al. 2014,IAUS, 299, 119: Probing protoplanetary disks with Aperture Masking

Ellerbroek et al. 2014, A&A, 563, A87: Relating jet structure to photometric variability: the Herbig Ae star HD 163296

Mendigutía et al. 2013, ApJ, 776, 44 Accretion Variability of Herbig Ae/Be Stars Observed by X-Shooter HD 31648 and HD 163296

Mendigutía et al. 2013, AN, 334, 129: Comparison between accretion-related properties of Herbig Ae/Be and T Tauri stars

11. List of targets proposed in this programme

Run	Target/Field	α(J2000)	δ(J2000)	ToT	Mag.	Diam.	Additional info	Reference star
AB	HD 100546	11 33 25.4	-70 11 41.2	6	6.7;4.0		B9	
AB	HD 142527	15 56 41.9	-42 19 23.3	6	8.3;3.9		F6	

Target Notes: Both stars are probably the strongest candidates hosting sub-stellar companions. The relevant R and L magnitudes are indicated in column 6 (L-magnitudes are bright enough to use 18 holes coronograph in SAM), the spectral types in Col. 8.

HD 142527 has detections of a sub-stellar companion from Hα and near-IR aperture masking, and several details were given in the figures above and references therein. We aim to confirm and improve previous detections, also providing different epoch measurements that could serve to constrain a possible orbit around the central star (During the time elapsed between the data shown in Fig. 1 and new observations in 2015, the possible companion would have completed 10% of a $\sim$ 33 years orbit).

Similarly, several reports provide circumstantial evidence of the presence of possible sub-stellar companions at several AUs from HD 100546 (e.g. Bouwman et al. 2003, A&A, 401, 577; Acke, B. & van den Ancker, M.E. 2006, A&A, 449, 267; Quanz et al. 2013, ApJ, 766, L1; Mulders et al. 2013, A&A, 557, A68; Brittain et al. 2013, ApJ, 767, 159; Brittain et al. 2014, ApJ, 791, 136; Walsh et al. 2014, ApJ, 791, L6). In this case we aim to actually detect the possible companion(s), or provide upper limits within our spatial resolution and contrast.

12. Scheduling requirements

13. Instrument configuration

Period	Instrument	Run ID	Parameter	Value or list
95	SPHERE	A	ZIMPOL-P1	None/N-Ha/FastPol
95	NACO	B	SAM IR-WFS	18holes mask, NB3.74 and NB4.05 filters.

6b. Co-investigators:

...continued from Box 6a.

S.	Lumsden	School of Physics and Astronomy,The University of Leeds,UK
B.	Norris	University of Sydney,School of Physics A28,AU
A.	Cheetham	University of Sydney,School of Physics A28,AU

F.1.7 TAC report 95A

Good pilot study to combine the capabilities of SPHERE/ZIMPOL and NACO/SAM to simultaneously detect gas and dust in circumplanetary discs around two Herbig AeBe stars. HD142527 is probably well justified as a target because it has the H-alpha emission already observed. The other source is less justified. Overall, it is not clear if this is a confirmation programme rather than giving new science

Run A (SPHERE): Alloc: 1x0.6H1 Ranking: This run has been ranked in the 2nd quartile of all runs at this telescope. Pressure: in Period 95 the number of requested nights on UT3 exceeded the available time by a factor of 2.7 . Scheduling comments: This run is approved conditionally to the effective possibility of offering SPHERE in VM during the first three months of the semester.

Run B (NACO): Alloc: 1x0.8H1 Ranking: This run has been ranked in the 2nd quartile of all runs at this telescope. Pressure: in Period 95 the number of requested nights on UT1 exceeded the available time by a factor of 3.9.

F.1.8 TAC report 98A

This proposal is a resubmission of a former accepted proposal that could not be executed due to NaCo technical failures. The aim is to detect and characterize circumplanetary disks around two known young proto-planets. The panel acknowledges the high scientific value of detecting and characterizing circum-planetary (or circumsecondary) disks and the compelling combined use of (existing) SPHERE/ZIMPOL and (future) NaCo/SAM observations. The applicants mention a "sub-stellar" detected object concerning HD142527. However, all recent results point towards a M-dwarf (0.2 M_{sol}, Biller et al. 2012; 0.13 M_{sol}, Lacour et al., 2015); the advantage of new observations using the 18-holes SAM mask over the existing 7-holes ones is not clearly explained.

GEMINI OBSERVATORY

AU-2012B-???

observing time request summary

Semester: 2015A **Observing Mode:** Classical **Gemini Reference:**

Instruments: GPI

Time Awarded: NaN **Thesis:** Yes

Band 3 Acceptable: No

Title: **Mapping the dust in planet-forming disks using polarimetric masking interferometry**

Principal Investigator: **Guillaume Schworer**

PI institution: University of Sydney, Sydney Institute for Astronomy School of Physics A28 NSW 2006, Australia

PI status: Grad Thesis

PI phone/e-mail: / guillaume.schworer@obspm.fr

Co-Investigators: Anthony Cheetham: University of Sydney, a.cheetham@physics.usyd.edu.au
Peter Tuthill: University of Sydney, p.tuthill@physics.usyd.edu.au
Barnaby Norris: University of Sydney, b.norris@physics.usyd.edu.au

---

Partner Submission Details *(multiple entries for joint proposals)*

		PI Request		NTAC Recommendation			
Partner	**Lead**	**Time**	**Min**	**Reference**	**Time**	**Min**	**Rank**
Australia	Schworer	1.0 night	1.0 night		NaN	NaN	
	Total Time	*10.0 hr*	*10.0 hr*		*0.0 hr*	*0.0 hr*	

Abstract

Intense interest has been focused upon a handful of young stellar objects believed to be in a transitional state between embedded Class II pre-main-sequence stars and more evolved Class III systems hosting a debris disk: the so-called transition disks. The confirmation of the disk-gap architecture revealed by sub-millimetre measurements and optical interferometry has inspired number of mechanisms to explain these gaps: extensive grain growth, photo evaporation, binarity and most excitingly a tidal barrier created by dynamical interaction with low-mass disk objects (such as exoplanets). These different mechanisms can be distinguished by studying the distribution of the gas and dust within the gaps. We propose here to make a pilot study in the Near-Infrared of 7 of the most promising transition disk candidates, using a novel differential polarimetric observing mode which offers unique science reach and a high contrast detection threshold at the required spatial scales.

TAC Category / Keywords

Galactic / Polarization, Planetary systems, Pre-main sequence stars, Formation, Dust

GEMINI OBSERVATORY

AU-2012B-???

observing time request summary

Scheduling Constraints

These observations would need to be executed in May, June or July to ensure all targets are observable within one night.

Observation Details (Band 1/2)

Observation	RA	Dec	Brightness	Total Time *(including overheads)*
HD 139614	15:40:46.382	-42:29:53.548	8.47 B Vega, 8.24 V Vega, 8.20 R Vega, 8.00 I Vega, 7.80 Y Vega, 7.67 J Vega, 7.33 H Vega, 6.75 K Vega	1.4 hr
Conditions: CC Any, IQ Any, SB Any/Bright, WV Any **Resources:** GPI Non Redundant Mask J Wollaston				
HD 100453	11:33:05.576	-54:19:28.538	8.09 B Vega, 7.79 V Vega, 7.80 R Vega, 7.50 I Vega, 7.20 Y Vega, 6.95 J Vega, 6.39 H Vega, 5.60 K Vega	1.4 hr
Conditions: CC Any, IQ Any, SB Any/Bright, WV Any **Resources:** GPI Non Redundant Mask J Wollaston				
HD 98800B	11:22:05.288	-24:46:39.050	10.06 V Vega, 8.38 R Vega, 8.20 I Vega, 7.50 Y Vega, 6.40 J Vega, 5.75 H Vega, 5.59 K Vega	1.4 hr
Conditions: CC Any, IQ Any, SB Any/Bright, WV Any **Resources:** GPI Non Redundant Mask J Wollaston				
HD 163296	17:56:21.288	-21:57:21.870	7.00 U Vega, 6.93 B Vega, 6.85 V Vega, 6.86 R Vega, 6.80 I Vega, 6.50 Y Vega, 6.20 J Vega, 5.53 H Vega, 4.78 K Vega	1.4 hr
Conditions: CC Any, IQ Any, SB Any/Bright, WV Any **Resources:** GPI Non Redundant Mask J Wollaston				
HD 150193A	16:40:17.923	-23:53:45.179	9.69 U Vega, 9.32 B Vega, 8.79 V Vega, 8.41 R Vega, 8.00 I Vega, 7.50 Y Vega, 6.95 J Vega, 6.21 H Vega, 5.48 K Vega	1.4 hr
Conditions: CC Any, IQ Any, SB Any/Bright, WV Any **Resources:** GPI Non Redundant Mask J Wollaston				
HD 141569	15:49:57.748	-03:55:16.343	7.22 U Vega, 7.20 B Vega, 7.12 V Vega, 7.00 R Vega, 7.00 I Vega, 6.90 Y Vega, 6.87 J Vega, 6.86 H Vega, 6.82 K Vega	1.4 hr
Conditions: CC Any, IQ Any, SB Any/Bright, WV Any **Resources:** GPI Non Redundant Mask J Wollaston				

HD 100546	11:33:25.441	-70:11:41.236	6.71 B Vega, 6.30 V Vega, 6.70 R Vega, 6.60 I Vega, 6.50 Y Vega, 6.43 J Vega, 5.96 H Vega, 5.42 K Vega	1.4 hr
Conditions: CC Any, IQ Any, SB Any/Bright, WV Any **Resources:** GPI Non Redundant Mask J Wollaston				

Scientific Justification

In recent years, intense interest has been focused upon a handful of young stellar objects believed to be in a transitional state between embedded Class II pre-main-sequence stars and more evolved Class III systems hosting a debris disk. These objects, known as transition disks, are characterized by a distinctive dip in their infra-red SED which suggests that a partially evacuated gap exists in the inner region of the protoplanetary disk (e.g. Calvet et al. 2002, ApJ, 568, 2). The profound implications for studies of planetary formation have become increasingly apparent with the confirmation of the disk-gap architecture by sub-millimetre measurements (e.g. Andrews et al. 2011, ApJ, 732, 42) and optical interferometry (e.g. Oloffson et al. 2011 A&A, 528, L6). A number of mechanisms have been proposed to cause these gaps, including extensive grain growth (Dullemond & Dominik 2005), photo evaporation (Clarke et al. 2001) and binarity (Ireland & Kraus 2008, ApJ, 678, L59), however most exciting for exoplanetary science is the potential for such systems to arise from the tidal barrier created by dynamical interaction with low-mass disk objects (e.g. Bryden et al. 1999, Papaloizou et al. 2007). These different mechanisms can be distinguished by studying the distribution of the gas and dust within the gaps. For example, a large (stellar) companion or photoevaporation would almost completely evacuate the inner regions while a less massive planetary companion would allow gas and small dust grains to exist within its orbit (Lubow et al. 1999). Furthermore, in the latter case, the measurement of the size and distribution of this material would allow the orbit and mass of the planetary companion to be constrained (Andrews et al. 2011).

This proposal builds upon our successful legacy of non-redundant masking discoveries in this area and extends it with the implementation of a differential polarimetric observing mode. Directly imaging the faint, tenuous dust in the disk which exists in such close proximity to the bright central star has proven to be observationally challenging, with previous direct imaging efforts relying on the thermal emission from the disk. Here, however, we make use of the fact that starlight scattered by dust grains in the disk can become highly polarized. By combining the high angular resolution afforded by sparse aperture masking with differential polarimetry, the unpolarized flux from the central star effectively cancels itself out, leaving a strong signal from which a high resolution dust density map can be recovered (See Figure 1). By operating at shorter wavelengths (J band), where the scattering signal is strong, we can achieve angular resolutions $\sim$3 times higher than images of thermal emission. Furthermore, since scattering is a strong function of dust grain size and wavelength, observations at multiple wavelengths we can measure the dust grain size as a function of spatial position in the disk, providing critical insight into the planetary formation process.

We have successfully demonstrated this technique in observations of the dust shells surrounding AGB stars (Norris et al., 2012, Nature, 484), wherein we observed the circumstellar shells and placed accurate constraints on the size of the shells and the size of the constituent dust grains (see Figure 1). Here, we propose a pilot study of 7 of the most favorable known transition disk objects. Simulations (Figures 1-4) imply that our data will enable us to recover the first polarized dust density map of such disks. A wealth of topical astrophysics is directly addressed by this, including the presence of sub-structure (e.g. density waves) within the disks, the geometrical extent of cavities, and the critical dust density profiles (both vertical and radial). This campaign lays the groundwork for future multi-wavelength imaging, enabling full characterization of the dust grain size as a function of spatial position in the disk.

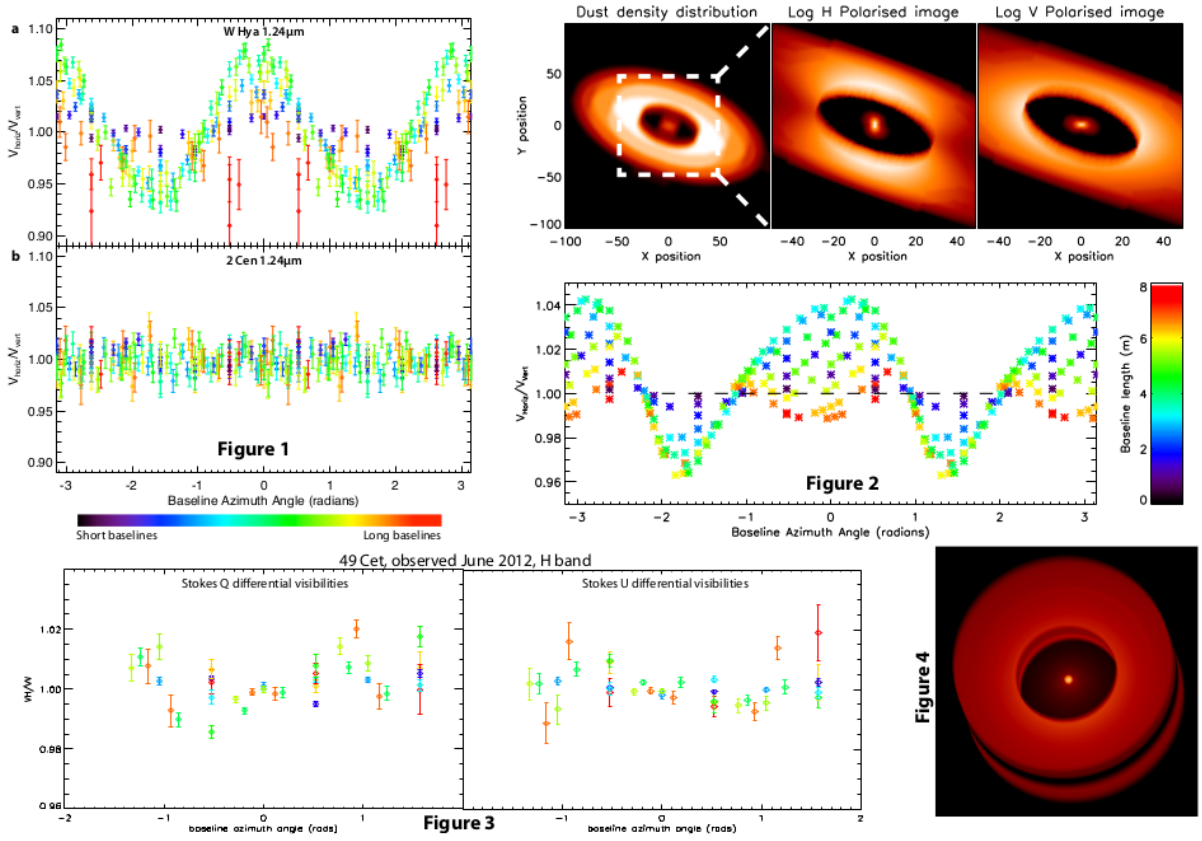

Fig. 1: The differential polarized observable obtained from a) an AGB star (W Hya) with a circumstellar dust shell and b) a star with no dust (2 Cen) from a previous observing campaign using the polarimetric aperture masking interferometry technique. The ratio of orthogonally polarized visibilities are plotted as a function of baseline azimuth (x axis) and baseline length (colour). The signal for a bare star is 1 everywhere (bottom) but when scattered by circumstellar dust shell it becomes strongly polarized (top) as a function of the azimuth. The periodic sinusoidal variation seen here is characteristic of a spherically symmetric scattering shell. Models fitted to this data at several wavelengths allowed shell geometry and grain size to be determined (Norris et al. 2012, Nature, 484). A similar method will be applied to the observations of transition disks proposed here.

Fig. 2: Simulated data from a simple model transition disk. The signal is more complex than for a spherical shell.

Fig. 3: Polarized differential visibilities for the transition disk 49 Cet, from ~1 hour of observing during June 2012 SAMPol observations. Data show the characteristic modified sinusoid of scattering by a dusty circumstellar region. Uncertainties in the longest baselines (orange & red) are large due to the low visibilities at these baselines, and will benefit from increased total integration time. Model fitting enables determination of disk geometry and density.

Fig. 4: Intensity image from a radiative transfer model of HD 142527 fitted to its SED. Full Stokes images are produced for fitting to SAMPol observations, which will allow the inner disk region to be accurately defined.

Experimental Design

The primary observations delivered by this ambitious proposal will be linear Stokes images of the polarized light in the inner disk and gap regions of our target sample. Our derived scattered-light distribution will then constrain (1) the distribution and (2) the grain size and composition of the dust in the inner regions of our sample of transition disks.

The transition disk phase represents a small fraction of the lifetime of a star, and few are known. Our target list represents the closest and brightest of these systems. Providing images of these targets at higher angular resolutions than previous studies represents a significant step forward in understanding their formation and evolution.

The angular scales we wish to explore are inaccessible through coronagraphy, due to the size of the occulting spot, and the disk structures and properties are best investigated through polarized differential quantities. To observe these systems, we will use the GPI Non Redundant Masking (NRM) mode, in combination with polarimetry. This technique was pioneered with notable success by our team at the NACO instrument on the VLT, where it was used to explore the properties of dust shells around AGB stars (Norris et al., 2012, Nature, 484). We therefore have substantial experience in construction of experiments to exploit this complex mode.

In brief, simultaneous polarization-differential imaging is delivered by use of a Wollaston Prism which splits starlight into orthogonal polarization states on-chip. The near-identical optical paths for the two states leads to a high degree of calibration precision, and what small non-common path errors there are are accurately measured and compensated by a channel-switching scheme which uses a half-wave plate upstream to periodically swap the input states. This (fairly orthodox) polarimetry setup is then reformulated in an interferometric context with the use of an aperture mask, leveraging its proven ability to deliver unsurpassed imaging fidelity for spatial structures in the limited range between about half and several diffraction-limited resolution elements from a bright stellar core (e.g. Huelamo et al. 2011 A&A 528, L7).

Data analysis will be performed using the suite of data analysis and modeling software specifically designed to analyze this differential polarimetric non-redundant masking data written by our research group in Sydney. The standard GPI pipeline will be used for extraction of the two polarization channels from the raw images.

Precise measurement of these relatively small polarization signals requires correct calibration of the residual systematic errors arising from GPI's instrumental polarization that remain even after the double-differential process. The instrumental polarization characterisation by Wiktorowicz et al. (2014, SPIE, 9147-305) should be sufficient for our purposes. As is normal for NRM observations, we require observations of point source calibrator stars with no polarized structure during the night, and have factored this into our requested time.

Finally we emphasize that these targets are observed here in a mode which provides complementary data to that obtained with the standard GPI coronagraphs, and is exempt from the GPI campaign target list duplication policy.

Technical Description

This program will employ the 10-hole Non-Redundant mask installed within the GPI instrument. The applicant list on this proposal includes all members of the GPI team responsible for commissioning this specific NRM mode. Masking interferometry is the most successful demonstrated technology with which to explore the relevant region of contrast-separation space.

With the benefit of extensive data both from laboratory testing and on-sky data, key elements of this observational mode at GPI have been fleshed out to the point where we are able to confidently predict operational parameters and limitations. This characterization also extends to the use of the polarimeter as described in the sections above.

The fractional polarization of our targets is greatest at short wavelengths, but the performance of the GPI AO system also declines here. Observing in J band provides a reasonable trade off between the expected signal and instrument performance.

Our simulated disk+star systems (Figures above), imply that measuring differential visibilities at the 1% level should be sufficient to image our targets. From on-sky performance of the GPI NRM mode, this level of performance should be provided by 24 exposures in each of 4 half-wave plate rotations.

Using previous on-sky data, we predict exposure times of between 1.45 and 20 seconds for our targets in J band. Including 20 seconds of frame write-out overhead between exposures and 15 minutes for acquisition, we expect to need 0.75-1.25 hrs per target. For our 7 targets and including 2 calibrator stars, this gives a total observing time of 10 hours, or 1 night.

Due to the incomplete commissioning of the GPI NRM mode, it is offered only for classical observing, allowing no constraints on observing conditions.

Band 3 Plan

This program is not suitable for band 3.

Classical Backup Program

This program as specified is suitable for poor conditions.

Justify Target Duplications

The GSA search revealed no duplicate observations.

See note in Experimental Design regarding duplication of GPI campaign targets.

Publications

Tuthill et al. 2010, SPIE Conference Series 7735.
Norris et al., 2012, Nature, 484.

Use of Other Facilities or Resources

There are no non-Gemini related proposals.

Previous Use of Gemini

Reference	Allocation	% Useful	Status of previous data

ITC Examples

No ITC exists for GPI.

F.1.9 TAC report

The proposal spent a lot of space exhorting the benefits of non-redundant masking. The proposers are advised that ATAC is composed of astronomers whose expertise tries to span the full range of astronomy done with Australian facilities. However, it cannot be expert in every part of astronomy, and every observing technique. In the case of non-redundant masking a short description of the key elements (i.e. doing closure-phase interferometry using baselines created by masking the 8m aperture) would have made the technique clearer to some TAC members.

In the end, however, it is the science the technique enables that is important to ATAC, rather than the technique itself. The proposing team should make sure to concentrate on the science in justifying the proposal, rather than the technique.

It was agreed that we would schedule a night of commissioning, immediately followed by your observations. We have scheduled these observations during the nights of 28 to 31 March 2015 (both inclusive). Scheduling 4 nights should give us sufficient time to test the NRM mode as well as carrying out the observations. You are kindly invited to attend these observations, which we believe will be important for their success since we have very limited experience with the NRM mode of GPI.

Bibliography

Alecian, E., Catala, C., Wade, G. A., et al. 2008, MNRAS, 385, 391 (cited on pages 122, 127, 133 and 136)

ALMA Partnership, Brogan, C. L., Pérez, L. M., et al. 2015, ApJ, 808, L3 (cited on page 18)

Andrae, R., Schulze-Hartung, T., & Melchior, P. 2010, ArXiv e-prints (cited on page 45)

Andre, P., Ward-Thompson, D., & Barsony, M. 1993, ApJ, 406, 122 (cited on page 9)

Andrews, S. M., Rosenfeld, K. A., Kraus, A. L., & Wilner, D. J. 2013, ApJ, 771, 129 (cited on page 77)

Andrews, S. M., Rosenfeld, K. A., Wilner, D. J., & Bremer, M. 2011, ApJ, 742, L5 (cited on page 3)

Andrews, S. M. & Williams, J. P. 2007, ApJ, 659, 705 (cited on page 61)

Andrews, S. M., Wilner, D. J., Hughes, A. M., Qi, C., & Dullemond, C. P. 2009, ApJ, 700, 1502 (cited on page 14)

Andrews, S. M., Wilner, D. J., Hughes, A. M., Qi, C., & Dullemond, C. P. 2010, ApJ, 723, 1241 (cited on page 14)

Andrews, S. M., Wilner, D. J., Zhu, Z., et al. 2016, ApJ, 820, L40 (cited on page 18)

Artymowicz, P. & Lubow, S. H. 1994, ApJ, 421, 651 (cited on pages 8 and 110)

Baldwin, J. E., Haniff, C. A., Mackay, C. D., & Warner, P. J. 1986, Nature, 320, 595 (cited on page 36)

Bell, C. P. M., Naylor, T., Mayne, N. J., Jeffries, R. D., & Littlefair, S. P. 2013, MNRAS, 434, 806 (cited on page 10)

Benisty, M., Perraut, K., Mourard, D., et al. 2013, A&A, 555, A113 (cited on pages 121, 122, 133 and 136)

Bergin, E. A. & Tafalla, M. 2007, ARA&A, 45, 339 (cited on page 12)

Bisyarina, A. P., Sobolev, A. M., Gorda, S. Y., & Parfenov, S. Y. 2015, Astrophysical Bulletin, 70, 299 (cited on pages 122, 133 and 136)

Born, M. & Wolf, E. 1980, Principles of Optics Electromagnetic Theory of Propagation, Interference and Diffraction of Light (cited on page 30)

Brown, J. M., Herczeg, G. J., Pontoppidan, K. M., & van Dishoeck, E. F. 2012a, ApJ, 744, 116 (cited on pages 54, 55, 77, 88, 104, 107, 108, 110 and 112)

Brown, J. M., Rosenfeld, K. A., Andrews, S. M., Wilner, D. J., & van Dishoeck, E. F. 2012b, ApJ, 758, L30 (cited on page 61)

Bruderer, S., van der Marel, N., van Dishoeck, E. F., & van Kempen, T. A. 2014, A&A, 562, A26 (cited on pages 55, 68, 71, 77, 94, 97, 104, 108 and 112)

Bryden, G., Chen, X., Lin, D. N. C., Nelson, R. P., & Papaloizou, J. C. B. 1999, ApJ, 514, 344 (cited on pages 3 and 55)

Buscher, D. F. & Longair, F. b. M. 2015, Practical Optical Interferometry (cited on page 25)

Calvet, N., D'Alessio, P., Hartmann, L., et al. 2002, ApJ, 568, 1008 (cited on page 3)

Camps, P., Misselt, K., Bianchi, S., et al. 2015, A&A, 580, A87 (cited on page 71)

Cardelli, J. A., Clayton, G. C., & Mathis, J. S. 1989, ApJ, 345, 245 (cited on pages 61 and 62)

Carmona, A., Pinte, C., Thi, W. F., et al. 2014, A&A, 567, A51 (cited on page 94)

Carpenter, J. M., Mamajek, E. E., Hillenbrand, L. A., & Meyer, M. R. 2006, ApJ, 651, L49 (cited on page 20)

Chiang, E., Kite, E., Kalas, P., Graham, J. R., & Clampin, M. 2009, ApJ, 693, 734 (cited on page 17)

Chiang, E. & Youdin, A. N. 2010, Annual Review of Earth and Planetary Sciences, 38, 493 (cited on page 17)

Christiaens, V., Casassus, S., Perez, S., van der Plas, G., & Ménard, F. 2014, ApJ, 785, L12 (cited on page 17)

Clarke, C. J., Gendrin, A., & Sotomayor, M. 2001, MNRAS, 328, 485 (cited on pages 3 and 55)

Cutri, R. M., Skrutskie, M. F., van Dyk, S., et al. 2003, VizieR Online Data Catalog, 2246 (cited on page 61)

Cuzzi, J. N., Hogan, R. C., & Shariff, K. 2008, ApJ, 687, 1432 (cited on page 18)

Dimitrova, T. L. & Weis, A. 2008, American Journal of Physics, 76, 137 (cited on page 28)

Dodson-Robinson, S. E. & Salyk, C. 2011, ApJ, 738, 131 (cited on page 111)

Draine, B. T. 2003, ARA&A, 41, 241 (cited on page 12)

Draine, B. T. 2006, ApJ, 636, 1114 (cited on pages 13 and 97)

Draine, B. T. & Lee, H. M. 1984, ApJ, 285, 89 (cited on page 77)

Draine, B. T. & Li, A. 2007, ApJ, 657, 810 (cited on page 81)

Drążkowska, J., Windmark, F., & Dullemond, C. P. 2014, A&A, 567, A38 (cited on page 17)

Duchêne, G. 1999, A&A, 341, 547 (cited on page 8)

Dullemond, C. P. & Dominik, C. 2005, A&A, 434, 971 (cited on pages 3 and 55)

Dullemond, C. P., Henning, T., Visser, R., et al. 2007, A&A, 473, 457 (cited on pages 12, 56, 107, 113 and 114)

Dullemond, C. P. & Monnier, J. D. 2010, ARA&A, 48, 205 (cited on page 3)

Duquennoy, A. & Mayor, M. 1991, A&A, 248, 485 (cited on page 8)

Duvert, G., Young, J., & Hummel, C. 2015, ArXiv e-prints (cited on page 50)

Erickson, K. L., Wilking, B. A., Meyer, M. R., Robinson, J. G., & Stephenson, L. N. 2011, AJ, 142, 140 (cited on page 61)

Evans, N., Calvet, N., Cieza, L., et al. 2009a, ArXiv e-prints (cited on page 7)

Evans, II, N. J., Dunham, M. M., Jørgensen, J. K., et al. 2009b, ApJS, 181, 321 (cited on page 10)

Fedele, D., Bruderer, S., van Dishoeck, E. F., et al. 2013, A&A, 559, A77 (cited on page 61)

Follette, K. B., Grady, C. A., Swearingen, J. R., et al. 2015, ApJ, 798, 132 (cited on pages 55, 77, 80, 88, 94 and 113)

Foreman-Mackey, D. 2016, The Journal of Open Source Software, 24 (cited on page 42)

Foreman-Mackey, D., Hogg, D. W., Lang, D., & Goodman, J. 2013, PASP, 125, 306 (cited on page 42)

Geers, V. C., Augereau, J.-C., Pontoppidan, K. M., et al. 2006, A&A, 459, 545 (cited on pages 12 and 114)

Geers, V. C., Pontoppidan, K. M., van Dishoeck, E. F., et al. 2007a, A&A, 469, L35 (cited on pages 54, 68, 77, 80, 97, 98 and 112)

Geers, V. C., van Dishoeck, E. F., Visser, R., et al. 2007b, A&A, 476, 279 (cited on page 54)

Ghez, A. M., Neugebauer, G., & Matthews, K. 1993, AJ, 106, 2005 (cited on pages 8 and 110)

Goodman, J. & Weare, J. 2009, PhD thesis, , Courant Institute, NYU (2009) (cited on page 42)

Goodman, J. W. 1985, Statistical Optics (cited on page 30)

Gorti, U. & Hollenbach, D. 2008, ApJ, 683, 287 (cited on page 56)

Greene, T. P., Wilking, B. A., Andre, P., Young, E. T., & Lada, C. J. 1994, ApJ, 434, 614 (cited on pages 9 and 10)

Haisch, Jr., K. E., Lada, E. A., & Lada, C. J. 2001, ApJ, 553, L153 (cited on page 2)

Hartigan, P., Edwards, S., & Ghandour, L. 1995, ApJ, 452, 736 (cited on page 16)

Henbest, N. & Couper, H. 1994, The guide to the galaxy (cited on page 5)

Heng, K. & Kenyon, S. J. 2010, MNRAS, 408, 1476 (cited on pages 17 and 56)

Henning, T. 2010, ARA&A, 48, 21 (cited on page 13)

Hernández, J., Calvet, N., Briceño, C., Hartmann, L., & Berlind, P. 2004, AJ, 127, 1682 (cited on page 122)

Hinkley, S., Carpenter, J. M., Ireland, M. J., & Kraus, A. L. 2011, ApJ, 730, L21 (cited on page 45)

Imanishi, K., Koyama, K., & Tsuboi, Y. 2001, ApJ, 557, 747 (cited on page 110)

Indebetouw, R., Mathis, J. S., Babler, B. L., et al. 2005, ApJ, 619, 931 (cited on page 88)

Ireland, M. J. 2013, MNRAS, 433, 1718 (cited on page 45)

Ireland, M. J. & Kraus, A. L. 2008, ApJ, 678, L59 (cited on pages 3 and 55)

Ireland, M. J., Mérand, A., ten Brummelaar, T. A., et al. 2008, in Proc. SPIE, Vol. 7013, Optical and Infrared Interferometry, 701324 (cited on pages 36 and 123)

Isella, A. & Natta, A. 2005, A&A, 438, 899 (cited on page 16)

Isella, A., Testi, L., Natta, A., et al. 2007, A&A, 469, 213 (cited on page 14)

Jeans, J. H. 1902, Philosophical Transactions of the Royal Society of London Series A, 199, 1 (cited on page 5)

Jennison, R. C. 1958, MNRAS, 118, 276 (cited on page 33)

Jochims, H. W., Ruhl, E., Baumgartel, H., Tobita, S., & Leach, S. 1994, ApJ, 420, 307 (cited on page 114)

Johansen, A., Henning, T., & Klahr, H. 2006, ApJ, 643, 1219 (cited on page 18)

Johansen, A., Oishi, J. S., Mac Low, M.-M., et al. 2007, Nature, 448, 1022 (cited on page 18)

Johnstone, D., Hollenbach, D., & Bally, J. 1998, ApJ, 499, 758 (cited on page 16)

Jones, A. P., Tielens, A. G. G. M., & Hollenbach, D. J. 1996, ApJ, 469, 740 (cited on page 115)

Juhász, A., Bouwman, J., Henning, T., et al. 2010, ApJ, 721, 431 (cited on page 13)

Kim, S.-H., Martin, P. G., & Hendry, P. D. 1994, ApJ, 422, 164 (cited on pages 77 and 88)

Kolmogorov, A. 1941, Akademiia Nauk SSSR Doklady, 30, 301 (cited on page 24)

Kraus, A. L., Ireland, M. J., Martinache, F., & Lloyd, J. P. 2008, ApJ, 679, 762 (cited on page 45)

Kroupa, P. 2002, Science, 295, 82 (cited on page 4)

Kurucz, R. L. 1979, ApJS, 40, 1 (cited on page 71)

Lacour, S., Tuthill, P., Amico, P., et al. 2011, A&A, 532, A72 (cited on page 59)

Lada, C. J. 1987, in IAU Symposium, Vol. 115, Star Forming Regions, ed. M. Peimbert & J. Jugaku, 1–17 (cited on page 9)

Lada, C. J. & Wilking, B. A. 1984, ApJ, 287, 610 (cited on page 9)

Le Bouquin, J.-B. & Absil, O. 2012, A&A, 541, A89 (cited on page 34)

Leinert, C., Zinnecker, H., Weitzel, N., et al. 1993, A&A, 278, 129 (cited on pages 8 and 110)

Li, A. & Draine, B. T. 2001, ApJ, 554, 778 (cited on page 81)

Li, A. & Greenberg, J. M. 1997, A&A, 323, 566 (cited on page 77)

Li, W., Evans, II, N. J., Harvey, P. M., & Colome, C. 1994, ApJ, 433, 199 (cited on page 121)

Liddle, A. R. 2007, MNRAS, 377, L74 (cited on page 47)

Loinard, L., Torres, R. M., Mioduszewski, A. J., & Rodríguez, L. F. 2008, ApJ, 675, L29 (cited on page 55)

Lombardi, M., Lada, C. J., & Alves, J. 2008, A&A, 489, 143 (cited on page 91)

Lubow, S. H., Seibert, M., & Artymowicz, P. 1999, ApJ, 526, 1001 (cited on pages 3 and 55)

Luhman, K. L. & Rieke, G. H. 1999, ApJ, 525, 440 (cited on page 107)

Maaskant, K. M., Min, M., Waters, L. B. F. M., & Tielens, A. G. G. M. 2014, A&A, 563, A78 (cited on pages 13, 55, 71, 77, 80, 91 and 97)

Mathis, J. S., Rumpl, W., & Nordsieck, K. H. 1977, ApJ, 217, 425 (cited on page 12)

McCaughrean, M. J. & O'dell, C. R. 1996, AJ, 111, 1977 (cited on pages 2 and 14)

McClure, M. K., Furlan, E., Manoj, P., et al. 2010, ApJS, 188, 75 (cited on page 61)

Menu, J. 2015, PhD thesis, , K.U. Leuven, (2015) (cited on page 11)

Millan-Gabet, R., Schloerb, F. P., & Traub, W. A. 2001, ApJ, 546, 358 (cited on page 121)

Monnier, J. D. 2000, in Principles of Long Baseline Stellar Interferometry, ed. P. R. Lawson, 203 (cited on page 33)

Monnier, J. D., Berger, J.-P., Millan-Gabet, R., et al. 2006, ApJ, 647, 444 (cited on pages 122, 132 and 136)

Monnier, J. D., Tuthill, P. G., Ireland, M., et al. 2009, ApJ, 700, 491 (cited on page 122)

Muto, T., Grady, C. A., Hashimoto, J., et al. 2012, ApJ, 748, L22 (cited on page 17)

Muzerolle, J., Calvet, N., & Hartmann, L. 1998, ApJ, 492, 743 (cited on page 15)

Natta, A., Grinin, V., & Mannings, V. 2000, Protostars and Planets IV, 559 (cited on page 7)

Natta, A., Prusti, T., & Krugel, E. 1993, A&A, 275, 527 (cited on pages 81 and 91)

O'dell, C. R. & Wen, Z. 1994, ApJ, 436, 194 (cited on page 2)

O'Donnell, J. E. 1994, ApJ, 422, 158 (cited on page 61)

Okamoto, Y. K., Kataza, H., Honda, M., et al. 2009, ApJ, 706, 665 (cited on page 122)

Ozawa, H., Grosso, N., & Montmerle, T. 2005, A&A, 429, 963 (cited on page 110)

Pauls, T. A., Young, J. S., Cotton, W. D., & Monnier, J. D. 2005, PASP, 117, 1255 (cited on page 50)

Piétu, V., Guilloteau, S., & Dutrey, A. 2005, A&A, 443, 945 (cited on page 14)

Pinilla, P., Benisty, M., & Birnstiel, T. 2012, A&A, 545, A81 (cited on page 111)

Pinte, C., Ménard, F., Duchêne, G., & Bastien, P. 2006, A&A, 459, 797 (cited on page 71)

Pirzkal, N., Spillar, E. J., & Dyck, H. M. 1997, ApJ, 481, 392 (cited on page 121)

Pogodin, M. A., Miroshnichenko, A. S., Tarasov, A. E., et al. 2004, A&A, 417, 715 (cited on page 136)

Ratzka, T., Köhler, R., & Leinert, C. 2005, A&A, 437, 611 (cited on pages 8 and 110)

Reipurth, B. & Zinnecker, H. 1993, A&A, 278, 81 (cited on pages 8 and 110)

Ribas, Á., Bouy, H., & Merín, B. 2015, A&A, 576, A52 (cited on page 20)

Robitaille, T. P., Whitney, B. A., Indebetouw, R., Wood, K., & Denzmore, P. 2006, ApJS, 167, 256 (cited on page 10)

Roddier, F. 1981, Progress in optics. Volume 19. Amsterdam, North-Holland Publishing Co., 1981, p. 281-376., 19, 281 (cited on page 25)

Salyk, C., Herczeg, G. J., Brown, J. M., et al. 2013, ApJ, 769, 21 (cited on page 113)

Schwarz, G. 1978, Ann. Statist., 6, 461 (cited on page 47)

Shakura, N. I. & Sunyaev, R. A. 1973, A&A, 24, 337 (cited on page 76)

Siebenmorgen, R. & Krügel, E. 2010, A&A, 511, A6 (cited on page 56)

Siess, L., Dufour, E., & Forestini, M. 2000, A&A, 358, 593 (cited on pages 88, 89, 90 and 110)

Stelzer, B., Huélamo, N., Micela, G., & Hubrig, S. 2006a, A&A, 452, 1001 (cited on page 110)

Stelzer, B., Micela, G., Hamaguchi, K., & Schmitt, J. H. M. M. 2006b, A&A, 457, 223 (cited on page 110)

Strom, K. M., Strom, S. E., Edwards, S., Cabrit, S., & Skrutskie, M. F. 1989, AJ, 97, 1451 (cited on pages 19 and 20)

Szűcs, L., Apai, D., Pascucci, I., & Dullemond, C. P. 2010, ApJ, 720, 1668 (cited on page 10)

ten Brummelaar, T. A., McAlister, H. A., Ridgway, S. T., et al. 2005, ApJ, 628, 453 (cited on page 35)

Tielens, A. G. G. M. 2008, ARA&A, 46, 289 (cited on pages 13, 81, 94, 114 and 115)

Tuthill, P. G. 1994, PhD thesis, Univ. of Cambridge, (1994) (cited on page 36)

van Cittert, P. H. 1934, Physica, 1, 201 (cited on page 30)

van der Marel, N., van Dishoeck, E. F., Bruderer, S., et al. 2016, A&A, 585, A58 (cited on pages 55 and 108)

van der Marel, N., van Dishoeck, E. F., Bruderer, S., et al. 2013a, Science, 340, 1199 (cited on page 17)

van der Marel, N., van Dishoeck, E. F., Bruderer, S., et al. 2013b, Science, 340, 1199 (cited on pages 55, 61, 68, 77, 97, 111 and 112)

van Kempen, T. A., van Dishoeck, E. F., Salter, D. M., et al. 2009, A&A, 498, 167 (cited on page 61)

Vicente, S. M. & Alves, J. 2005, A&A, 441, 195 (cited on page 13)

Weidenschilling, S. J. 1977, MNRAS, 180, 57 (cited on pages 15 and 94)

Weingartner, J. C. & Draine, B. T. 2001, ApJ, 548, 296 (cited on page 81)

Wilking, B. A., Lada, C. J., & Young, E. T. 1989, ApJ, 340, 823 (cited on page 54)

Williams, J. P. & Cieza, L. A. 2011, ARA&A, 49, 67 (cited on pages 7, 10, 17, 20, 55 and 108)

Wood, K., Wolff, M. J., Bjorkman, J. E., & Whitney, B. 2002, ApJ, 564, 887 (cited on page 77)

Wright, E. L., Eisenhardt, P. R. M., Mainzer, A. K., et al. 2010, AJ, 140, 1868 (cited on page 61)

Wyatt, M. C. 2008, ARA&A, 46, 339 (cited on page 2)

Wyatt, M. C., Panić, O., Kennedy, G. M., & Matrà, L. 2015, Ap&SS, 357, 103 (cited on pages 19, 107, 108 and 109)

Zacharias, N., Monet, D. G., Levine, S. E., et al. 2005, VizieR Online Data Catalog, 1297 (cited on page 61)

Zinnecker, H. & Yorke, H. W. 2007, ARA&A, 45, 481 (cited on page 10)

Résumé

The dust- and gas-rich disks surrounding numerous pre-main-sequence stars are of key interest for unveiling how planetary system are formed, and are the initial conditions for planetary formation. Protoplanetary disks have a rich structure, with different physics, e.g., radiation, gravitation, electrostatic, magneto-hydrodynamics, playing a role in different regions of the disk. They are under constant evolution, due to a combination of various physical and chemical processes, e.g., accretion, photo-evaporation, gas-dust interactions, grain growth, and the potential interaction with massive bodies forming within the disk. The overall disk structure, and hence its observational appearance, is a good proxy for the ongoing processes.

This PhD reports the first direct imaging of the full extents of a polycyclic aromatic hydrocarbon and very small grains ring in a young circumstellar disk, presents a revised model for the IRS-48 object to explain the rich and complex dust- and gas-environment observed from near-infrared to centimeter wavelengths, and sets limits on how much silicates grains, hence replenishment, is to be expected in the PAH and VSG ring. Also, an improved astrometric orbit and the spectral type of the spectroscopic binary MWC-361 are determined. This leads to a precise characterization of the stellar parameters of this binary, opening a new window on the studying of the disappearance of the circumsecondary disk of the binary, while the circumprimary disk is present.

Mots Clés

Interferometry, model-fitting, Bayes analytics, disk dissipation, circumstellar disk, young stellar object, IRS-48, MWC-361

Abstract

La poussière et le gaz qui entourent beaucoup d'étoiles jeunes est d'un intérêt critique pour comprendre la formation planétaire; ils représentent les conditions initiale de la formation planétaire. Les disques proto-planétaire ont une structure riche, avec différents processus physiques à l'œuvre dans différentes régions du disque. Les grandeurs en jeu s'étalent sur plusieurs ordres de grandeur en échelles spatiales, période orbitale, températures, et bien plus en ce qui concerne la densité de gaz et poussière. Les variations extrêmes de ces paramètres clés impliqués dans la structure et la composition de ces objets impliquent nécessairement l'utilisation combinée de différentes techniques d'observation.

Ce travail a permis d'imager pour la première fois l'intégralité spatiale d'un disque composé d'hydrocarbures polycyclique aromatique (PAH) et de très petits grains autour d'un objet stellaire jeune. Il propose un modèle révisé pour cet objet de façon à expliquer l'environnement riche et complexe de gaz et poussières observé en proche infrarouge et en ondes millimétriques, et pose des limites sur la quantité attendue de grains silicatés qui peut se trouver dans ce disque. Aussi, une nouvelle orbite astrométrique ainsi que les types spectraux de la binaire spetroscopique MWC-361 sont déterminés. Ceci permet la détermination précise des paramètres stellaires de la binaire, rendant possible l'étude future des causes de la disparition du disque circumsecondaire, alors que le disque circumprimaire est toujours présent.

Keywords

Interférométrie, ajustement de modèles, analyse Bayesienne, dissipation des disques, disques circumstellaires, objets stellaires jeunes, IRS-48, MWC-361